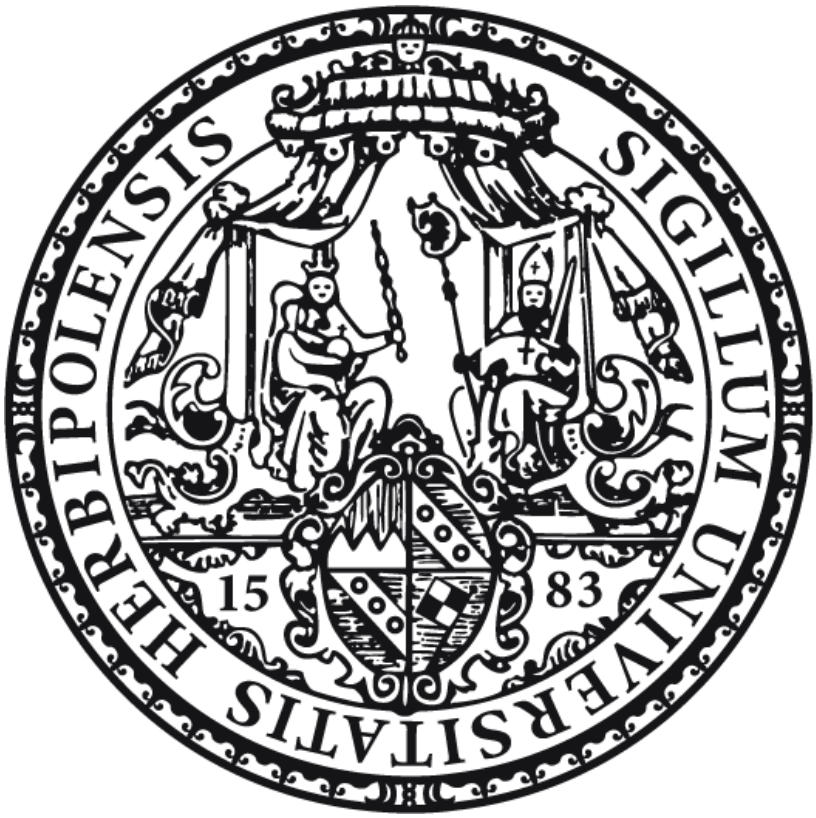

NRF2 links antioxidant and immune-relevant features in melanoma

NRF2 verknüpft antioxidative und immunrelevante Eigenschaften im Melanom

Doctoral thesis for a doctoral degree at the Graduate School of Life Sciences,
Julius-Maximilians-Universität Würzburg,
Section Biomedicine

submitted by
Christina Jessen

from
Eckernförde

Würzburg, 2020

Submitted on: .....

Office stamp

Members of the thesis committee

Chairperson:	Prof. Dr. Manfred Gessler
Primary Supervisor:	Prof. Dr. Svenja Meierjohann
Supervisor (Second):	Prof. Dr. Thomas Rudel
Supervisor (Third):	Prof. Dr. Stefan Gaubatz

Date of Public Defence: .....

Date of Receipt of Certificates: .....

Substantial parts of this thesis were published in the following article:

Jessen C, Kreß JKC, Baluapuri A, Hufnagel A, Schmitz W, Kneitz S, Roth S, Marquardt A, Appenzeller S, Ade CP, Glutsch V, Wobser M, Friedmann-Angeli JP, Mosteo L, Goding CR, Schilling B, Geissinger E, Wolf E, Meierjohann S. "The transcription factor NRF2 enhances melanoma malignancy by blocking differentiation and inducing COX2 expression" *Oncogene*, **in press**, https://doi.org/10.1038/s41388-020-01477-8

Table of Contents

1. Summary

The transcription factor NRF2 is considered as the master regulator of cytoprotective and ROS-detoxifying gene expression. Due to their vulnerability to accumulating reactive oxygen species, melanomas are dependent on an efficient oxidative stress response, but to what extent melanomas rely on NRF2 is only scarcely investigated so far. In tumor entities harboring activating mutations of NRF2, such as lung adenocarcinoma, NRF2 activation is closely connected to therapy resistance. In melanoma, activating mutations are rare and triggers and effectors of NRF2 are less well characterized.

This work revealed that NRF2 is activated by oncogenic signaling, cytokines and pro-oxidant triggers, released cell-autonomously or by the tumor microenvironment. Moreover, silencing of NRF2 significantly reduced melanoma cell proliferation and repressed well-known NRF2 target genes, indicating basal transcriptional activity of NRF2 in melanoma. Transcriptomic analysis showed a large set of deregulated gene sets, besides the well-known antioxidant effectors. NRF2 suppressed the activity of MITF, a marker for the melanocyte lineage, and induced expression of epidermal growth factor receptor (EGFR), thereby stabilizing the dedifferentiated melanoma phenotype and limiting pigmentation markers and melanoma-associated antigens. In general, the dedifferentiated melanoma phenotype is associated with a reduced tumor immunogenicity. Furthermore, stress-inducible cyclooxygenase 2 (COX2) expression, a crucial immune-modulating gene, was regulated by NRF2 in an ATF4-dependent manner. Only in presence of both transcription factors was COX2 robustly induced by H_2O_2 or TNFα. COX2 catalyzes the first step of the prostaglandin E2 (PGE2) synthesis, which was described to be associated with tumor immune evasion and reduction of the innate immune response.

In accordance with these potentially immune-suppressive features, immunocompetent mice injected with NRF2 knockout melanoma cells had a strikingly longer tumor-free survival compared to NRF2-proficient cells. In line with the *in vitro* data, NRF2-deficient tumors showed suppression of COX2 and induction of MITF. Furthermore, transcriptomic analyses of available tumors revealed a strong induction of genes belonging to the innate immune response, such as *RSAD2* and *IFIH1*. The expression of these genes strongly correlated with immune evasion parameters in human melanoma datasets and NRF2 activation or PGE2 supplementation limited the innate immune response *in vitro*.

In summary, the stress dependent NRF2 activation stabilizes the dedifferentiated melanoma phenotype and facilitates the synthesis of PGE2. As a result, NRF2 reduces gene expression of the innate immune response and promotes the generation of an immune-cold tumor microenvironment. Therefore, NRF2 not only elevated the ROS resilience, but also strongly contributed to tumor growth, maintenance, and immune control in cutaneous melanoma.

2. Zusammenfassung

Der Transkriptionsfaktor NRF2 gilt als Masterregulator der antioxidativen Zellantwort. Im Melanom ist die Rolle von NRF2 bisher nur wenig untersucht worden, obwohl das Melanom anfällig für oxidativen Stress ist und somit eine besondere Abhängigkeit von antioxidativen Prozessen besteht. In Tumorentitäten mit NRF2 aktivierende Mutationen, wie z.B. dem Lungenadenokarzinom, ist die NRF2 Aktivierung mit einer Therapieresistenz verbunden. Allerdings sind diese aktivierenden Mutationen im Melanom selten und Mechanismen, die zu einer NRF2 Aktivierung führen, sind kaum bekannt.

Die vorliegende Arbeit zeigt, dass NRF2 hier vor allem durch onkogene Signalwege, Zytokine und pro-oxidative Trigger aktiviert wird. Zudem verringerte die NRF2 Inhibierung die Zellproliferation und reduzierte die Expression von bekannten NRF2 Zielgenen. Dies weist darauf hin, dass die basale Transkriptionsaktivität von NRF2 im Melanom wichtig ist. Neben den bekannten Zielgenen waren außerdem eine Vielzahl von ROS-unabhängigen Gen-Sets dereguliert. Zum einen reduzierte NRF2 die Aktivität von MITF, dem melanozytären *Lineage Marker* und induzierte die Expression des epidermalen Wachstumsfaktorrezeptors, EGFR. Dadurch stabilisiert NRF2 den undifferenzierten Melanom-Phänotyp, welcher allgemein mit einer verminderten Expression von Pigmentierungsmarkern und Melanom-assoziierten Antigenen verbunden ist. Zum anderen regulierte NRF2 die Expression von Cyclooxygenase 2 (COX2), in Abhängigkeit von dem Transkriptionsfaktor ATF4. COX2 wurde basal und nach H_2O_2 oder TNFα Stimulation nur in Anwesenheit beider Transkriptionsfaktoren exprimiert. COX2 katalysiert die Prostaglandin E2 (PGE2) Synthese und es wurde beschrieben, dass hohe Konzentrationen an PGE2, sowohl die Immunevasion von Tumoren erleichtert als auch die angeborenen Immunantwort reduziert.

In Übereinstimmung mit diesen potenziell immun-evasiven Eigenschaften zeigten immunkompetente Mäuse, denen NRF2-knockout Melanomzellen injiziert wurden, im Vergleich zu Kontrollzellen, ein deutlich längeres tumorfreies Überleben. Die NRF2-abhängige COX2 Erhöhung und MITF Hemmung, wurde zudem in den Maustumoren bestätigt. Darüber hinaus zeigten die NRF2-defizienten Tumore eine starke Induktion von Genen des angeborenen Immunsystems, wie z.B. *RSAD2* und *IFIH1*. Die Expression dieser Gene korrelierte mit Immunevasionsparametern in Datensätzen des humanen Melanoms und eine NRF2 Aktivierung oder PGE2 Zugabe unterdrückte die Genexpression der angeborene Immunantwort bereits *in vitro*.

Somit stabilisiert stress-induziertes NRF2 den undifferenzierten Melanom-Phänotyp und fördert die immunmodulierende PGE2 Produktion. Infolgedessen reduziert NRF2 die angeborene Immunantwort und unterstützt die Entstehung einer immun-suppressiven Tumormikroumgebung, welche das Tumorwachstum erleichtert. Die endogene NRF2 Aktivierung im Melanom fördert somit nicht nur die ROS-Resilienz, sondern auch die Tumoraufrechterhaltung und das Tumorwachstum im immunkompetenten Organismus.

3. Introduction

3.1 Melanoma – a severe type of skin cancer

Skin cancer – often emerging on sun exposed areas – is characterized by an abnormal growth of skin-associated cells. It is one of the most frequent types of malignant neoplasms and can be classified into two major subtypes, melanoma and non-melanoma skin cancer (NMSC). The two largest groups of NMSC are the basal cell carcinoma (BCC) and the squamous cell carcinoma (SCC), both develop from epidermal cells, the keratinocytes. Keratinocytes account for the majority of cells in the epidermis. BCC arises from basal cells, which generate new skin cells in the bottom of the epidermis. Unlike SCC, which emerges from squamous cells, located in the middle and outer layer of the epidermis. Another rare, but highly aggressive NMSC is the Merkel cell carcinoma (MCC), arising from Merkel cells in the deepest epidermal layer.
On the contrary, melanomas arise from melanin-producing cells, the melanocytes. Melanocytes are located at the epidermal - dermal junction of the skin, but also in the uvea, mucosa and to a lesser extent in a wide range of other tissues. Therefore, melanomas develop from melanocytes in any part of the body. Different melanoma subtypes are further characterized according to their location, such as skin cutaneous melanoma (SKCM), uveal melanoma or mucosal melanoma. Even though, all skin cancer types indicate worldwide a rising incidence over the last decades, melanoma is associated with a higher mortality rate than NMSC. This high mortality rate is related to the high metastatic capacity, primarily of SKCM, the most common form of melanoma in Caucasians [1].

3.1.1 Skin cutaneous melanoma – Progression from melanocytes to melanoma

Like mentioned above, skin cutaneous melanoma arises from melanocytes, which derive from the progenitor cells of the neural crest. The primary function of melanocytes is the photoprotection of other skin cells. Synthesis of melanin and transfer of melanin-containing melanosomes into neighboring keratinocytes protects against DNA damage, induced by ultraviolet radiation (UVR). Keratinocytes play a crucial role in the stimulation of melanocyte functions by secretion of cytokines and growth factors. One example is the p53-dependent secretion of α-melanocyte-stimulating hormone (α-MSH), an agonist of the melanocortin 1 receptor (MC1R). MC1R is expressed on the surface of melanocytes and activates cAMP signaling, which in turn promotes the melanin synthesis, also known as melanogenesis [2]. The MC1R belongs to the family of G-protein coupled receptors (GPCRs) and ligand binding results in the transmission of $G_{\alpha s}$ proteins, which stimulate adenylyl cyclase (AC) activity. The AC enzyme cleaves cytoplasmic adenosine triphosphate (ATP) to generate cyclic adenosine monophosphate (cAMP), which serves as a second messenger in eukaryotic signal transduction.

Increased cAMP levels activate the protein kinase A (PKA), which translocates into the nucleus to phosphorylate the cAMP response element-binding protein (CREB). CREB recruits transcriptional coactivators and activates transcription by binding to the cAMP response element (CRE) of its target genes [3]. An important target of cAMP signaling is the microphthalmia-associated transcription factor (MITF). MITF possess a CRE consensus motif in its promoter region and is a crucial regulator of the melanin production [4]. This signaling pathway, is also called the "tanning response", which provides delayed protection against further UVR-induced DNA damage by melanin synthesis. Two distinct types of melanin are important in the skin, the black-brownish eumelanin, responsible for the photoprotective effect, as well as the yellow-reddish pheomelanin. Reduced activity of MC1R, e.g. caused by polymorphisms, impairs eumelanin production and causes a red hair/fair skin phenotype, which is associated with an increased susceptibility for melanoma development [5, 6]. The loss of the photoprotective eumelanin causes an increase of DNA damage and oxidative stress, due to the cytotoxic and carcinogenic effects of UVR [6]. Moreover, for pheomelanin synthesis cysteine is needed, which in turn limits the cysteine supply for antioxidant mechanisms [7], which further increases oxidative stress and DNA damage. Both types of melanin share the same first synthesis step, the conversion of tyrosine to dopaquinone, which is catalyzed by the rate-limiting enzyme tyrosinase (*TYR*). For eumelanin synthesis, dopaquinone is converted into dopachrome by the dopachrome tautomerase (*DCT*) and further conversion to eumelanin is catalyzed by tyrosinase related protein 1 (*TYRP1*). In the presence of the sulfur-containing amino acid L-cysteine (Cys), dopaquinone is converted into pheomelanin. The transcription of the pigmentation-related enzymes *TYR*, *DCT* and *TYRP1* is controlled by MITF [8, 9].

In contrast to keratinocytes, melanocytes display a longer lifespan, due to a slow-proliferative phenotype and anti-apoptotic mechanisms [10, 11]. Thus, melanocytes and melanin production must be tightly regulated, and loss of this control, e.g. by deregulated signal transduction, causes malignant transformation to melanoma.

A well-established model for melanocyte development into advanced melanoma is the Clark model of tumor progression (Figure 1) [12].

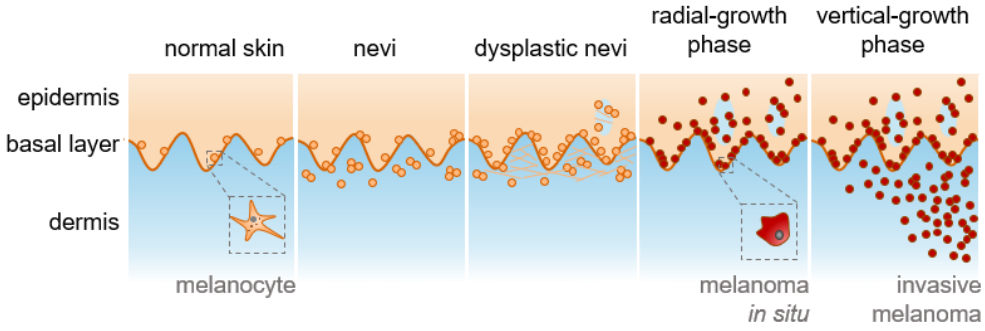

Figure 1 – Progression from melanocytes to advanced melanoma
Schematic overview of melanocytic tumor progression. Normal melanocytes form benign nevi after initial mutation events. Atypical growth of nevi leads to formation of dysplastic nevi, which can further progress to melanoma *in situ*. Melanoma *in situ* is characterized by an intra-epidermal irregular growth pattern, referred to as radial-growth-phase. Melanomas become invasive after entering the vertical-growth phase. By infiltration of vascular systems melanoma migrate to distant sites and form metastasis. Figure based on Clark model, modified from [17].

The Clark model is based on histopathological and morphological differences between the individual transformation steps of melanocytes. If melanocytes change their appearance from a dendritic-like morphology to a more oval shaped one, melanocytic nevi are formed. Those hyperplastic lesions are benign proliferations, which frequently develop after acquisition of an initiating mutation, such as the oncogene *BRAF*^{V600E} [13] and reside in a senescence-like state. Genetic analysis revealed that most nevi never progress to melanoma and remain as nests in the epidermal basal layer [14]. Thus, dysplastic nevi often arise *de novo* and rarely from benign hyperplasia, in contrast to the progressive Clark model [12, 14]. Those pre-malignant lesions are larger, have irregular borders and a higher mutational burden than benign lesions [15, 16]. Dysplastic nevi remain in the epidermis but display a lateral growth. A high number of dysplastic nevi is associated with an increased risk for melanoma development [17]. The transformation to melanoma is defined by the accumulation of pathogenic alterations and an irregular cell proliferation throughout all layers of the epidermis. Thus, the cells pass into a radial-growth-phase (RGP) [15]. This state of precursor lesions is called melanoma *in situ* and can be successfully treated by complete surgical resection. Once melanoma cells invade the dermis, they have entered the vertical-growth-phase (VGP) and have become invasive [15]. Finally, when melanoma cells dissociate from the primary tumor and move to distant sites, they have become metastatic and are able to infiltrate the vascular and lymphatic system [15, 16]. Notably, most melanomas never undergo all described stages during malignant transformation, hence the linear progression from melanocytes to melanoma cannot be generalized [14]. The Clark model can rather be interpreted as visualization of the histopathological appearance of the stages [12]. In contrast to that, recent classifications also consider the mutational changes and genetic evolution during melanoma development. In general, each developmental stage is associated with an increase of the mutational burden during progression from precursor lesions to melanomas [14].

3.1.2 Genetic alterations in skin cutaneous melanoma

Melanoma displays one of the highest mutation frequencies compared to other tumor entities [18]. The high mutational heterogeneity results from the accumulation of somatic mutations, which are caused by DNA damages induced by the high UV exposure [19]. Analysis of the genetic alterations during melanoma progression identified a distinct evolutionary process for individual melanocytic neoplasia and melanoma subtypes [14, 20]. As an initiating event for melanocytic transformation an activating mutation in an oncogene occurs, which is followed by loss of a tumor suppressor during progression.

The primary oncogenic event is generally associated with the activation of the mitogen-activated protein kinase (MAPK) signaling cascade, which results in the induction of proliferation-related genes, like *MYC*, *MITF* or members of the AP1 family. Under physiological conditions, the MAPK signaling cascade is activated by extracellular ligand

binding on receptor tyrosine kinases (RTK) that causes dimerization and autophosphorylation of the cytosolic receptor domain. This recruits cytoplasmic docking proteins, like growth factor receptor bound protein 2 (GRB2), containing an SH2 domain and acting as signaling molecule for guanine nucleotide exchange factors, such as SOS1. Once this gets activated, it leads to the exchange of GDP to GTP, which binds and activates membrane-bound RAS protein. RAS in turn activates the RAF protein kinase, which leads to the phosphorylation of MEK and finally MAPK, also known as extracellular signal-regulated kinases (ERK) and activates downstream transcription factors [21] (Figure 2). Activating mutations occur throughout the pathway, but with 50 % the most common mutation in melanoma is a point mutation in the *BRAF* gene [22]. The mutation usually leads to the substitution of the amino acid valine (V) to glutamic acid (E) or lysine (K) at position 600. This mutation is sufficient for the formation of benign nevi, but not for further malignant transformation [23, 24]. Other activating alterations are located upstream of BRAF, for example point mutations in the *NRAS* gene. Almost 30 % of melanomas harbor a mutation in NRAS at position 61 (Q61K/L/R/H), resulting in amino acid point mutation and activation of the MAPK signaling cascade [22]. *NRAS* and *BRAF* mutations are mutually exclusive, which demonstrates their roles in the same pathway. By classification of melanoma into chronically sun damaged (CSD) and not chronically sun damaged (non-CSD) cutaneous melanoma [16, 25], the *NRAS* and *BRAF* mutations arise more likely on skin with intermittent UV exposure [14, 20, 24]. This classification is based on mutational signatures and anatomic sites of the melanomas.

The proto-oncogene RAS acts as an intersection between the MAPK pathway and the PI3K/AKT signaling cascade. The PI3K/AKT signaling pathway can be activated by extracellular stimuli through RTKs and by the RAS protein. RAS recruits the catalytic subunit, p110, of the phosphatidylinositol-4,5-bisphosphate 3-kinase (PI3K) to the membrane, which has a conserved Ras binding domain (RBD) [26]. The PI3K heterodimer is activated after recruitment of the regulatory p85 subunit. This results in the phosphorylation of the PI3K substrate phosphatidylinositol-(4,5)-bisphosphate (PIP2) to phosphatidylinositol- (3,4,5)-trisphosphate (PIP3). The reverse conversion of PIP3 to PIP2 is catalyzed by the tumor suppressor phosphatase and tensin homolog (PTEN). PIP3 serves as a docking site for the SH domains of several proteins, such as phosphoinositide-dependent kinase-1 (PDK1) and protein kinase B (PKB or AKT). This activation of the PI3K/AKT pathway promotes cell proliferation and reduces apoptotic mechanisms (Figure 2) [27]. In melanoma, the PI3K/AKT pathway as well as the MAPK signaling pathway are also activated by mutations in RTKs, such as ERBB4 and c-KIT, the latter mostly occurring in mucosal melanoma [28-30]. Mutations in RTKs occur mostly as secondary oncogenic events, responsible for the transition to the next progression stage.

For the malignant transformation, the accumulation of various oncogenic events is necessary. This includes several gain-of-function as well as loss-of-function alterations, resulting in growth advantages. Around 20 % of melanoma harbor a loss-of-function

mutation in the PI3K/AKT pathway inhibitor PTEN [22]. Loss of neurofibromin 1 (NF1), the negative regulator of RAS signaling also occurs in 14 % of melanoma patients [22].
The mutations mentioned above are somatic mutations, associated with sporadic melanoma. Moreover, there are also genetic predispositions that cause familial melanoma. The most prominent germline mutations are alterations in cell cycle related genes, such as cyclin-dependent inhibitor 2A (*CDKN2A*) and cyclin-dependent kinase 4 (*CDK4*). Both proteins are involved in cell cycle control and progression. The *CDKN2A* locus encodes for two distinct proteins, INK4A, an inhibitor of CDK4 and the alternative reading frame (ARF). ARF initiates p53-dependent cell cycle arrest and apoptosis. In melanoma, mutations of those genes causes loss of cell cycle control [31, 32]. It was also reported that germline mutations in RTKs may increase the risk for melanoma development [23]. The MC1R variants of the red hair/fair skin phenotype, mentioned above, are also germline alterations, with an increased risk for BRAF-mutant melanoma [5, 33]. Taken together, melanocytes accumulate various genetic alterations, caused by UVR-induced DNA damage. The genetic mutations promote the malignant transformation and the mutational heterogeneity of melanomas. As explained in the following, the discovery of these alterations improved the treatment options for melanoma drastically.

3.1.3 Current therapeutic strategies

As mentioned before, early stage melanoma is cured by surgical resection of the malignant lesion. However, treatment of unresectable advanced melanoma remains challenging. Twenty years ago, melanoma was a devastating and fatal disease, without any effective treatment options after metastasizing. The standard care of treatment included chemotherapy with dacarbazine and immunotherapy with interleukine-2 (IL-2) [34, 35], which, however, did not significantly extend the patients' median overall survival of nine months. Fortunately, during the last decade, the treatment landscape of melanoma dramatically improved. Substantial clinical benefits are achieved by targeted therapy options and by immune checkpoint inhibition.

3.1.3.1 Targeted therapy

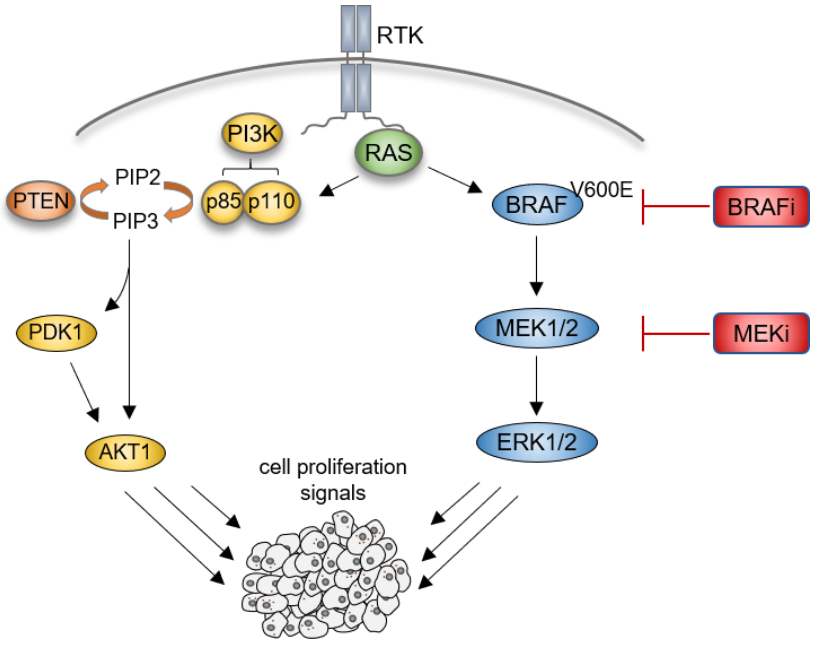

Figure 2 – Inhibition of the activated MAPK signaling pathway by targeted therapy in melanoma
MAPK signaling cascade is activated in melanoma by mutations in RTK, RAS or BRAF. PI3K signaling is activated by recruitment of the subunit p110 to membrane-bound RAS and subsequent recruitment of the regulatory p85 subunit. Activated PI3K phosphorylates PIP2 to PIP3, which leads to activation of PDK1 and AKT1. Activation of both signaling pathways leads to cell survival and proliferative signals. Activated MAPK signaling is inhibited by BRAF inhibitors (BRAFi), such as vemurafenib in combination with MEK inhibitors (MEKi), such as trametinib.

The targeted therapy for advanced melanoma treatment is based on the blockage of MAPK signaling by small molecule inhibitors (Figure 2). Since around half of melanomas harbor the activating $BRAF^{V600E/K}$ mutation, highly selective $BRAF^{V600E/K}$ inhibitors were developed. In 2011, vemurafenib the first selective BRAF inhibitor was approved by the U.S. Food and Drug Administration (FDA) and the European Medicines Agency (EMA) [36, 37]. Vemurafenib significantly improved overall and progression free survival rates compared to dacarbazine treatment [38, 39]. Furthermore, targeted therapy with BRAF inhibitors displayed lesser adverse effects and a high tolerance compared to conventional chemotherapy. However, after an initial rapid treatment response and tumor regression, patients develop resistances towards targeted therapy after around six months of treatment [40]. Resistance mechanisms involve acquired genomic and non-genomic alterations, most frequently causing reactivation of MAPK signaling [41-43]. Since, activated BRAF signaling is dependent on downstream MEK activation, MEK inhibitors were developed [44]. The combination therapy of BRAF together with MEK inhibition demonstrates an even better overall survival compared to BRAF inhibitor monotherapy. Even though the patients' relapse is delayed by several months, the development of resistances is still an issue to overcome [45-48].

3.1.3.2 Immunotherapy – checkpoint inhibition

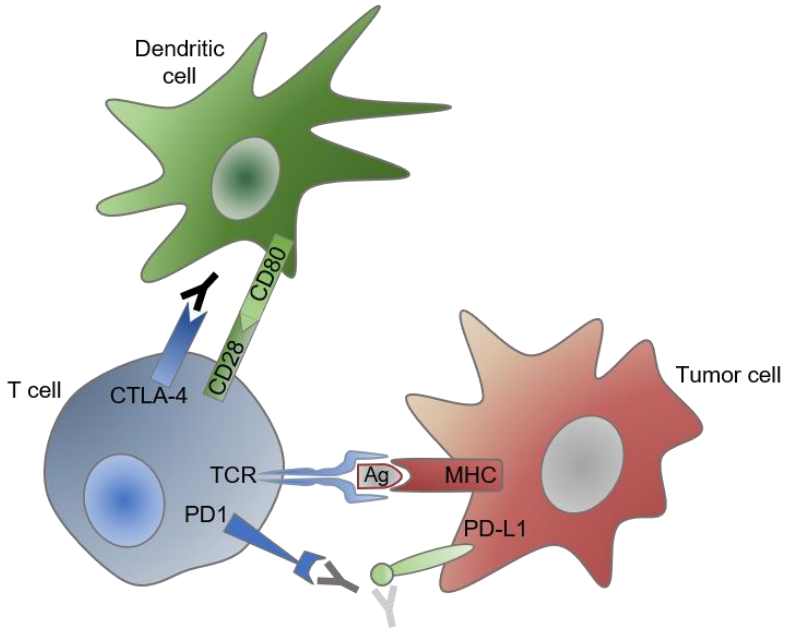

Figure 3 – Immunotherapy by checkpoint inhibition
Schematic overview of T cell activation by antigen presenting cells, such as dendritic cells or tumor cells. The antigen (Ag) is presented by the major histocompatibility complex (MHC) and bound by the T cell receptor (TCR). Simultaneous binding of CD28 and CD80 receptor of dendritic cells gives a positive activating signal, activating the T cell. Inhibitory signals are induced by binding of CTLA-4 to CD80 or PD-L1 of the tumor cell to PD1 at the T cell surface. During immune checkpoint inhibition therapy, these checkpoints are inhibited by specific antibodies. Overview was modified from [56]

In addition to the targeted therapy, immune checkpoint inhibition has gained increasing relevance in melanoma therapy in the last years. This kind of immunotherapy potentiates the host anti-tumor immune response by immune checkpoint inhibition with specific monoclonal antibodies. The expression of immune checkpoint molecules on the surface of tumor and dendritic cells suppresses T cell activation, thus leading to tumor immune evasion (Figure 3). The first approved antibody, ipilimumab, targets cytotoxic T-lymphocyte-associated antigen 4 (CTLA-4), expressed on dendritic cells, and enhances overall survival of patients with metastatic melanoma [49], but also causes autoimmune-like toxicities [50, 51]. Other approved antibodies, such as nivolumab, target the programmed cell death 1 (PD-1) receptor (Figure 3). Binding of PD-1 to the PD-Ligand 1 (PD-L1), expressed on antigen presenting cells (APC) and tumor cells inhibits T cell activation. Diverse clinical trials demonstrated the clinical benefit of nivolumab compared to ipilimumab and the combination of both monoclonal antibodies was even more effective [52-54]. However, this treatment is accompanied by severe immune-related toxicities [55]. In general, around 35 – 60 % of melanoma patients initially respond to either mono- or combined immunotherapy but still 43 % of the initial responders acquire resistances towards therapy [55, 56]. Several studies suggest, that primary and acquired resistances are not exclusively caused by genomic changes in the tumor itself, but also by alterations in the tumor microenvironment (TME) [57-61].

3.2 The redox homeostasis in melanoma

3.2.1 Oxidative stress in melanoma

The tumor microenvironment (TME) influences the tumor development in several ways. One way is the induction of intra- and extracellular reactive oxygen species (ROS) levels. For example, it was shown that high levels of ROS lead to immune cell suppression in the TME [62, 63]. ROS are highly reactive, oxygen-containing molecules, which are produced by partial reduction of oxygen. The most common ROS are hydrogen peroxide (H_2O_2), the hydroxyl radical ($OH^{\bullet}$) and the superoxide radical ($O_2^{\bullet -}$). In general, ROS are by-products of normal cell activity, such as metabolic processes within the mitochondria and peroxisomes. Furthermore, NADPH oxidases, cyclooxygenases, and lipoxygenase reactions can release ROS [64]. ROS can have pro- and antitumorigenic effects, depending on cell type and concentration. At low levels ROS act primarily as second messenger signaling molecules, which are essential for normal cell proliferation and support growth-factor signaling by blocking inhibitory phosphatases such as PTEN [65]. High concentrations of ROS induce oxidative stress, causing DNA damage and cell death [7]. In most cancer cells, ROS levels are enhanced, due to diverse intrinsic as well as extrinsic factors (Figure 4). Owing to ROS adaption mechanisms, these elevated levels promote tumor progression. Cells of the melanocytic lineage, such as melanoma, are particularly prone to an accumulation of ROS. One major contributor to this pro-oxidant state is the external UVR, which is absorbed by melanin. The melanin synthesis consists of several oxidation steps, which generate H_2O_2 and $O_2^{\bullet -}$ [66]. Other factors that enhance ROS in melanoma are metabolic dysregulation, such as enhanced mitochondrial respiration [67], or oncogenic signaling. For example, activation of NADPH oxidases by enhanced PI3K/AKT signaling [68], due to activating mutations in NRAS and RAC1 [69, 70], amplification of AKT3 or loss of PTEN [71], increases intracellular ROS levels. Thus, cell viability is dependent on a balance between ROS production and elimination, called the redox homeostasis. Diverse antioxidant mechanisms secure the redox homeostasis and prevent oxidative stress in the cell (Figure 4).

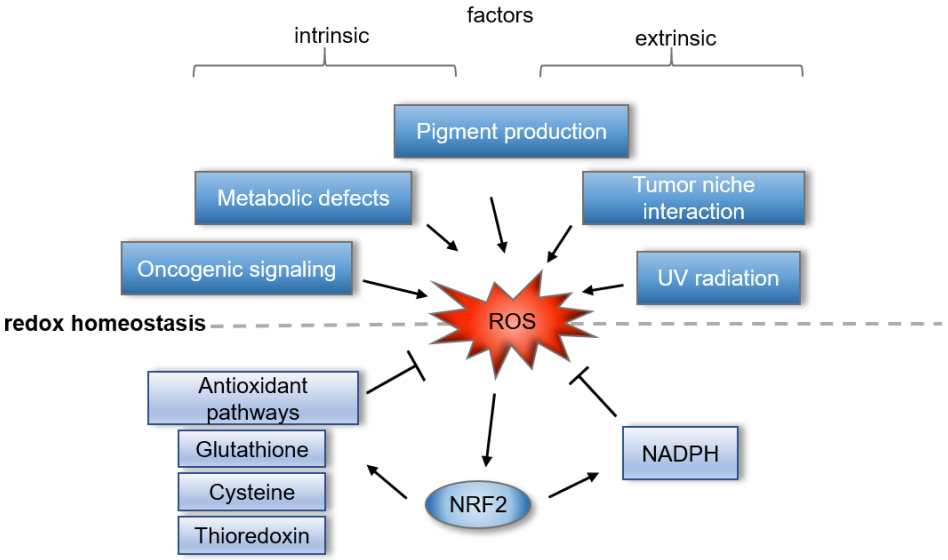

Figure 4 – The redox homeostasis in melanoma
Melanoma cells are prone to an accumulation of reactive oxygen species (ROS). Oxidative stress is induced by diverse intrinsic and extrinsic factors. Intrinsic factors inducing oxidative stress include oncogenic signaling, metabolic defects and pigment production. Pigment production is enhanced after UV radiation in melanocytic cells. Extracellular stresses from the tumor microenvironment increases ROS. For securing the redox homeostasis cells developed antioxidant pathways, such as the glutathione and thioredoxin system, where cysteine is an important cofactor and NADPH the main reducing agent. Various antioxidant systems are controlled by the transcription factor NRF2. Overview was modified from [8].

3.2.2 The antioxidant defense system

Melanomas need to upregulate their intracellular antioxidant systems to adapt to the enhanced ROS concentrations and benefit from the pro-tumorigenic effects of ROS. The intracellular antioxidant system consists of enzymatic antioxidants, which directly remove ROS, together with cofactors and reducing equivalents and of non-enzymatic antioxidants, such as vitamin A or retinol [72].

There are three major enzymatic antioxidant mechanisms in the cell. One is the multi-enzyme detoxification pathway, consisting of superoxide dismutases (SODs), catalases (CATs) and peroxiredoxins (PRDX1-6). The first step of $O_2^{\bullet-}$ detoxification is the reduction to H_2O_2 by SODs and detoxification of H_2O_2 is further catalyzed by CATs or PRDXs, depending on the context. For the reduction of its substrate PRDXs utilize thioredoxin (Trx) as a cofactor, which is the crucial component of another enzymatic antioxidant system [73]. The thioredoxin (Trx) system consists of thioredoxin reductases (TXNRD) and small redox protein thioredoxin, encoded by the *TXN1/2* gene. Trx reduces oxidized cysteine residues and disulfide bonds by self-oxidation but is also an important cofactor for other redox processes. Oxidized Trx is recycled by reduction with TXNRD and the cofactor NADPH [74].

The most abundant enzymatic antioxidant system is the glutathione system, including the tripeptide glutathione (GSH), glutathione reductase (*GSR*), glutathione peroxidases (*GPX*) and glutathione-S-transferases (GSTs). The biosynthesis of GSH is a two-step ATP-dependent process. First, L-glutamate and cysteine are converted into γ-glutamylcysteine by γ-glutamylcysteine ligase (γ-GCL). The γ-GCL consist of a catalytic

subunit (*GCLC*) and a modifier subunit (*GCLM*). The second GSH synthesis step is the addition of glycine to the C-terminus and is catalyzed by glutathione synthetase (*GSS*). Glutathione exist in a reduced (GSH) and an oxidized (GSSG) state and their ratio is an indicator of the intracellular oxidative stress. For ROS scavenging GSH is oxidized to GSSG by *GPX* and *GSR* catalyzes the reduction of GSSG to GSH with NADPH as cofactor [75].

Melanomas display diverse mechanisms to upregulate their antioxidant systems. Melanoma cells are dependent on CDK4/6-mediated senescence suppression and it was shown, that activated CDK4/6 suppressed ROS-mediated senescence by phosphorylating and activating the cell cycle regulator FOXM1 [76]. Furthermore, Park and colleagues determined, that the transcription factor FOXM1 reduces intracellular ROS levels by activating the expression of antioxidant genes, such as *SOD2*, *CAT* and *PRDX3* [77]. A key factor for mitochondrial capacity and oxidative stress resistance is the transcriptional co-activator peroxisome proliferator-activated receptor-gamma coactivator 1 alpha (PGC-1α). PGC-1α can be activated by MITF and facilitates oxidative stress resistance in melanoma [78, 79]. ROS-mediated senescence can also be suppressed by c-MYC expression, an increase of which is characteristic for several cancer types. In melanoma it was shown that the senescence suppression was promoted by the c-MYC target gene cystathionase (CTH) [80]. CTH is an important enzyme in the transsulfuration pathway (TSP), which allows the *de novo* synthesis of cysteine (Cys). Cys has antioxidant properties itself and is a crucial component of GSH and Trx. Another cellular way to ensure sufficient cysteine levels is the import of cystine, the oxidized form of cysteine, which is formed extracellularly due to oxidizing conditions. In exchange with glutamate, cystine is imported by the antiporter system xCT. The xCT antiporter is a heterodimer, consisting of the light chain subunit SLC7A11 and the heavy chain subunit SLC3A2 [81, 82]. Once inside the cell, cystine is reduced to Cys by TXNRD and GSR. Interestingly, previous studies of our group showed that melanoma are highly dependent on the *de novo* synthesis of cysteine [80]. Besides *CTH*, the antioxidant-associated transcription factors *FOXM1* and *NFE2L2* are also c-MYC target genes [80, 83, 84].

3.3 NRF2 - the master regulator of the oxidative stress response

The transcription factor, Nuclear Factor, Erythroid 2 Like 2, encoded by the *NFE2L2* gene and commonly referred to as NRF2, is crucial for the activation of a wide range of antioxidant and detoxifying systems. Thus, NRF2 is considered to be the master regulator of the oxidative stress response. NRF2 belongs to the cap'n'collar (CNC) basic-region leucine zipper (bZIP) family of transcriptions factors and binds as heterodimer, preferably with small MAF transcriptional activators, to the antioxidant response elements (ARE) in the promoter regions of its target genes.

3.3.1 The role of NRF2 in the xenobiotic stress response

After its discovery in 1994, NRF2 was regarded as a stress-induced transcription factor activating the expression of various xenobiotic responses [85, 86] (Figure 5). Referring to the above-mentioned antioxidant systems, NRF2 promotes GSH synthesis, utilization, and regeneration, by transcriptional activation of *GCLC*, *GCLM*, *GSR1* and *GPX2* and *4*. Furthermore, NRF2 secures cystine import by induction of *SLC7A11* expression [85, 87]. The Trx-based antioxidant system is also controlled by NRF2 because it regulates expression of *TXN1* and *TXNRD1*. Moreover, NRF2 can activate transcription of *PRDX1* and *PRDX6* [85]. For the regeneration of glutathione and thioredoxin the reducing source is NADPH. NRF2 fosters NADPH production and regeneration, by regulation of malic enzyme 1 (*ME1*), glucose-6-phosphate 1-dehydrogenase (*G6PD*) and 6-phosphogluconate dehydrogenase (*PGD*) as well as other components of the pentose phosphate pathway [88, 89] (Figure 5).

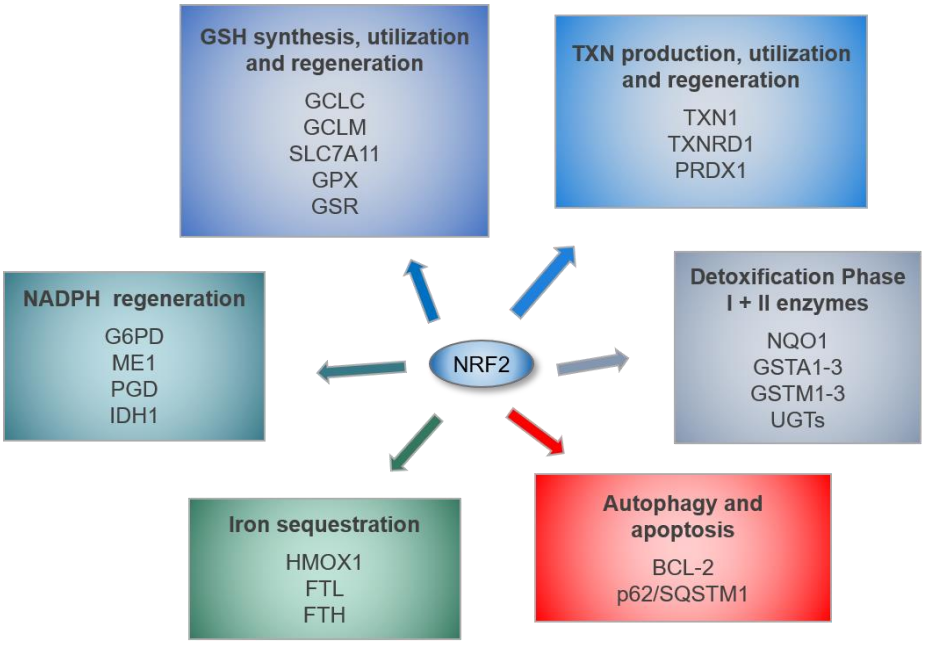

Figure 5 – NRF2 regulates a wide gene network
The transcription factor NRF2 controls antioxidant systems, by regulating glutathione (GSH) synthesis, utilization and regeneration, the thioredoxin-based system as well as NADPH regeneration. NRF2 further controls various drug-metabolizing enzymes, including phase I and II detoxifying enzymes and iron sequestration. NRF2 regulates autophagy by inducing p62/SQSTM1 expression. Overview modified from [86].

Besides the regulation of antioxidant systems, NRF2 facilitates detoxification by phase I and phase II drug-metabolizing enzymes. The phase I reaction includes oxidation, reduction, and hydrolysis, which typically involves cytochrome P450 monooxygenase (CYP). CYP1B1, CYP2B9 are regulated by NRF2. Furthermore, NRF2 controls expression of various dehydrogenases (*ALDH1A1, ADH7, AKR1B1*). One of the best-known NRF2-controlled phase I enzymes is the NAD(P)H quinone oxidoreductase 1 (*NQO1*), which is important for conversion of quinone to hydroquinone. Quinones are organic compounds, which serve as electron acceptors in electron transport chains, such as cellular respiration or also pigmentation. The detoxification of quinones by *NQO1* prevents the production of cytotoxic semiquinones and of ROS due to redox cycling

mechanisms [90]. Moreover, NRF2 controls heme and iron metabolism, primarily by activation of heme oxygenase 1 (*HMOX1*), which cleaves heme to form biliverdin to foster heme degradation [91], and by the regulation of the heavy and light chains of ferritin (*FTH1*, *FTL1*). Ferritin is crucial for intracellular iron storage and transport in a soluble and nontoxic state [85, 89]. The phase II enzymes, in general, catalyze conjugation reactions to inactivate reactive metabolites. NRF2 target genes of this group include GSH S-transferases (*GSTA1, GSTM1, MGST1*) and UDP glucuronosyltranferases (*UGT1A1, UGT2B7*). Furthermore NRF2 enhances autophagy by induction of p62 sequestosome 1 protein (p62/*SQSTM1*) and blocks apoptosis by regulation of BCL-2 [85, 89] (Figure 5). Thus, NRF2 controls stress adaption by promoting a stress-inducible transcriptional program and facilitating anabolic pathways, such as pentose phosphate pathway, which is beneficial for cell proliferation [85, 92].

3.3.2 Canonical and non-canonical activation of NRF2

Although NRF2 is ubiquitously expressed in all cell types, its stress-inducible activation is tightly controlled by a complex transcriptional, epigenetic, and post-translational network. Without stabilization the NRF2 protein has a short half-life of 15-20 min. The most prominent regulatory pathway is the KEAP1-NRF2 signaling pathway. Under physiological conditions, NRF2 is marked for proteasomal degradation by binding to Kelch-like ECH-associated protein 1 (KEAP1). KEAP1 is part of the KEAP1-Cullin (CUL)3-RING box protein (RBX)1 E3 ubiquitin ligase complex (Figure 6A). Binding of CUL3 to the Bric-à-Brac (BTB) domain leads to homodimerization of KEAP1, thus two KEAP1 molecules bind to one NRF2 molecule (Figure 6A, C). The KELCH repeat domain of KEAP1 initially binds to the high-affinity ETGE motif of NRF2 and subsequent the low-affinity DLG motif binds to the KELCH domain of the second KEAP1 subunit (Figure 6). Under homeostatic conditions the lysine-rich cluster (KKKKKKKK) between the DLG and ETGE motif of NRF2 is polyubiquitinated, thus marked for degradation by the proteasome. After induction of oxidative, electrophilic, or xenobiotic stresses, the cysteine residues (marked with Ox) in KEAP1 undergo conformational changes by oxidation, leading to the dissociation of KEAP1 from NRF2. Thus, NRF2 gets stabilized, accumulates, and translocates into the nucleus. The NRF2 protein consists of seven highly conserved NRF2-ECH homology (Neh1-7) domains, of which Neh1 mediates DNA binding and heterodimerization (Figure 6B). After dimerization with members of the small MAF transcriptional activators (MAFF/G/K), NRF2 regulates target gene transcription by binding to the ARE sequence in the promoter of its target genes [93]. The NRF2 activation can be further stabilized by binding of p21 to NRF2, after dissociation of KEAP1 [94]. KEAP1 itself, is a NRF2 target gene, controlling the stress response in a negative feedback loop.
Recently, other E3 ubiquitin ligase complexes were identified to regulate cellular NRF2 protein levels, such as the β-TrCP-SKP1-CUL1-RBX1 in conjugation with glycogen synthase kinase 3 (GSK3) and Synoviolin 1 (HRD1) [95].

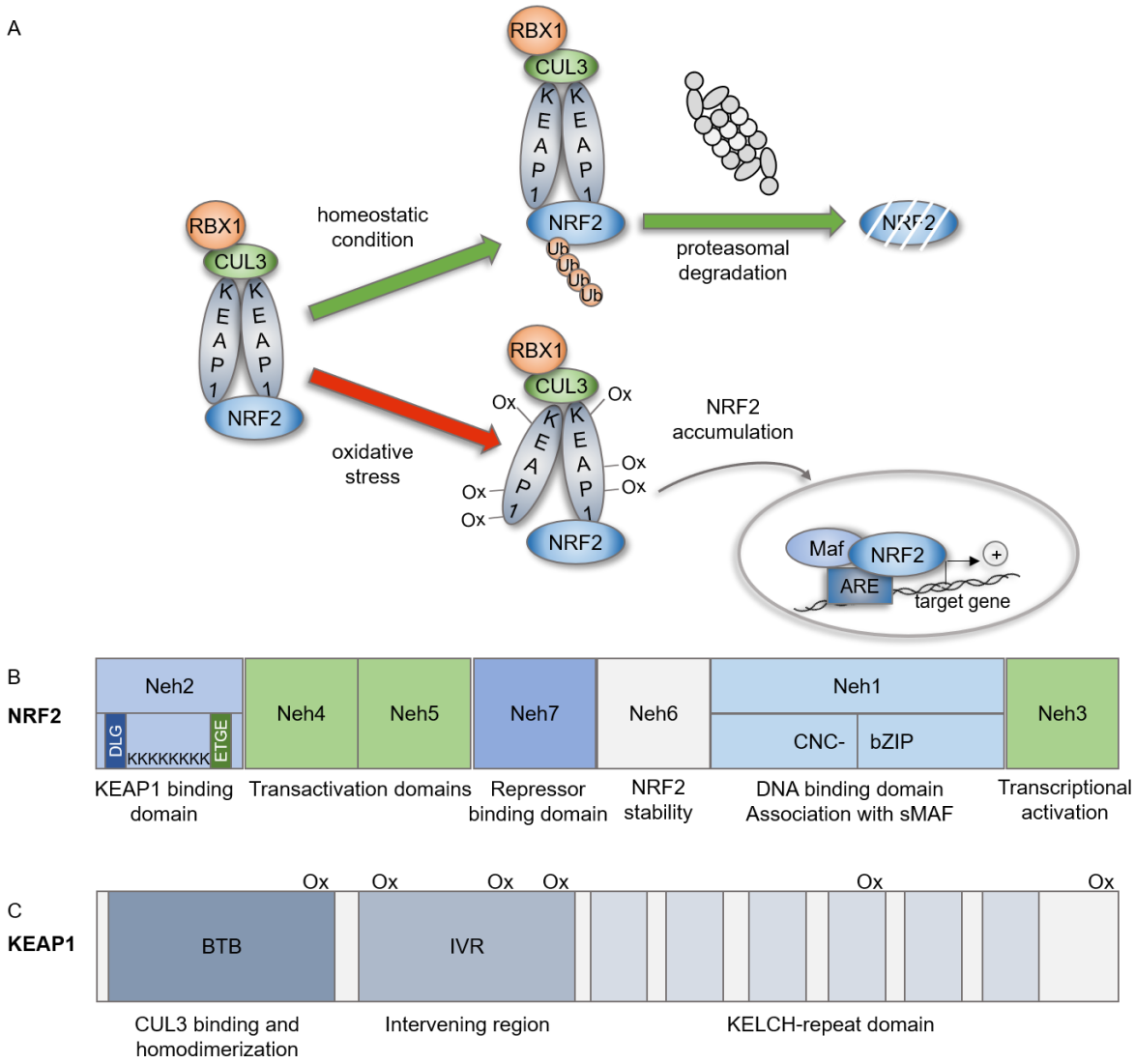

Figure 6 – The KEAP1-NRF2-ARE pathway and protein domain structure of NRF2 and KEAP1
A: Under physiological conditions NRF2 protein levels are strictly controlled by the KEAP1-CUL3-RBX1 E3 ubiquitin ligase complex. After binding of the E3 ubiquitin ligase complex, NRF2 is polyubiquitinated and degraded by the proteasome. After sensing of oxidative stress, cysteine residues of KEAP1 get oxidized (Ox) and NRF2 accumulates, dimerizes with small MAFs and binds to the antioxidant response element (ARE) within the promotor of its target genes. **B**: Domain structure of the NRF2 protein. NRF2 consists of seven NRF2-ECH homology (Neh1-7) domains. The Neh2 domain facilitates KEAP1 binding, with its DLG and ETGE motif, after KEAP1 binding, the lysine rich region (KKKKKKK) gets ubiquitinated. Neh1 enables DNA binding and association with sMAF transcriptional co-activators. **C**: Domain structure of KEAP1 protein. The Bric-à-Brac (BTB) domain binds to CUL3 and enables homodimerization of KEAP1. NRF2 binds with its DLG and ETGE motif to the KELCH-repeat domain of KEAP1. The position of the Cysteine residues, which act as oxidative stress sensors are marked with Ox. The schematic overviews were modified from [86]

Except for its regulation on protein level, NRF2 can also be activated on transcriptional level, since its promoter region contains various transcription factor binding sites. NRF2 itself contains two ARE-like sequences, which enables autoregulation to ensure stress-inducible gene expression. Furthermore, the transcription start site (TSS) of NRF2 contains binding sites for c-MYC, c-JUN [84] as well as nuclear factor κB (NF-κB). NF-κB is activated as an inflammatory response due to extracellular stimuli, such as oxidative stress, cytokines, radicals, and viral antigens. The induction of NRF2 by NF-κB was demonstrated after lipopolysaccharide treatment in monocytes [96].

The KEAP1-NRF2 interaction can also be interrupted by competitor proteins for KEAP1 binding, which causes NRF2 accumulation and activation. The most prominent competitor protein is the autophagy cargo receptor p62/SQSTM1. In response to stimuli of selective autophagy signaling, for example by mTORC1 or PKC-δ, p62/SQSTM1 gets phosphorylated and binds the KEAP1-CUL3-RBX1 complex for autophagic degradation. Furthermore, NRF2 controls p62/SQSTM1 expression in a positive feedback loop (Figure 5) [97]. Modification of KEAP1 and subsequent activation of ARE genes by NRF2 can be chemically mimicked by exposure to agents, such as tert-butylhydroquinone (tBHQ) or the isothiocyanate sulforaphane (SFN) [85].

3.3.3 Hyperactivation and functions of NRF2 in cancer

The role of KEAP1 as the primary NRF2 repressor was first identified owing to the observation that mutational or epigenetic alterations in the *KEAP1* gene causes NRF2 hyperactivation in several cancer entities. In addition to loss-of-function mutations in *KEAP1,* gain-of-function mutations in *NFE2L2* are also possible. In both cases the mutations mostly concern the mutual interacting domains of KEAP1 and NRF2, which leads to an enhanced NRF2 stabilization. This constitutive activation of the NRF2 pathway was identified as promoter for cancer progression, metastasis, and therapy resistances. The majority of mutations were identified in lung adenocarcinoma, alterations in either one of the genes are found in around 21 % of lung cancer patients [98]. In addition, activating mutations were described in head and neck, esophagus, bladder and liver cancer as well as in SCC [86]. In melanoma somatic alterations in KEAP1 or NRF2 are rare, but a case report described frameshift mutations of *KEAP1* in acral lentiguous melanoma (ALM), which increased drug resistances [99]. Furthermore, DeNicola and colleagues demonstrated that the NRF2 pathway is activated by physiological activation of oncogenes, such as RAS, BRAF and c-MYC, causing a reduced intracellular redox environment and enhancing tumorigenesis of pancreatic cancer [84]. The precise role of activated NRF2 in cancer initiation and progression is controversial. Owing to its chemoprotective functions, NRF2 has a cancer preventive role by neutralizing chemical carcinogens and preventing DNA damage [100]. Of note, chemical activation of NRF2, with dimethyl fumarate (DMF), is approved for therapy of multiple sclerosis [101] and psoriasis [102]. However, activation of NRF2 in already established cancer cells promotes cancer progression and metastasis through ROS detoxification and metabolic reprogramming, thus acting like an oncogene [100, 103, 104]. NRF2 facilitates therapy and inhibitors resistances in glioma, melanoma [105], lung [103] and head and neck cancer [106].

Besides its role in chemoresistance, very little is known about the role of NRF2 in melanoma. Hintsala et. al. showed that high nuclear NRF2 expression levels in primary melanoma is associated with a more invasive phenotype, thus it might be a negative prognostic marker in melanoma [107]. This observation is in accordance with the findings that supplementation of antioxidants, such as N-acetylcysteine (NAC), promote

melanoma metastasis by coping with the enhanced redox status in distant tumor sites [108, 109]. Although recent advances emerged in understanding the role of NRF2 in melanoma and other cancer entities, its mechanism of action and changes in its transcriptome need to be further validated.

3.4 Aim of the project

Even though, therapeutic approaches against melanoma took a big step forward in the last decade, initial and adaptive resistance mechanisms are still challenging for therapy of advanced melanoma patients. Increasing evidence emerges, that the transcription factor NRF2 plays a role in therapy resistances in various cancer entities. As the master regulator of the oxidative stress response, NRF2 might be particularly crucial for melanoma maintenance. Although melanoma is especially dependent on a balanced redox status, to what extent melanoma rely on NRF2 is only scarcely investigated so far. The role of stress-induced transcription factors in cancer have long been underestimated, but presumably they are important in mediating plasticity and adaption to changing conditions, caused by the tumor microenvironment or cancer therapy. For example, in lung cancer it was shown that the transcription factor NRF2 mediates therapy resistance [110]. First hints for the role of NRF2 in melanoma therapy were reported recently. A strong increase of NRF2 activity contributed to vemurafenib resistances in A375 melanoma cells under BRAF-inhibitor therapy [111]. Furthermore, NRF2 induces PD-L1 expression in melanocytes after UV-A radiation and the shRNA mediated NRF2 knockdown enhanced the response towards anti-PD-1 immunotherapy in a mouse model [112]. However, the mechanisms how NRF2 influences targeted and immunotherapy resistances is incompletely understood.
The aim of this thesis was the comprehensive analysis of the dependency of melanoma on NRF2 activity by using melanoma cell lines and mouse models. The study integrated genome-wide transcriptomic analysis and genome-wide NRF2 binding studies. The relevance of NRF2 in melanoma maintenance and progression was investigated by *in vitro* and *in vivo* studies, implemented by the generation of human and murine CRISPR/Cas9 mediated NRF2 knockout cell lines.

4. Material and Methods

4.1 Material

4.1.1 Cell lines and cell culture reagents

Table 1 – Cell lines

Cell line	Supplier	Driver mutation	Type
781	S. Meierjohann (Würzburg, Germany)	$BRAF^{V600E}$	murine malignant melanoma, isolated after subcutaneous injection of D4M3A into flanks of C57BL/6 mice (M.Staus)
781 Nfe2l2$^{-/-}$	this work	$BRAF^{V600E}$	murine malignant melanoma, CRISPR/Cas9 knockout line
A375	ATCC	$BRAF^{V600E}$	malignant melanoma
A549	ATCC	$KRAS^{G12S}$, $KEAP1^{G333C}$	human lung adenocarcinoma
B16-F1	ATCC	$BRAF^{V600E}$	murine melanoma
D4M3A	C. Brinkerhoff (Hanover, NH, USA)	$BRAF^{V600E}$	murine malignant melanoma
LOXIMVI	NCI/NIH	$BRAF^{V600E}$	human malignant amelanotic melanoma, metastasis
M14	NCI/NIH	$BRAF^{V600E}$	human amelanotic melanoma
SK-MEL-2	NCI/NIH	$NRAS^{Q61R}$	human malignant melanoma, metastasis
SK-MEL-3	ATCC	$BRAF^{V600E}$	human malignant melanoma, metastasis
SK-MEL-28	ATCC	$BRAF^{V600E}$	malignant melanoma
UACC-257	NCI/NIH	$BRAF^{V600E}$	human malignant melanoma
UACC-62	NCI/NIH	$BRAF^{V600E}$	human malignant melanoma
UACC-62 Nfe2l2$^{-/-}$	this work	$BRAF^{V600E}$	human malignant melanoma, CRISPR/Cas9 knockout line
melan-a	Wellcome Trust Functional Genomic Cell Bank	na	murine melanocytes, D.C. Bennett, et al. Int. J. Cancer 39, 414-418 (1987)
NHEM	PromoCell	na	normal human epidermal melanocytes

Table 2 – Cell culture reagents

Reagent	Source	Identifier
Cholera Toxin	Sigma-Aldrich	C8052
DMEM	PAN	P04-03550
DMEM, high glucose	Invitrogen	21013-024
Fetal bovine serum (FBS)	Sigma-Aldrich	F7524
Ham's F10 Nutrient mix	Invitrogen	31550023
Insulin, transferrin, selenium (ITS) supplement (100 x)	Capricorn Scientific	ITS-H
3-isobutyl-1-methylxanthine (IBMX)	Sigma-Aldrich	I5879
OptiMEM	Invitrogen	11058-021
12-O-tetradecanoylphorbol 13-acetate (TPA)	Merck	CAS 16561-29-8
Penicillin/Streptomycin	Sigma-Aldrich	P0781
Trypsin 0.5 % / EDTA 0.2 % in PBS	PAN	P10-024100

4.1.2 Plasmids and siRNAs

Table 3 – Plasmids and expression vectors

Name	Insert	Source	Identifier
pU6-(BbsI)_CBh-Cas9-T2A-mCherry	-	Addgene	#64324
pE7584 Hygro#20	-	M. Gessler (Würzburg, Germany)	
pSB_ET-iE	-	M. Gessler (Würzburg, Germany)	
	$BRAF^{V600E}$	S. Meierjohann (Würzburg, Germany)	
	MITF	S. Meierjohann (Würzburg, Germany)	
	Nfe2l2	S. Meierjohann (Würzburg, Germany)	
	$NRAS^{Q61K}$	S. Meierjohann (Würzburg, Germany)	
	Ptgs2	This work	
pCMV(CAT)T7-SB100X	-	M. Gessler (Würzburg, Germany)	
peGFP-N1	-	Clontech	6085-1
pcDNA3.1	-	Invitrogen	V790-20
	Nfe2l2	This work	

pLuc-Tyr-200	-	C. Goding (Oxford, UK)
pGL4.74[hRluc/TK]	-	S. Gaubatz (Würzburg, Germany)

Table 4 – siRNAs

Name	Sequence	Source	Identifier
sictrl	MISSION Universal negative control #1	Sigma-Aldrich	SIC001
siFOXM1_1	5'-CAACUCUUCUCCCUCAGAUtt-3'	Sigma-Aldrich	SASI_Hs01_00243977
siFOXM1_2	5'-CAUCAGAGGAGGAACCUAAtt-3'	Sigma-Aldrich	SASI_Hs01_00243978
siNFE2L2_1	5'-GGAGAAAAUGACAAAAGCtt-3'	ambion	ID3347
siNFE2L2_2	5'-GGAGCUAUUAUCCAUUCCUtt-3'	ambion	ID107967

4.1.3 Reagents, compounds, and inhibitors

Table 5 – Reagents, compounds and inhibitors

Reagent	Source	Identifier
Acetic acid	Roth	3738
Albumin Bovine Fraction V (BSA)	Serva	11930
Ammonium peroxodisulfate (APS)	Sigma-Aldrich	101201
Ampicillin	Roth	HP62.2
Aprotinin	Sigma-Aldrich	A6279
Bacto Agar	BD	214030
Bromophenol blue sodium salt	Roth	A512
2, 3 -cGAMP	Sigma-Aldrich	SML1229
Chloroform	Sigma-Aldrich	C2432
Crystal violet	Roth	T123
Deoxynucleotid triphosphates (dNTPs)	Sigma-Aldrich	DNTP100A
Diethyldicarbonate (DEPC)	Roth	K028.1
3,8-Diamino-5-ethyl-6-phenylphenanthridiniumbromid (EtBr)	Roth	2218
1,4-Diazabicyclo[2.2.2]octane (DABCO)	Sigma-Aldrich	D2522
Dimethyl sulfoxide (DMSO)	Roth	4720

3-(4,5-Dimethylthiazol-2-yl)-2,5-diphenyltetrazoliumbromid (MTT)	Sigma-Aldrich	M2128
5, 5'-Dithiobis(2-nitrobenzoic acid) (DTNB)	Sigma-Aldrich	D8130
Doxycycline	Sigma-Aldrich	324385
Ethylenediamine tetraacetic acid disodium salt dihydrat (EDTA)	Roth	8043
Epidermal growth factor (EGF)	Peprotech	AF-100-15
Ethanol	Fisher Chemicals	64-17-5
Formaldehyde	Roth	4979
Glycerol	Roth	3783.2
Glycine	Serva	23390
Glycogen RNA grade	Thermo Fisher Scientific	R0551
Hepes Pufferan	Roth	9105.3
Hoechst 34580	Invitrogen	H21486
Hydrogen peroxide 30%	Sigma-Aldrich	H1009
4-Hydroxytamoxifen (4-OHT)	Selleckchem	S7827
Hygromycin	Capricorn	HY6-H
Interferon-γ (IFNγ)	H. Herrmanns (Würzburg, Germany)	
Isoamyalkohol	Roth	8930
Isopropanol	Sigma-Aldrich	278475
Ketaset (100 mg/ml)	Zoetis	-
LB-Agar (Luria/Miller)	Roth	X969.1
LB-Medium (Luria/Miller)	Roth	X968.3
Leupeptin	Sigma-Aldrich	L2884
L-glutathione reduced (GSH)	Sigma-Aldrich	G4251
Methanol	Sigma-Aldrich	322415
Mowiol 4-88	Roth	0713.2
N-acetylcysteine (NAC)	Sigma-Aldrich	A9165
Nicotinamide adenine dinucleotide phosphate, reduced (NADPH)	Biomol	16156
Nonfat dried milk powder	Applichem	A0830
Nonidet P40	Applichem	A1694

Paraformaldehyde (PFA)	Roth	0335.2
PD184532	Axon Medchem	1368
Phenol	Roth	38
Phenylmethanesulfonyl fluoride (PMSF)	Sigma-Aldrich	78830
Ponceau S	Sigma-Aldrich	P7170
Potassium ferricyanide ($K_3Fe(CN)_6$)	Sigma-Aldrich	13746-66-2
Potassium ferrocyanide ($K_4Fe(CN)_6$)	Sigma-Aldrich	14459-95-1
Prostaglandin E2 (PGE2)	Tocris biosciences	2296
Puromycin	Sigma-Aldrich	540411
Rotiphorese Gel 40 (37,5:1)	Roth	T802.1
Sodium chloride (NaCl)	Roth	9265.3
0.9 % NaCl (for injection)	Braun	2350710
Sodium deoxycholate	Sigma-Aldrich	30970
Sodium dodecyl sulfate (SDS)	Sigma-Aldrich	75746
Sodium flouride (NaF)	Sigma-Aldrich	S7920
Sodium orthovanadate (Na3VO4)	Sigma-Aldrich	S6508
R,S-Sulforaphane (SFN)	Biomol	LKT-S8044.25
5-Sulfosalicylic acid hydrate (SSA)	Sigma-Aldrich	390275
SYBRGreen	Invitrogen	S7563
TEMED	Roth	2367.3
tert-butylhydroquinone (tBHQ)	J.P. Friedmann-Angeli (Würzburg, Germany)	
Tumor necrosis factor-α (TNFα)	H. Wajant (Würzburg, Germany)	
Trametinib	Selleckchem	S2673
Tris Pufferan	Roth	4855.1
Triton-X-100	Roth	3051.2
Tween 20	Roth	9127.1
Vemurafenib	Axon Medchem	1624
Xylavet (20 mg/ml)	Cp-Pharma	-
β-mercaptoethanol	Roth	4227.1
X-Gal	Stratagene	300201

4.1.4 Buffers and ready-to-use kits

Table 6 – Buffers

Buffer	Components
Blotting buffer (1 x)	25 mM Tris, 192 mM glycine, 20 % MeOH
ChIP elution buffer	1 % SDS in 100 mM $NaHCO_3$
ChIP lysis buffer I	5 mM PIPES pH 8.0, 85 mM KCl, 0.5 % NP-40
ChIP lysis buffer II	50 mM HEPES pH 7.9, 140 mM NaCl, 1 mM EDTA, 1 % Triton-X-100, 0.1 % deoxycholate
ChIP wash buffer I	20 mM Tris HCl pH 8.1, 150 mM NaCl, 2 mM EDTA, 0.1 % SDS, 1 % Triton-X-100
ChIP wash buffer II	20 mM tris HCl pH 8.1, 500 mM NaCl, 2 mM EDTA, 0.1 % SDS, 1 % Triton-X-100, 1 mM PMSF, 0.1 M NaF, 200 µM Na_3VO_4, 10 µg/ml leupeptin, 10 µg/ml aprotinin
ChIP wash buffer III	10 mM Tris pH 8.1, 250 mM LiCl, 1 mM EDTA, 1 % NP-40, 1 % deoxycholate
DNA loading dye (6 x)	0.25 % bromophenol blue, 0.25 % xylene cyanol FF, 30 % glycerol
GSH assay buffer (Tietze assay)	143 mM phosphate buffer, 6.3 mM EDTA, pH 7.5
Inhibitors for lysis	1 mM PMSF, 0.1 M NaF, 200 µM Na3VO4, 10 µg/ml leupeptin, 10 µg/ml aprotinin
Mowiol-DABCO	10 % Mowiol 4-88, 25 % glycerol, 2.5 % DABCO in 1x PBS
PBS (1 x)	137 mM NaCl, 2.7 mM KCl, 4.3 mM Na2HPO4, 1.47 mM KH_2PO_4, pH 7.4
Reprofast buffer (10 x)	100 mM $(NH4)_2SO_4$, 200 mM Tris pH 8.8, 100 mM KCl, 20 mM $MgSO_4$, 1 % Triton-X-100, 1 % BSA
RIPA lysis buffer	50 mM Tris pH 8.0, 50 mM NaCl, 1 % NP-40, 0.1 % SDS, 0.5 % deoxycholat
SDS loading dye (5 x)	312.5 mM Tris pH 6.8, 10 % SDS, 50 % glycerine, 0.005 % bromophenol blue, 25 % β-mercapthoethanol
SDS running buffer (5 x)	250 mM Tris, 960 mM glycine, 0.5 % SDS
Separating gel buffer	1.5 M Tris HCl pH 8.8
Stacking gel buffer	0.5 M Tris HCl pH 6.8
TAE (1 x)	40 mM Tris HCl pH 8.0, 1 mM EDTA
TBS-T (1 x)	10 mM Tris pH 7.9, 150 mM NaCl, 0.1 % Tween-20
Tris-EDTA (1 x TE)	10 mM Tris, 20 mM acetic acid, 1 mM EDTA pH 8.0
X-Gal staining solution	1 mg/ml X-Gal, 40 mM citric acid/sodium phosphate buffer, 5 mM $K_4Fe(CN)_6$, 5 mM $K_3Fe(CN)_6$, 150 mM NaCl, 2 mM $MgCl_2$

Table 7 – Commercially available kits, reagents and magnetic beads

Name	Source	Identifier
AMPure XP Beads	Beckman Coulter	A63880
Bradford Reagent	Sigma-Aldrich	B6916
CellROX® Deep Red Flow Cytometry Assay Kit	Thermo Scientific	C10491
Dual-Luciferase® Reporter Assay	Promega	E1910
Dynabeads™ Protein G	Invitrogen	10003D
E.Z.N.A Endo-free Plasmid Midi Kit	Omega Bio-tek	D6915
GenElute™ PCR Clean-Up Kit	Sigma-Aldrich	NA1020
GenElute™ Plasmid Miniprep Kit	Sigma-Aldrich	PLN70
iTaq™ Universal SYBR® Green Supermix	Biorad	172-5120
Monarch DNA Gel Extraction Kit	New England BioLabs	T1020
NEBNext® Multiplex Oligos for Illumina	New England BioLabs	E7600
NEBNext® Poly(A) mRNA Magnetic Isolation Module	New England BioLabs	E7490
NEBNext® Ultra™ II DNA Library Prep Kit for Illumina	New England BioLabs	E7645
NEBNext® Ultra™ II RNA Library Prep Kit for Illumina	New England BioLabs	E7770
PGE2 high sensitivity ELISA Kit	Enzo Life Sciences	ADI-930-001
QIAamp DNA Mini Kit	Qiagen	51306
QIAquick PCR Purification Kit	Qiagen	28104
Qubit DNA quantification assay	Thermo Scientific	Q33230
RNAeasy Mini Kit	Qiagen	74106
RNase-free DNase Set	Qiagen	79254
StrataClone Blunt PCR Cloning Kit	Agilent Technologies	240205
Experion RNA Standard Sensitivity Analysis Kit	BIORAD	7007103
RevertAid First Strand cDNA Kit	Thermo Scientific	K1622
TRIzol Reagent	Invitrogen	15596018
SuperSignal West Pico Plus Chemiluminescent Substrate	Thermo Scientific	34580
WesternBright Chemiluminescent Substrate Sirius	Advansta	541020

4.1.5 Enzymes, transfection reagents and molecular weight markers

Table 8 – Enzymes and associated buffers

Name	Source	Identifier
AfeI (Eco47III)	Thermo Fisher Scientific	ER0322
AgeI	New England Biolabs	R0552S
BbsI	New England Biolabs	R0539S
Buffer R (10 x)	Thermo Fisher Scientific	BR5
FastAP Thermosensitive Alkaline Phosphatase	Thermo Fisher Scientific	EF0651
Fastdigest buffer	Thermo Scientific	B64
NEBuffer 1.1 (10 x)	New England Biolabs	B7201S
NheI	Thermo Fisher Scientific	ER0972
T4 DNA Ligase	New England Biolabs	M0202S
T4 Polynucleotide Kinase (PNK)	New England Biolabs	M0201S
TANGO buffer, 10x	Thermo Scientific	BY5
***Taq* DNA polymerase**	Invitrogen	10342020
His-*Taq* DNA polymerase	M. Gessler (Würzburg, Germany)	-
Q5 High Fidelity DNA polymerase	New England Biolabs	M0491S
Glutathione reductase (GR)	Sigma	G3664
Proteinase K	Qiagen	19131
RNAse A	Applichem	A2760

Table 9 – Transfection reagents

Name	Source	Identifier
FuGENE® HD Transfection Reagent	Promega	E2311
Lipofectamine™ 3000 Transfection Reagent	Invitrogen	L3000015
X-tremeGENE™ siRNA Transfection Reagent	Roche	SITRAN-RO

Table I0 – Protein and DNA ladders

Name	Source	Identifier
100 bp DNA marker plus	GeneOn	306-005
1 kb Plus DNA Ladder	Thermo Fisher Scientific	10787-018
PageRuler™ Prestained Protein Ladder	Thermo Fisher Scientific	26617

4.1.6 Primary and secondary antibodies with respective dilutions

Table I1 – Primary antibodies

Antibody	Source	Identifier	Dilution (WB, IF)
ATF4	Cell Signaling	#11815	1:1000
beta-ACTIN	Santa Cruz Biotechnology	sc-47778	1:5000
CD3	abcam	ab16669	IHC: 1:100
Cleaved Caspase 3 (Asp173)	Cell Signaling	#9664	1:1000
cleaved PARP (Asp214)	Cell Signaling	#5625	1:1000
COX2	bimake/Cell signaling	A5523/#12282	1:1000
EGFR	Cell Signaling	#4267	1:1000
p-ERK (Thr202/Tyr204)	Cell Signaling	#9101	1:1000
FOXM1	Cell Signaling	#5436	1:1000
p-H2Ax (Ser139)	Cell Signaling	#2577	1:1000
HMOX1	Santa Cruz Biotechnology	sc-136960	1:500
MDA5	Cell Signaling	#5321	1:1000
MITF	C. Goding (Oxford, UK)	-	1:1000
MLANA	abcam	ab210546	1:2000
NRF2	abcam	ab62352	1:1000, 1:500
NQO1	Santa Cruz Biotechnology	sc-271116	1:500
p-P53(Ser15)	Cell Signaling	#9284	1:1000
PUMA	Cell Signaling	#4976	1:1000
p-STAT1(Tyr701)	Cell Signaling	#9167	1:1000
STING	Cell Signaling	#13647	1:1000
p-TBK1/NAK (Ser172)	Cell Signaling	#5483	1:1000
TUBULIN	Sigma	T6074	1:3000, 1:500

TYR	abcam	ab170905	1:2000
VINCULIN	Sigma	V9131	1:10000

Table I2 – Secondary antibodies

Antibody	Source	Identifier	Dilution (WB, IF)
Alexa Fluor® 488 goat anti-mouse IgG	Life Technologies	A11001	-, 1:500
Alexa Fluor® 594 goat anti-mouse IgG	Life Technologies	A11032	1:3000, 1:500
Alexa Fluor® 594 goat anti-rabbit IgG	Life Technologies	A11037	-, 1:500
goat anti-mouse IgG (H+L)	Thermo Scientific	31444	1:3000
goat anti-rabbit IgG (H+L)	Bio-Rad	170-6515	1:10000

4.1.7 Oligonucleotides used for qPCR and cloning

All oligonucleotides were obtained from Sigma-Aldrich.

Table I3 – Oligonucleotides used for human gene expression

Gene	Forward sequence (5'->3')	Reverse sequence (5'->3')
ACO2	TCCCAGTTCACCATCACTCC	ATGTCCTTCCTGTCCCACTG
ACTB	GGCATCCTGACCCTGAAGTA	GGGGTGTTGAAGGTCTCAAA
ATP6V04A	AGCCCCTCCCACATTTAACA	CATCACAGCGAACAGGAAGG
AURKA	AATGATTGAAGGTCGGATGC	CCTGGCTCCCTCTGTTACAA
CCNB1	CGGGAAGTCACTGGAAACAT	AAACATGGCAGTGACACCAA
DCT	GGTTCCTTTCTTCCCTCCAG	AACCAAAGCCACCAGTGTTC
EGFR	AGTGCTGGATGATAGACGCA	CCTGAATGACAAGGTAGCGC
FOXM1	ACCCAAACCAGCTATGATGC	GAAGCCACTGGATGTTGGAT
G6PD	AAGAACGTGAAGCTCCCTGA	AATATAGGGGATGGGCTTGG
GCLM	TGTGTGATGCCACCAGATTT	TTCACAATGACCGAATACCG
IFIH1	TCCAACTGCTGAACCTCCTT	GCAATCCGGTTTCTGTCTTC
IFIT1	GCAGCCAAGTTTTACCGAAG	GCCCTATCTGGTGATGCAGT
ISG15	AACCTCTGAGCATCCTGGTG	GAAGGTCAGCCAGAACAGGT

HMOX1	CTTCTTCACCTTCCCCAACA	CTTCTTCACCTTCCCCAACA
LIG1	GGTGCAGGTGTGTTTGTACG	GAAGACAAACTCGCCCTCTG
MAFF	GAGAGCTGAGCGAGAACACG	CGTAGCCACGGTTTTTGAGT
ME1	GGATTGCACACCTGATTGTG	TCTTCATGTTCATGGGCAAA
MITF	GGGCTTGATGGATCCTGCTT	GCCAGTGCTCTTGCTTCAGA
MLANA	GCTCATCGGCTGTTGGTATT	GGGAACCACAGGTTCACAGT
NDUFA3	GGGGCCTCGCTGTAATTCTG	GACGGGCACTGGGTAGTTG
NFE2L2	GAGAGCCCAGTCTTCATTGC	GTTTGGCTTCTGGACTTGGA
NQO1	AGCCCAGATATTGTGGCTGA	CGGAAGGGTCCTTTGTCATA
PCNA	TGGAGAACTTGGAAATGGAAA	GAACTGGTTCATTCATCTCTATGG
PLK1	AAGATCTGGAGGTGAAAATAGGG	AGGAGTCCCACACAGGGTCT
PPARGC1A	TCAGTACCCAGAACCATGCA	GGGACGTCTTTGTGGCTTTT
PTGS2	TGAAACCCACTCCAAACACA	GAGAAGGCTTCCCAGCTTTT
RFC4	CAGTACTAAACCCCCGCTGA	TTCAGCACTGCAACCACTTC
RPA3	AAGCCTGTCTGCTTCGTAGG	AAGCCTGTCTGCTTCGTAGG
RPS14	CTCAGGTGGCTGAAGGAGAG	GCAGCCAACATAGCAGCATA
RSAD2	GGGAGAGGTGGTTCCAGAAT	ACCACCTCCTCAGCTTTTGA
SLC7A11	TTTGCACCCTTTGACAATGA	GGAAAACAAAGCTGGGATGA
TOP2A	AATCTCAGAGCTTCCCGTCA	TGCCTCTGCCAGTTTTTCTT
TYR	CCGCTATCCCAGTAAGTGGA	TACGGCGTAATCCTGGAAAC

Table 14 – Oligonucleotides for murine gene expression

Gene	Forward sequence (5'->3')	Reverse sequence (5'->3')
actb	GCTACAGCTTCACCACCACA	AAGGAAGGCTGGAAAAGAGC
B2m	CTGACCGGCCTGTATGCTAT	CCGTTCTTCAGCATTTGGAT
Cd3g	GACTTGTGGCTTGACTGACA	CTCGAGGGTCTTTGGCATTG
Cd8a	TCAGTTCTGTCGTGCCAGTC	GCCGACAATCTTCTGGTCTC
Gzmb	GCATTCCCCACCCAGACTAT	GCTTCACATTGACATTGCGC
H2-D1	GGGAAACACAGAAAGCCAAG	AGCCAGACATCTGCTGGAGT
H2-K1	CAGGTGGAAAAGGAGGGGAC	CACGCTAGAGAATGAGGGTCA
H2-Q4	GAGCTTGGCCATCATTGCAG	AGACAGGGTCCTGGTGTGTA

Hmox1	CACGCATATACCCGCTACCT	CCAGAGTGTTCATTCGAGCA
Ifih1	TCACTGATCTGCCCTCTCCT	CCTTCTCGAAGCAAGTGTCC
Ifit1	ATGGGAGAGAATGCTGATGG	AGGAACTGGACCTGCTCTGA
Isg15	AAGAAGCAGATTGCCCAGAA	TCGCTGCAGTTCTGTACCAC
Maff	GCGAGTTGAGCGAGAACAC	GTAGCCGCGGTTCTTGAGT
Nfe2l2	AGGACATGGAGCAAGTTTGG	TTCTTTTTCCAGCGAGGAGA
Nqo1	CTGGCCCATTCAGAGAAGAC	GTCTGCAGCTTCCAGCTTCT
Prf1	CGCATGTACAGTTTTCGCCT	TGGTAAGCATGCTCTGTGGA
Psmb8	AGTACTGGGAGAGGCTGTTG	TTGTCCCAGCCACAGATCAT
Psmb9	TGCAAACGTGGTGAAGAACA	CATCCCTCCCATGGTTCCAT
Ptges3	TGCTTCTGCAAAGTGGTACG	TCGCTTCCTCCAAGACAACT
Ptgs2	GGCCATGGAGTGGACTTAAA	ACCTCTCCACCAATGACCTG
Rsad2	AAGGTTTTCCAGTGCCTCCT	ATTCAGGCACCAAACAGGAC
Slc7a11	TCCACAAGCACACTCCTCTG	TGCATATCTGGGCGTTTGTA
Tap1	CTGAAGTCTGGACCACGAGT	TGGGTGAACTGAAGCTGGTA
Tap2	CGGACATGGCTTTACTTGGG	GCAGCTCTCCCACTTTTAGC
Tmem173	GGCATCAAGAATCGGGTTTA	ATCCTGTGACATGGCAAACA

Table 15 – Oligonucleotides for ChIP validation

Gene region	Forward sequence (5'->3')	Reverse sequence (5'->3')
GAPDHS neg. ctrl	GGCAGCAAGAGTCACTCCA	TGTCTCTTGAAGCACACAGGTT
HMOX1-ARE	GTGGCCGTGTTTTTCCTG	GGCGGTGACTTAGCGAAAAT
NQO1-ARE	ATGTCTCCCCAGGACTCTCA	CGGATTACTGTGGTGCCCTA

Table 16 – CRISPR/Cas9 guide RNAs and validation primers

Name	Sense/Forward (5'->3')	Antisense/Reverse (5'->3')
murine gRNA Nfe2l2_1	CACCGTGAAGACTGAACTTTCAGCG	AAACCGCTGAAAGTTCAGTCTTCAC
murine gRNA Nfe2l2_3	CACCGTCCTCGCTGGAAAAAGAAGT	AAACACTTCTTTTTCCAGCGAGGAC

human gRNA NFE2L2_2	CACCGCATACCGTCTAAATCAACAG	AAACCTGTTGATTTAGACGGTATGC
gRNA_non-targeting (human)	CACCGGCGAGGTATTCGGCTCCGCG	AAACCGCGGAGCCGAATACCTCGCC
gRNA_non-targeting (murine)	CACCGGTATTACTGATATTGGTGGG	AAACCCCACCAATATCAGTAATAGC
CRISPR_val	GGGCGTACTTGGCATATGAT	GACAGGTATCCGGTAAGCGG
CRval_mNrf2	CATGCCTTGGTTCTCACTCA	TCAATAGTCCCGTCCAGGAG
CRval_hNrf2	GAGAGCCCAGTCTTCATTGC	GTTTGGCTTCTGGACTTGGA

Table 17 – Cloning and sequencing primers

Name	Sense/Forward (5'->3')	Antisense/Reverse (5'->3')
cloning: mPtgs2-NheI	GCGGCTAGCATGCTCTTCCGAGCTGTGCT	-
cloning: mPtgs2-AfeI	-	GCGAGCGCTTTACAGCTCAGTTGAACGCCT
T3 fwd	ATTAACCCTCACTAAAGGGA	-
T7 rev	-	GCCCTATAGTGAGTCGTATTAC
T7 fwd	AATACGACTCACTATAGG	-
TYMV fwd	AGATCGCCTGGAGCAATTCC	-
IRES rev	-	CACACCGGCCTTATTCCAAG

Table 18 – Primers for murine genotyping

Name	Sense/Forward (5'->3')	Antisense/Reverse (5'->3')
$BRAF^{V600E}$	TGAGTATTTTTGTGGCAACTGC	CTCTGCTGGGAAAGCGGC
Tyr-Cre^{ERT2}	GCGGTCTGGCAGTAAAAACTATC	GTGAAACAGCATTGCTGTCACTT
***Cre* (internal positive control)**	CTAGGCCACAGAATTGAAAGATCT	GTAGGTGGAAATTCTAGCATCATCC
$Nfe2l2^{+/+}$	GCCTGAGAGCTGTAGGCC	GGAATGGAAAATAGCTCCTGCC
$Nfe2l2^{-/-}$	GCCTGAGAGCTGTAGGCC	GGGTTTTCCCAGTCACGAC

4.1.8 Mouse models

Table 19 – Genetic mouse models

Mouse strain	Genetic background
C57BL/6	wt
C57BL/6	Tyr-CreER^{T2}; Braf$^{V600E/wt}$; *Nfe2l2*$^{+/+}$ [113]
C57BL/6	Tyr-CreER^{T2}; Braf$^{V600E/wt}$; *Nfe2l2*$^{-/-}$ [114]

4.1.9 Technical equipment and consumables

Table 20 – Technical equipment

Device	Manufacturer
Amersham™ nitrocellulose membranes	GE Healthcare
Cary 50 spectrophotometer	Varian
CTR 6000 inverted microscope	Leica
Hera Cell 150i incubator	Thermo Scientific
Mastercycler ep Realplex	Eppendorf
Mini-PROTEAN Tera Electrophoresis system	Biorad
Microplate reader TriStar LB941	Berthold
NanoDrop ND-1000 spectrophotometer	NanoDrop Technologies
Nitrocellulose membrane (Amersham™ Protan™ 0.45 µM)	GE Healthcare
Operetta High-Content Imaging Station	Perkin Elmer
PET trans well membrane	Corning
Photo Image Station 4000MM	Kodak
Sonifier W-250 D	Branson
Trans Blot Cell	Biorad
VENTANA DP 200 slide scanner	Roche
Whatman Paper (blotting paper GB46)	Hartenstein

4.1.10 Software

Table 21 – Software for data analysis

Software	Source
APE	M. Wayne Davis
Carestream Molecular Imaging	Carestream
CaryWinUV	Varian
ChemiDoc Imaging Systems	Biorad
DAVID Bioinformatics Resources 6.8	Laboratory of Human Retrovirology and Immunoinformatics (LHRI)
Gene Set Enrichment Analysis (GSEA)	BROAD Institute
Fiji (ImageJ)	W. Rasband
Integrated Genome Browser	Freese NH, Norris DC, Loraine AE
Leica Application Suite	Leica
Mastercycler ep Realplex	Eppendorf
MicroWin 2000	Berthold Technologies
ND-1000 V3.3.0	Thermo Scientific
Prism 8.4.2	Graphpad Software Inc.
QuPath	P. Bankhead

4.2 Methods

4.2.1 Cell culture methods

4.2.1.1 Maintenance of mammalian cell cultures

All cells were cultivated in a standard incubator at 37 °C and 5 % CO_2 and were always kept subconfluently. Cancer cell lines were maintained in DMEM with 10 % FBS and 1 % penicillin/streptomycin (P/S) (D10). The murine melanocytes (melan-a) were maintained in DMEM with high glucose, 10 % FBS, 1 % P/S, 200 nM TPA and 50 ng/ml cholera toxin. For normal human epidermal melanocytes (NHEM) Ham's F10 media was supplied with 20 % FBS, 1 % P/S, 100 nM TPA, 200 pM cholera toxin, 100 µM IBMX, and 1:1000 ITS premix. The cell growth was observed under a standard light microscope. If confluency reached 80 %, cells were passaged. For passaging, cells were washed once with EDTA-PBS and shortly covered with 1 x Trypsin-EDTA. After resuspension in media, cells were passed, depending on the cell type (1:5 - 1:10), on new cell culture dishes. Cell number was determined with a Neubauer hemocytometer. The hemocytometer consists of two chambers with a volume of 0.1 mm^3. Triple lines divide each chamber into nine large squares with an area of 1 mm x 1 mm. Those squares are further divided into 16 smaller squares. Cells in those 16 squares in each corner of the chamber were counted. The cell number was calculated with the following equation: N x 10^4/ml (N: number of counted cells).

Thawing and freezing of cells

Frozen cells were rapidly thawed at 37 °C and immediately transferred into 5 ml of the respective culture media. After centrifugation (1000 rpm, 5 min), the cell pellets were resuspended in fresh culture medium and seeded on a 10 cm dish for overnight incubation. On the next day, depending on cell density, media was changed, or cells passaged.

For cryopreservation, cells were trypsinized, centrifuged (5000 rpm, 5 min) and resuspended in respective freezing media containing 20 % FBS and 5 % DMSO. Before transfer to long-term liquid nitrogen storage, cells were frozen at – 80°C for at least two days.

Cell treatment

For experiments with indicated compounds or inhibitors, cells were seeded one day prior treatment. Appropriate controls were used, and cells were collected after indicated time periods. For cGAMP treatment, cells were transfected with cGAMP by usage of Lipofectamine 3000 transfection reagent, according to manufacturer's protocol. The ratio of P3000 reagent to cGAMP (400 µg/ml) was 8 µl : 20 µl in 250 µl OptiMEM, which was mixed with 15 µl Lipofectamine 3000 reagent in 250 µl OptiMEM. The cGAMP-lipofectamine mix was incubated at RT for 15 min and added dropwise to the cells.

4.2.1.2 Transfection of mammalian cell lines

Generation of stable transfected cell lines

Stable transfection of plasmid DNA was done by sleeping beauty-mediated transposition. In the presence of the sleeping beauty transposase vector (pCMV(CAT)T7-SB100X), the pSB-ET-iE vector allows integration of the gene of interest (GOI) by transposition. The doxycycline responsive T6 promoter drives expression of GOI and enhanced GFP (EGFP), the latter being separated from GOI by an IRES site. Cells were seeded one day prior transfection in a 6-well plate, so that cells reach 70 % confluency on the day of transfection. Concentration of DNA was kept constant at 2 µg with a 1:1 ratio of pSB-ET-iE to pCMV(CAT)T7-SB100X. Human melanoma cell lines were transfected with Fugene HD transfection reagent and for murine melanoma cells Lipofectamine 3000 transfection reagent was used, both according to manufacturer's protocol. Briefly, the ratio used for Fugene HD reagent to DNA was kept at 6:2 in 100 µl of OptiMEM. For Lipofectamine transfection the ratio of P3000 reagent to DNA was kept at 4:2 in 125 µl OptiMEM, which was mixed with 7.5 µl Lipofectamine 3000 reagent in 125 µl OptiMEM. The transfection mix was incubated at RT for 20 min and added dropwise to the cells. After overnight incubation, the media was replaced with fresh media. After recovery for one day puromycin selection was started, in general with 2 µg/ml puromycin for most cell lines. For selection of the murine melanoma cell line 781, 4 µg/ml puromycin was used. Cells were kept under selection pressure for at least one week and transfection of peGFP-N1 plasmid served as "kill control".

Knockdown by siRNA transfection

Knockdown of a gene of interest (GOI) was done by siRNA transfection. One day prior to transfection cells were seeded in a 6 cm dish. On the day of transfection with approximately 60 % confluency, cells were transfected with XtremeGENE siRNA transfection reagent according to manufacturer's instructions. In general, 120 nM siRNA was transfected with the ratio of 2:5 to transfection reagent. In UACC-62 cells, efficient knockdown was obtained by using 80 nM siRNA in a ratio 1:3. 6 h after transfection media was changed, and on the next day cells were re-seeded for downstream experiments.

Generation of CRISPR/Cas9 knockout cell lines

CRISPR/Cas9 knockout cells were generated by transfection of one (human) or two (murine) guideRNAs. The cloning of the respective gRNA expressing plasmids is characterized in 4.2.3.3. Transfection of human and murine melanoma cells was done as described above. Respective pU6-(BbsI)CBh-Cas9-T2A-mCherry constructs containing gRNAs were co-transfected with pE7584 Hygro#20, carrying the hygromycin resistance in a ratio of 1:1. Transfection efficiency was determined by verifying the mCherry fluorescence of the Cas9 vector. Transient selection for transfected cells was done with

350 ng/ml hygromycin for 3 days. For clonal selection cells were counted, diluted, and the cell suspension was seeded on a 48-well plate with 1 cell/well.
Growth of cell clones were closely monitored and after expansion knockout of NRF2 was validated by immunoblot assay. Genomic DNA was isolated from positive clones by QIAamp DNA Mini Kit according to manufacturer's protocol and the CRISPR validation primers were used to amplify specific regions within the target gene. Figure 7 displays the schematic overview of gRNA target sites and validation primers for the human and murine *NFE2L2* genes.

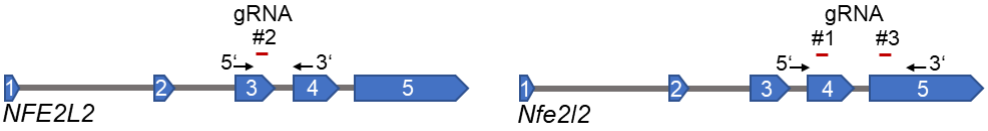

Figure 7 – Schematic overview of used gRNA and validation primer sites

Amplification of specific gDNA regions was done with commercially available Taq-polymerase according to manufacturer's protocol. In case of inconclusive sequencing results of PCR products, subcloning with StrataClone Blunt PCR Cloning Kit (Figure 8) was done and colony PCR products were sequenced to confirm site-specific cutting (Eurofins Genomics).

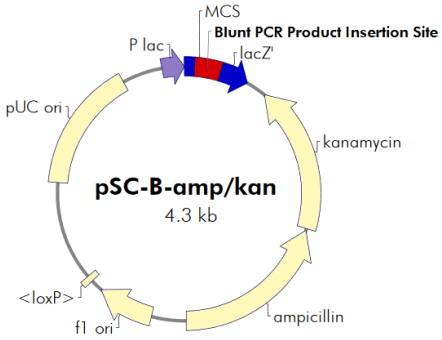

Figure 8 – Vector map of StrataClone Blunt PCR Cloning Vector pSC-B-amp/kan

4.2.1.3 Growth and migration assays

Proliferation assay by manual cell number determination
A defined number of cells was seeded in duplicates or triplicates in a 6-well plate. After the indicated treatment, cells were detached, centrifuged (5000 rpm, 5 min), resuspended in a defined volume of PBS, and counted using a Neubauer hemocytometer.

Cell viability determination by MTT assay
A suitable number of cells was seeded in 96-well plates and after attachment treated as indicated. At the endpoint of the experiment, 20 µl of MTT solution (5 mg/ml) was added directly into 100 µl of media and incubated for 2 h in a standard incubator. The media was aspirated and replaced by 150 µl of DMSO to solubilize the cells. The

generated formazan dye was dissolved on a shaker for 20 min at RT and absorbance was analyzed in a microplate reader at 590 nm with reference filter of 620 nm.

Crystal violet staining

To visualize cell density on cell culture dishes, media was aspirated after indicated treatment and cells were washed twice with PBS. Fixation was done with ice-cold methanol for 10 min and after aspiration a 2 % crystal violet in 2 % ethanol solution was added, just enough that the wells were covered. After 20 min of staining on a rocking shaker at RT, the staining solution was aspirated for re-use and cells were washed with PBS until the background got clear.

Senescence-associated β-galactosidase activity assay

For identification of senescent cells, the senescence-associated β-galactosidase activity assay was used. Cells were plated in 6-well plates and after indicated treatment the assay was performed. After washing twice with 1x PBS, cells were fixed with 3.7 % formaldehyde in PBS at RT for 5 – 10 min. After another washing step, the X-gal staining solution was added to each well and incubated under standard cell culture conditions for 12 – 16 h. The staining solution was washed away twice with 1x PBS and stained cells were stored in 1x PBS protected from light at 4 °C. Staining was detected under a phase-contrast light microscope.

Soft agar growth assay

For analysis of 3-dimensional colony growth of melanoma cells, soft agar growth assay was performed. For this, a 6-well plate was coated with two distinct layers of Bacto™ Agar. For the lower layer 2.4 % agar was dissolved in DMEM with 20 % FCS and 1 % P/S (D20) to a concentration of 0.6 % agar and 15 % FBS. The 6-well plate was carefully coated without bubble formation. For the upper layer 2.4 % agar was dissolved to 0.3 % in D20 and 15,000 cells were added. The cell suspension was carefully poured upon the lower layer. The stock solution of 2.4 % agar was kept at 50 °C to prevent solidifying. Cells were maintained in agar for 14 days to allow visible colony formation and D20 was added twice a week. Microscopy was done at 3 days, 7 days, 14 days, and colony formations were quantified by counting colonies of more than 8 cells in representative images.

Trans-well migration assay

Determination of migration capacities was done by a trans-well migration assay. For the migration assay cell culture inserts of PET membranes with 0.8 µm pore size were set into 24-well plates and equilibrated with DMEM with 1 % FBS and 1 % P/S (1 % starving medium) for 15 min. After siRNA transfection, 8,000 cells in 250 µl 1 % starving media were seeded in one cell culture insert. 1 % starving media was added in the 24-well plate beneath the insert and cells were starved for 1 day. Migration was started by replacing the 1 % starving medium below the insert with DMEM plus 10 % FBS and 1 % P/S. Cells

were permit to migrate for 16 h and migrated cells were dyed with crystal violet staining after removal of residual cells on top of the membrane with an cotton swap.

4.2.1.4 Assays for determination of intracellular components and activities

PGE2-ELISA assay

For measuring secreted PGE2 concentrations, 60,000 melanoma cells were seeded into 6-well plates and treated as indicated. After 24 h, cells received 800 µl fresh culture medium and secretion of PGE2 into the medium was allowed for 2 days. The medium was collected and PGE2 levels were analyzed with the PGE2 high-sensitivity ELISA Kit, accordingly to the manufacturer's instruction. Absorbance at 405 nm was measured with a microplate reader system.

Dual-reporter luciferase assay

For the determination of MITF activity by luciferase assay, cells were seeded in 12-well plates and pretreated for one day with indicated concentrations of doxycycline to induce MITF expression. The next day, cells were transfected with 950 ng of the Tyr-Luc-200 luciferase reporter construct (promoter element of the tyrosinase gene containing 200 bp upstream of transcription start site) and 400 ng or 800 ng of pcDNA3.1-NRF2 construct. Total concentration of transfected DNA was kept constant at 2 µg by adding appropriate amounts of empty pcDNA3.1 vector. As transfection control and for normalization, 50 ng of pGL4.74[hRluc/TK] vector (pRenilla) was used. Transfection was done with Fugene HD transfection reagent in a 5:2 ratio accordingly to manufacturer's protocol, and cells were constantly kept under doxycycline treatment. After 48 h, the transfected cells were lysed and assayed with the Dual-Luciferase® Reporter Assay according to the manufacturer's protocol. Firefly and Renilla luciferase activity were measured with a microplate reader system. The Firefly luciferase activity were normalized to Renilla luciferase activity.

CellROX assay

To analyze intracellular reactive oxygen species concentrations, the CellROX assay was used. Cells were seeded in triplicates in a 96-well plate and treated as indicated. Incubation of cells with 500 µM H_2O_2 for 30 min served as positive control. CellRox assay was performed according to the manufacturer's protocol. Co-staining of CellROX with Hoechst was performed for nuclear staining. Immediately after staining, images and quantifications were done using the deep red (660 nm) and Hoechst channel of the Operetta microscope.

Glutathione measurement by Tietze assay

Intracellular glutathione (GSH) concentrations were determined by using the modified Tietze assay [115, 116]. This assay allows quantitative determination of total and oxidized

glutathione levels by recycling oxidized glutathione disulfide (GSSG) to GSH by glutathione reductase (GR) in presence of the reducing agent NADPH. Cells were seeded in 6-well plates and treated as indicated. After cell collection and counting, for each measurement, $2x10^5$ cells were reconstituted in 1x PBS (50 µl) and mixed with 5 % sulfosalicylic acid in GSH assay buffer (100 µl) in a ratio of 1:2. To solubilize cells, samples were frozen at – 80 °C and thawed at RT for three times and subsequently centrifuged (12,000 rpm, 4 °C, 15 min). Defined GSH concentrations in the range between 10 µM and 320 µM were used to prepare a standard curve. 0.34 mM NADPH and 6 mM DTNB were each freshly prepared in GSH assay buffer. For GSH determination, 0.34 mM NADPH (700 µl), 6 mM DTNB (100 µl), H_2O (100 µl) and cell pellet supernatant or GSH standard (50 µl) were added to a 1.5 ml cuvette (ratio of: 7:1:1:0.5) and incubated for 20 min at RT. The reaction was started by adding 1 U/ml of glutathione reductase (GR) (50 µl). GSH concentrations were determined by observing the rate of change in absorption at 412 nm in a spectrophotometer for 10 min. Concentrations of GSH were calculated relative to specified standard concentrations and cell number.

4.2.2 Protein biochemistry

4.2.2.1 Cell lysis and protein analysis by SDS-PAGE and immunoblot

Protein expression levels were determined by SDS-PAGE with downstream immunoblot assay (western blot). After the indicated treatment, cells were washed once and collected with a silicon rubber in 1x PBS. The cells were pelleted by centrifugation (5000 g, 5 min, RT). The pellet was lysed on ice for 0.5 h – 2 h in RIPA lysis buffer with freshly added inhibitors. To pellet cell debris, the lysate was centrifuged (13000 g, 15 min, 4 °C). The volume of RIPA lysis buffer varied between 20 µl and 50 µl, depending on the cell pellet size. Protein concentration of lysates were analyzed by Bradford assay with a standard spectrophotometer and a defined BSA standard curve.

For separation of proteins according to their molecular weight, denaturing discontinuous sodium dodecyl sulfate polyacrylamide gel electrophoresis (SDS-PAGE) was used. In general, equal amounts of proteins, usually 30 µg – 40 µg, were diluted with lysis buffer and 1x SDS loading dye. Protein separation was done with a 12 % polyacrylamide gel run at 25 mA/gel for around 3 h. The SDS-PAGE consists of two distinct gel layers, the stacking gel (125 mM stacking gel buffer, 4 % Rotiphorese Gel 40, 0.1 % SDS, 0.05 % APS, 0.11 % TEMED) on top of the separating gel (375 mM separating gel buffer, 12 % Rotiphorese Gel 40, 0.1 % SDS, 0.05 % APS, 0.1 % TEMED). The molecular weight of proteins was determined by running a molecular weight standard alongside the samples.

Proteins were transferred on a nitrocellulose membrane, using the wet blotting system from Biorad. The gel, membrane, Whatman papers and sponges were soaked in 1x blotting buffer before setting up the blot. The gel and membrane were placed between

three Whatman papers and one sponge on each side. The transfer was performed at 4 °C for 1.5 h. The current was set to 250 mA for one and to 350 mA for two gels.
The proteins on the membrane were stained with Ponceau-S to validate protein transfer and incubated in 5 % BSA in 1x TBS-T for 30 min up to 1 h at RT to block unspecific binding. Incubation with the primary antibody was performed overnight at 4 °C with indicated dilutions in 5 % BSA/TBS-T. After three washing steps, each with 1x TBS-T for 5 min, the membrane was incubated with the secondary antibody in 5 % BSA/TBS-T for 1 h at RT. The membrane was washed three times with 1x TBS-T and incubated with SuperSignal West Pico Plus Chemiluminescent Substrate or WesternBright Chemiluminescent Substrate Sirius for 1 min. Protein signals were detected with the Photo Image Station 4000MM (Kodak) or the ChemiDoc Imaging System (Biorad).

4.2.2.2 Immunofluorescence

For protein localization immunofluorescence was performed. Cells attached on coverslips in 6-well plates were washed with 1x PBS and fixed in 4 % PFA for 10 min. Plates could then be stored in 1x PBS at 4 °C. If not indicated otherwise, all washing steps were performed three times with 1x PBS and incubation was done at RT. After washing, permeabilization in 0.2 % Triton X-100/PBS for 10 min was done, coverslips were washed once with 0.1 % Triton X-100/PBS and twice with 1x PBS. Subsequently, cells were quenched in 100 mM glycine/PBS and washed. Blocking and antibody incubation was done upside down on parafilm in a humidifier chamber. Cells were blocked in 1 % BSA/PBS for 30 min and primary antibody incubation was done in 1 % BSA/PBS for 1 h at RT with indicated dilutions. After washing, secondary antibody incubation was carried out with the respective Alexa Fluor® antibody in the dark for 1 h. After another washing step nuclear counterstaining was performed by incubation with Hoechst 34580 (1:10,000 in PBS) for 10 min. After the final washes, coverslips were rinsed once with ddH_2O and embedded with Mowiol-DABCO on microscope slides. Fluorescence was analyzed by inverted fluorescent microscopy (Leica).

4.2.3 RNA and DNA methods

4.2.3.1 RNA isolation and cDNA synthesis

Total RNA was isolated from cells by collecting cells either in 1x PBS with subsequent centrifugation or direct resuspension in TRIzol reagent. TRIzol reagent was used according to the manufacturer's manual, if possible, with only half of the indicated volumes. All centrifugation steps were performed at 4 °C and full speed. In brief, after homogenization of the cells in TRIzol, chloroform was added. The mix was vigorously shaken, and the phases were separated by centrifugation. The aqueous phase, containing RNA, was transferred into a new reaction tube and RNA was precipitated with the equal

amount of 100 % isopropanol. After 10 min incubation and centrifugation, the RNA pellet was washed twice with 75 % ethanol.
The isolated RNA was dried at 42 °C for 7 min and resuspended in DEPC-H_2O. To purify RNA, another precipitation step was done. 300 mM sodium acetate pH 5.2 and 2x of total volume 100 % EtOH was added to the RNA and incubated for 2 h or overnight at - 80 °C. The suspension was centrifuged for 30 min to pellet RNA and after a final washing step with 75 % EtOH, isolated RNA was dried and resuspended in DEPC-H_2O. RNA concentration was determined by NanoDrop spectrophotometer.
0.5 µg – 4 µg of total RNA was applied for cDNA synthesis and the RevertAid First Strand cDNA Synthesis Kit with random hexamer primers was used according to the manufacturer's protocol.

4.2.3.2 Quantitative real-time polymerase chain reaction (qPCR)

Quantitative real-time PCR was performed in a standard real-time thermocycler and for each gene with technical duplicates or triplicates. Amplification was performed in presence of SYBR green with an in-house His-Taq polymerase. The standard reaction contained following reagents and a standard 3-step cycler program was used:

µl	reagent
14.25	H_2O
2.50	10x Reprofast buffer
0.70	dNTP mix (10 mM)
0.75	SYBR-Green (1:2000)
0.30	His-Taq Polymerase
0.75	Primer forward (10 µM)
0.75	Primer reverse (10 µM)
5.00	cDNA (5 ng/µl)

temperature	time	
95 °C	2 min	
95 °C	15 s	
60 °C	20 s	40x
72 °C	30 s	
95 °C	15 s	
60 °C	15 s	
60 - 95 °C	20 min	
95 °C	15 s	

Gene expression of the gene of interest (GOI) was normalized to a housekeeping gene (HG), by determination of individual cycle thresholds (Ct). For human gene expression the expression levels of *ACTB* or *RPSI4* and for murine gene expression *Actb* served as housekeeping gene.

The relative expression was calculated as followed:

$$\Delta Ct = Ct\ (GOI) - Ct\ (HG)$$

$$\Delta\Delta Ct = \Delta Ct\ (sample) - \Delta Ct\ (reference)$$

Relative expression was calculated by using:

$$2^{\Delta\Delta Ct(GOI)}:2^{\Delta\Delta Ct(HG)}$$

4.2.3.3 Agarose gel electrophoresis

For analysis of DNA fragments and cloning intermediate products, agarose gel electrophoresis was done. Depending on the size of examined DNA products 1 %, 1.5 % or 2 % agarose were dissolved in 1x TAE buffer. Before loading, samples were mixed with

6 x DNA loading dye. Agarose gel electrophoresis was carried out at 120 - 140 V for 40 – 60 min. For visualization, the agarose gel was incubated in an ethidium bromide (2 µg/ml) bath for 10 min and DNA was detected under a UV transilluminator. The sizes of DNA fragments were determined by running a DNA ladder alongside the samples.

4.2.3.4 Generation of expression vectors

Generation of inducible pSB-ET-iE constructs for exogenous gene expression

For generation of stable expressing cell lines, the gene of interest (GOI) was cloned into the transposase vector pSB-ET-iE (Figure 9), which allows integration of the GOI in the presence of the sleeping beauty transposase (encoded on pCMV (CAT)T7 SB100x). The GOI was amplified from 0.5 µg of melanoma cDNA, expressing the GOI, by polymerase chain reaction (PCR) with respective cloning oligonucleotides (4.1.7 Table 16). Amplification was done with the proofreading Q5-Polymerase according to the manufacturer's protocol and confirmed by 1.5 % agarose gel electrophoresis (140 V, 40 min). The PCR product was purified, using the PCR Clean Up Kit according to manufacturer's instructions. The purified PCR product as well as the pSB-ET-iE plasmid were digested with indicated restriction enzymes for 1.5 h at 37 °C. After purification and control by agarose gel electrophoresis the fragment was ligated into the digested vector by T4 DNA ligase according to the manufacturer's protocol and incubated for 20 min at RT.

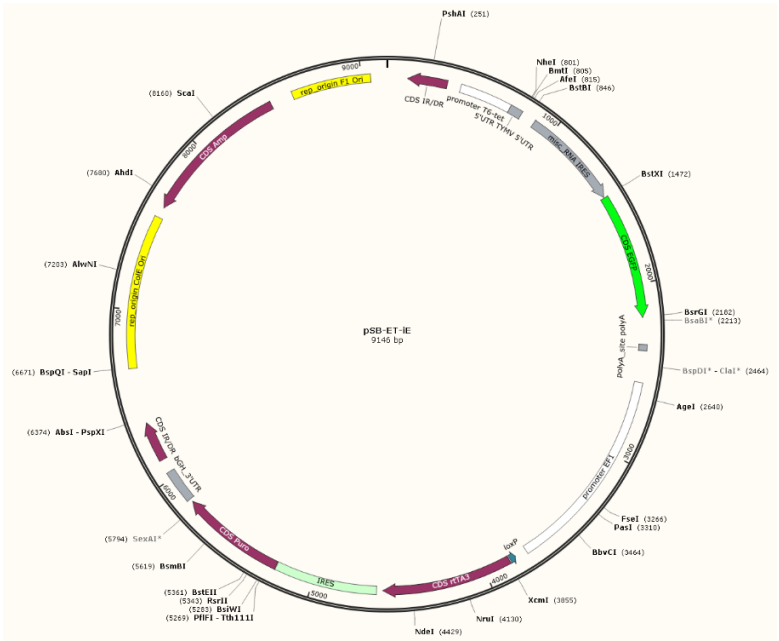

Figure 9 – Vector map of pSB-ET-iE expression vector

Bacterial transformation

The ligation reaction was added to 50 µl of *E.coli* DH5α bacteria and incubated on ice for 20 min. Transformation into *E.coli* DH5α was done by heat shock at 42 °C for 90 s. LB media was added and the bacteria were out grown at 37 °C and 550 rpm. After

agitation for 1 h the bacteria were plated on LB-plates containing 50 µg/ml ampicillin and incubated at 37 °C overnight. Cloning of the GOI was analyzed by colony PCR with IRES-5-reverse and TYMV-forward primer and positive clones were verified by sequencing (Eurofins Genomics).

Generation of pcDNA3.1-NRF2 construct for luciferase assay

For the luciferase assay (4.2.1.4) the Nfe2l2 cDNA was cut from pSB-ET-iE with NheI and AfeI restriction enzymes (1.5 h, 37 °C) and purified by 1.5 % agarose gel electrophoresis with the Monarch DNA Gel Extraction Kit according to manufacturer's instructions. The vector backbone pcDNA3.1 (Figure 10) was cut sequentially with NheI and EcoRV, each at 37 °C for 1.5 h, according to manufacturer's instructions. Ligation and transformation were done as described above. Cloning of the GOI was analyzed by colony PCR with T7-forward and an insert specific reverse primer. Positive clones were verified by sequencing (Eurofins Genomics).

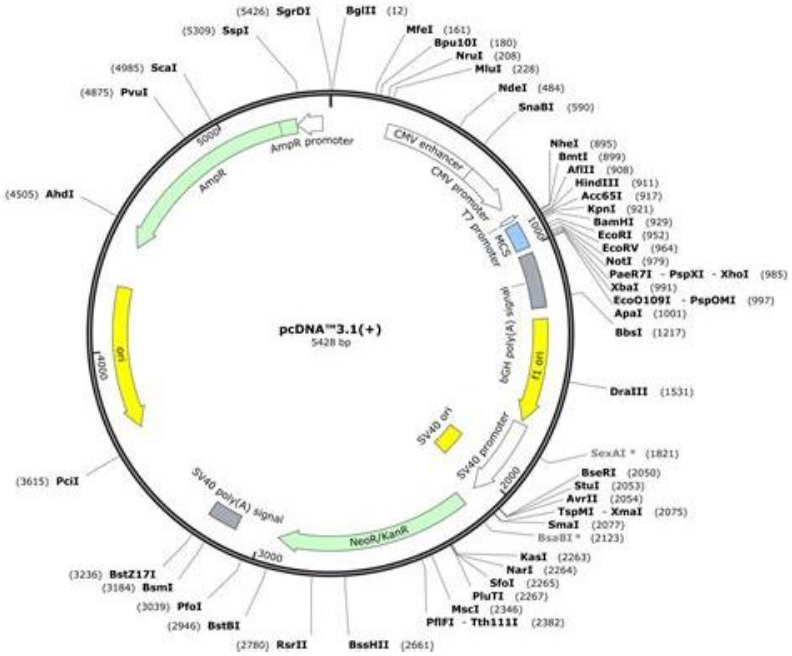

Figure 10 – Vector map of pcDNA3.1(+) expression vector

4.2.3.5 Generation of gRNA duplexes for CRISPR/Cas9 knockout cell lines

For generation of CRISPR/Cas9 knockout cell lines, the respective gRNAs were cloned into the Cas9 containing vector pU6-(BbsI)_CBh-Cas9-T2A-mCherry (Figure 11). The gRNA sequences were designed by using the GPP sgRNA Designer of BROAD institute (https://portals.broadinstitute.org/gpp/public/analysis-tools/sgrna-design). First, 2 µg of Cas9-vector was digested with BbsI, according to manufacturer's instruction. After confirmation of digestion efficiency with 0.8 % agarose gel electrophoresis and purification with PCR Clean up Kit, the digested vector was dephosphorylated by using FastAP alkaline phosphatase according to the manufacturer's protocol. After

purification, vector integrity was confirmed with 0.8 % agarose gel electrophoresis and the vector was stored at -20 °C.

The gRNA duplex was prepared by ligation of the respective forward and reverse oligonucleotides in a concentration of 100 µM. In presence of T4 polynucleotide kinase and 1x ligation buffer, the gRNA duplex was prepared by incubation for 30 min at 37 °C, heating to 95 °C for 5 min in a cycler and cool down to RT for 1 h. After dilution 1:250 the gRNA duplex was stored at -20 °C.

Ligation of digested vector and diluted gRNA duplex (ratio 1:1) was done with T4 DNA ligase according to manufacturer's protocol for 20 min at RT. Transformation was carried out as mentioned above.

Confirmation of insertion was done by control digestion with the restriction enzymes BbsI and AgeI in NEBuffer 1.1, according to manufacturer's guidelines. Digestion was validated by 0.8 % agarose gel electrophoresis. Positive clones have a band at 9 kb, whereas negative clones displayed two bands at 800 bp and 8.5 kb. With positive clones, sequencing for specific gRNA was done (Eurofins Genomics).

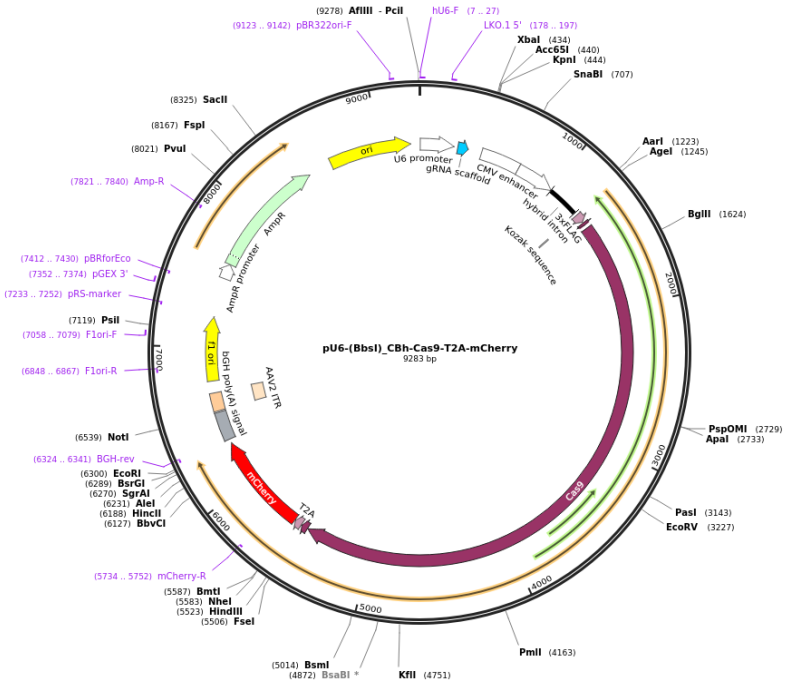

Figure II – Vector map of pU6-(BbsI)_CBh-Cas9-T2A-mCherry CRISPR/Cas9 vector

4.2.3.6 Purification of plasmid DNA

For transfection of plasmid DNA, high purity plasmid DNA preparations were prepared by using the GenElute™ Plasmid Miniprep Kit or E.Z.N.A Endo-free Plasmid Midi Kit. In brief, 5 ml or 50 ml LB-media containing 50 µg/ml ampicillin were inoculated overnight with the respective plasmid construct. After spinning down the bacteria by centrifugation (4000 g, 10 min, 4 °C), lysis and plasmid DNA isolation was done according to the manufacturer's instruction.

4.2.4 Chromatin immunoprecipitation (ChIP) and ChIP sequencing

Cross-linking and cell lysis

Chromatin immunoprecipitation (ChIP) was done with 2 x 10^6 UACC-62 cells per sample. After indicated treatments, cells were cross-linked with 1 % formaldehyde for 10 min at RT with slow agitation. The reaction was stopped by adding 125 mM glycine and incubation for 5 min at RT with slow agitation. Cells were washed twice with ice-cold 1x PBS and collected in a suitable reaction tube. After centrifugation (1200 g, 5 min, 4 °C), the cell pellet was lysed in 3 ml ChIP lysis buffer I with freshly added inhibitors for 20 min on ice. After centrifugation (1200 g, 5 min, 4 °C), the cell pellet was shock-frozen in liquid nitrogen and stored at -80 °C. The nuclei were resuspended in 1.5 ml ChIP lysis buffer II, with freshly added inhibitors and incubated on ice for 10 min. The chromatin was fragmented to an approximate length of 150 to 200 bp using a Branson sonifier. Sonication was done with a pulse for 10 s at an amplitude of 25 % and pause for 45 s for a total of 15 min. Before and after sonication a sample was taken to confirm appropriate chromatin fragmentation. During size check the fragmented chromatin was stored at 4 °C on ice.

Size check: reversing crosslinks and protein degradation

The samples, taken before and after sonication, were centrifuged (13000 g, 15 min, 4 °C) and 50 µl was transferred into a new reaction tube. 200 mM NaCl as well as 200 µg/ml RNase A were added after incubation at 37 °C for 1 h, the cross-link was reversed at 65 °C and 550 rpm agitation overnight. On the next day, after the samples were cooled to RT, 400 µg/ml proteinase K was added and incubated at 45 °C with 550 rpm agitation for 2 h. DNA was isolated with phenol/chloroform DNA purification.

Size check: phenol/chloroform isolation of DNA

1 ml of a phenol/chloroform/isoamyl alcohol mix in a ratio of 25:24:1 was added per sample and vortexed for 15 s. The aqueous phase, containing nucleic acids, was transferred into a new reaction tube and precipitation of DNA was performed by adding 40 µg/ml glycogen, 0.1x volume of 3 M sodium acetate and 2x volume of 100 % EtOH (-80 °C, 30 min). After centrifugation (13,000 g, 10 min, 4 °C), the DNA pellet was washed once with 70 % EtOH (13,000 g, 5 min, 4 °C) and dried at RT. After resuspension in 50 µl 1x TE buffer, DNA concentration was determined by NanoDrop spectrophotometer and chromatin fragmentation was confirmed by 1.5 % agarose gel electrophoresis.

Chromatin immunoprecipitation

For chromatin immunoprecipitation (ChIP), 30 µl per sample protein G magnetic Dynabeads™ were washed three times with 1 ml BSA-PBS (5 mg/ml) and incubated overnight at 4 °C with 3 µg of the indicated antibody diluted in 600 µl BSA-PBS on a rotation wheel. On the next day, after three washing steps with BSA-PBS, 80 µg of chromatin in 600 µl ChIP lysis buffer II + inhibitors were added to the protein G coupled

antibody. Binding of chromatin and antibody was allowed for 6 h at 4 °C with gentle rotation. 1 % of applied chromatin amount was kept as input control.
After chromatin immunoprecipitation, beads were washed with ChIP wash buffer I, II and III, each three times for 3 min at 4 °C on a rotation wheel. Inhibitors were added freshly to all buffers before use. The beads were washed once with 1x TE + inhibitors and transferred into a new reaction tube. Elution was done twice for 15 min at RT on a rotating wheel with 250 µl of freshly prepared ChIP elution buffer and the eluates were combined. The 1 % input control was treated alongside the eluates.
Crosslinks were reversed by addition of 160 mM NaCl and 20 µg/ml RNase A and incubation at 37 °C for 1 h before shaking at 550 rpm at 65 °C overnight. Proteins were degraded by adding 5 mM EDTA and 200 µg/ml proteinase K at 45 °C for 2 h. Chromatin DNA was purified using the QIAquick PCR Purification Kit according to the manufacturer's protocol and eluted in 50 µl EB buffer.
For quantification of chromatin enrichment after ChIP, commercial SYBR green containing master mixes were used, according to the manufacturer's instructions. As template DNA 1 µl of purified chromatin was used.

iTaq universal SYBR Green supermix:

µl	reagent
3.2	H_2O
5.0	iTaq universal SYBR Green supermix
0.4	Primer forward (10 µM)
0.4	Primer reverse (10 µM)
1.0	DNA

temperature	time	
95 °C	2 min	
95 °C	15 s	
60 °C	30 s	40x
95 °C	15 s	
60 °C	15 s	
60 - 95 °C	20 min	
95 °C	15 s	

SYBR Select master mix:

µl	reagent
3.2	H_2O
5.0	SYBR Select master mix
0.4	Primer forward (10 µM)
0.4	Primer reverse (10 µM)
1.0	DNA

temperature	time	
50 °C	2 min	
95 °C	2 min	
95 °C	15 s	
60 °C	1 min	40x
95 °C	15 s	
60 °C	15 s	
60 - 95 °C	20 min	
95 °C	15 s	

ChIP-sequencing

For ChIP-sequencing (ChIP-Seq), chromatin from 3 x 10^7 UACC-62 cells was isolated and immunoprecipitated as described above. Purified ChIP-DNA was quantified using the Qubit® DNA quantification assay system. 4 ng DNA was used for cDNA library preparation using the NEBNext® Ultra II DNA Library Prep Kit for Illumina® according to the manufacturer's instructions. Size-selection was performed using Agencourt AMPure XP beads and DNA fragments were amplified by 12 cycles of PCR. cDNA library quality was analyzed with a Fragment Analyzer. Sequencing was done by Dr. Carsten

Ade (Department of Biochemistry and Molecular Biology, University of Würzburg) using a NextSeq500 Illumina platform.

Data analysis

Sequencing data were uploaded and processed by using the Galaxy web platform (usegalaxy.org) and Cistrome Analysis Pipeline (cistrome.org/ap/root).

All FASTQ files were uploaded to the galaxy platform and individual FASTQ files of one sample were concatenated. Files were converted to FASTQsanger by using FASTQ groomer, following mapping to human genome hg38 by using Burrows-Wheeler Alignment (BWA) tool generating BAM files. BEDgraph files were created by using the MACS2 package for peak calling, which were converted to bigWig files. Peak calling was done with an FDR cut off of ≤ 0.05. The bigWig files were visualized with the integrative genome browser (IGB) and transferred to Cistrome Analysis Pipeline for downstream analyzation. Analysis of ChIP enrichment in specific genomic regions were performed with the *cis*-regulatory element annotation system (CEAS) tool. Further analysis included comparisons of control and treatment conditions as well as motif recognition by SeqPos motif tool. Direct target genes prediction was done by binding and expression target analysis (BETA). For this, the bed files of NRF2 enriched peaks were compared with the differential expression data of RNA-sequencing after NRF2 knockdown. Genes with a peak at ±5 kb to the promoter sites were considered to be direct targets. With those predicted target genes, gene ontology (GO) term analysis with the database for annotation, visualization and integrated discovery (DAVID) was performed.

4.2.5 RNA isolation for RNA-sequencing

After indicated treatment or tumor resection, RNA was isolated using the RNeasy Kit with on-column DNase digestion according to the manufacturer's instruction. The quality of total RNA was determined using the Experion Automated Electrophoresis System or a Fragment analyzer. 1 µg of total RNA was used for Poly-A+ RNA isolation using the NEBNext Poly(A) mRNA Magnetic Isolation Module. NEBNext® Ultra™ II RNA Library Prep Kit for Illumina® was used for library preparation according to the manufacturer's protocol. cDNA libraries were amplified with 12 PCR cycles. Library quality and quantity were determined with the Experion Automated Electrophoresis System or a Fragment analyzer.

Sequencing was performed by Dr. Carsten Ade (Department of Biochemistry and Molecular Biology, University of Würzburg) using a NextSeq500 Illumina (NB500931) platform (single end sequencing, 75 cycles).

Afterwards, data were processed by Dr. Susanne Kneitz (Department of Physiological Chemistry, University of Würzburg), all human data were aligned to the genome (Homo_sapiens.GRCh38.dna.toplevel.fa) using STAR [117]. Expected read counts for each gene were calculated using RSEM [118]. Differential expression was calculated by

the Bioconductor/R package and DESeq2 software [119], followed by gene set enrichment analysis (GSEA, BROAD Institute).
For murine NRF2 knockout experiments *in vitro* and *in vivo*, sequencing and all data processing steps were performed by Apoorva Baluapuri (Department of Biochemistry and Molecular Biology, University of Würzburg), the FASTQs were checked for quality using FASTQC (Babraham Bioinformatics) followed by alignment to mm10 mouse genome build using Bowtie2 (v2.3.4.1) [120], using -N 1 option. All aligned reads containing files were normalized to same reads depth using Samtools (v1.3). These read normalized files were then used for differential expression regulation analysis using edgeR protocol [121] implemented in R v3.5.2. Briefly, the reads from bam files were read into R using readGAlignment function, followed by extraction of read counts for every gene with summarizeOverlaps function. Non expressed genes were removed, and dispersion was calculated followed by p- and q- value calculation using Benjamini Hochberg correction. All further graphs were generated using ggplot2 (https://ggplot2.tidyverse.org).

Data availability
The RNA sequencing data have been deposited in NCBI's Gene Expression Omnibus under the Bioproject accession number PRJNA601317 and GEO accession number GSE141912.

4.2.6 LC/MS-Analysis

Sample preparation and mass spectrometry were performed by Dr. Werner Schmitz (Department of Biochemistry and Molecular Biology, University of Würzburg).
Extraction of lipids in tissue homogenate: Tissue samples were cut into small pieces and homogenized with Ultraturrax after addition of 49 vol. of H2O. 270 µl homogenate were mixed with 30 µl 10% acetic acid and 300 µl n-butanol / methanol (3/1, v/v). After the addition of 300 µl heptane / ethyl acetate (3/1, v/v) and 280 µl 1% acetic acid, samples were mixed and centrifuged (2 min. max rpm in an Eppendorf centrifuge). The resulting upper phase was transferred into a new Eppendorf cup, the lower phase was reextracted with 400 µl heptane/ethyl acetate (3/1, v/v). Upper phases were combined and evaporated at 35 °C under a stream of N2 gas.
The equipment used for LC/MS analysis was a Thermo Scientific Dionex Ultimate 3000 UHPLC system hyphenated with a Q Exactive mass spectrometer (QE-MS) equipped with a HESI probe. For LC/MS analysis, the residues of the lipid extractions were dissolved in 100 µl of isopropyl alcohol. Chromatographic separation was achieved by applying 3 µl dissolved sample on a Acclaim RSLC 120 C8 (2.2 µm particles, 50 × 2.1 mm), combined with a Javelin particle filter and a Acclaim 120 C8 (5 µm particles, 10 × 2 mm) precolumn using a linear gradient of mobile phase A (CH3CN/H2O/formic acid (10/89.9/0.1, v/v/v)) and mobile phase B (CH3CN/2-propanol/H2O/formic acid (45/45/9.9/0.1, v/v/v/v)). The column was kept at 40 °C and the LC gradient program

was 20 % solvent B for 2 min, followed by a linear increase to 100 % solvent B within 5 min, then maintaining 100 % B for 27 min, then returning to 20 % B in 1 min and 5 min 20 % solvent B for column equilibration before each injection. The column temperature was set to 40 °C, the flow rate was maintained at 350 µL/min. The eluent was directed to the ESI source of the QE-MS from 2.0 min to 29 min after sample injection. For MS analysis, the following MS scan parameters were used: Scan Type: Full MS in alternating pos./neg. mode; Runtime: 2 min -29 min; Resolution: 70,000; AGC-Target: 3E6; Maximum Injection Time: 200 ms; Scan Range: 200 -1500 m/z. HESI Source Parameters: Sheath gas flow rate: 30; Auxiliary gas flow rate: 10; Sweep gas flow rate: 3; Spray voltage: 2.5 kV in pos.mode and 3.6 kV in neg.mode; Capillary temperature: 320 °C; S-lens RF level: 55.0; Aux Gas Heater temperature: 120 °C. Peaks corresponding to the calculated lipid masses were integrated using TraceFinder software. Specific peak areas were normalized to total lipid peak areas. Ultrapure water was obtained from a Millipore water purification system. LC/MS solvents, LC/MS ammonium acetate and standard compounds were purchased from Merck.

4.2.7 Melanoma mouse models

4.2.7.1 Subcutaneous injection of murine melanoma cell lines

For validation of *in vivo* tumor growth of murine *Nfe2l2* wt and *Nfe2l2* knockout cell lines, cells were subcutaneously injected into flanks of C57BL/6 wt mice. The cells were detached of cell culture plates by 1x Trypsin-EDTA. After counting with a hemocytometer, 10,000 cells were resuspended in 200 µl PBS and pipetted into a syringe. Before injection, mice were anesthetized with 7.2 µl/g ketamine/xylazine in 0.9 % NaCl (3:1:12), the right flank of the mice were shaved and disinfected. After pulling up the skin with a tweezer, the cells were injected with visible bump formation. Tumor onset and growth was monitored daily.

4.2.7.2 Genetic mouse model for melanoma initiation

All mice were maintained on a C57BL/6 background. The Tyr-Cre^{ERT2}, $BRAF^{V600E/wt}$ melanoma model with development of benign melanocytic hyperplasia has been described in [113]. In this mouse model, expression of a conditional $Braf^{V600E}$ allele is initiated by the activation of a Cre recombinase, driven under the melanocyte specific tyrosinase promoter (*Tyr-*Cre^{ERT2}). After Cre activation with 4-hydroxytamoxifen (4-OHT), benign pigment lesions developed at the application site on the skin. The *Tyr-*Cre^{ERT2}*-*$Braf^{V600E}$ model was crossed with a constitutive bi-allelic $Nfe2l2^{-/-}$ mice [114].

The status of *Tyr-Cre*, *BRAF*^{V600E} and *Nfe2l2* of each mouse was analyzed by PCR.

Tyr-Cre

µl	reagent
16.7	H_2O
2.5	10x Reprofast buffer
0.5	dNTP mix (10 mM)
0.3	His-Taq Polymerase
1.0	Primer Tyr-Cre forward
1.0	Primer Tyr-Cre reverse (10 µM)
1.0	Primer pos. ctrl forward
1.0	Primer pos. ctrl reverse (10 µM)
1.0	template gDNA

temperature	time	
95 °C	3 min	
95 °C	30 s	
51.7 °C	1 min	35x
72 °C	1 min	
72 °C	2 min	
4 °C	hold	

BRAF^{V600E}

µl	reagent
18.7	H_2O
2.5	10x Reprofast buffer
0.5	dNTP mix (10 mM)
0.3	His-Taq Polymerase
1.0	Primer BRAF forward (10 µM)
1.0	Primer BRAF reverse (10 µM)
1.0	template gDNA

temperature	time	
95 °C	3 min	
95 °C	30 s	
63 °C	1 min	35x
72 °C	1 min	
72 °C	2 min	
4 °C	hold	

Nfe2l2

µl	reagent
17.6	H_2O
2.5	10x Reprofast buffer
0.5	dNTP mix (10 mM)
0.4	His-Taq Polymerase
1.0	Primer Nrf2 forward (10 µM)
1.0	Primer Nrf2 wt reverse (10 µM)
1.0	Primer Nrf2 ko reverse (10 µM)
1.0	template gDNA

temperature	time	
95 °C	5 min	
95 °C	30 s	
56 °C	1 min	35x
72 °C	1 min	
72 °C	5 min	
4 °C	hold	

Mice with the genetic background *Tyr-Cre*^{ERT2}; *Braf*$^{V600E/wt}$; *Nfe2l2*$^{+/+}$ and *Tyr-Cre*^{ERT2}; *Braf*$^{V600E/wt}$; *Nfe2l2*$^{-/-}$ at the age 6-8 weeks were used for induction of melanocytic hyperplasia. Development of benign melanocytes was accomplished by local administration of 1 ml of 1 mM 4-OHT in ethanol. Before treatment, mice were anesthetized like described above. The hair at the back of the mice, around 2 mm above the tail root, was removed and 4-OHT was applied. In total 1 ml of 1 mM 4-OHT was applied three times on three consecutive days. Mice were closely monitored for 9 months, until the experiment was terminated.

4.2.7.3 Immunohistochemistry

Mouse tumors were fixed in 4 % PFA, embedded in paraffin and sectioned. Sections and staining were performed by Sabine Roth (Institute of Pathology, University of Würzburg). Sections were deparaffinized, rehydrated, and stained with hematoxylin and eosin or processed for immunohistochemistry for CD3. Immunohistochemical staining for CD3 used in a dilution of 1:100, was performed using standard immunohistochemical methods. After peroxidase blocking and heat pretreatment with citrate buffer pH 6,0 in a steamer for 8 minutes, the primary antibody was incubated for 1 hour and detected with a 2-step polymer system, HRP conjugated, followed by the manufacturer's instructions. For quantification, slides were digitized by using VENTANA DP 200 slide scanner and quantification was done by positive cell detection with QuPath open-source software platform [122]. After vector stain estimation for each slide, whole tumors, excluding necrotic parts, were quantified for positive nuclear DAB staining.

4.2.8 Statistical analysis

If not indicated otherwise all data display mean ± standard deviation (SD). Individual statistical tests are specified in each figure legends. In general, unpaired two-tailed Student's t-test was used to compare two groups, for more than two groups one-way ANOVA with Bonferroni's multiple comparisons test was used. For comparison of two or more groups in response to different stimuli, two-way ANOVA with Tukey's or Sidak's multiple comparison tests were performed. Experiments with p values ≤ 0.05 were considered to be statistically significant. All statistical analyses were performed using GraphPad Prism 8.4.1 software.

5. Results

5.1 Basal expression of NRF2 in melanoma cells

Since melanomas are particularly prone to an accumulation of reactive oxygen species (ROS) [7], melanoma cells might express basal levels of NRF2 even without further stress induction. To investigate, whether NRF2 is expressed in melanoma cell lines under physiological conditions in comparison to other tumor entities, RNA-sequencing data were extracted from the BROAD Institute Cancer Cell Line Encyclopedia (CCLE). In total, the dataset encompasses 1,457 cell lines derived from 22 different human cancer entities. Cell lines belonging to skin melanoma displayed the highest gene expression of *NFE2L2* (Figure 12A) and its well-known target gene *NQO1* (Figure 12B). The basal protein expression of NRF2 was analyzed in a panel of human melanoma cell lines and compared to the expression in the normal human epidermal melanocytes NHEM and the KEAP1-mutant non-small cell lung cancer cell line A549 (Figure 12C). In all analyzed cell lines basal levels of NRF2 were detected, though to a varying extent. Thus, melanoma cell lines exhibit basic NRF2 expression levels under standard culture conditions.

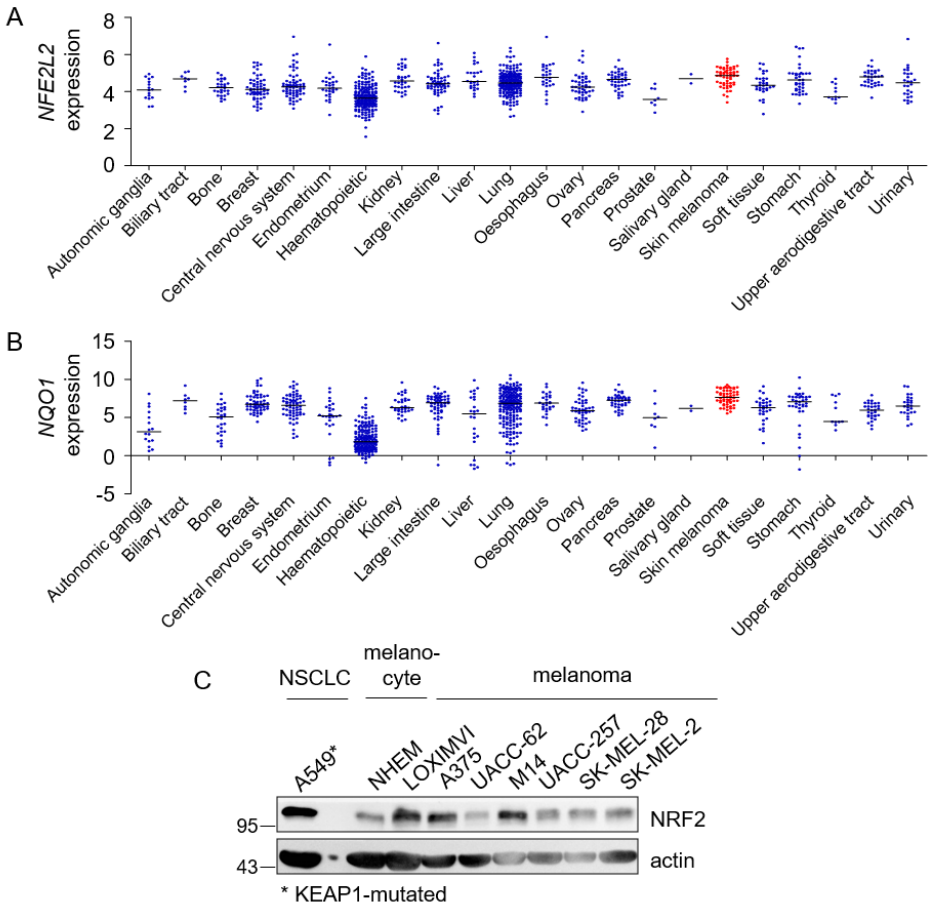

Figure 12 – Basal NRF2 expression in melanoma
A: *NFE2L2* and **B**: *NQO1* expression in 22 cancer entities. Data were extracted from RNA sequencing data of the BROAD Institute Cancer Cell Line Encyclopedia (CCLE) (https://portals.broadinstitute.org/ccle) **C**: Immunoblot showing NRF2 expression in KEAP1-mutated A549 lung adenocarcinoma cells, normal human epidermal melanocytes (NHEM) as well as indicated human melanoma cell lines. Actin served as loading control.

5.1.1 Melanoma-associated oncogenic signaling activates NRF2 in melanocytes

As NRF2 is strictly regulated by degradation under physiological conditions, factors that lead to NRF2 expression in melanoma were investigated. Previous studies showed, that NRF2 expression is induced by diverse oncogenes, such as BRAF, RAS or c-MYC [84]. About 50 % of melanomas harbor a $BRAF^{V600E}$ driver mutation [123, 124], hence it was evaluated if induction of $BRAF^{V600E}$ in melanocytes activates NRF2. Melan-a cells, a murine melanocytic cell line, harboring a doxycycline-inducible $BRAF^{V600E}$ expression vector, were treated with 100 ng/ml doxycycline (dox). Protein expression of p-ERK1/2 confirmed activation of the p-ERK signaling pathway by $BRAF^{V600E}$ induction (Figure 13A). Upon $BRAF^{V600E}$ activation, NRF2 was translocated into the nucleus as evaluated by immunofluorescence (Figure 13B). Transcription of *Nfe2l2* itself was not enhanced, whereas expression of well-known NRF2 target genes *Hmox1*, *Slc7a11* and *Nqo1* were increased after oncogene induction (Figure 13C). The activation of the $NRAS^{Q61K}$ oncogene, which occurs in around 30 % of melanoma patients [124, 125], showed similar effects. After $NRAS^{Q61K}$ induction with 50 ng/ml dox, NRF2 target gene expression was elevated (Figure 13D) in melan-a cells. However, no change in *Nfe2l2* expression was observed (Figure 13D), in accordance with the $BRAF^{V600E}$ results. Thus, melanoma driver mutations, like $BRAF^{V600E}$ and $NRAS^{Q61K}$ were confirmed as inducers of NRF2 activity in melanocytes.

Previous studies showed that NRF2 deficiency in keratinocytes promotes skin carcinogenesis and tumor initiation, but did not alter tumor progression [104]. This tumor preventing role of NRF2 was also seen in liver [126] and lung [127] cancer initiation. To investigate, if NRF2 deficiency also promotes melanoma formation, a well-established melanoma mouse model for melanocytic hyperplasia was used [113]. In this mouse model expression of a conditional $BRAF^{V600E}$ allele is initiated by the activation of a Cre recombinase, driven under the melanocyte specific tyrosinase promoter (Tyr-Cre^{ERT2}). After Cre activation with 4-hydroxytamoxifen (4-OHT), benign pigment lesions are reported to develop at the application site on the skin. In a *Pten* deficient genetic background these benign lesions develop into metastatic melanoma [113]. For this work, the *Tyr-*Cre^{ERT2}*-*$BRAF^{V600E}$ model was crossed with $Nfe2l2^{-/-}$ mice, which were constitutively NRF2 deficient [114]. After local application of 1 mM 4-OHT on the shaved skin, the formation of benign melanocytic lesions was monitored. Neither $Nfe2l2^{-/-}$ nor $Nfe2l2^{+/+}$ mice developed tumors until the end of the experiment, which was terminated after 280 days (Figure 13E). Mice were weighed (Figure 13F) and application sites were photographed (Figure 13G). No obvious differences were detectable in weight or hyperplasia formation, moreover NRF2 was expendable for nevi formation (Figure 13F, G). Taken together, it was determined that NRF2 is induced by activation of oncogenic driver $BRAF^{V600E}$, but the NRF2 deficiency did not promote melanoma formation in the $BRAF^{V600E}$-driven melanoma mouse model.

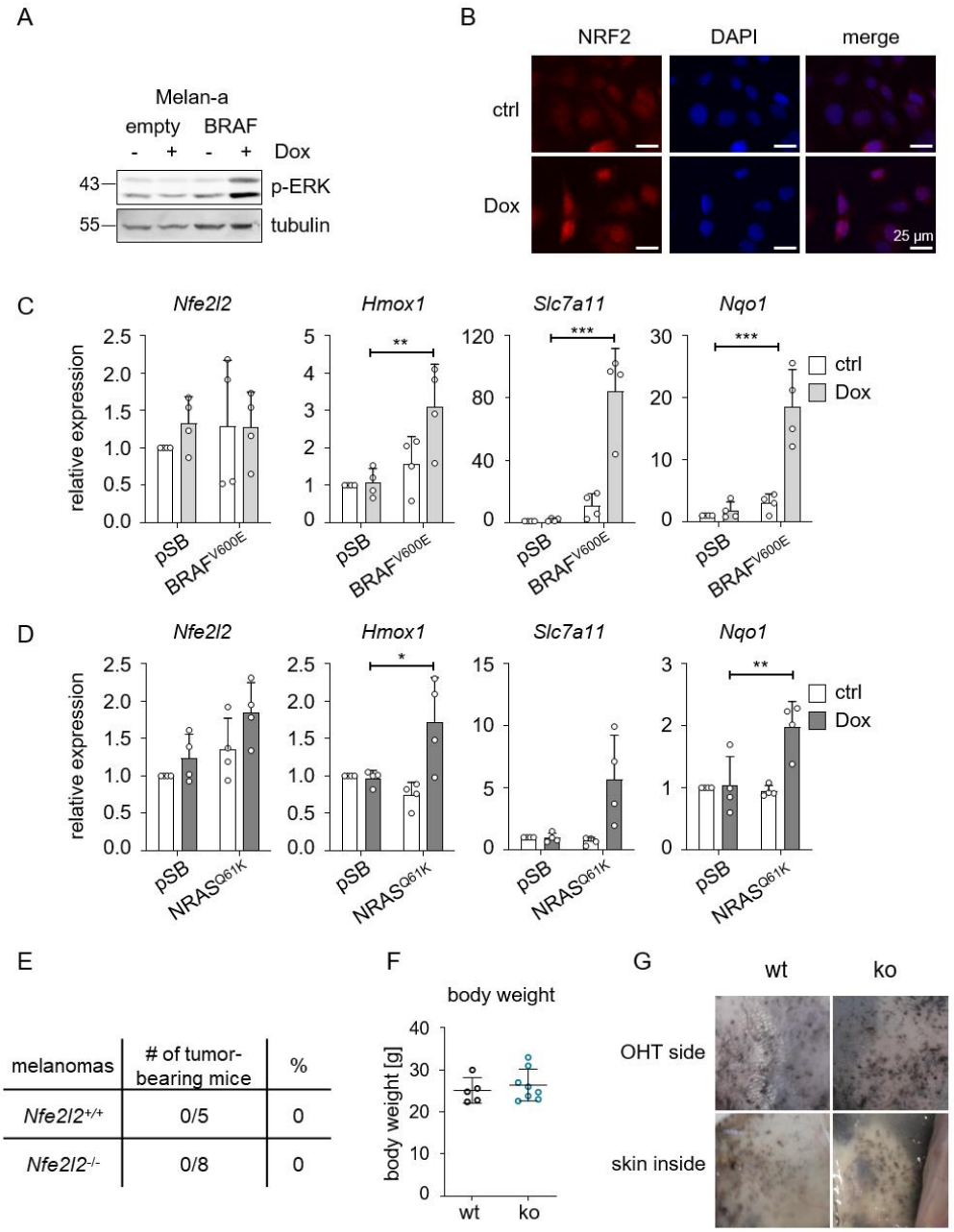

Figure 13 – Oncogenic signaling translocates NRF2 into the nucleus
A: Immunoblot for p-ERK (Thr 202/Thr 204) expression after Dox-dependent BRAF^{V600E} induction in the murine melanocyte cell line melan-a (100 ng/ml, 24 h). Tubulin served as a loading control. **B**: Corresponding immunofluorescence of NRF2, nuclear staining with DAPI and merged image after BRAF^{V600E} induction. **C**: Real-time PCRs of *Nfe2l2* and indicated target genes in BRAF^{V600E}-expressing melan-a cells after Dox treatment (100 ng/ml, 24 h). **D**: Real-time PCRs of *Nfe2l2* and target genes in NRAS^{Q61K}-expressing melan-a cells after Dox treatment (50 ng/ml, 7 d). Real-time PCR experiments were performed in four replicates and two-way ANOVA with Tukey's multiple comparisons test was carried out (*p<0.05, **p<0.01, ***p<0.001). Error bars represent SD. **E**: Table of tumor bearing mice after hyperplasia induction with 1 mM 4-OHT in Tyr-Cre^{ERT2}, *BRAF$^{V600E/wt}$*, *Nfe2l2$^{+/+}$* or *Nfe2l2$^{-/-}$* melanoma mouse model. **F**: Weight of *Nfe2l2$^{+/+}$* and *Nfe2l2$^{-/-}$* mice at the endpoint (280 d) of the experiment. **G**: Picture of OHT application sites, outside (top) and the inside (bottom) of the skin of *Nfe2l2$^{+/+}$* and *Nfe2l2$^{-/-}$* mice at the endpoint of the experiment (280 d).

For target gene activation, the transcription factor NRF2 forms heterodimers primarily with small MAF proteins [128]. Since NRF2 itself was activated, but not transcriptionally deregulated after oncogene induction (Figure 13C, D), *MAF* expression levels were analyzed. For this purpose, expression data of melanoma cell lines treated with the $BRAF^{V600E}$ inhibitor vemurafenib (vem) were extracted from a publicly available dataset [129]. No changes were seen for *NFE2L2* (Figure 14A), *MAFG* (Figure 14B) or *MAFK* (Figure 14D) transcription levels. However, gene expression of *MAFF* (Figure 14C) was significantly reduced after $BRAF^{V600E}$ inhibition. This was confirmed by real-time PCR in UACC-62 and SK-MEL-28 melanoma cells after treatment with 2 µM of vemurafenib or 50 nM of MEK1/2 inhibitor trametinib (trame) for 24 h (Figure 14E). Furthermore, induction of $BRAF^{V600E}$ in melan-a cells increased *Maff* gene expression (Figure 14F). Thus, $BRAF^{V600E}$ activation resulted in NRF2 translocation and *MAFF* induction, which facilitated increased NRF2 target gene expression.

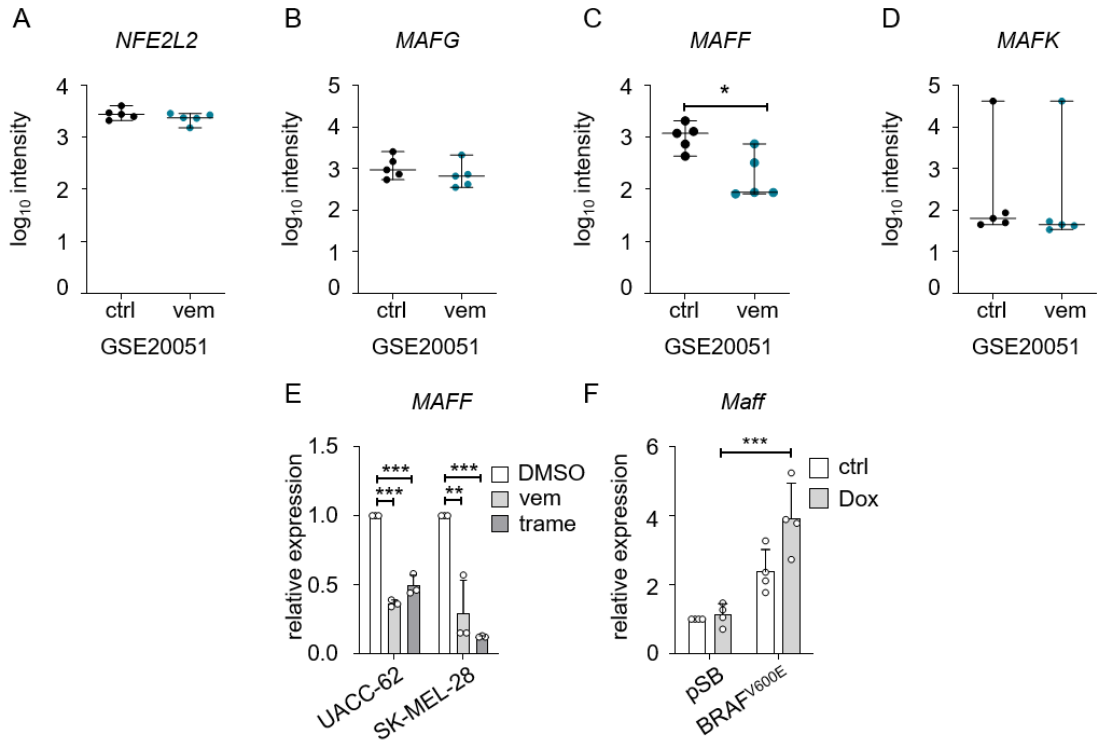

Figure 14 – Expression of NRF2 binding partner *MAFF* is $BRAF^{V600E}$-dependent
A-D: Expression of *NFE2L2* (A), *MAFG* (B), *MAFF* (C) and *MAFK* (D) in melanoma cells treated with $BRAF^{V600E}$-inhibitor vemurafenib, data extracted from microarray analysis GSE20051. (Boxplots display median with range, in C two-tailed student's t test was performed, *p<0.005) **E**: Real-time PCR of *MAFF* in melanoma cell lines after vemurafenib (vem, 2 µM, 24 h) and trametinib (trame, 50 nM, 24 h) treatment. **F**: Real-time PCR of *Maff* after $BRAF^{V600E}$ induction in transgenic melan-a cells (100 ng/ml Dox, 24 h). Experiments were performed in three (E) or four (F) replicates and two-way ANOVA with Tukey's multiple comparisons test was perfomed (*p<0.05, **p<0.01, ***p<0.001). Error bars represent SD.

5.1.2 Distinct effectors activate NRF2 in melanoma cell lines

Besides the activation of NRF2 by internal oncogenic factors, it is well established that the transcription factor NRF2 serves as the master regulator of detoxification mechanisms and oxidative stress responses. To test whether oxidative stress activates NRF2 in established melanoma cells, a panel of human melanoma cell lines were treated with various stress inducers. As a classical oxidative stress inducer, hydrogen peroxide (H_2O_2) was used. In addition, cells were treated with sulforaphane (SFN) and tert-butylhydroquinone (tBHQ), which are known NRF2 stabilizers [130, 131].

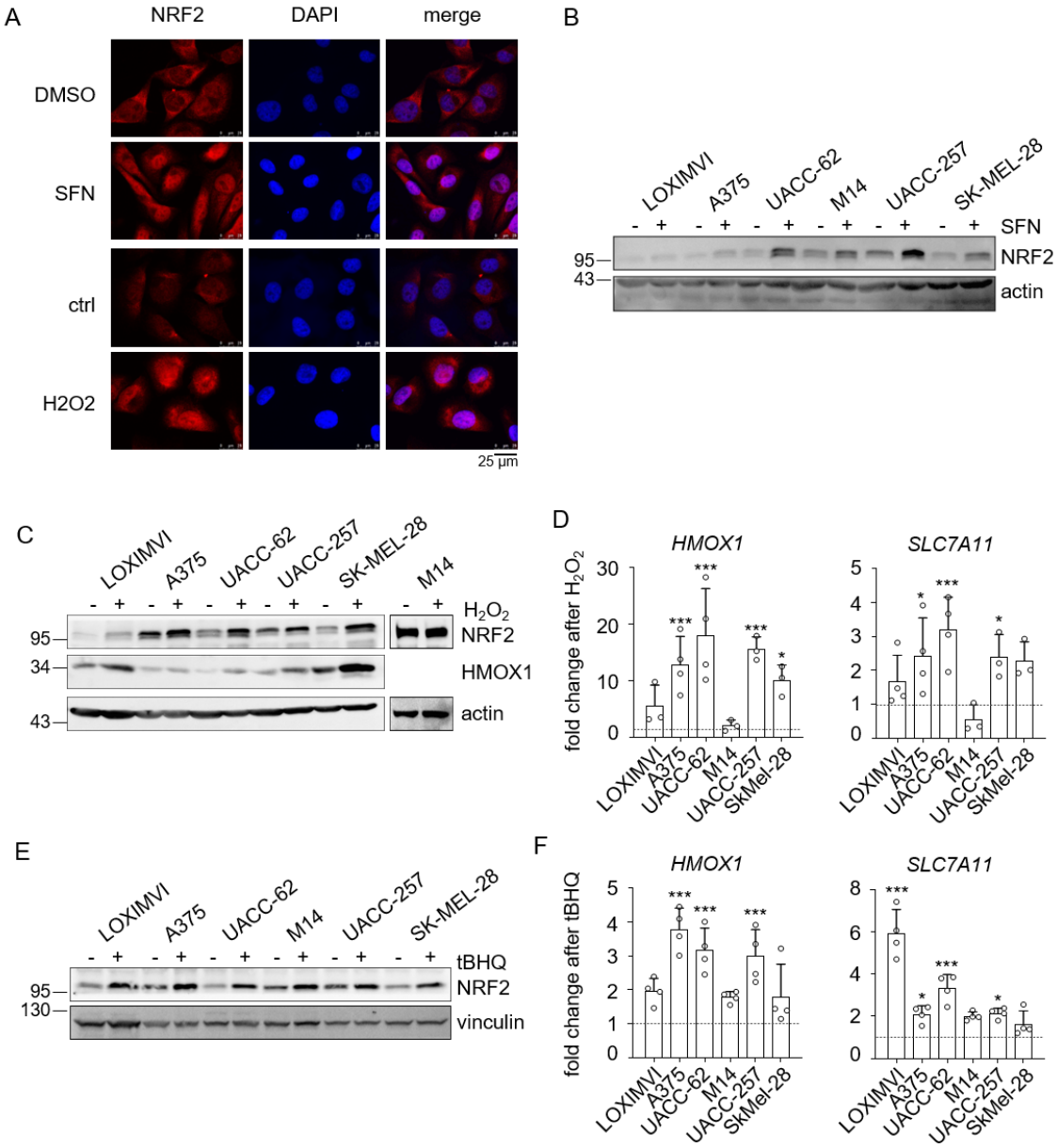

Figure 15 – Stabilizers and oxidative stress activate NRF2
A: Representative immunofluoerescence images of UACC-62 melanoma cells for NRF2 (red) and DAPI (blue) after SFN (7.5 µM, 24 h) and H_2O_2 (400 µM, 5 h) treatment. **B**: Immunoblot of NRF2 in indicated melanoma cells in response to SFN treatment (7.5 µM, 24 h). **C**: Immunoblot for NRF2 and its target HMOX1 after H_2O_2 treatment (400 µM, 5 h) in indicated melanoma cell lines. **D**: Corresponding real-time PCR for NRF2 target gene expression *HMOX1* and *SLC7A11*. **E**: Immunoblot after tBHQ treatment (10 µM, 24 h). **F**: Corresponding real-time PCR for *HMOX1* and *SLC7A11*. Experiments were done four times and two-way ANOVA with Sidak's multiple comparisons test was carried out (*p<0.05, ***p<0.001). Error bars represent SD. Actin and vinculin served as loading controls.

Treatment of UACC-62 cells with either 7.5 µM SFN (Figure 15A, top) or 400 µM H_2O_2 (Figure 15A, bottom) translocated NRF2 into the nucleus as shown by immunofluorescence. Furthermore, the immunoblot of SFN treatment in indicated human melanoma cell lines showed an increase of NRF2 protein levels in most melanoma cell lines (Figure 15B). Activation of NRF2 by 400 µM H_2O_2 elevated NRF2 protein expression in five out of six cell lines (Figure 15C) and was supported by an enhanced expression of the NRF2 target genes *HMOX1* and *SLC7A11* (Figure 15D). Induction of NRF2 and its target genes by 10 µM tBHQ was seen in all tested melanoma cell lines (Figure 15E, F).

In tumors, T lymphocytes or macrophages of the tumor microenvironment secrete diverse cytokines, such as tumor necroses factor-α (TNFα) or interferon-γ (IFNγ) [132]. To test, whether pro-inflammatory signals led to NRF2 activation, the melanoma cell panel was treated with 50 ng/ml TNFα. All analyzed melanoma cell lines displayed NRF2 induction under this condition (Figure 16A). Moreover, increased target gene expression was observed in UACC-62 cells (Figure 16B). In UACC-62 cells NRF2 protein levels were also enhanced after treatment with indicated concentrations of IFNγ (Figure 16C).

In conclusion, it was determined that NRF2 is activated in melanoma by cell autonomous factors, such as oncogenic signaling as well as by extrinsic effectors from the tumor microenvironment, like oxidative stress-inducers or secreted cytokines.

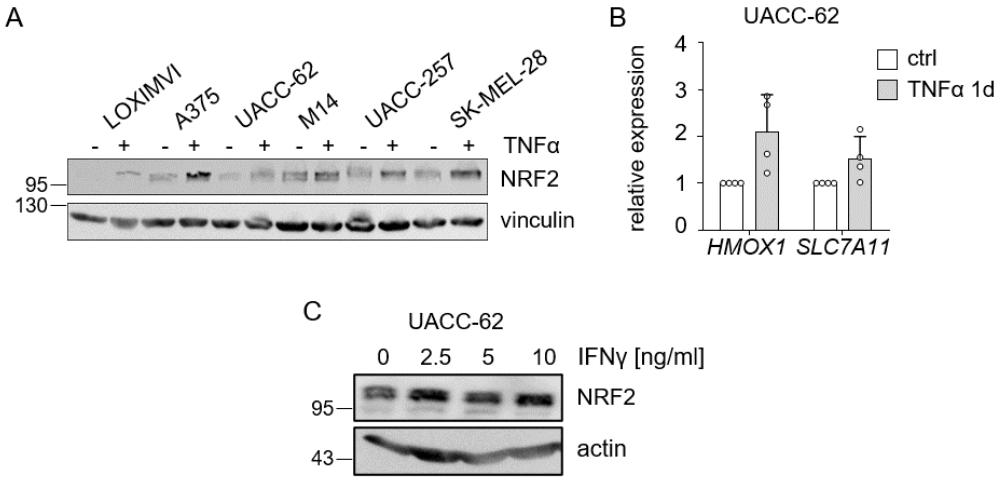

Figure 16 – Cytokine secretion promotes NRF2 stabilization
A: Immunoblot for NRF2 after TNFα treatment (50 ng/ml, 24 h). Vinculin served as loading control **B**: Real-time PCR for *HMOX1* and *SLC7A11* in UACC-62 melanoma cells treated with TNFα (50 ng/ml, 24 h). Real-time PCR was done with four independent replicates. Error bars represent SD. **C**: Immunoblot for NRF2 after indicated IFNγ concentrations for 1 h. Actin served as loading control.

5.2 Reduction of NRF2 impairs malignant features of melanoma cells

5.2.1 NRF2 knockdown compromises melanoma growth abilities

The results above show that the transcription factor NRF2 is activated by diverse intrinsic as well as extrinsic factors. Since NRF2 deficiency did not promote melanoma formation in the mouse model for melanocytic hyperplasia, the effects of NRF2 deficiency in established melanoma cells were investigated. Knockdown of NRF2 was validated by immunoblot assay for NRF2 expression as well as NQO1 protein expression. Two independent siRNAs displayed a prominent reduction of both proteins in most melanoma cell lines (Figure 17A). In A375 cells NRF2 protein levels did not show a knockdown, despite the NQO1 protein reduction, which suggest a more transient knockdown effect in this cell line.

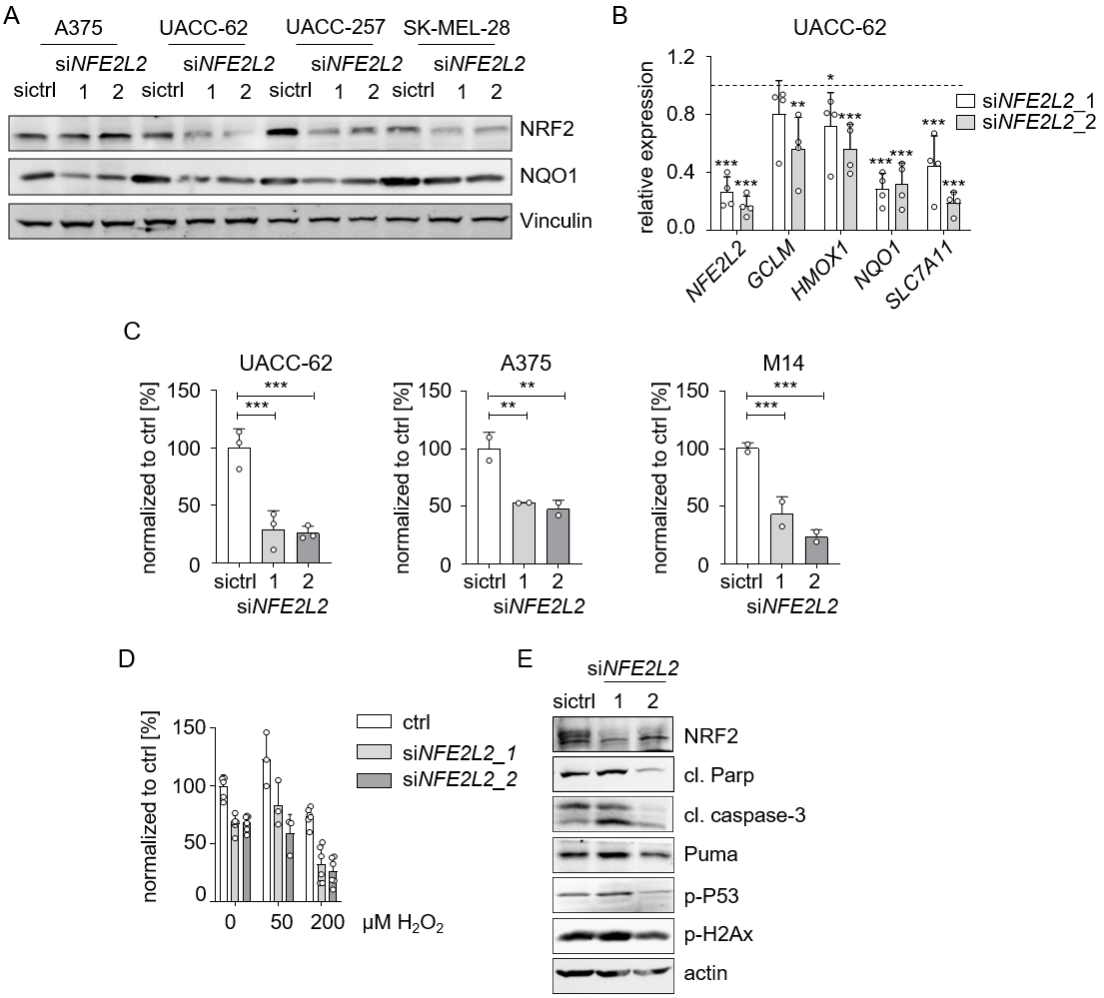

Figure 17 – NRF2 knockdown reduces melanoma cell proliferation
A: Immunoblot of NRF2 and NQO1 after siRNA mediated NRF2 knockdown for 2 d. Vinculin served as loading control. **B**: Real-time PCR of *NFE2L2* and its target genes after NRF2 knockdown in UACC-62 melanoma cells (3 d). Relative expression levels referred to control siRNA are shown (dotted line). Experiment were done four times. **C**: Proliferation assay of indicated melanoma cell lines with control siRNA or two independent *NFE2L2*-specific siRNAs. Cells were counted after 5 days. The experiments were carried out three times in duplicates (UACC-62) or two times in triplicates (A375, M14). **D**: Cell viability, as determined by MTT assay, in UACC-62 cells after transfection with control or *NFE2L2*-specific siRNA (3 d). For the last 24 h, cells were additionally treated with H_2O_2. MTT was done in triplicates. **E**: Immunoblot of NRF2, cleaved PARP (Asp214) (cl. PARP), cleaved caspase-3 (Asp175) (cl. caspase-3), PUMA, p-p53 (Ser15) and p-H2Ax (Ser139) after siRNA mediated NRF2 knockdown. Actin served as loading control. Two-tailed Student's t test was carried out to detect significant differences between control siRNA and single *NFE2L2*-specific siRNAs (*p<0.05, **p<0.01, ***p<0.001). Error bars represent SD.

After NRF2 knockdown, expression of *NFE2L2* itself and bona fide target genes, like *GCLM*, *HMOX1*, *NQO1* and *SLC7A11* were reduced in UACC-62 cells (Figure 17B). Melanoma proliferation was highly reduced after 5 days of siRNA mediated NRF2 knockdown in all three melanoma cell lines (Figure 17C). Moreover, NRF2 knockdown sensitized UACC-62 cells towards oxidative stress induction by H_2O_2 as determined by MTT cell viability assay (Figure 17D). Although, a growth deficit is visible after NRF2 knockdown, apoptosis associated proteins, like cleaved caspase-3, cleaved PARP or PUMA were not increased in the knockdown situation (Figure 17E). Phosphorylation of DNA damage associated proteins, like p53 and γH2Ax also displayed no conclusive change after siRNA mediated NRF2 knockdown (Figure 17E). Thus, NRF2 deficiency compromises melanoma cell proliferation not by apoptosis induction.

To test if other pro-tumorigenic features, in addition to proliferation, are also affected by NRF2 knockdown, UACC-62 cells were further investigated. First, 3D colony formation was determined by soft agar growth assay (Figure 18A). After 7 days of growth, NRF2 knockdown significantly prevented colony formation. Furthermore, NRF2 knockdown impaired migration capacities of UACC-62 cells, determined after 3 days of siRNA mediated NRF2 knockdown by trans-well migration assay (Figure 18B).
A well-established function of NRF2 is to secure glutathione (GSH) levels to neutralize intracellular ROS. Thus, intracellular ROS level as well as GSH concentration were determined after NRF2 knockdown. CellROX assay validated accumulation of ROS after NRF2 knockdown for 3 days (Figure 18C). This was accompanied by a reduction of total GSH concentrations (Figure 18D). Taken together, it was verified that the induced NRF2 deficiency led to significant reduction of malignant features in established melanoma cell lines, concurrent with increased intracellular stress levels due to reduced GSH concentrations.

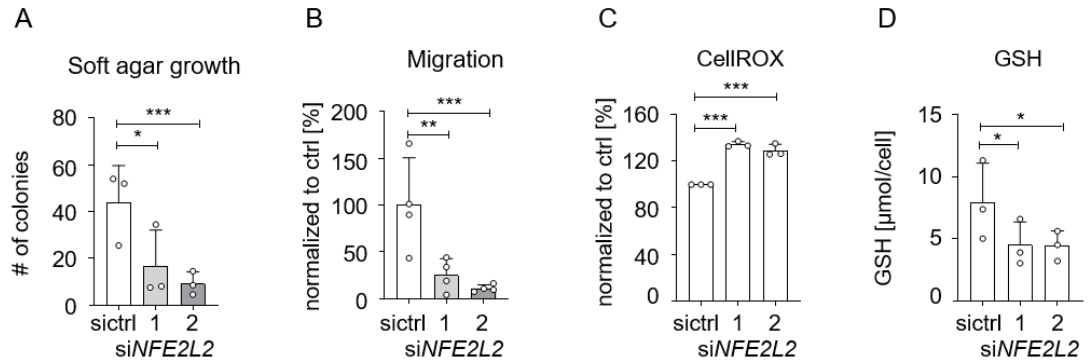

Figure 18 – NRF2 knockdown impairs malignant growth and intracellular glutathione levels
A: Soft agar growth of UACC-62 after siRNA mediated NRF2 knockdown. Colonies were counted after 7 d. Experiment was performed three times in duplicates. **B**: Trans-well migration assay of UACC-62 after NRF2 knockdown, migration was allowed for 16 h and migrated cells were counted after crystal violet staining. **C**: Measurement of intracellular ROS levels in UACC-62 cells after transfection with control or *NFE2L2*-specific siRNA for 3 d. CellROX assay was performed three times in triplicates. **D**: Intracellular glutathione concentration in UACC-62 cells after transfection with control or *NFE2L2*-specific siRNA (3 d) (measured by Tietze assay). GSH assay was performed three times in duplicates. Two-tailed student's t test was performed to detect significant differences between control siRNA and single *NFE2L2*- specific siRNAs (*p<0.05, **p<0.01, ***p<0.001). Error bars represent SD.

5.2.2 NRF2 knockdown impairs cell cycle progression

For a better overview of regulated genes and pathways after NRF2 reduction, genome-wide transcriptional analysis was performed. After 3 days of siRNA mediated NRF2 knockdown 944 genes were reduced, and 357 transcripts were increased (Figure 19A). The gene set enrichment analysis (GSEA) of hallmark gene sets showed a reduction of the HALLMARK "Reactive oxygen species pathway" (Figure 19B, D) with a FDR q value of 0.38, however the expression of well-known NRF2 target genes was validated in Figure 17B. Interestingly, GSEA of KEGG pathway gene sets showed highest enrichment in genes involved in DNA replication, cell cycle and repair mechanisms (Figure 19C, E). Validation of gene involved in DNA replication *TOP2A*, *PCNA*, *RPA3*, and *RFC4* was done by real-time PCR (Figure 19F). Thus, NRF2 knockdown decreased an unexpected high set of replication-associated genes.

The highest upregulated KEGG pathway gene sets were involved in mitochondrial functions, such as oxidative phosphorylation and the citrate cycle (Figure 19C). Furthermore, the neurodegenerative diseases, such as Alzheimers and Parkinsons disease are associated with mitochondrial dysfunction, which are further related to an altered NRF2 activity [133, 134]. The GSEA enrichment plot of Oxidative Phosphorylation (OxPhos) is displayed in Figure 19G and enhanced expression of the mitochondria-associated genes *PPARGC1A*, *ATP6V04A*, *NDUFA3* and *ACO2* was validated by real-time PCR in both siRNAs (Figure 19H). Furthermore, GSEA of KEGG pathways revealed the cell cycle pathway to be one of the highest decreased gene sets (Figure 19C), which is supported by the enrichment plot in Figure 20A.

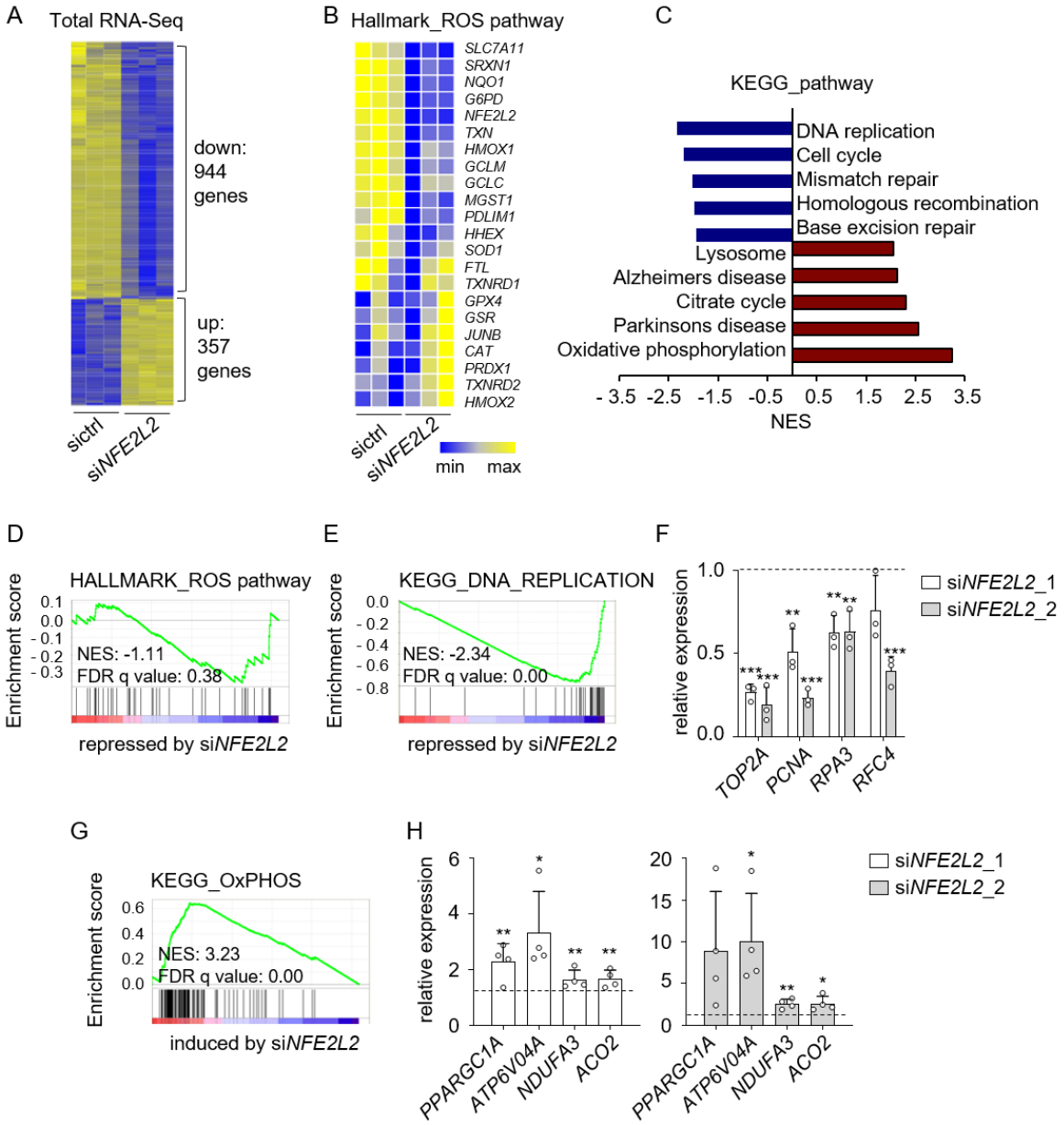

Figure 19 – NRF2 knockdown reduces ROS-related as well as DNA replication genes
A: Heatmap showing significantly regulated genes by *NFE2L2* knockdown identified by RNA sequencing (UACC-62, 3 d) (LogFC >2). RNA-sequencing was done in triplicates. **B**: Heatmap of expression of the HALLMARK gene set "reactive oxygen species (ROS) pathway" in UACC-62 cells transfected with non-targeting or *NFE2L2*-specific siRNA, each in triplicates. **C**: Gene set enrichment analysis (GSEA) of altered transcripts included in KEGG pathways after knockdown of *NFE2L2*. NES: Normalized enrichment score. **D**: GSEA enrichment plot of HALLMARK gene set "Reactive oxygen species (ROS) pathway". **E**: GSEA enrichment plot of the KEGG pathway gene set "DNA replication". **F**: Validating real-time PCR of *TOP2A*, *PCNA*, *RPA3* and *RFC4* gene expression, involved in DNA replication gene set, validated in three independent experiments. **G**: GSEA enrichment plot of the KEGG pathway gene set "Oxidative Phosphorylation (OxPHOS)". **H**: Validating real-time PCR of *PPARGC1A*, *ATP6V04A*, *NDUFA3* and *ACO2* gene expression. si*NFE2L2*_1 after 2 d, si*NFE2L2*_2 after 3 d. **F**, **H**: validated in three (F) and four (H) independent experiments. Two-tailed Student's t test was performed to detect significant differences between control siRNA and single *NFE2L2*- specific siRNAs (*p<0.05, **p<0.01, ***p<0.001). Error bars represent SD.

Cell cycle genes, which are downregulated after siRNA mediated NRF2 knockdown were validated by real-time PCR (Figure 20B). In parallel, the cell cycle master regulator, FOXM1, was also highly regulated on transcript as well as on protein levels after NRF2 knockdown (Figure 20B,C). Comparison of real-time PCR of cell cycle related FOXM1 target genes after knockdown of NRF2 or FOXM1 showed reduction of gene expression to a similar extent under both conditions (Figure 20B, D). Furthermore, siRNA mediated *FOXM1* knockdown in UACC-62 cells (Figure 20E) impaired melanoma cell proliferation (Figure 20F), similarly to NRF2 knockdown (Figure 17C). Since apoptosis induction was excluded (Figure 17E), senescence associated β-galactosidase assay was performed to test if NRF2 is involved in preventing senescence induction. Knockdown of NRF2 (Figure 20G, top) or FOXM1 (Figure 20G, bottom) showed senescent staining to a similar extent. Thus, the reduction of cell proliferation after NRF2 knockdown is facilitated by cell cycle alleviation at least in part due to FOXM1 impairment, thus promoting the senescent cell state.

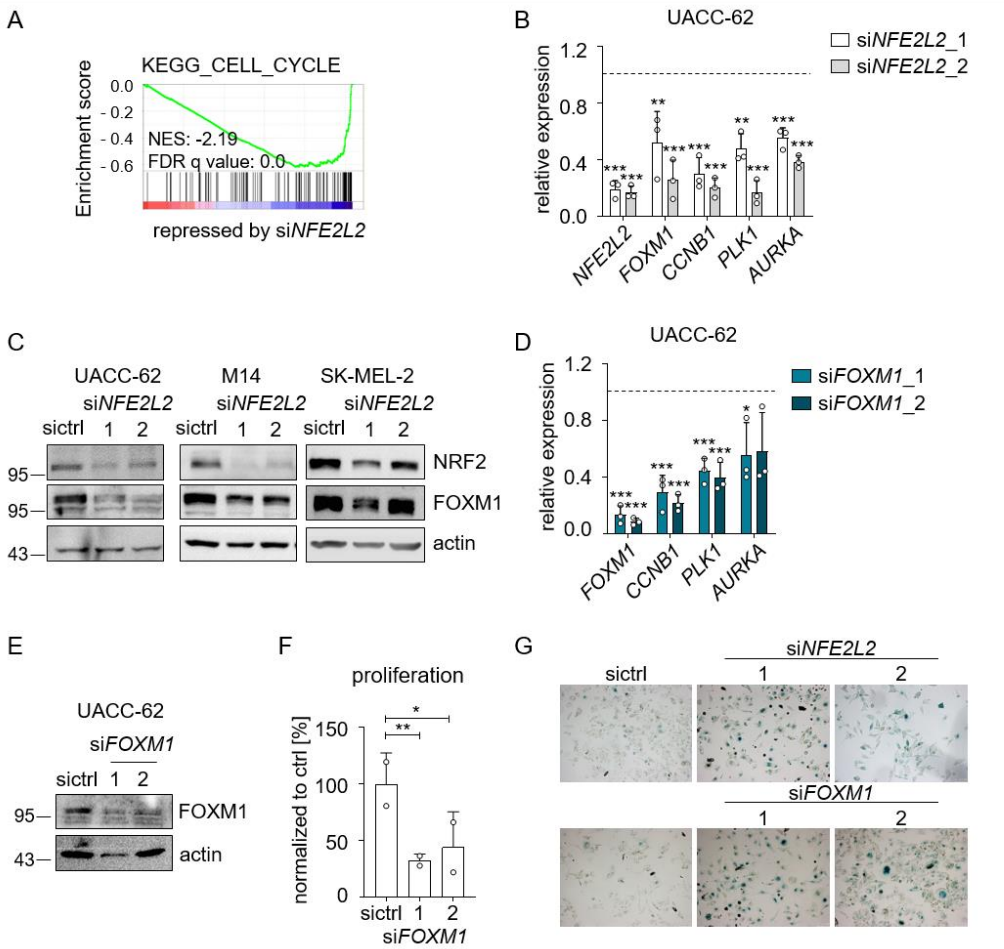

Figure 20 – NRF2 knockdown impairs cell cycle progression partly by FOXM1 reduction
A: GSEA enrichment plot of the KEGG pathway gene set "Cell cycle". **B**: Real-time PCR of indicated cell cycle-related genes after siRNA mediated knockdown (3 d) of *NFE2l2*. **C**: Immunoblot showing the expression of FOXM1 after siRNA mediated NRF2 knockdown (3 d) in UACC-62, M14 and SK-MEL-2 melanoma cells. **D**: Real-time PCR of indicated cell cycle-related genes after siRNA-mediated knockdown of *FOXM1* (3 d). Relative expression levels referred to control siRNA are shown (dotted line). **E**: Immunoblot of FOXM1 after siRNA-mediated *FOXM1* knockdown in UACC-62 cells. **F**: Proliferation assay of UACC-62 cells treated with non-targeting siRNA or two independent siRNAs directed against *FOXM1*. Cells were counted 5 days after transfection. **G**: β-galactosidase senescence-associated assay after siRNA mediated knockdown of NRF2 or *FOXM1*. All experiments were performed in three replicates and two-tailed Student's t test was carried out to detect significant differences between control siRNA and single *NFE2L2*- or *FOXM1*-specific siRNAs (*p<0.05, **p<0.01, ***p<0.001). Error bars represent SD.

5.3 NRF2 is necessary for stress dependent COX2 induction

5.3.1 *PTGS2* is the most alleviated transcript after NRF2 knockdown

A

genes	log_2FC
PTGS2	-4.55
ART3	-3.70
LRRC17	-3.42
FST	-3.40
ADAM19	-3.40
EGFR	-3.37
SERTAD4	-3.36
CXCL8	-3.27
SSC5D	-3.24
PLEKHS1	-3.19

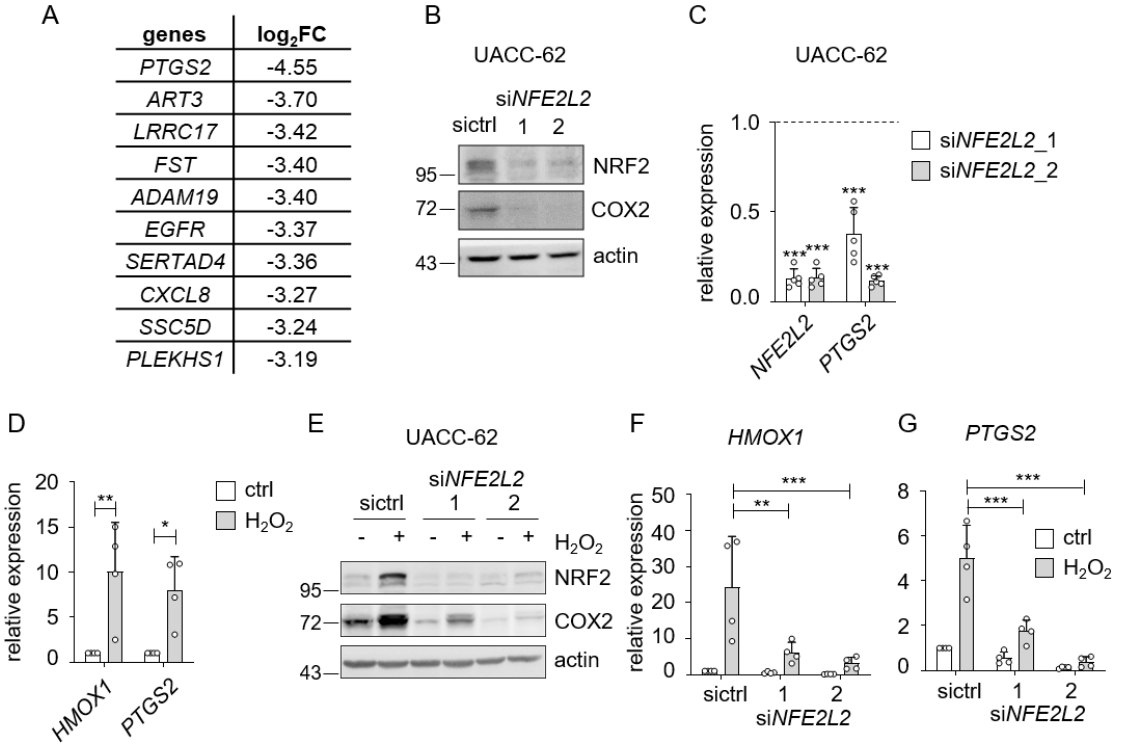

Figure 21 – *PTGS2* is the most alleviated transcript after NRF2 reduction
A: List of the top ten genes most reduced after NRF2 knockdown determined by RNA-sequencing. **B**: Immunoblot for NRF2 and COX2 protein expression after NRF2 knockdown (3 d) in UACC-62. Actin served as loading control. **C**: Corresponding real-time PCR of *NFE2L2* and *PTGS2* expression. The relative gene expression, referred to non-targeting siRNA (dotted line), is shown. Real-time PCR was performed five independent times and unpaired two-tailed Student's t test was performed for each siRNA. (***p<0.001). **D**: Real-time PCR of *HMOX1* and *PTGS2* in UACC-62 after H_2O_2 treatment (400 µM, 5 h), done four times. Unpaired two-tailed Student's t test for each gene was performed (**p<0.01, *p<0.05). **E**: Immunoblot of NRF2 and COX2 in UACC-62 cells after a combination of H_2O_2 treatment (400 µM, 5 h) and siRNA-mediated NRF2 knockdown (3 d). Actin served as loading control. **F, G**: Corresponding real-time PCR of *HMOX1* (F) and *PTGS2* (G) expression levels. Significance was calculated by two-way ANOVA with Sidak's multiple comparisons posttest (**p<0.01, ***p<0.001). All error bars represent SD.

After examining the effects of the NRF2 knockdown on functional gene groups, changes on individual gene expression were analyzed. The table in Figure 21A displays the log_2(fold change) (log_2FC) of the top ten most alleviated transcripts after genome-wide transcriptomic analysis after NRF2 knockdown. The expression change of *PTGS2*, with a log_2FC of -4.55, showed the highest reduction after 3 days of siRNA mediated NRF2 knockdown in UACC-62 melanoma cells. *PTGS2* encodes for the inducible cyclooxygenase 2 (COX2) protein, which catalyzes the conversion of arachidonic acid into lipid mediators, such as prostaglandins and thromboxane. Activation of COX2 in cancers strongly elevates prostaglandin E2 (PGE2) levels, thereby fostering an immune-evasive tumor environment [135, 136]. Reduction of COX2 was confirmed on protein (Figure 21B) as well as on mRNA expression levels (Figure 21C) after NRF2 knockdown. Oxidative stress induction by 400 µM H_2O_2 for 5 h elevated *PTSG2* levels not only in UACC-62 cells (Figure 21D), but also in a panel of other melanoma cell lines (Figure 22A, B). *PTGS2* gene expression increased to a comparable extent as *HMOX1* expression after

H_2O_2 treatment (Figure 15D, 21D and 22B). The oxidative stress dependent *PTGS2* and *HMOX1* induction was reduced after siRNA mediated NRF2 knockdown in UACC-62 cells (Figure 21E, F, G), as well as in the melanoma cell line A375 (Figure 22C, D, E). Notably, the extent of COX2 induction correlated with the NRF2 knockdown efficiency (Figure 22C, D, E). Taken together, stress induced COX2 expression is dependent on functioning NRF2 stabilization.

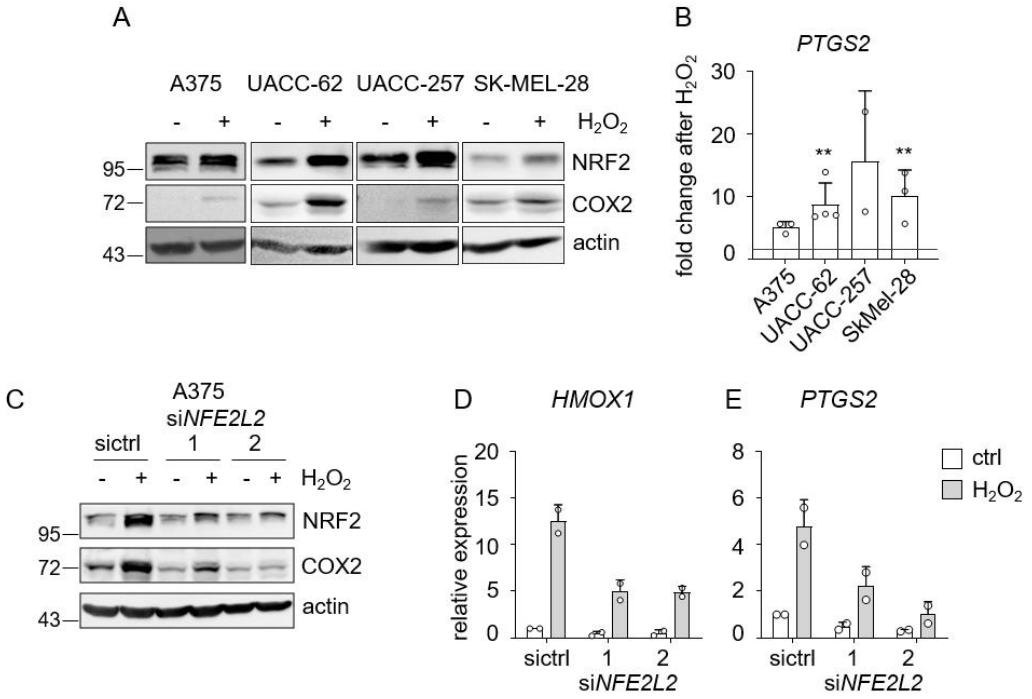

Figure 22 – *PTGS2* expression is controlled by NRF2 in diverse melanoma cell lines
A: Immunoblot for NRF2 and COX2 in indicated melanoma cell lines after H_2O_2 treatment (400 µM, 5 h). **B**: Corresponding real-time PCR of *PTGS2* expression. The experiment was performed two times for UACC-257 and three times for all other cell lines. Unpaired two-tailed Student's t test for each cell line (except UACC-257) referred to the respective control was performed (**p<0.01). **C**: Immunoblot of NRF2 and COX2 in A375 cells after a combination of H_2O_2 treatment (400 µM, 5 h) and siRNA mediated *NFE2L2* knockdown for 2d. **D, E**: Corresponding real-time PCR of *HMOX1* (D) and *PTGS2* (E) expression. Actin served as loading control and all error bars represent SD. Two independent experiments were done in A375.

5.3.2 NRF2 knockout cells secret reduced PGE2 levels

Since the transient siRNA mediated knockdown of NRF2 was not sufficient to completely abolish all NRF2 activity (Figure 21E, 22C), NRF2 knockout cell lines were generated to further investigate the NRF2-dependent COX2 induction. To eliminate remaining NRF2 activity, CRISPR/Cas9 mediated *NFE2L2* knockout (NRF2-ko) UACC-62 cells were established. Sequencing of genomic DNA of NRF2 wildtype (wt) and NRF2-ko cells confirmed premature stop codons in the amino acid sequences of both alleles in the NRF2-ko cell line (Figure 23A, B). Knockout of NRF2 abolished basal levels and oxidative stress dependent induction of NRF2 as well as COX2 (Figure 23C). Furthermore, the elevation of *HMOX1* as well as *PTGS2* expression by H_2O_2, was reduced in the knockout situation (Figure 23D). To confirm this effect, two independent UACC-62 NRF2-ko cell lines (2 and 3) were evaluated after H_2O_2 dependent stress induction. Both clearly showed decreased basal as well as stress inducible COX2 levels than the NRF2 wt cells (Figure 23E).

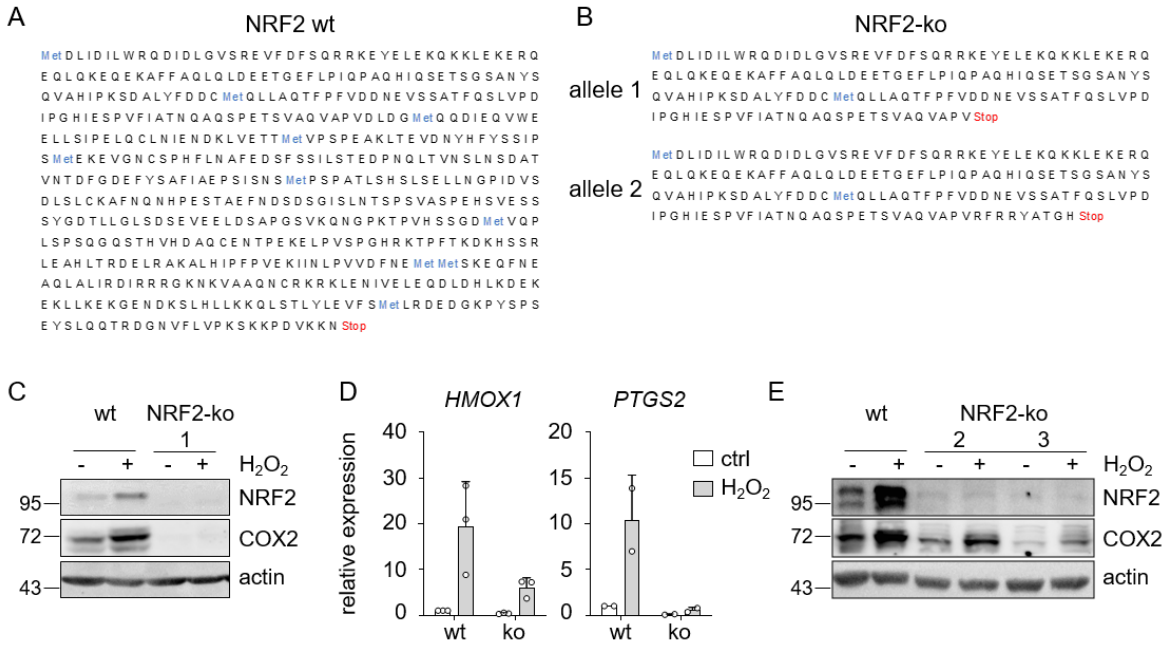

Figure 23 – COX2 induction is abolished in CRISPR/Cas9 generated *NFE2L2*$^{-/-}$ melanoma cells
A,B: Protein sequence of human NRF2 wt (A) and CRISPR/Cas9 NRF2 knockout (B) UACC-62 cells. **C**: Immunoblot for NRF2 and COX2 after H_2O_2 treatment of UACC-62 NRF2 wt and NRF2 knockout cells (400 µM, 5 h). Actin served as loading control **D**: Corresponding real-time PCR of *HMOX1* and *PTGS2* expression referred to the wt control condition. The experiment was done twice, and error bars represent SD. **E**: Immunoblot of NRF2 and COX2 in two independent CRISPR/Cas9 NRF2 knockout UACC-62 cell lines after H_2O_2 treatment (400 µM, 5 h). Actin served as loading control.

As mentioned above, higher COX2 expression and activity favor a immune-cold microenvironment by an increase of PGE2 concentration levels [135, 136]. Figure 24A displays a schematic overview of PGE2 synthesis. The membrane bound arachidonic acid (AA) is liberated from cell membrane phospholipids by phospholipase A_2 (PLA_2). AA is converted to prostaglandin H2 (PGH2) and this step is catalyzed by COX1 or COX2. Depending on the availability and activity of downstream enzymes, PGH2 is further converted to prostaglandins PGD2, PGI2, PGE2 or to thromboxane A2 (TXA2). It was

previously described that PGE2 promotes tumor cell evasion in melanoma [135, 136]. Thus, PGE2 concentrations were evaluated in NRF2-ko UACC-62 cells compared to UACC-62 wt cells. To address this, an ELISA assay to detect secreted PGE2 lipids was performed (Figure 24B). In UACC-62 NRF2-ko cells PGE2 levels were almost undetectable in contrast to UACC-62 NRF2 wt cells without any treatment (Figure 24B, left bar). Using a dox-inducible pSB-ET-iE_NRF2 expression vector system, PGE2 concentrations were increased in UACC-62 wt cells (Figure 24B, middle bar). The NRF2-dependent PGE2 increase was further enhanced by concurrent application of 10 µM tBHQ, a known NRF2 stabilizer (Figure 24B, right bar). The protein levels of NRF2 as well as COX2 were elevated after 3 days of 250 ng/ml dox treatment in UACC-62 cells containing the pSB-ET-iE_NRF2 expression vector, as shown by immunoblot assay (Figure 24C). In summary, NRF2 secured PGE2 levels by regulating COX2 induction.

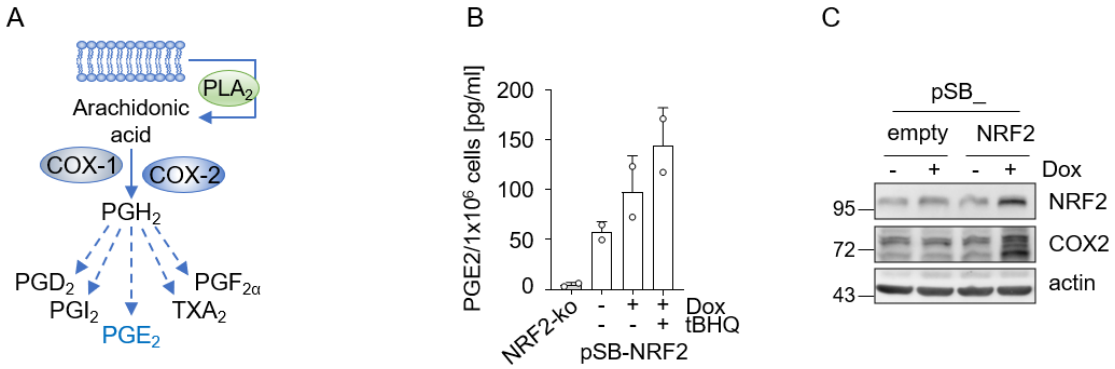

Figure 24 – Secreted PGE2 levels are dependent on NRF2 expression levels
A: Schematic overview of COX2 involvement in PGE2 synthesis. **B**: ELISA assay for secreted PGE2 concentration in the supernatant of UACC-62 NRF2 wt and NRF2 knockout cells as well as after Dox-inducible NRF2 expression (1000 ng/ml, 2 d) and tBHQ (10 µM, 2 d) in UACC-62 NRF2 wt cells, done in duplicates. **C**: Immunoblot for NRF2 and COX2 in UACC-62 NRF2 wt cells transfected with Dox-inducible NRF2 expression vector pSB-NRF2 or empty vector control (250 ng/ml Dox, 3 d). Actin served as loading control.

5.3.3 NRF2-mediated *PTGS2* induction is dependent on ATF4 expression

Previously, it was shown that NRF2 mediates gene regulation by downstream activation of the activating transcription factor (ATF) 4 [137]. Therefore, the influence of ATF4 expression on regulation of *PTGS2* was evaluated. In 501mel melanoma cells, ATF4 bound to the promoter region of *PTGS2* (Figure 25A) and artificial ATF4 overexpression strongly enhanced *PTGS2* RNA expression and COX2 protein levels (Figure 25B, C). Like the NRF2-ko UACC-62 cells, the H_2O_2-dependent *PTGS2* induction was alleviated in CRISPR/Cas9 generated ATF4-ko UACC-62 cells (Figure 25D, E). Thus, ATF4 is required for the COX2 induction mediated by oxidative stress. Furthermore, H_2O_2-dependent NRF2 induction was blunted in the ATF4-ko cell lines, which indicates that the transcription factors may regulate each other. The overexpression of NRF2 in ATF4 wildtype UACC-62 cells strongly enhanced COX2 expression on RNA and protein level (Figure 25F, G). However, COX2 induction was prevented after NRF2 overexpression in ATF4-ko UACC-62 cells (Figure 25F, G). These results suggest that the NRF2-dependent COX2 induction is mediated by ATF4.

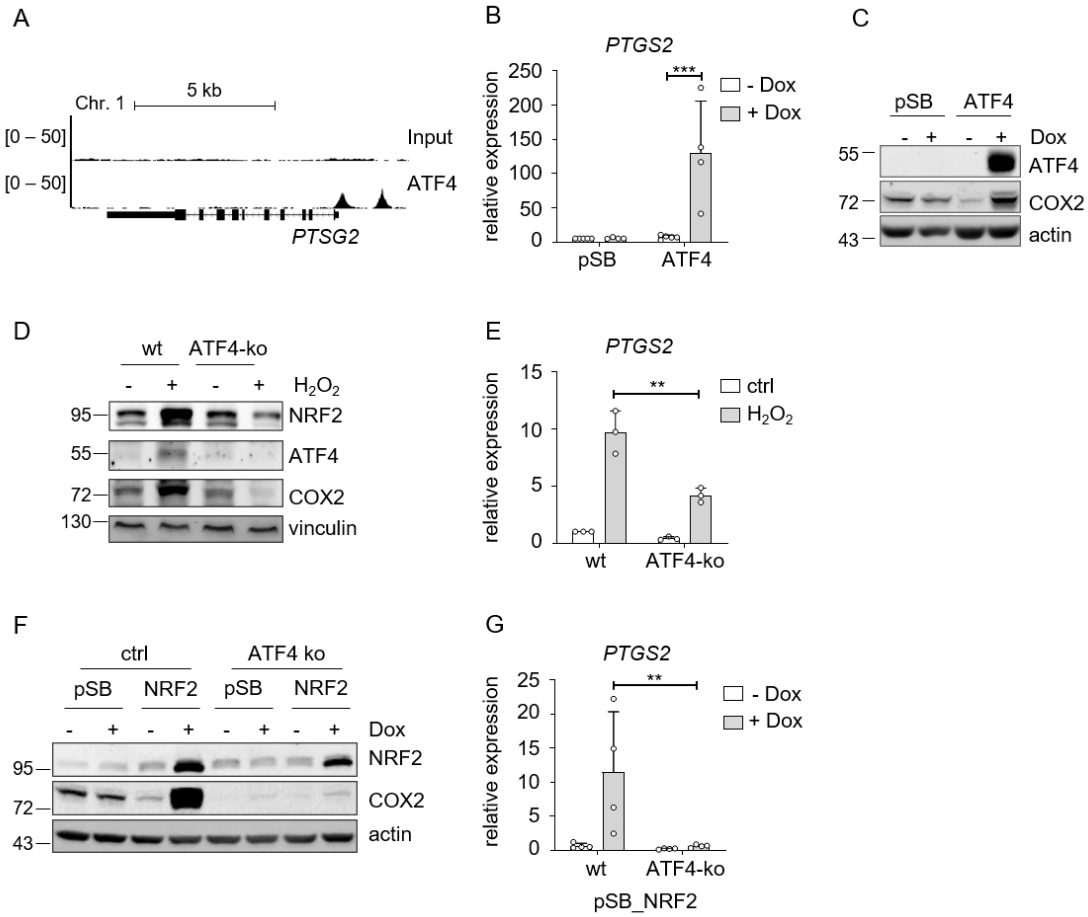

Figure 25 – NRF2-mediated *PTGS2* induction is dependent on ATF4 expression
A: Genome browser tracks of promoter regions of *PTGS2* with ATF4 binding, evaluated by ATF4 ChIP-Seq analysis in human 501mel melanoma cells and an input control. **B**: Real-time PCR, showing *PTGS2* expression in UACC-62 cells transfected with control vector (pSB) or an inducible ATF4 expression vector (pSB_ATF4) after incubation with 100 ng/ml doxycycline for 3 days. Data are derived from four experiments. **C**: Corresponding immunoblot, showing ATF4 and COX2 expression. Actin served as loading control. **D**: Immunoblot of NRF2, ATF4 and COX2 in UACC-62 wt and ATF4-ko cells after H_2O_2 treatment (400 µM, 5 h). Vinculin served as loading control. **E**: Real-time PCR for *PTGS2*, using the same conditions as described in **D**. The experiment was done three times. **F**: Immunoblot, showing NRF2 and COX2 expression in control vector or NRF2-expressing UACC-62 cells (ctrl) and ATF4-ko cells. Where indicated, cells were stimulated with 500 ng/ml Dox for 3 days. Actin served as loading control. **G**: Corresponding real-time PCR, performed four times independently. For all real-time PCRs two-way ANOVA with Tukey's multiple comparisons posttest was carried out (**p<0.01, ***p<0.001). Error bars represent SD. The experiments in **B**-**G** were performed by A. Hufnagel and J.Kreß, both Department of Pathology, Würzburg.

5.4 NRF2 stabilizes dedifferentiation in melanoma

5.4.1 NRF2 suppresses MITF activity in melanoma cells

In addition to the analysis of downregulated transcripts after siRNA mediated NRF2 knockdown, gene ontology (GO) term analysis of the 357 upregulated transcripts (Figure 19A) with the database for annotation, visualization and integrated discovery (DAVID) was performed. This bioinformatic tool permits functional annotation of biological GO-terms and identifies enriched GO-terms according to their p-values. Functional annotation of biological processes revealed induction of genes involved in localization and metabolic processes as well as pigmentation-related genes (Figure 26A). Pigmentation is particularly important in melanoma, because the pigmentation status

is associated with the differentiation state of melanoma [138]. Furthermore, the pigmentation process serves as protection from UVR-induced DNA damage in melanocytes. The pigmentation-associated enzymes tyrosinase (*TYR*) and dopachrome-tautomerase (*DCT*) are transcriptionally regulated by the microphthalmia-associated transcription factor (*MITF*) [8, 9]. MITF is the master regulator of the melanocytic lineage, which is also known to regulate gene expression of Melanoma Antigen Recognized By T cells 1 (MART1/*MLANA*) [139]. The table in Figure 26B shows the log_2FC with the related p values of these pigmentation-associated genes, determined by the transcriptomic analysis. In contrast to its target genes *MLANA*, *DCT* and *TYR*, the gene expression of *MITF* itself was not changed. Equally, protein expression of MITF (Figure 26C) remained largely unaltered after 3 days of siRNA mediated NRF2 knockdown in UACC-62 cells. In contrast, protein levels of TYR and MLANA were elevated (Figure 26D). In accordance with these findings, protein levels of MITF remained unchanged and MLANA protein levels were enhanced in NRF2-ko cells (Figure 26E). Thus, the observed alterations in pigmentation-related proteins by NRF2 are not caused by modifications of MITF expression levels.

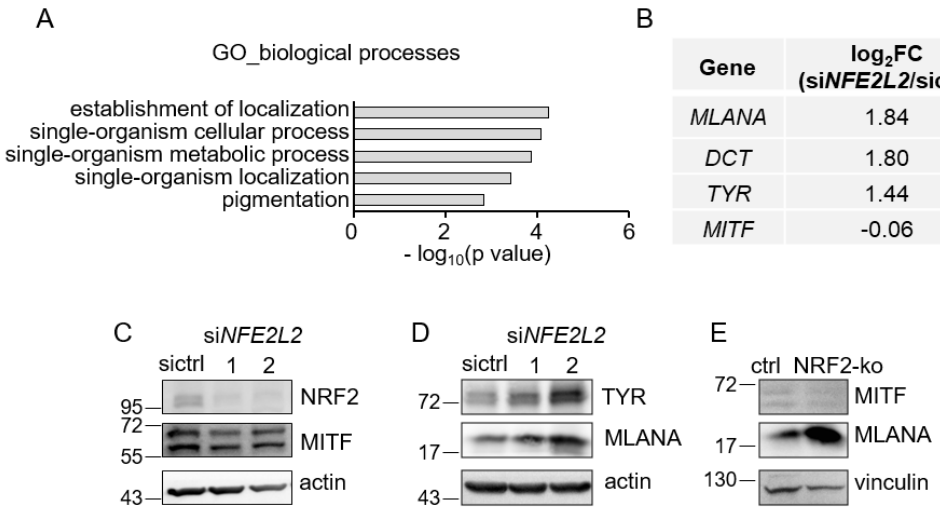

Gene	log_2FC (si*NFE2L2*/sictrl)	p value
MLANA	1.84	6.67E-05
DCT	1.80	3.57E-03
TYR	1.44	1.87E-27
MITF	-0.06	0.87

Figure 26 – MITF target genes are induced after NRF2 reduction in melanoma cells
A: Gene ontology (GO) term analysis of biological processes induced after knockdown of NRF2 in UACC-62 cells (analyzed by DAVID functional annotation tool, https://david.ncifcrf.gov). **B**: Expression changes of *MITF* and associated target genes *DCT*, *TYR*, *MLANA* after NRF2 knockdown in UACC-62 cells, as detected by RNA sequencing. **C, D:** Immunoblot of NRF2 and MITF (C) or TYR and MLANA (D) after siRNA mediated knockdown of NRF2 (3 d) in UACC-62. Actin served as loading control. **E**: Immunoblot of MITF and MLANA in NRF2 wt and NRF2 knockout UACC-62 cells. Vinculin served as loading control.

Since no effect on MITF expression was detectable, it was hypothesized that NRF2 might inhibit MITF activity. This hypothesis was tested by a dual reporter luciferase assay. To do so, UACC-62 cells stable expressing a doxycycline-inducible pSB-ET-iE_MITF expression vector were treated with indicated concentrations of dox for 3 days. The promoter element 200 bp upstream of the *TYR* transcription start site was used as luciferase reporter construct and a *Renilla* firefly construct served as internal transfection control. After 1 day of dox treatment, the cells were co-transfected with the luciferase reporter, *Renilla* firefly vector and pcDNA3.1_NRF2 constructs. Transfection with NRF2 strongly suppressed the dox induced MITF activity at the *TYR* luciferase reporter (Figure 27A). Even though, NRF2 knockdown showed no effect on MITF expression levels, it was revealed that exogeneous overexpression of NRF2 in UACC-62 decreased MITF protein levels (Figure 27B). It therefore seems that strong NRF2 activity reinforces MITF inhibition, leading to reduced protein levels. Due to its role in melanocytic differentiation the transcription factor MITF determines the differentiated state of melanoma cells. A low endogenous MITF expression is associated with a undifferentiated invasive phenotype, whereas melanoma cell lines with high MITF expression are considered to be highly differentiated and proliferative [140, 141]. The so far investigated UACC-62 melanoma cell line belongs to the $MITF^{low}$ expressing group. Thus, the effect of the NRF2 knockdown on pigmentation-related genes in the $MITF^{high}$ expressing cell lines, UACC-257 and SK-MEL-28, was analyzed. Real-time PCR of the MITF target genes *DCT*, *TYR* and *MLANA* after siRNA mediated NRF2 knockdown showed significant increase in gene expression, especially predominant in the $MITF^{low}$ expressing cell lines UACC-62 and A375 (Figure 27C). The cell lines with a higher basal MITF expression, UACC-257 and SK-MEL-28, (Figure 27D) also displayed a slight suppression of MITF activity by NRF2, but the effect was much weaker than that observed in $MITF^{low}$ cells. Taken together, NRF2 suppresses the activity of the melanocytic transcription factor MITF and interferes with melanoma differentiation, prevalently in $MITF^{low}$ expressing melanoma.

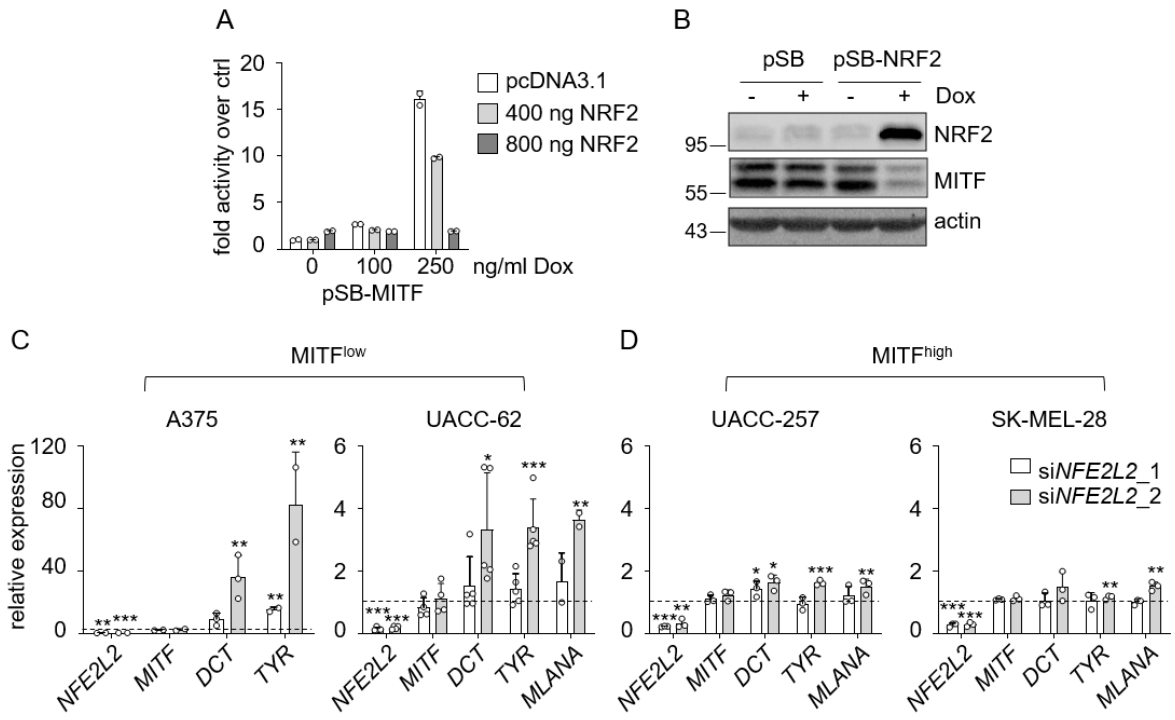

Figure 27 – NRF2 suppresses MITF activity in MITF^{low} cells
A: Luciferase assay of UACC-62 cells after MITF induction (100 or 250 ng/ml, 3 d) and cotransfection with 400 ng or 800 ng of pcDNA3.1-NRF2 and a tyrosinase promoter construct for 2 d. Luciferase assay was measured twice in duplicates. **B**: Immunoblot of NRF2 and MITF after doxycycline-dependent NRF2 induction in UACC-62 cells (250 ng/ml Dox, 3 d). Actin served as loading control. **C, D**: Real-time PCR of *NFE2L2* as well as *MITF* and its target genes *DCT*, *TYR* and *MLANA* after *NFE2L2* knockdown in MITF^{low} cells (A375, UACC-62) (C) and MITF^{high} cells (UACC-257, SK-MEL-28) (D). Please note that *MLANA* is not expressed in A375 cells, and quantification was therefore not possible in this cell line. Expression is shown relative to control siRNA treated cells (dotted line). Experiments were performed at least in three replicates and unpaired two-tailed Student's t test was carried out to compare expression in cells treated with individual *NFE2L2*-targeting siRNAs with those transfected with non-targeting siRNA(*p<0.05, **p<0.01, ***p<0.001). Error bars represent SD.

5.4.2 COX2 negatively correlates with MITF expression in melanoma

In a previous study it was shown that $MITF^{low}$ expressing melanoma cells have a higher basal level of inflammatory signaling as well as a higher responsiveness to pro-inflammatory cytokines, like TNFα [142]. In addition, TNFα can further dedifferentiate melanoma cells by suppression of MITF [142]. Since, TNFα can also increase COX2 expression and thus the secretion of PGE2 in prostate cancer cells [143, 144], the effect of TNFα on COX2 and MITF was analyzed in melanoma. To test if *PTGS2* and *MITF* are inversely regulated by TNFα, in melanoma, gene expression data were extracted from a publicly available dataset of MZ7 melanoma cells treated with TNFα (GSE71798 [142]). Comparison of control and TNFα treated MZ7 melanoma cells showed enhanced *PTGS2* expression accompanied by *MITF* reduction (Figure 28A). To analyze if the *PTGS2* induction is dependent on NRF2, TNFα treatment of UACC-62 control and NRF2-ko cells was performed. Interestingly, *PTGS2* induction was completely abolished in NRF2-ko UACC-62 cells, as demonstrated on mRNA and protein level (Figure 28B, C). Extracting FPKM values of the TCGA data set Skin Cutaneous Melanoma, verified the negative correlation of *PTGS2* and *MITF* gene expression (Figure 28D) (Correlation extracted from cbioportal.org and visualized by Dr. Silke Appenzeller, Comprehensive Cancer Center Mainfranken, Würzburg). To determine, if MITF induction itself suppresses COX2 expression, UACC-62 cells with a dox-inducible pSB-ET-iE_MITF expression vector were treated with 250 ng/ml dox for 3 days. In the last 5 h of dox treatment, 400 µM H_2O_2 were added (Figure 28E). The exogenous MITF expression reduced the COX2 inducing effect of H_2O_2 as shown in the immunoblot and by corresponding real-time PCR for *PTGS2* expression (Figure 28E, F). Thus, NRF2 facilitates the induction of COX2 partly by suppression of MITF.

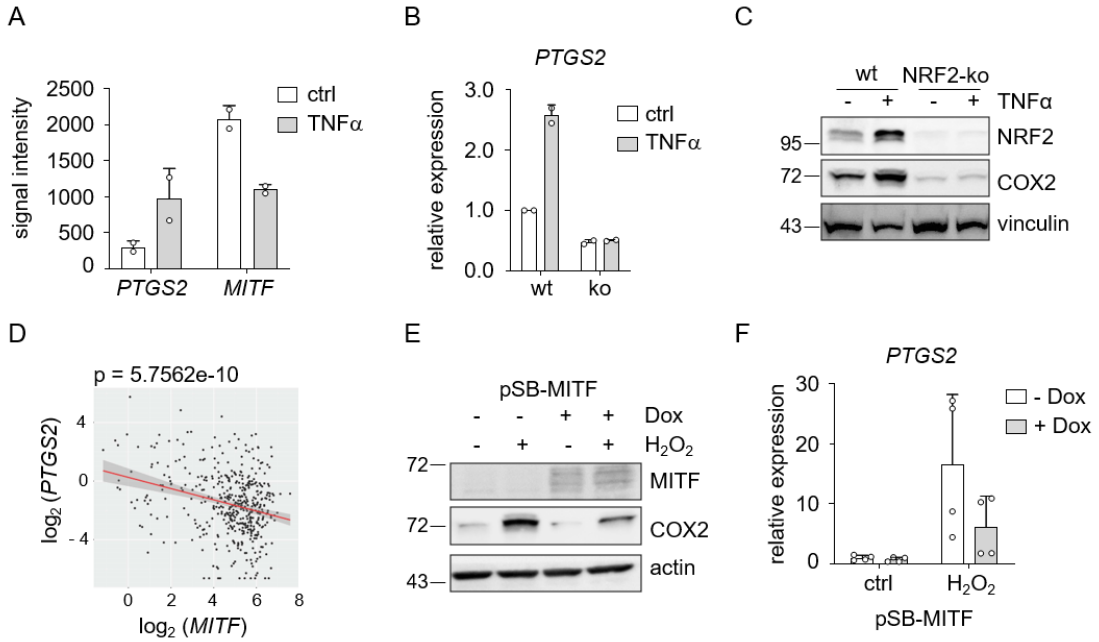

Figure 28 – *PTGS2* expression negatively correlates with *MITF* expression levels
A: RNA expression of *PTGS2* and *MITF* in MZ7 melanoma cells after TNFα treatment (1000 U/ml, 24 h). Data were extracted from GSE71798. **B**: Real-time PCR of *PTGS2* gene expression in UACC-62 NRF2 wt and NRF2 knockout cells after TNFα treatment (50 ng/ml, 3 d). Experiment was done twice. **C**: Corresponding immunoblot of NRF2 and COX2 protein expression. Vinculin served as loading control. **D**: Linear regression analyses of MITF and PTGS2 mRNA (n = 472) (Adj R2 = 0.076577 Intercept = 4.4372 Slope = - 0.20477 p = 5.7562e-10). The results shown here are based upon data derived from the TCGA dataset Skin Cutaneous Melanoma, and FPKM values were downloaded from www.cbioportal.org and visualized by Dr. Silke Appenzeller (Comprehensive Cancer Center Mainfranken, Würzburg) **E**: Immunoblot of MITF and COX2 in UACC-62 cells expressing the Dox-inducible MITF expression vector pSB_MITF. Where indicated, cells were treated with Dox (250 ng/ml, 3 d) and H_2O_2 (400 µM, 5 h) was added before harvesting. Actin served as loading control. **F**: Corresponding real-time PCR for *PTGS2* expression referred to ctrl -Dox condition. Experiment was done twice in duplicates. Error bars represent SD.

5.4.3 NRF2 and EGFR are regulated by a positive feedback loop

In addition to the negative correlation with *PTGS2*, MITF expression also negatively correlates with several receptor tyrosine kinases, like *AXL* and epidermal growth factor receptor (*EGFR)* [145-148]. Since *EGFR* also belonged to the top ten most alleviated transcripts revealed by the genome-wide transcriptomic analysis after siRNA mediated NRF2 knockdown (Figure 21A), the contribution of MITF to this suppression was examined. First, principal component analysis (PCA) in 53 melanoma cell lines for *MITF* (left) and *EGFR* (right) extracted from https://systems.crump.ucla.edu/dediff/index.php from the Graeber lab (University of California, Los Angeles, USA) (Figure 29A) [149] was analyzed. The PCA revealed that cell lines, which express high MITF levels (Figure 29A, left), display only a low EGFR expression (Figure 29A, right). This mutual exclusivity was confirmed on protein level in a panel of human melanoma cell lines by immunoblot assay (Figure 29B). Secondly, dox-dependent MITF induction in UACC-62 cells led to the suppression of EGFR by MITF induction for 3 days and 5 days (Figure 29C, D), which confirmed that MITF contributes to the EGFR regulation. Conversely, siRNA-dependent downregulation of NRF2 in UACC-62 cells led to reduced EGFR RNA and protein expression (Figure 29E, F). This effect was also validated in two more human melanoma

cell lines (Figure 29G). Notably, the degree of EGFR reduction was dependent on NRF2 knockdown efficiency. Additionally, it was reported previously that NRF2 itself is regulated by EGFR signaling [150], thus EGFR and NRF2 regulate each other in a positive feedback loop. In summary, our data indicate that NRF2 plays an important role in maintaining an undifferentiated phenotype in melanoma cells by suppressing MITF and enhancing EGFR expression.

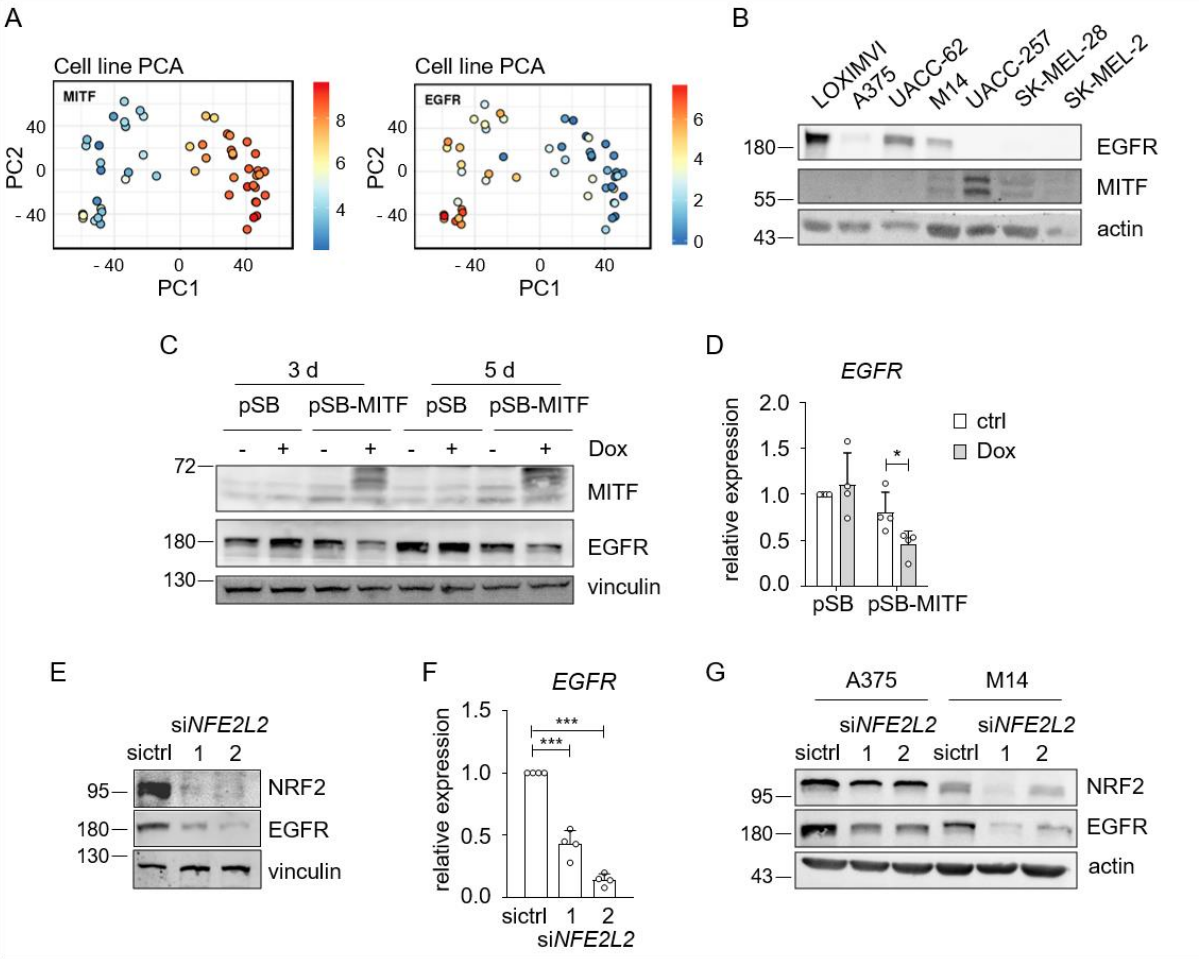

Figure 29 – High MITF activity is associated with low EGFR expression
A: Melanoma gene expression color maps, showing the expression of *EGFR* and *MITF* in 53 melanoma cell lines, visualized in the context of principal component analysis of RNA expression data. Data are derived from https://systems.crump.ucla.edu/dediff/index.php. **B**: Immunoblot of EGFR and MITF protein expression in indicated melanoma cell lines. Actin served as loading control. **C**: Immunoblot of MITF and EGFR expression after Dox-inducible expression of MITF (250 ng/ml Dox). Vinculin served as loading control. **D**: Real-time PCR of *EGFR* gene expression in UACC-62 cells after MITF induction (250 ng/ml Dox, 3 d). **E**: Immunoblot showing NRF2 and EGFR expression after siRNA-dependent knockdown of *NFE2L2* in UACC-62 cells. Vinculin served as loading control. **F**: Corresponding real-time PCR of *EGFR* gene expression. **G**: Immunoblot showing NRF2 and EGFR expression after siRNA-dependent knockdown of NRF2 in A375 (1 d) and M14 (3 d) cells. Actin served as loading control. Experiments were performed at least in four replicates, and unpaired two-tailed Student's t test was carried out to calculate significant differences (*p<0.05, ***p<0.001). Error bars represent SD

5.5 NRF2 indirectly regulates the expression of identified melanoma genes

After activation, the transcription factor NRF2 is translocated into the nucleus and forms heterodimers, preferably with small MAF proteins. The heterodimer binds to the antioxidant response element (ARE) at promoter sites of target genes. To evaluate if NRF2 binds directly to the promoter sites of regulated transcripts, identified by RNA sequencing, chromatin immunoprecipitation (ChIP) with downstream next-generation sequencing (ChIP-Seq) was performed. For ChIP, the basal levels of NRF2 binding sites were analyzed in UACC-62 DMSO treated cells and to evaluate enhanced NRF2 occupancy after NRF2 stabilization, UACC-62 cells were treated with SFN. After crosslinking of proteins to the DNA and chromatin fragmentation, NRF2 bound DNA fragments were isolated with a NRF2-specific antibody. Real-time PCR analysis showed enrichment of known NRF2 binding sites in DMSO treated samples compared over input control (Figure 30A, left). NRF2 binding on the AREs of *NQO1* and *HMOX1* was further enhanced after SFN treatment (Figure 30A, right). First analysis after ChIP-sequencing was the determination of genome-wide peak positions, with *cis*-regulatory element annotation system (CEAS), compared to nearest transcription start sites (TSS). In both conditions NRF2 binding sites were distributed throughout the genome, with a predominance at intronic (35.1 %/42.6 %) and intergenic (36.3 %/37.4 %) regions (Figure 30B). Only 12.0 % in DMSO or 10.4 % in SFN-treated cells displayed NRF2 binding sites in direct proximity (< 10 kb) to promoter regions of the nearest gene (Figure 30B). Overall, this observation is in accordance with previously published ChIP-Seq data of NRF2 as well as of the stress-induced AP-1 transcription factor, which also discovered a high number of transcription factor binding sites at distant sites from a TSS (> 100 kb) [151, 152].

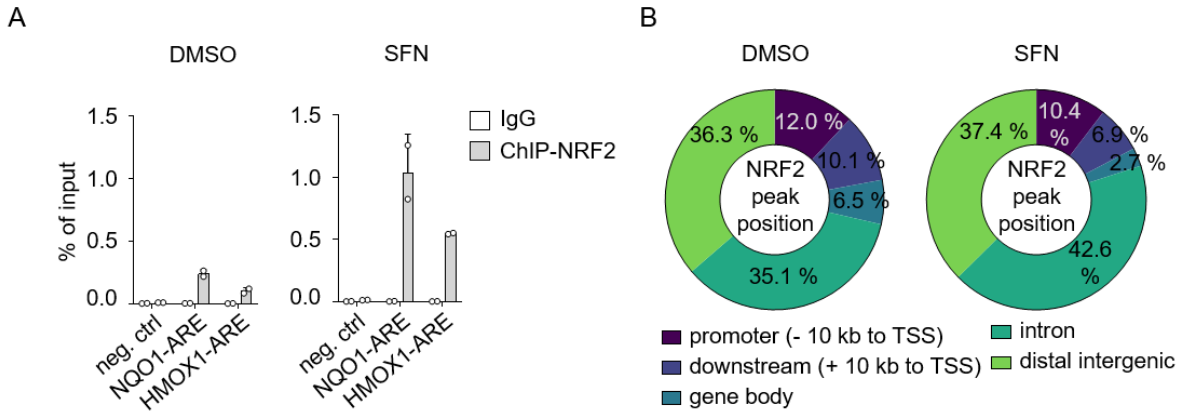

Figure 30 – Enrichment of NRF2 at known binding sites and genome-wide peak positions
A: Validation of ChIP experiments by real-time PCR on known NRF2 binding sites (antigen response elements, ARE) of *NQO1* and *HMOX1* after DMSO and SFN (7.5 µM, 24 h) treatment in UACC-62 cells. **B**: Genome-wide peak distribution determined after ChIP-sequencing by *cis*-regulatory element annotation system (CEAS).

Comparison of DMSO and SFN enriched peaks revealed a strong overlap between the peak positions (Figure 31A), with only nine peaks to be exclusively enriched in DMSO treated cells. In total, the SFN condition showed around 4,846 NRF2 binding sites, of which 313 peaks were also found under basal conditions. Motif analysis of NRF2 binding sites in both conditions displayed the highest motif enrichment for documented *NFE2L2* binding sites (Figure 31B), confirming the specificity of the ChIP-Seq analysis. The ChIP-Seq data of SFN and the gene expression data of the NRF2 knockdown RNA-Seq were then combined to predict potential direct target genes of NRF2. Genes with a peak of 5 kb around the TSS were determined as a direct target gene. The Binding and Expression Target Analysis (BETA-basic) was carried out to predict direct target genes with this threshold. GO term analysis with the predicted direct NRF2 target genes was performed with the bioinformatic tool DAVID. Genes, which are activated by NRF2 (downregulated in NRF2 knockdown) belonged to detoxification and oxidation processes, including genes like *NQO1*, *SLC7A11* (Figure 31C). Classification of predicted suppressed genes (upregulated after NRF2 knockdown) is not displayed due to small-sized GO terms. The complete list of predicted target genes and overrepresented transcription factor motifs are found in the appendix (Table 22, 23).

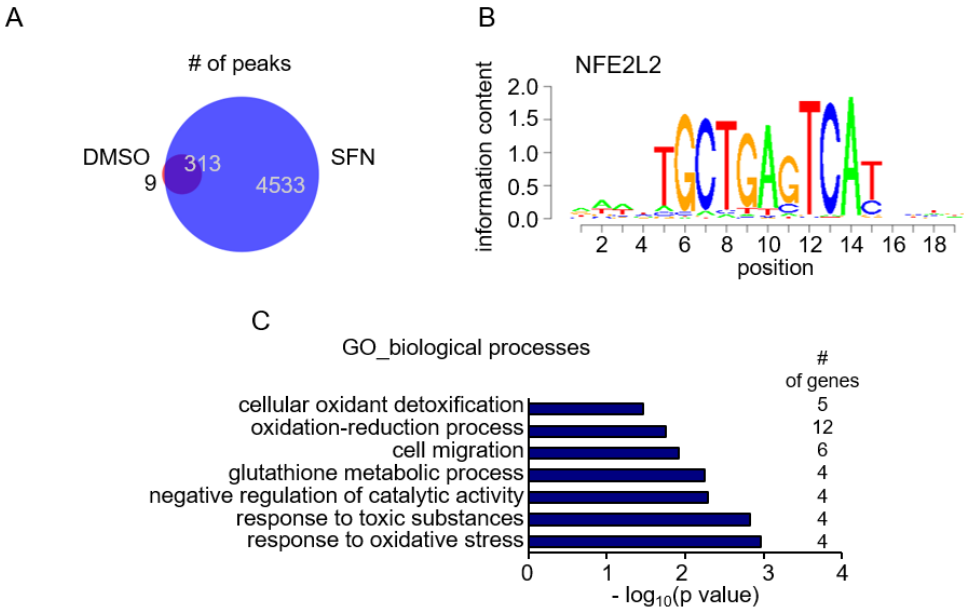

Figure 31 – Positively regulated direct target genes are involved in detoxification processes
A: Venn diagram of NRF2 peak overlap in DMSO and SFN treated UACC-62 cells after MACS2 peak calling of ChIP-sequencing. **B**: Most enriched sequence pattern in the ChIP-seq peak regions with DMSO or SFN (7.5 µM, 24 h) treatment detected by SeqMotif analysis. **C**: GO term analysis with associated number of genes of activated direct NRF2 target genes (with peak at ± 5 kb around promoter site) predicted by binding and expression target analysis (BETA-basic) after NRF2 ChIP-sequencing of SFN treated cells.

Figure 32 shows genome browser tracks of the well-characterized NRF2 target genes *HMOX1* (Figure 32A) and *NQO1* (Figure 32B). The genomic regions for *PTGS2* (Figure 32C) and *EGFR* (Figure 32D) did not reveal NRF2 enrichment near promoter sites of those genes, despite the high regulation of *PTGS2* and *EGFR* after NRF2 knockdown. In accordance with the previous finding, that MITF itself is not altered after

NRF2 inhibition, no binding site of NRF2 at the MITF promoter region was observed (Figure 32E).

Taken together, ChIP sequencing of NRF2 binding sites verified known directly bound target genes, like *HMOX1* and *NQO1*, and the *NFE2L2* sequence motif. However, NRF2 binding was not enriched at the promoter regions of *PTGS2* or *EGFR*, which were strongly reduced in the NRF2 knockdown cells. Thus, NRF2 might regulate gene expression not exclusively by direct binding to promoter regions of its target gene, which was previously reported [153].

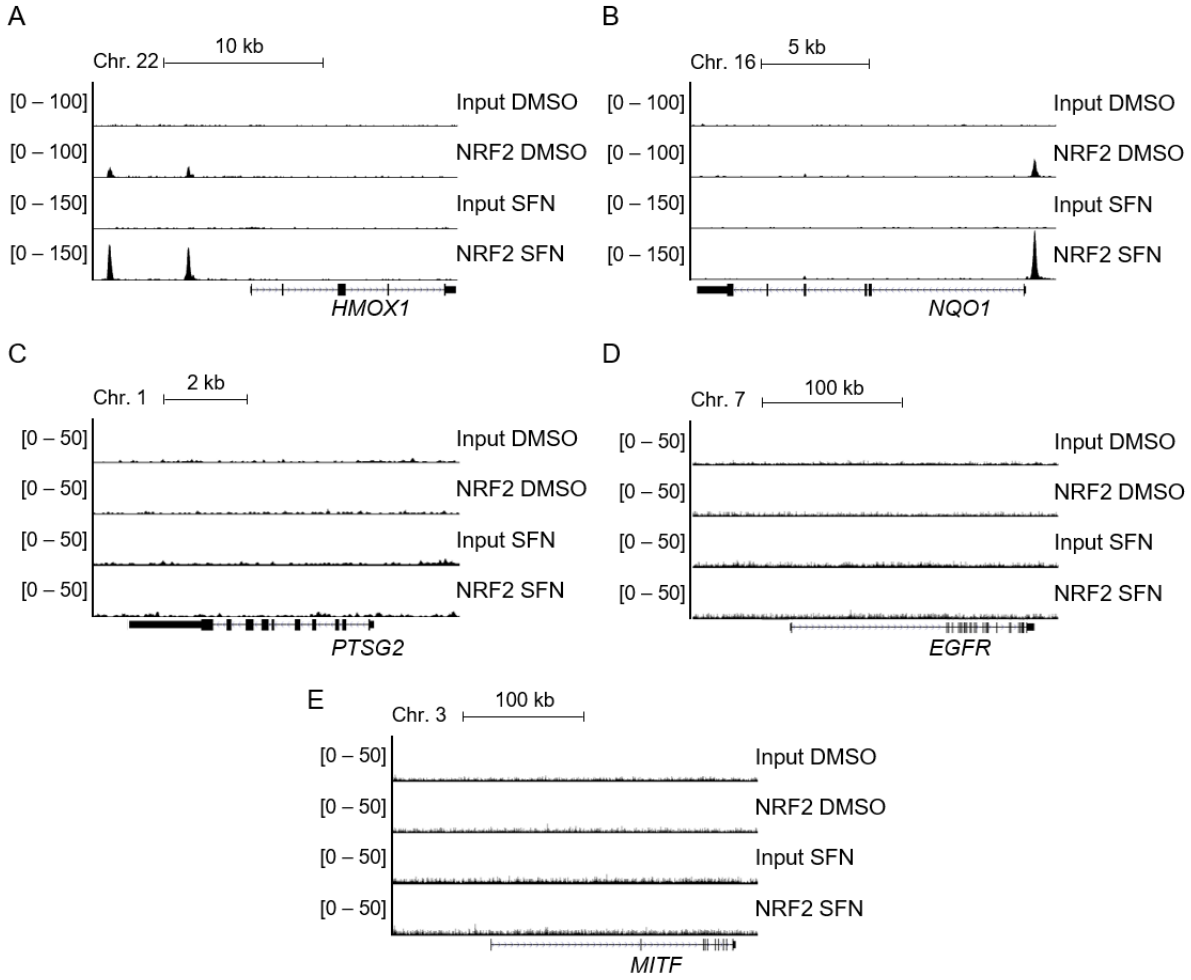

Figure 32 – Peak enrichment of NRF2 binding at known target genes
A-E: Genome browser tracks of promoter regions of *HMOX1* (A), *NQO1* (B), *PTGS2* (C), *EGFR* (D) and *MITF* (E) with NRF2 binding, evaluated by ChIP-Seq analysis. Where indicated, NRF2 was stabilized by treatment with sulforaphane (7.5 µM SFN, 24 h).

5.6 NRF2 impacts murine melanoma growth and development *in vitro* and *in vivo*

5.6.1 Murine NRF2 knockout cells reduce stress-dependent target gene expression

The results derived from the *in vitro* experiments, suggest that NRF2 regulates crucial processes in human melanoma cell lines, such as dedifferentiation and immunomodulation. Therefore, the impact of NRF2 in melanoma formation and maintenance was investigated *in vivo*. For the *in vivo* experiments, murine CRISPR/Cas9 *Nfe2l2* knockout 781 cells were generated. Murine 781 melanoma cells were derived from tumor tissue of *Tyr-Cre*^{ERT2};*BRAF*^{V600E};*Pten*$^{flox/flox}$ mice [113] and one round of subcutaneous injection into C57BL/6 mice. The murine 781 cells were particularly suitable as a melanoma mouse model, since the BRAF^{V600E} mutation in combination with PTEN loss are common alterations causing human melanoma development [22]. Furthermore, the murine 781 cells resemble the genotype of the human UACC-62 melanoma cell lines and their low MITF expression. Genomic sequencing validated premature stop codons in the amino acid sequence of both alleles in the NRF2-ko (Figure 33B) compared to NRF2 wt 781 cells (Figure 33A). Furthermore, treatment with 7.5 µM SFN for 24 h showed neither NRF2 protein induction (Figure 33C) nor translocation into the nucleus (Figure 33D) in the 781 NRF2-ko cell line. Thus, the NRF2-ko 781 cells were suitable for further downstream experiments.

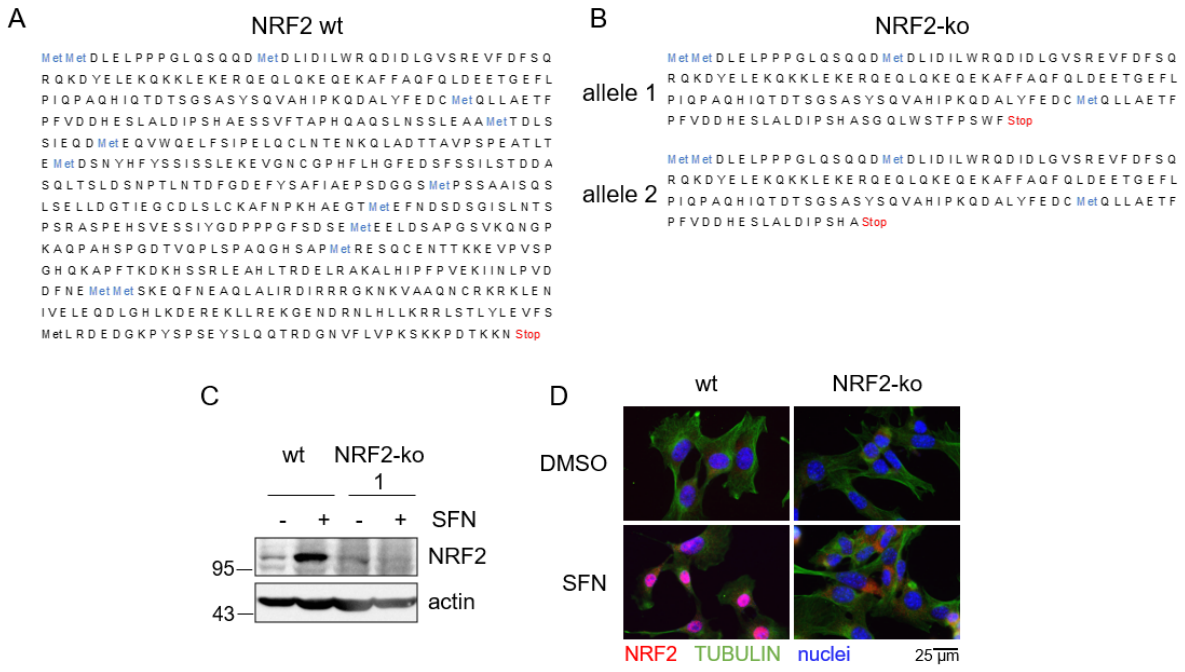

Figure 33 – Establishment of murine CRISPR/Cas9 generated *Nfe2l2* knockout cells
A, B: Protein sequence of murine NRF2 wt (A) and CRISPR/Cas9 NRF2 knockout (B) 781 cells. **C**: Immunoblot for NRF2 after SFN treatment of 781 NRF2 wt and NRF2 knockout cells (7.5 µM, 24 h). Actin served as loading control **D**: Representative merged immunofluorescence images for NRF2 (red), tubulin (green) and Hoechst (blue) after SFN treatment of 781 NRF2 wt and NRF2 knockout cells (7.5 µM, 24 h).

For further validation of compromised NRF2 activity in murine 781 NRF2-ko cells, oxidative stress was induced with 400 µM H_2O_2 for 5 h. Real-time PCR for *Nfe2l2* and target gene expression verified reduced basal expression and inducibility of *Nfe2l2* and its targets *Hmox1, Slc7a11*, *Nqo1* (Figure 34A). Consistent with the previous findings of NRF2-dependent COX2 regulation, *Ptgs2* induction was impaired in NRF2-ko cells (Figure 34A). Likewise, COX2 protein induction was abolished in 781 NRF2-ko cells (Figure 34B). After oxidative stress induction by 25 µM H_2O_2 for 24 h, NRF2-ko showed a higher sensitivity than NRF2 wt cells, as visualized under a light microscope (Figure 34C) and confirmed by MTT proliferation assay (Figure 34D). To validate the suppressive effect on COX2, another two 781 NRF2-ko clones (2 and 3) were evaluated after H_2O_2 induced stress. In clone number 2, NRF2 induction was still possible, though to a lower extent, assuming an incomplete NRF2 knockout. Here, ROS-induced COX2 was only weakly suppressed compared to control cells. In clone number 3, NRF2 induction as well as COX2 induction were entirely blunted (Figure 34E). Thus, the murine 781 NRF2-ko cell lines confirmed the NRF2-dependent COX2 regulation. For the *in vivo* model and further downstream experiments, the 781 NRF2-ko clone 1 was used.

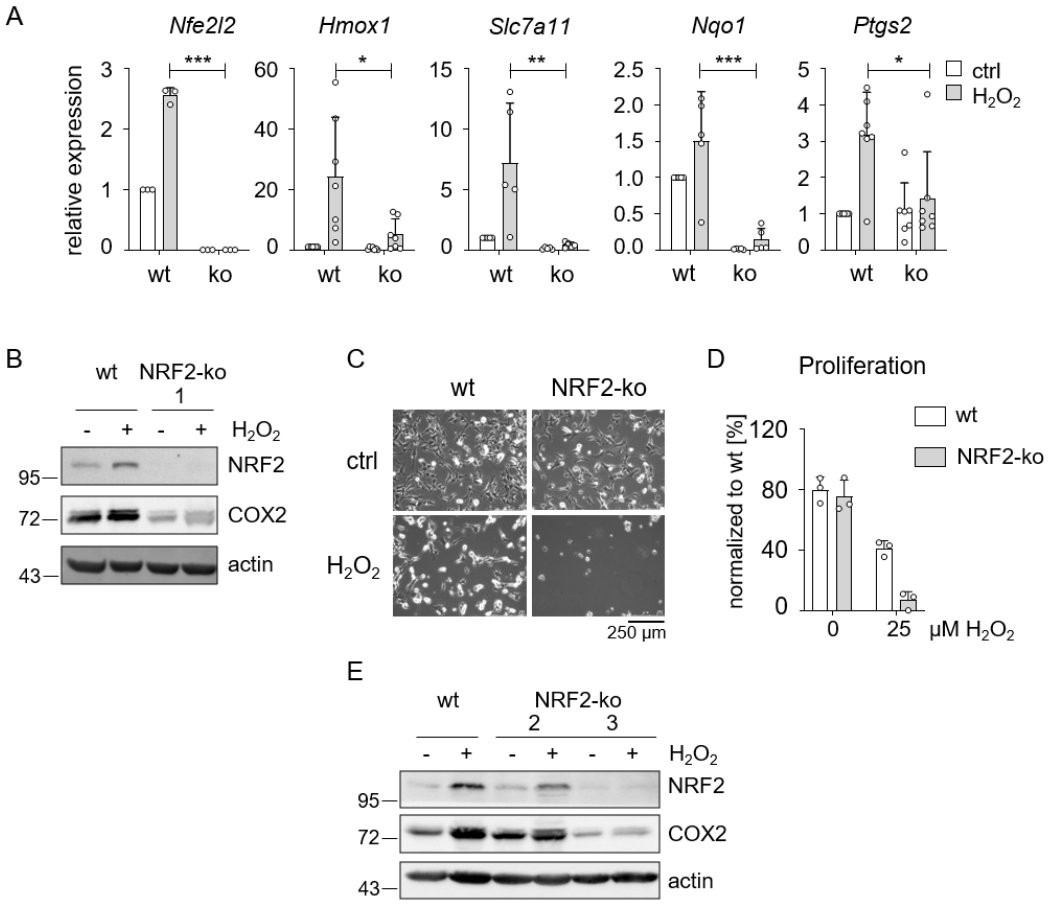

Figure 34 – Murine *Nfe2l2*$^{-/-}$ cells reduce stress-dependent target gene induction
A: Real-time PCR of indicated genes in murine melanoma NRF2 wt and NRF2 knockout cell line 781 after H_2O_2 treatment (400 µM, 5 h). *Hmox1, Slc7a11* and *Nqo1* are classical NRF2 target genes and served as control. Experiments were performed at least three times and two-way ANOVA with Sidak's multiple comparisons posttest was carried out (*p<0.05, **p<0.01, ***p<0.001). Error bars represent SD. **B**: Corresponding immunoblot of NRF2 and COX2. Actin served as loading control. **C**: Representative images of control and NRF2 knockout 781 cells after H_2O_2 treatment (25 µM, 24 h). **D**: MTT viability assay of 781 cells after H_2O_2 treatment (25 µM, 24 h). **E**: Immunoblot of NRF2 and COX2 in two distinct CRISPR/Cas9 NRF2 knockout 781 cells after H_2O_2 treatment (400 µM, 5 h). Actin served as loading control.

5.6.2 *Nfe2l2* $^{-/-}$ cells display a poorer melanoma engraftment *in vivo*

Mice with the *Tyr-Cre*^{ERT2};*BRAF*^{V600E};*Nfe2l2*$^{-/-}$ genotype did not develop melanomas from benign lesions as revealed in the melanocytic hyperplasia mouse model (Figure 13E – G). However, nevi formation was still possible and independent of the *Nfe2l2* status, hence NRF2 is dispensable for the development of benign lesions. In another murine melanoma model, the role of NRF2 in established murine melanoma cell lines was examined. To do so, 781 control and 781 NRF2-ko cells were subcutaneously injected into the flanks of immunocompetent C57BL/6 wildtype mice. Whereas 100 % of mice injected with 781 control cells developed tumors, engraftment and subsequent tumor growth were seen in only 60 % of the mice injected with NRF2-ko cells (Figure 35A). If no tumor formation was detectable, the experiment was terminated after 90 days. Furthermore, the tumor onset of NRF2-ko melanomas was significantly delayed with a mean of 34 days compared to 17 days as observed for NRF2 wt tumors (Figure 35B). This went along with a prolonged tumor free survival of the NRF2-ko injected mice (Figure 35C). To analyzed differences in gene and protein expression, tumors were resected when they reached a volume of 800 – 1000 mm^3. Real-time PCR with cDNA of all available tumors, validated reduced gene expression of *Nfe2l2* and *Nqo1* (Figure 35D). Immunoblot analysis of isolated tumors revealed reduced NRF2 protein levels in NRF2-ko tumors, with one exception (Figure 35E). The re-expression effect of NRF2 is most likely caused by tumor infiltrating cells or cells of the tumor microenvironment. In addition, the reduction of COX2 protein as well as re-expression of MITF were observed in the NRF2-ko tumors (Figure 35E). Along with reduced COX2 protein expression levels, PGE2 concentrations were reduced in NRF2-ko tumors as determined by mass spectrometry (Figure 35F). Taken together, the murine *in vivo* model of NRF2-dependent melanoma engraftment demonstrated that NRF2 is crucial for the growth of established melanoma cells and for the maintenance of an $MITF^{low}$ status of melanoma cells. Furthermore, NRF2 is responsible for securing the potential immune-suppressive COX2 levels also *in vivo*.

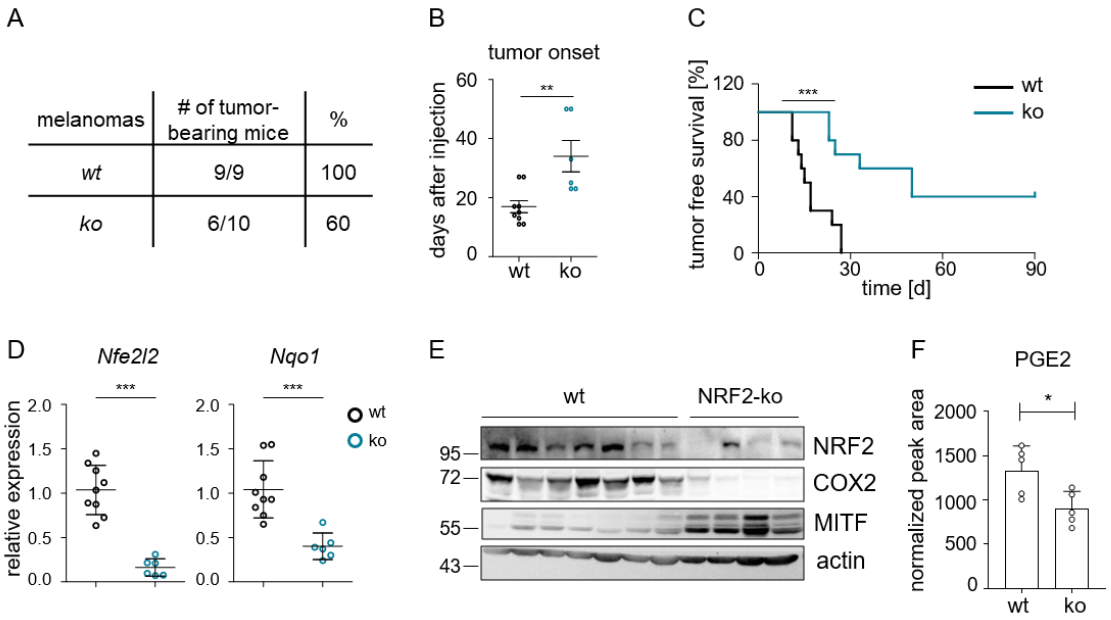

Figure 35 – *Nfe2l2* knockout impairs tumor engraftment *in vivo*
A: Table showing the number of tumor-bearing mice after subcutaneous injection of 10,000 781 control cells and NRF2 knockout cells into the flanks of C57BL/6 mice. Mice without tumor growth were followed up and sacrificed after 90 days. **B, C**: Corresponding tumor onset (B) and tumor-free survival (C). **p<0.01 two-tailed Student's t test, unpaired (B), ***p<0.001, Mantel-Cox test (C). **D**: Real-time PCR of *Nfe2l2* and its target gene *Nqo1* in resected tumors of NRF2 wt and NRF2 knockout 781 melanoma cells. (NRF2 wt n=9, NRF2-ko n=6). **E**: Immunoblot of COX2 and MITF in tumors comprised of 781 control and 781 NRF2 knockout cells excised at the experimental endpoint. Actin served as loading control. **F**: Prostaglandin E2 (PGE2) levels in control tumors and NRF2 knockout tumors (n=5 per group), measured by mass spectrometry. Preparation and analysis of mass spectrometry was done by Dr. Werner Schmitz, Department of Biochemistry and Molecular Biology, Würzburg. *p<0.05 (two-tailed Student`s t test, unpaired).

5.7 NRF2 suppresses immune-related functions

To investigate the genome-wide transcriptional program altered by NRF2 in tumors compared to cultivated cells, next-generation sequencing of isolated RNA from NRF2 wt and NRF2-ko cell lines and the corresponding tumors, as described in the previous section, was performed. Control and NRF2-ko tumors are subsequently termed "*in vivo*", whereas analyzed cell lines are designated "*in vitro*". The genome browser tracks of the genomic region of *Nfe2l2* revealed intron-retention between exon 3 and 4 of *Nfe2l2* in NRF2-ko cells (*in vitro*) as well as NRF2-ko tumors (*in vivo*) (Figure 36A). GSEA of gene expression data in NRF2-ko compared to control cells (*in vitro*) validated repression of genes included in the HALLMARK gene set "reactive oxygen species (ROS) pathway" (Figure 36B). This gene set even had the highest negative normalized enrichment score (NES). The GSEA enrichment plot of the ROS pathway with indicated NES and FDR q value is shown in Figure 36C. Moreover, successive enriched gene sets were also involved in detoxification, metabolic and stress response mechanisms, which reflect well-known NRF2 functions (Figure 36B). On the other hand, HALLMARK gene sets with the highest NES are involved in inflammatory related responses, like type I and type II interferon pathways (Figure 36B). These data suggest a role of NRF2 in the suppression of inflammatory and immune-related mechanisms.

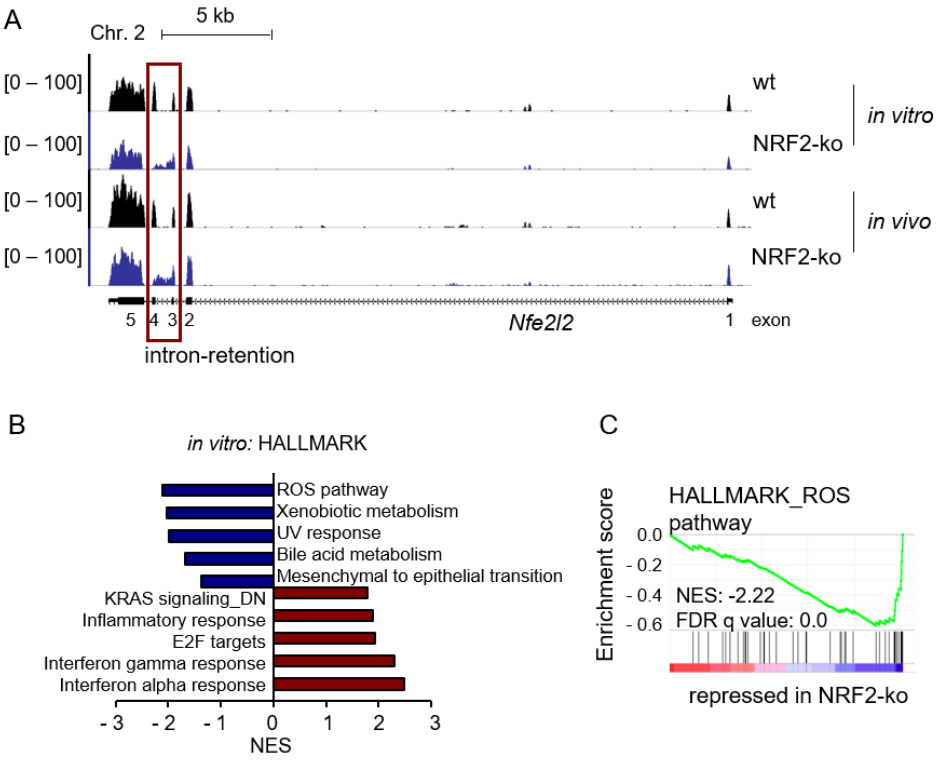

Figure 36 – NRF2 knockout reduces detoxification genes
A: Genome browser tracks of bedgraph files for Nfe2l2 gene region in cells and cell derived tumors of NRF2 wt and NRF2 knockout 781 cells. RNA-sequencing was done in triplicates and one representative bedgraph file for each sample is displayed. **B**: Functional characteristics of altered transcripts in the NRF2 knockout cell lines as revealed by GSEA analysis (Hallmarks). NES: Normalized enrichment score. **C**: GSEA enrichment plot of the Hallmark gene set "reactive oxygen species pathway" (ROS) repressed NRF2 knockout cells.

Likewise, GSEA of regulated genes in NRF2-ko compared to control tumors displayed the highest negative enrichment in genes of the HALLMARK gene set "ROS pathway" and other detoxification pathways (Figure 37A, B). Equally to the *in vitro* conditions, the *in vivo* results suggest a strong repression of inflammatory and immune-related factors by NRF2 (Figure 37A). The volcano plot in Figure 37C visualizes highly regulated genes in NRF2-ko tumors. In the lower left corner repressed genes, like oxidative response genes, are located. The genes, which are induced by NRF2-ko, are distributed along the right site of the volcano plot and involve several immune-associated factors (Figure 37C). Thus, the NRF2-ko in cells as well as in cell-derived tumors indicated a transcriptional program associated with a higher immune-response.

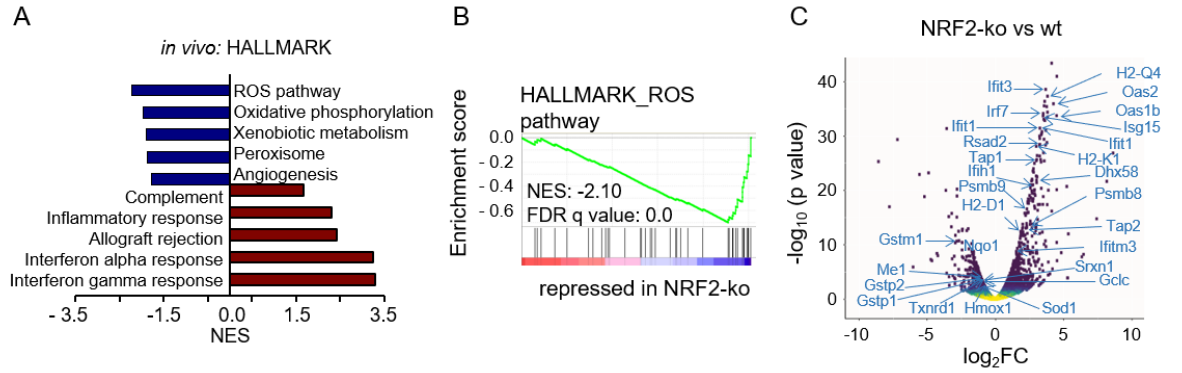

Figure 37 – NRF2 knockout reduces detoxification genes in cell-derived tumors
A: Functional characteristics of altered transcripts in NRF2 knockout tumors, as revealed by GSEA analysis (Hallmarks). NES: Normalized enrichment score. **B**: GSEA enrichment plot of the Hallmark gene set "reactive oxygen species pathway" (ROS) repressed in NRF2 knockout tumors. **C**: Volcano plot representing highly deregulated genes in tumors derived from *Nfe2l2* knockout cells versus wildtype cells determined by RNA-sequencing

Since the NRF2-ko induced several inflammatory and immune-related pathways, the delayed tumor growth of NRF2-ko cells might be due to a stronger immune response, with higher T cell infiltration. GO term analysis by GSEA in NRF2-ko tumors also showed enrichment of genes involved in the innate and adaptive immune responses. The GO term immune effector processes, including genes related to T cell cytotoxicity, was highly enriched (Figure 38A). Genes like, perforin 1 (*Prf1*) and granzyme B (*Gzmb*) are secreted by cytotoxic T lymphocytes and natural killer cells (NK) to promote pore formation and causing apoptosis in target cells. Both genes were significantly induced in NRF2-ko tumors, as validated by real-time PCR (Figure 38B). However, the T lymphocytes markers *Cd3g* and *Cd8* showed only a slight trend towards increased expression levels (Figure 38B). Next, IHC staining for Cd3 was performed to independently determine T cell infiltration into developed tumors (Figure 38C, D). Figure 38C shows the IHC images of one representative control and NRF2-ko tumor, the later showing a stronger staining for Cd3. The quantification of Cd3 staining, done for all available IHC sections (n=6 per group), showed a slight trend towards higher T cell infiltration in NRF2-ko cell derived tumors (Figure 38D). In summary, the higher induction of *Prf1* and *Gzmb* compared to the T cell associated genes *Cd3g* and *Cd8*, suggest a stronger induction of the innate immune response than an adaptive immune response in NRF2-ko tumors. This is further supported by the modest increase of T cell infiltration. However, the difference in T cell infiltration might have been more dominant earlier during tumor development. Since all tumors were resected at the same size, the NRF2-ko tumors might have already adapted to an altered immune system.

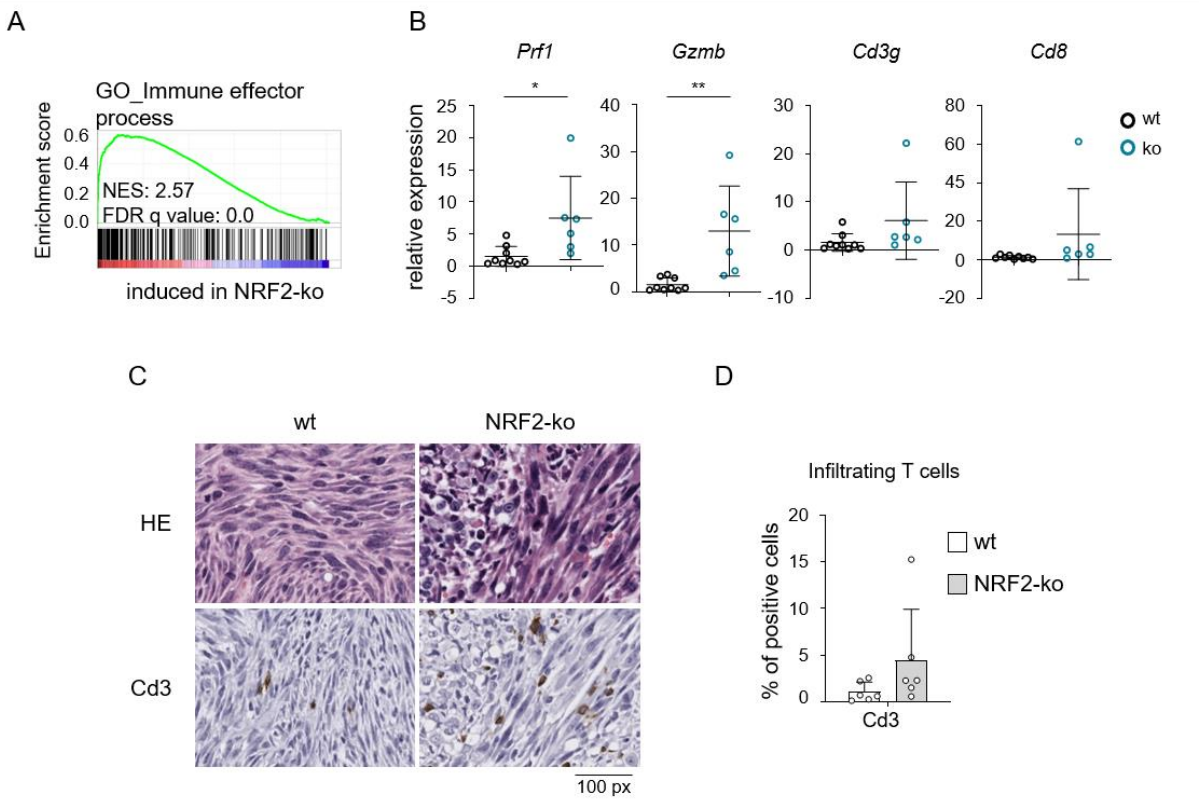

Figure 38 – Trend towards higher T cell infiltration in NRF2-ko tumors
A: GSEA enrichment plot of the Gene Ontology gene set "Immune effector response" induced in NRF2 knockout tumors. **B**: Relative expression of cytotoxic T cell markers in tumors derived from 781 control and NRF2 knockout cells, as measured by real-time PCR with all available tumors. Significance was calculated with two-tailed Student's t test (*p<0.05, **p<0.01). **C, D**: Representative IHC images (C) and quantification (D) of CD3+ T cell infiltration into 781 control (n=6) and NRF2 knockout tumors (n=6). IHC staining was done by Sabine Roth, Department of Pathology, Würzburg. Quantification was done with positive cell detection of QuPath open-source software.

Since GSEA of HALLMARK gene sets revealed regulation of immune-relevant signaling pathways, GSEA of KEGG pathways was performed in NRF2-ko cells and cell-derived tumors. The GSEA of KEGG pathway gene sets validated a strong induction of genes involved in antigen processing and presentation in both NRF2-ko conditions (Figure 39A, B). To evaluate differences *in vitro* to *in vivo,* caused by influences of the tumor microenvironment, the effect on antigen processing and presentation of the NRF2 knockout, as measured by RNA sequencing, was compared between the *in vitro* and *in vivo* conditions. The enhancement of genes involved in antigen processing and presentation facilitate the recognition of tumor cells by cytotoxic T cells. Antigen processing and presentation genes involve for example proteasome 20S subunit beta 8 and 9 (*Psmb8*, *Psmb9*), which are responsible for peptide cleavage. Furthermore, transporter 1 and 2 (*Tap1*, *Tap2*) transport the cleaved antigen to the endoplasmic reticulum and transfer it on to the major histocompatibility complex class I (MHC class I). MHC class I are formed by *H2-D1*, *H2-K1* or *H2-Q4*, together with beta-2-microglobulin (*B2m*). Comparison of the fold changes of these genes revealed a stronger induction in NRF2-ko tumors than in NRF2-ko cells (Figure 39C). This might be due to a higher immune response in the immune-competent microenvironment. Highly induced genes *in vivo* are shown in the top left corner (Figure 39C). The increased gene

expression was validated by real-time PCR in NRF2-ko cells (Figure 39D) as well as in NRF2-ko tumors (Figure 39G). It is well established that the proteasomal subunits *Psmb8* and *Psmb9* as well as the transporters *Tap1* and *Tap2* are rapidly induced by cytokines, such as interferon alpha (IFN-α) or gamma (IFN-γ) [154-156]. GSEA of HALLMARK gene sets revealed strong enrichment of the interferon gamma response pathway (Figures 36B, 37A and 39E). IFN-γ regulates gene expression via activation of the JAK/STAT pathway. After binding to the interferon gamma receptor (IFNGR1/2), the janus protein tyrosine kinase (JAK) is phosphorylated, which in turn phosphorylates signal transducers and activators of transcription (STAT1). Phosphorylated STAT1 activates target gene expression, like *Tap1* or *Psmb8* [157, 158]. Interestingly, NRF2-ko cells displayed increased basal levels of phosphorylated STAT1 (p-STAT1) at position Tyr701 (Figure 39F), which induces STAT1 dimerization and activation. The increased p-STAT1 levels after NRF2-ko support a deregulated JAK/STAT pathway. Thus, the NRF2-dependent repression of antigen processing genes is most likely facilitated by compromised JAK/STAT signaling.

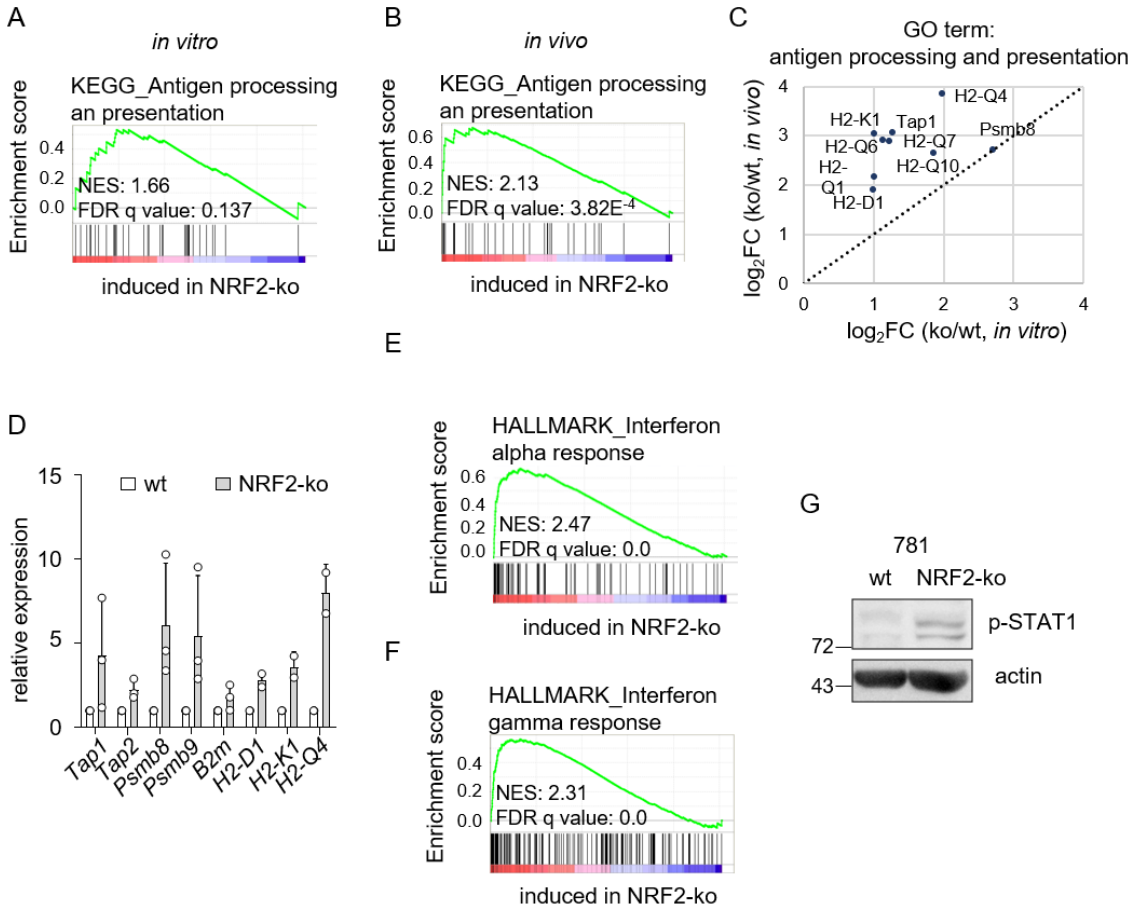

Figure 39 – Genes involved in antigen processing and presentation are induced in NRF2-ko cells and tumors
A, B: GSEA enrichment plot of the KEGG pathway gene set "Antigen processing and presentation" in analyzed 781 cells (A) and corresponding tumors (B). **C**: Induction of significantly regulated genes from the KEGG pathways "Antigen processing and presentation" in the NRF2 knockout *in vitro* condition compared to the NRF2 knockout *in vivo* condition. **D**: Real-time PCR of indicated genes involved in antigen processing and presentation in NRF2 wt and NRF2 knockout 781 cells. Experiment was done two or three times, as indicated. **E**: GSEA enrichment plot of the Hallmark gene set "Interferon alpha response" (*in vitro*) **F**: GSEA enrichment plot of the Hallmark gene set "Interferon gamma response" (*in vitro*). **G**: Immunoblot for p-STAT1 (Tyr701) in 781 NRF2 wt and NRF2 knockout cells. Actin served as loading control. **H**: Relative expression of antigen processing and presentation genes in tumors derived from 781 control and NRF2 knockout cells, as measured by real-time PCR with all available tumors. All error bars represent SD and significance was calculated with unpaired two-tailed Student's t test (*p<0.05, **p<0.01, ***p<0.001).

Previously, it was shown, that *Stat1*$^{-/-}$ mice are more susceptible for viral infections [159], thus the cytokine-JAK/STAT signaling pathway is also involved in the antiviral response of the immune system. Furthermore it was reported, that a NRF2 deficiency increased basal levels of genes involved in this antiviral response [160]. The antiviral response is involved in cytosolic DNA recognition and is part of the innate immune response. Besides from virus infection, cytosolic DNA is also present and released in fast-growing tumor tissue.

GSEA showed an enrichment of the GO term "Defense response to virus" in NRF2-ko cells under *in vitro* and *in vivo* conditions (Figure 40A, B). Many of these genes are crucial for the subsequent activation of the innate immune system and type I interferon response, which is tightly linked to COX2 signaling [161]. Representative genes for the innate immune response are, 2'-5'-oligoadenylate synthetases (*Oas1a*, *Oas1b*, *Oas2*), crucial enzymes for degradation of cellular and viral RNA, radical S-adenosyl methionine domain containing 2 (*Rsad2*=viperin), which inhibits virus replication, as well as interferon induced with helicase C domain 1 (*Ifih1*) and DExD/H-Box helicase 58 (*Ddx58*=Rig-I) that both sense viral nucleic acids. Isg15 ubiquitin like modifier (*Isg15*) and its target gene interferon protein with tetratricopeptide repeats 1 (*Ifit1*) are further involved in defense response to virus. Like previously described for the genes belonging to the "Antigen processing and presentation" group (Figure 39B) the "Defense response to virus" genes are enriched to a stronger extent in NRF2-ko tumors compared to the *in vitro* condition (Figure 40C). Moreover, all listed genes are targets of stimulator of interferon response cGAMP interactor 1 (STING), which is encoded by *Tmem173* and the pattern recognition receptor for detection of cytosolic nucleic acids. Recently, it was shown that STING expression is negatively regulated by NRF2 in human lung cancer cells [153]. The induction of innate immune response-associated genes was validated by real-time PCR in NRF2-ko cells (Figure 40D) and in NRF2-ko tumors (Figure 40E). Thus, NRF2-ko conditions improved STING activity, leading to an increase in gene expression and a stronger innate immune response, even in absence of a tumor microenvironment.

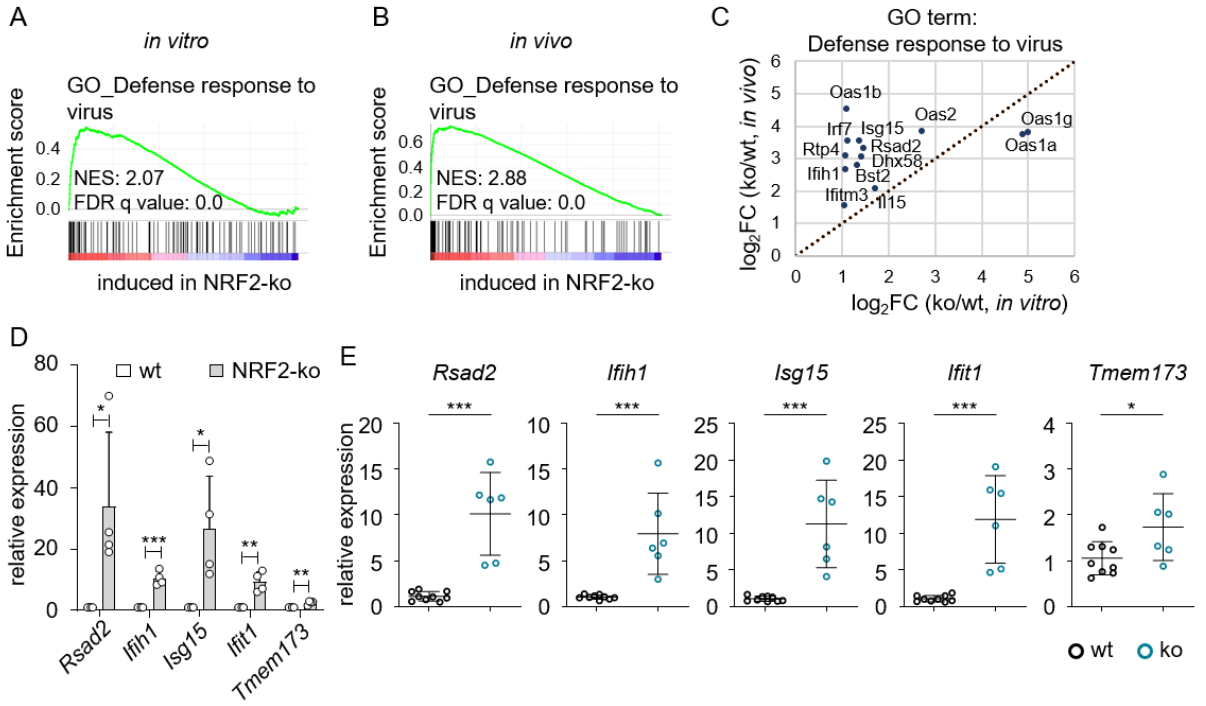

Figure 40 – Innate immune response induction is more prominent in the *in vivo* situation
A, B: GSEA enrichment plot of the Gene Ontology gene set "Defense response to virus" in analyzed 781 NRF2-ko cells (A) and tumors (B). **C**: Induction of significantly regulated genes from the GO term "Defense response in virus" in NRF2 knockout cell lines versus controls and NRF2 knockout versus control tumors. **D**: Real-time PCR of indicated genes involved in the defense response in virus in NRF2 wt and NRF2 knockout 781 cells. Real-time PCR was done four times. **E**: Relative expression of defense response to virus genes in tumors derived from 781 control and NRF2-ko tumors, as measured by real-time PCR with all available tumors. All error bars represent SD and significance was calculated with unpaired two-tailed Student's t test (*p<0.05, **p<0.01, ***p<0.001).

The genes mentioned above are part of a gene set previously described to be indicative of STING activation [162]. Interestingly, NRF2 knockout melanomas show a strong elevation of almost the entire STING activation signature, as visualized in a heatmap plot (Figure 41A). Accordingly, STING was expressed at higher levels in NRF2-ko compared to control tumors (Figure 41B), matching the increased gene expression (Figure 40E). Since the STING pathway related "Defense response to virus" gene set was also deregulated in the NRF2-ko 781 cell line (Figure 40), the causal relationship between NRF2 and the STING pathway was further investigated *in vitro*. After ectopic dox-inducible NRF2 expression in 781 wt cells, the expression of *Rsad2*, *Ifih1*, *Isg15* and *Ifit1* was decreased (Figure 41C), however regulation of *Tmem173* was not detectable (Figure 41C). Furthermore, induction of NRF2 by doxycycline led to a strong increase of COX2 protein levels as determined by immunoblot (Figure 41D). Previously, it was established that *Ptgs2* expression, correlating with increased PGE2 levels, promote an anti-inflammatory phenotype in melanoma and other cancer cell lines, which can be inhibited by genetic ablation of *Ptgs2* and *Ptgs1* and *-2* [136]. Furthermore, in tumors with high COX1 and/or COX2 expression, PGE2 blocks the infiltration of natural killer cells and dendritic cells, thus limiting the innate immune response [135]. Therefore, NRF2 might indirectly facilitated the innate immune response due to PGE2 elevation. To test this, 781 wt cells were treated with PGE2 and simultaneously the innate immune

response was activated by cGAMP addition. Intriguingly, the induction of MDA-5, encoded by *Ifih1*, was reduced by the addition of PGE2 (Figure 41E). Equally, the levels of p-TBK1, responsible for STING phosphorylation were decreased (Figure 41E). Furthermore, induction of the gene expression of STING-associated targets was also compromised after PGE2 addition (Figure 41F). The reducing effect on gene expression was higher after NRF2 induction than after PGE2 addition, however PGE2 was partly involved in the NRF2-dependent suppression of the innate immune response.

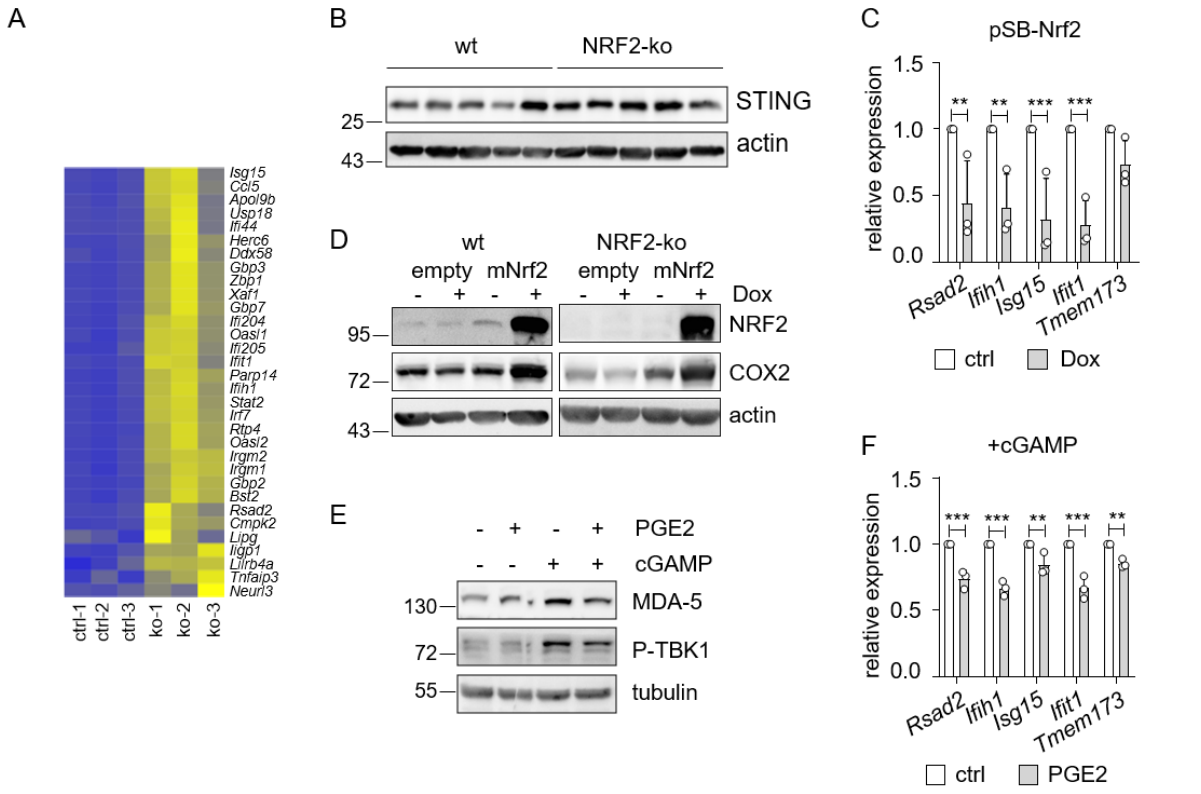

Figure 41 – NRF2 represses innate immune response partly by *PTGS2* regulation
A: Heatmap displaying the expression of DNA sensing pathway genes, corresponding to the cGAS/STING pathway, as derived from [160], in wt and NRF2 knockout mouse tumors. **B**: Immunoblot of STING protein expression in tumors comprised of 781 control and NRF2 knockout cells excised at the experimental endpoint. Actin served as loading control. **C**: Real-time PCR of *Rsad2*, *Ifih1*, *Isg15*, *Ifit1* and *Tmem173* in response to Dox-inducible NRF2 expression in 781 cells (250 ng/ml, 3 d). **D**: Immunoblot of NRF2 and COX2 protein expression in response to Dox-inducible NRF2 expression in 781 NRF2 wt and NRF2 knockout cells (250 ng/ml, 3 d). Actin served as loading control. **E**: Immunoblot of the DNA sensing pathway proteins MDA-5 (encoded by *Ifih1*) and P-TBK1 (Ser172) after pathway activation by cGAMP (4 µg/ml, 4 h) and co-treatment with PGE2 (5 µM, 1 d) in 781 NRF2 wt cells. Tubulin served as loading control. **F**: Real-time PCR of *Rsad2*, *Ifih1*, *Isg15*, *Ifit1* and *Tmem173* after pathway activation by cGAMP (4 µg/ml, 4 h) and co-treatment with PGE2 (5 µM, 1 d). Experiments were done three times and for C and F, two-way ANOVA with Sidak's multiple comparisons posttest was carried out (**p<0.01, ***p<0.001). Error bars represent SD.

The "Defense response to virus" was not enriched in the previous described RNA sequencing dataset from UACC-62 cells after NRF2 knockdown (Figure 19). Since it was previously reported, that the cGAS/STING pathway is frequently defect and cannot be activated by cytosolic DNA in human melanoma [163], cGAMP stimulation was investigated in three human melanoma cell lines. Accordingly, TBK1 phosphorylation was not seen in UACC-62 and M14 cells after STING pathway stimulation with cGAMP (Figure 42A). The human melanoma cell line SK-MEL-3 was sensitive towards STING

pathway activation by cGAMP (Figure 42A) [163]. The addition of PGE2 and NRF2 stabilization by tBHQ led to an accumulation of NRF2 protein levels (Figure 42B) and reduced *RSAD2*, *IFIH1*, *IFIT1* and *ISG15* gene expression (Figure 42C) in this cell line. To further evaluate the innate immune response genes in human melanomas, the patient survival in relation to *RSAD2* and *IFIH1* expression was analyzed. To do so, RNA expression data from the TCGA SKCM metastatic melanoma dataset was used. With a high *RSAD2* or *IFIH1* expression patient survival was significantly prolonged (Figure 42D, E), supporting the mouse model data of this thesis. With the Tumor IMmune Estimation Resource (TIMER) database, the influence of *RSAD2* and *IFIH1* on immune cell infiltration was analyzed. TIMER utilizes RNA expression data to identify immune infiltrates [164]. Both genes correlated positively with a higher infiltration of all immune cell types (Figure 42F, G). Taken together, the NRF2-dependent suppression of the innate immune response genes is at least partly facilitated by the induction of COX2 and associated higher PGE2 levels in murine and human melanoma cell lines.

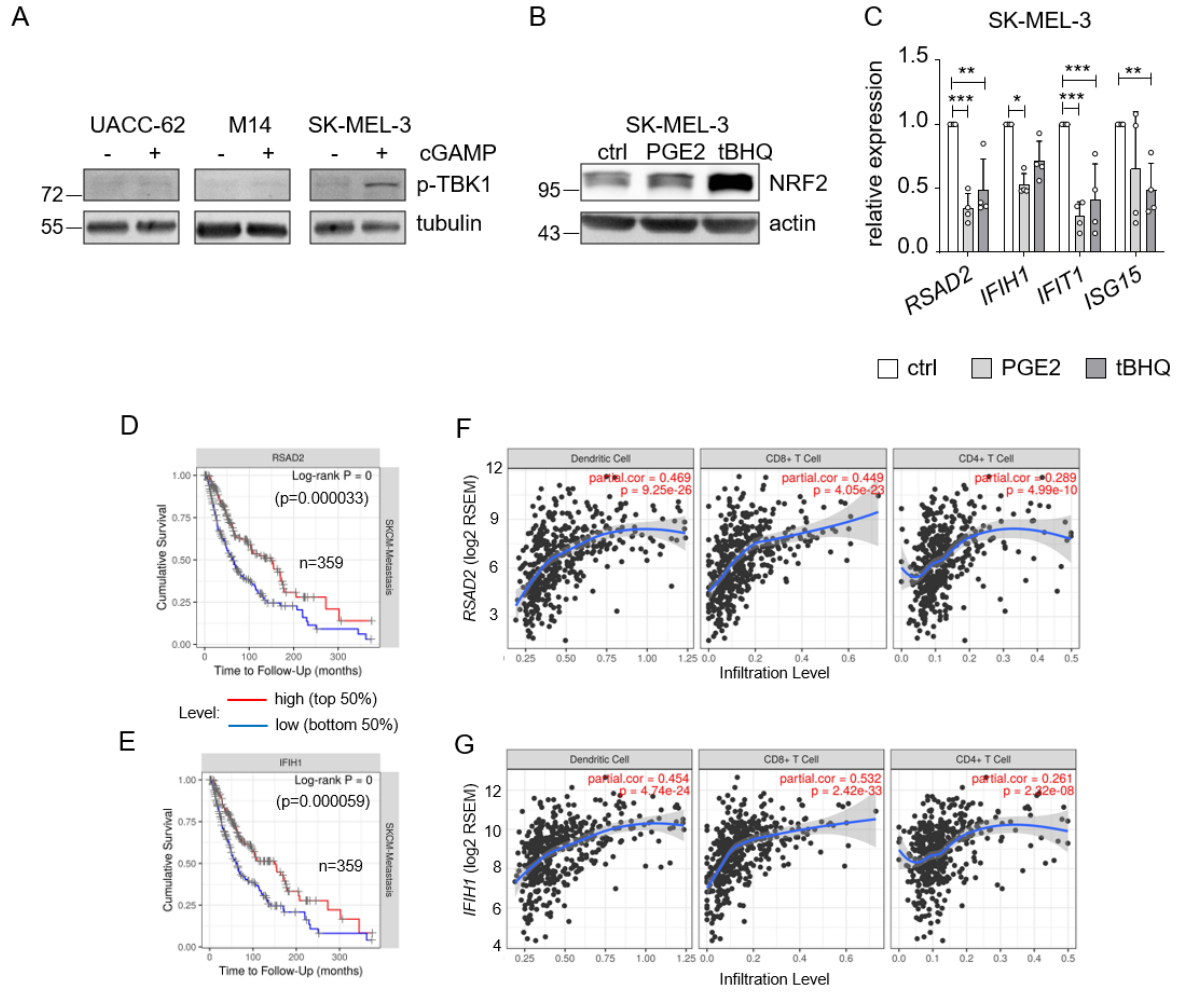

Figure 42 – Relevance of the innate immune response in human melanoma
A: Immunoblot of the p-TBK1 (Ser172) after pathway activation by cGAMP (4 µg/ml, 4 h) in indicated cell lines. Tubulin served as loading control. **B**: Immunoblot showing NRF2 activation in SK-MEL-3 cells after stimulation with PGE2 (5 µM) or tBHQ (10 µM) for 8 h. Actin served as loading control. **C**: Corresponding real-time PCR of *RSAD2*, *IFIH1*, *ISG15* and *IFIT1*. Two-way ANOVA with Tukey's multiple comparisons posttest was carried out (**p<0.01, ***p<0.001). Error bars represent SD. **D, E**: Kaplan-Meier plot of cumulative survival in SKCM metastatic melanomas with high or low RSAD2 (D) and IFIH1 expression (E) (https://cistrome.shinyapps.io/timer/). **F, G**: Infiltration of indicated immune cell populations into SKCM melanomas in relation to RSAD2 (F) and IFIH (G) expression, as determined by the Tumor Immune Estimation Resource TIMER (https://cistrome.shinyapps.io/timer/).

6. Discussion

6.1 The NRF2-dependent stress response in melanoma

In the first part of this thesis, a closer look was taken at the general role of NRF2 in human melanoma cells lines. It was hypothesized that melanoma cells might be more dependent on a stabile NRF2 expression, due to its predisposition towards higher ROS levels and the need for a balanced redox homeostasis. The cancer cell panel derived from different cancer entities verified that melanoma cells displayed one of the highest *NFE2L2* mRNA expression levels. Furthermore, the results confirm that the melanoma oncogenes $BRAF^{V600E}$ and $NRAS^{Q61K}$ are sufficient to activated NRF2 in melanocytes, which is in accordance with previous findings of DeNicola and colleagues [84]. In addition, the results of this thesis demonstrated that NRF2 secures the oxidative stress response in melanoma by increasing GSH levels and reducing intracellular ROS concentrations. The reduction of NRF2 expression inhibited cell proliferation and malignant features of the melanoma cells. Intriguingly, the RNA-Seq analysis of human melanoma cells with NRF2 knockdown revealed a highly deregulated transcriptional program, which goes beyond the differential expression of well-characterized NRF2 target genes.

Particularly, the expression of genes involved in DNA replication, cell cycle and DNA repair were highly reduced after NRF2 knockdown in UACC-62 melanoma cells. A strong reduction was seen in cyclin B1 (*CCNB1*) expression, a crucial cell cycle regulator. In line with this, NRF2 deficiency caused a strong decrease of *Ccnb1* in proliferating hepatocytes in a mouse model for liver regeneration [165]. Furthermore, the cell cycle regulator FOXM1 was highly reduced after NRF2 knockdown in the human melanoma cell line UACC-62. The transcription factor FOXM1 is a key factor for cell cycle progression and is overexpressed in diverse cancer entities, such as basal cell carcinoma and non-small cell lung cancer (NSCLC) [166, 167]. FOXM1 promotes cell cycle progression by promoting G2/M specific gene expression and regulates, for example, *CNNB1* and the polo like kinase 1 (*PLK1*), promoting G2/M transition [168]. Moreover, it was shown, that FOXM1 is involved in the DNA damage response by regulating homologous recombination via recombinase *RAD51*, *BRCA2* and *BRIP1* [169-171]. During homologous recombination RAD51 binds to the DNA and mediates homology recognition and strand exchange. The assembly of RAD51 on single stranded DNA is promoted by direct binding of BRCA1 and BRCA2. BRCA1 interacting protein 1 (BRIP1) associates with BRCA1 and further promotes homologous recombination of damaged DNA [169-171]. The cell cycle regulators *CCNB1* and *PLK1* as well as *RAD51*, *BRCA2* and *BRIP1* were strongly decreased in human UACC-62 melanoma cells after siRNA mediated NRF2 knockdown, this might partly be mediated by the strong FOXM1 reduction.

In melanoma, high FOXM1 expression is associated with a poorer overall survival and an increased cell proliferation [172] and FOXM1 inhibition induced senescence in keratinocytes [173]. In compliance with this, the NRF2 as well as the FOXM1 knockdown reduced cell proliferation and induced senescence to a similar extent.

There are two possibilities, how the NRF2 knockdown impairs cell cycle gene expression and FOXM1 reduction. The first one might be that NRF2 directly promotes FOXM1 expression, e.g. by transcriptional activation. This NRF2-dependent FOXM1 reduction in turn would cause the observed cell cycle arrest. However, this direct transcriptional regulation is rather unlikely since the ChIP-Seq analysis of NRF2 did not reveal NRF2 occupancy at the promoter site of FOXM1.

The second possibility might be, that NRF2 regulates cell proliferation independently of FOXM1. In general, proliferating cells can exit the cell cycle and reside in a quiescent cell state, these quiescent cells do not express genes associated with cell cycle progression, such as G2/M specific genes [174, 175]. Since the expression of FOXM1 is dependent on a functional cell cycle progression [176], the FOXM1 reduction might be an secondary effect arising after a cell cycle arrest caused by NRF2 silencing. The theory that NRF2 promotes cell cycle progression is supported by the network analyses of Malhotra, et. al, who first reported that cell cycle regulators and proliferative genes are direct transcriptional targets of NRF2 under basal conditions [15]. In contrast to the ChIP-Seq analysis of this thesis, they compared control mouse embryonal fibroblasts (MEF) and MEFs with genomic NRF2 knockout [177]. Furthermore Mitsuishi and colleagues demonstrated that NRF2 promotes cell proliferation by facilitating metabolic reprogramming [92]. In proliferating cells, such as the KEAP1-mutant NSCLC cell line, A549, NRF2 redirects glucose and glutamine towards the purine nucleotide synthesis and away from the citric acid cycle (TCA) and the GSH synthesis [92]. This promotion of cellular metabolic activities was beneficial for proliferation and survival and was further reinforced by proliferative signals [92]. Moreover, NRF2-deficiency causes a glutathione-dependent growth arrest, which could be rescued by glutathione supplementation in primary epithelial cultures [178]. Thus, knockdown of NRF2 might lead to cell cycle arrest due to metabolic reprogramming, and this in turn reduces expression of FOXM1 and cell cycle related genes as a secondary effect.

For further distinction of those two possibilities, rescue experiments with artificial FOXM1 overexpression were conducted. However, exogenous FOXM1 expression was not sufficient to rescue G2/M specific gene expression (data not shown). This supports the hypothesis, that FOXM1 is not the primary factor for the growth arrest after NRF2 knockdown.

The observation that NRF2 enables metabolic reprogramming was supported by Sayin and colleagues. They discovered a metabolic bottleneck created by NRF2 activation in mouse and human KEAP1-mutant KRAS-driven lung adenocarcinoma cell lines. This NRF2 dependent metabolic bottleneck redirects exogenous glutamine into antioxidant programs, thus limiting availability for other biosynthetic reactions, such as the TCA [179]. In line with this, the transcriptomic analysis after NRF2 knockdown in UACC-62

melanoma cell lines showed an increase of genes involved in oxidative phosphorylation and the TCA. These findings suggest that basal NRF2 might promote metabolic reprogramming also in melanoma.
The discrepancies of the human and murine RNA-Seq analysis, especially regarding the cell cycle regulation, might be explained by the different approaches to reduce NRF2 expression levels. In the human cell lines, transient siRNA transfection was used to knockdown NRF2. In the mouse cell line NRF2 was knocked out by the CRISPR/Cas9 approach. The later included clonal selection for NRF2 knockout clones, which simultaneously selected for proliferating cells. Thus, the murine NRF2 knockout cell line might have developed adaption mechanisms to overcome the reduced cell proliferation.

To verify, if the regulated transcripts, identified after NRF2 knockdown, are direct NRF2 transcriptional target genes, ChIP with downstream next-generation sequencing was conducted. Unexpectedly, the genome-wide binding analysis of NRF2 revealed that the majority of NRF2 peaks were in intronic and intergenic regions and to a lesser extent at promoter sites of nearby genes. Even in well-characterized NRF2 target genes, the transcription factor binding sites (TFBS) are located distal from the TSS (up to 10 kb). These findings are in accordance with previously conducted global transcription profiling of NRF2 binding sites performed in MEFS, lymphoid, hepatoma and KEAP1-mutant A549 NSCLC cells [151, 177, 180, 181]. Although diverse studies showed this intronic and intergenic distribution of NRF2 binding sites, the exact mechanisms how NRF2 regulates transcription on those sites is not investigated so far [151, 177, 180, 181]. Thus, it should be evaluated, if the intergenic NRF2 binding sites are found at other *cis*-regulatory elements, such as enhancers or superenhancers. For this, the NRF2 peaks could be mapped to epigenetic features, such as methylation and acetylation, to distinguish between promoters and enhancers. For example, on promoters, histone H3 is trimethylated on lysine residue 4 (H3K4me3) and monomethylated on enhancers (H3K4me1) [182]. Since, no ChIP-Seq data of this epigenetic marks were available for UACC-62 melanoma cells, this remains to be investigated in future studies.

Interestingly, the global transcription profile of NRF2 resembles the profile of the transcription factor activator protein 1 (AP-1) [183]. The AP-1 is a heterodimeric complex composed of transcription factors belonging to the bZIP transcription family. It consists of members of the JUN, FOS and ATF/CREB, and MAF families and is activated by extracellular stimuli, such as cytokines, stressors, and growth factors. AP-1 is involved in regulation of various cellular processes, such as cell proliferation, migration, and invasion [184]. The AP-1 complex mainly recognizes either 12-O-tetradecanoylphorbol-13-acetate (TPA) response elements (5′-TGAG/CTCA-3′) or cAMP response elements (CRE, 5′-TGACGTCA-3′) [185]. For AP-1 binding sites it is further known that they bind to distal enhancers together with YAP/TAZ/TEAD [186]. This complex forms chromatin loops to target promoters and controls cell cycle progression, which promotes oncogenic growth [186].

Previous studies showed, that some binding sites of NRF2 and AP-1 overlap [187]. Furthermore, the analysis of TFBS overrepresentation using SeqMotif, verified that the enriched binding motifs of the NRF2 ChIP-Seq were associated with proteins belonging to the AP-1 complex (Appendix Table 23). Furthermore, these sequence motifs include the ARE motif, which indicates the possibility of NRF2 interaction with these proteins. It was previously demonstrated, that NRF2 and JUN family proteins can interact and activate antioxidant genes [188]. Recent bioinformatic analysis of binding data sets revealed, that there are overlapping target genes for NRF2 and ATF4 [189]. However, the cytoprotective genes are mostly activated by a NRF2-MAFG heterodimer after stress induction [177, 180].
To validate if NRF2 might interact with the AP-1 transcription complex in melanoma, comparisons of genome-wide transcription factor binding sites in combination with analyses of NRF2 binding partners should be conducted.
Notably, the newly identified genes regulated by NRF2, such as *PTGS2*, *MITF* and *EGFR*, as described in this thesis did not show NRF2 enrichment at their TSS. This clearly indicates that NRF2 regulates gene expression also through indirect mechanisms to a larger extent. Olagnier et. al. demonstrated that NRF2 post-transcriptionally controls *TMEM173* expression levels by regulating its mRNA stability [153]. Thus, NRF2 might not solely regulate target gene expression by direct TSS binding, but also through binding at other *cis*-regulatory elements or other post-transcriptional regulatory mechanisms. Furthermore, the NRF2-dependent stress response might not be exclusively regulated by NRF2-sMAFs heterodimers, but also in accordance with other stress-related transcription factors, e.g. those belonging to the AP-1 complex.

6.2 NRF2 stabilizes melanoma dedifferentiation

The investigations of the role of NRF2 in melanoma revealed that NRF2 suppresses the activity of MITF, the master regulator of the melanocytic lineage. MITF is a transcription factor of the basic helix-loop helix leucine zipper family and binds to E boxes (5'-CACGTG-3') and M boxes (5'-TCATGTG-3'). Theses motifs are mostly found in genes belonging to pigmentation processes [190]. Notably, MITF also upregulates the transcriptional co-activator peroxisome proliferator-activated receptor-gamma coactivator 1 alpha (PGC-1α), which is a key activator for the mitochondrial biogenesis [78, 79]. Besides regulation of the mitochondrial biogenesis, reconstitution of PGC-1α suppressed melanoma metastasis [191]. After reduction of the NRF2 expression levels in the human UACC-62 melanoma cells, PGC-1α was highly upregulated (Figure 19H) just like the pigmentation-related genes *TYR*, *DCT* and *MLANA* (Figure 27C). Thus, by suppression of the MITF activity, NRF2 stabilizes the dedifferentiated, less invasive cell state in melanoma cells. In line with this, it was previously shown that NRF2 facilitates dedifferentiation in melanocytes, as the overexpression of NRF2 reduced pigmentation markers such as TYR in normal human melanocytes [192].

Cutaneous melanoma is one of the most heterogenous cancer entities and thus a good model for studying cancer cell population heterogeneity. Analysis of the different cancer cell subpopulations in melanoma revealed specific phenotypic states with defined gene expression profiles [140]. The simplest model distinguishes between two cellular phenotypes, the proliferative and the invasive phenotype. When melanoma cells become metastatic, they have to change their phenotypic state, which is called the phenotypic-switch [140]. Recent studies revealed, that in melanoma the master regulator of the melanocytic lineage MITF is differentially expressed in these phenotypic states [193]. Besides the positive effect of MITF on pigmentation, diverse studies have shown that the MITF levels are instrumental in regulating DNA damage repair, metabolism, lysosome biogenesis, proliferation, invasion, and melanoma differentiation [194]. Melanoma cells expressing low levels of MITF ($MITF^{low}$) are in a dedifferentiated, slow-cycling, invasive cell state. A moderate increase of MITF expression promotes proliferation and inhibits invasion. And further increase of MITF ($MITF^{high}$) expression causes melanoma differentiation [138, 195]. This model is called the MITF rheostat model [195]. Key drivers for melanoma dedifferentiation and MITF activity shifts are intra- or intercellular stress- and inflammation-inducing signals. In melanoma different stress-induced transcription factors are responsible for MITF suppression and subsequent dedifferentiation.
For example, the pro-inflammatory cytokine, TNFα, represses MITF expression by induction of the AP-1 component JUN [142]. When melanomas are driven into dedifferentiation, e.g. by cytokines such as TNFα, they can more easily escape T cell recognition due to reduction of melanocytic antigens [196]. Furthermore, the MITF target genes *TYR*, *DCT* and *MLANA* are crucial for an efficient T cell response, since they serve as melanoma antigens [197, 198].

Moreover, dedifferentiation is induced after amino acid starvation by activation of the transcription factor ATF4, which inhibits MITF transcription [199, 200]. ATF4 is the key transcriptional mediator of the integrated stress response, activated after amino acid starvation, viral infection, heme deprivation and endoplasmic reticulum (ER) stress [201]. ATF4 has pro-tumorigenic effects by promoting cell proliferation, migration and drug resistances in various cancer entities, such as malignant gliomas or colon cancer cells [202, 203]. ATF4 further activates the expression of the receptor tyrosine kinase, AXL in melanoma [199].
The dedifferentiated state of melanoma cells is often associated with a high expression of RTKs, such as AXL and EGFR, which in turn are inversely correlated with MITF expression [146, 149].

In general, the differentiated melanoma subtype is more susceptible to current therapeutic approaches and targeting the dedifferentiated subpopulation might improve the efficacy of melanoma therapy. Smith, et. al. showed that upon BRAF inhibition in melanoma, endothelin 1 (EDN1) is induced and facilitates drug resistance. Targeting of EDN1 signaling improved response to BRAF inhibition by suppression of AXL-high subpopulations [204]. In addition, Tsoi, et. al discovered that dedifferentiated

melanomas are more sensitive to ferroptosis induction. Thus, co-targeting of ferroptosis might increase the efficiency of melanoma therapy [149]. Therefore, a high expression of RTKs contributes to resistances towards targeted therapy with BRAF/MEK inhibitors [145, 146, 149, 204].

I could observe that NRF2 positively regulated EGFR expression in the human UACC-62 melanoma cell lines. Thus, NRF2 stabilizes the dedifferentiated phenotype not only by repression of MITF activity but by simultaneously induction of EGFR expression.
In lung cancer NRF2 activation by KEAP1 loss-of-function mutations enhances resistances towards EGFR, BRAF, MEK and ALK inhibitors and is significantly associated with a T cell exclusion program [205-207]. Furthermore, EGFR-mutant lung cancers poorly respond to immune checkpoint inhibitors and display an uninflamed microenvironment [208, 209]. This seems to be facilitated by EGFR, because the addition of EGFR inhibitors enhances the inflammatory T cell recruitment [210]. In melanoma high levels of EGFR, for example induced by NRF2, might be associated with immune checkpoint inhibitor resistances. However, this hypothesis remains to be evaluated.
Altogether, these results suggest that suppression of MITF by NRF2 facilitates the reduced immunogenicity of melanomas, caused by loss of melanoma-specific antigens. Consequently, NRF2 enables drug resistances and the immune escape by promoting the dedifferentiated cell state of melanoma.

6.3 NRF2 promotes synthesis of the immune-suppressive PGE2 and limits the innate immune response

By RNA sequencing, *PTGS2* was identified as the gene with the most prominent repression after NRF2 knockdown. *PTGS2* encodes for the inducible cyclooxygenase COX2. Cyclooxygenases catalyze the conversion of arachidonic acid into PGH2, the first step of the PGE2 synthesis. In contrast to the constitutively expressed COX1 protein, the inducible COX2 protein is an immediate-early response gene activated at inflammation sites and during tumor development. In tumors, COX2 promotes growth, angiogenesis, and tissue invasion [211-213].
NRF2 induced COX2 in a stress- and cytokine-dependent manner. Moreover, the basal COX2 levels were dependent on NRF2 expression. The NRF2-induced and basal COX2 expression was almost completely abolished in NRF2-knockout cell lines and was also reduced by artificial MITF expression. These results suggest that NRF2 stabilizes COX2 expression under basal conditions. In addition, NRF2 induces COX2 expression at least partly via MITF suppression, in melanoma exposed to a stressful microenvironment. In absence of NRF2, TNFα-dependent *PTGS2* induction was strongly reduced, which revealed an unprecedented role of NRF2 in promoting cytokine-mediated tumor-protective effects. This fits with the previous discovery that dedifferentiated melanoma cells displayed a higher level of inflammatory signaling and a higher response to

cytokines [142]. Recent publications show, that TNFα activates the NF-κB signaling pathway, which induces COX2 expression as well as *NFE2L2* gene expression [96, 214, 215]. Thus, the findings of this thesis further indicate, that NRF2 is necessary to activate COX2 expression downstream of the NF-κB signaling pathway.

The exact mechanism how NRF2 controls COX2 induction on chromatin level could not be completely resolved, since no NRF2 binding site on the *PTGS2* promoter site was observed. However, an ATF4 binding site on the *PTGS2* promoter in 501mel melanoma cells was seen. The transcription factor ATF4 was responsible for regulation of COX2 expression in melanoma, since artificial NRF2 overexpression was unable to induce COX2 in ATF4 knockout cell lines. More precisely, the robust upregulation of *PTGS2* was only possible in presence of NRF2 and ATF4 together. A link between ATF4 and COX2 was previously observed in kidneys driven into autophagy. In kidneys driven into autophagy by cadmium-induced or lupus nephritis-induced kidney injury, it was shown, that COX2 induction was dependent on ER-stress mediated ATF4 activation [216, 217]. DeNicola, et.al further demonstrated, that NRF2 mediates gene expression of serine/glycine biosynthesis enzymes via ATF4 regulation in NSCLC [137]. Thus, ATF4 is the responsible transcription factor for *PTGS2* induction downstream of NRF2 and the joint activation of both transcription factors is necessary to induce *PTGS2* expression. Referring to the *PTGS2* suppression by MITF, it is likely that ATF4 and MITF interact to control COX2 induction. In accordance with this, it was recently reported that MITF negatively impacts ATF4 expression by increasing the ratio between monosaturated and saturated fatty acids [218]. This suppresses inflammation and promotes the differentiated cell state in melanoma [218]. As described above, ATF4 itself can suppress MITF expression, thus both transcription factors are connected by a mutually negative feedback loop that also affects *PTGS2* expression.
Intriguingly, NRF2 was described to trigger the expression of phospholipase A2 protein PRDX6, which catalyzes the release of arachidonic acid and therefore acts upstream of COX2 [219], demonstrating that activation of NRF2 might enable the generation of immune-relevant small lipid mediators on several levels.

The synthesis of the prostanoid lipid PGE2 is dependent on COX1 and COX2 expression and the results of this thesis showed that secreted PGE2 levels were clearly reduced in NRF2 knockout cells and resected tumors. In melanoma and other cancer entities, high tumor derived PGE2 levels are associated with an immune-evasive microenvironment. PGE2 limits T cell activation by inhibition of T cell receptor signaling [220]. Moreover, it was shown that in melanoma, PGE2 inhibits recruitment of natural killer cells as well as dendritic cells, impairing tumor recognition by the immune system [135]. Zelenay and colleagues revealed a COX2-dependent inflammation signature, which drives tumor immune-evasion and progression of melanomas [136]. Their study demonstrated that in COX-proficient cells PGE2 is the key suppressor of type I interferon (IFN) signaling and T cell mediated tumor control. The genetic ablation of *Ptgs2* or the simultaneous

knockout of *Ptgs1* and *Ptgs2* restored tumor control by the innate as well as the adaptive immune system [136].
In line with this, the tumor engraftment and development of murine *Nfe2l2*$^{-/-}$ cells was highly impaired in the immune-competent syngeneic melanoma mouse model and the transcriptomic analysis of available tumors revealed high upregulation of immune response pathways, especially of the "Defense response to virus" gene set, which is part of the innate immune response and activates type I IFN signaling.

Type I IFNs are activated as an antiviral immune response after sensing of cytosolic nucleic acids. As part of the innate immune response the receptors MDA-5 and RIG-1 recognize dsRNA, emerging from RNA viruses or transcribed from dsDNA by the RNA polymerase III. Another sensor of cytosolic DNA is cyclic GMP-AMP synthase (cGAS). After DNA sensing by cGAS, stimulator of interferon genes (STING) is activated via synthesized cyclic GMP-AMP (2'-5'-cGAMP) [221]. Importantly, cytosolic dsDNA can arise from pathogens, but also from the host cell. Damaged or apoptotic cells can release parts of their nuclear and mitochondrial DNA. Furthermore, cancer cells are prone to release of DNA due to their chromosome instability. After cytosolic nucleic acid sensing the TBK1-IRF3 axis is activated to release type I IFN and activates the host immune system. Thus, the host type I IFN as well as an activated innate immune response have been linked to efficient cancer therapies [222]. The results of this thesis support the role of PGE2 in alleviating the induction of the innate immune response, as reduced PGE2 levels correlate with a strong "Interferon alpha response" and "Defense response in virus" expression signature. *In vitro*, both NRF2 as well as PGE2 suppressed these expression signatures, showing that this mechanism is also active in a cancer-cell autonomous manner, without the influence from the tumor microenvironment.
In summary, this thesis identified the NRF2-ATF4 axis as a major regulator of the basal as well as stress induced COX2 expression levels. By stabilizing COX2, NRF2 enhances PGE2 and alleviates the innate immune response.

In compliance with these results, a link between NRF2 and the innate immune response was recently described. Olagnier and colleagues demonstrated that NRF2 suppresses cytosolic nucleic acid sensing by negatively regulating the adaptor protein STING in human cells [153]. Furthermore, the same group discovered an increased immunity against herpes simplex virus-2 (HSV-2) infection in *Nfe2l2*$^{-/-}$ mice [160], due to an enhanced type I IFN signaling.
In melanoma high intrinsic STING activity is associated with an increased antigenicity, which renders the tumor cells more susceptible to T cell dependent lysis [223]. However, many melanoma cell lines display inactivation of the cGAS/STING signaling pathway, causing tumor immune evasion [163]. Accordingly, in human melanomas high expression of *RSAD2* or *IFIH1*, which are expressed in response to cGAS/STING activation, was associated with higher infiltration of immune cells, like dendritic cells, CD4+ and CD8+ T cells (Figure 41F,G). In line with this only the NRF2 knockout tumors showed signs of T cell infiltration, likely promoted by the enhanced innate immune

response. Furthermore, the suppression of the cGAS/STING signaling pathway in human melanoma was confirmed in this thesis, where the human UACC-62 cells cGAMP failed to phosphorylate TBK1.
This might be one reason for the fact that the transcriptomic profiling of UACC-62 cells after siRNA mediated NRF2 knockdown did not reveal regulation of the innate immune response genes. Another rationale might be that the UACC-62 cell line is a long-established melanoma cell line in contrast to the more naïve 781 murine cells. This naïve cell state might be more sensitive to inflammation and immune responses. Without the pressure from the tumor microenvironment, the long-established melanoma cell lines might have lost some of the immune-related gene expressions, such as major histocompatibility complex class (MHC) I molecules on their cell surfaces.
To further investigate the NRF2 effect on the immune response, transcriptomic profiling should be done in the human SK-MEL-3 cell line, which is able to respond to cGAS/STING activator and where innate immune response gene expression was strongly reduced after NRF2 activation by tBHQ or PGE2 supplementation. Concludingly, it appears that the inhibitory effect of NRF2 on innate immune response only occurs in human melanoma cells with a functional STING signaling pathway.

Notably, reduced tumor immunogenicity can also be caused by diminished antigen presentation of tumor cells. Defects in the antigen processing or the major histocompatibility complex (MHC) I assembly lead to loss of T cell-mediated control [224]. Jerby-Arnon, et. al. further discovered a T cell exclusion program, which includes repression of antigen processing and presentation genes, leading to immune checkpoint inhibitor resistances [225]. In accordance with this, diverse genes involved in antigen processing and trafficking as well as MHC I assembly and expression were repressed by NRF2 in this study. In addition, the NRF2 knockout cells showed higher levels of STAT1 phosphorylation. It was previously reported, that the assembly and the expression of MHC I is regulated by an IFN/STAT1 signaling pathway and an inhibition of STAT1 in head and neck cancer cells facilitates tumor immune escape [226]. Thus, the expression of antigen processing and presentation genes is tightly linked to type I IFN signaling. Thus, both gene sets “interferon alpha response”, resembling type I IFN signaling, and “Antigen processing and presentation” involve overlapping genes. In support of this, the NRF2 knockout displayed activated type I IFN signaling, which favors STAT1 phosphorylation and consequently an increase of antigen processing and presentation genes, which enables immune control.
The upregulation of genes involved in “Antigen presentation and processing” and “Defense response to virus” was more pronounced in the resected tumors than in the cell culture. This supports the crucial function of an immune-competent tumor microenvironment to assess immune-related gene expression.

For the closer examination of the immune-suppressive effects of NRF2, further experiments with immune-competent and immune-deficient mice could be conducted.

Moreover, with different mouse models it might be distinguished between the effects of tumor intrinsic NRF2 and effects originating from NRF2 in the TME or from the immune cells. For the evaluation of the tumor-specific immune-suppressive effect of NRF2, the murine NRF2 knockout cells could be injected into immune-deficient mice. Here, different mice models are available to study the distinct components of the immune system. For example, nude mice are homozygous for *Foxn1*^{nu}, these mice lack hair follicles and the thymus, making them T cell deficient [227]. The so called Scid mice are homozygous for the *Prkdc*^{scid} mutation and are both T and B cell deficient, but display a high natural killer (NK) cell activity [228]. Similarly, Rag-deficient mice are also B and T cell deficient, with a functional innate immune response [229]. To simultaneously deplete the innate immune response, these mice strains can be crossed with the NOD mice strain, which is deficient for NK cells, macrophages, antigen presenting cells (APC) and complement activity [230]. Depending on the genomic mice background and the tumor growth of the NRF2 deficient murine cell lines, the immune-suppressive effect of NRF2 could be assigned to the specific type of immune cells, such as NK, T or B cells. To validate effects of NRF2 in the TME, tumor growth could be evaluated in a conventional *Nfe2l2*$^{-/-}$ mouse model by injection of murine NRF2 wildtype cells. It was reported, that NRF2 suppresses pro-inflammatory signaling also in macrophages [231], thus a NRF2 deficient tumor microenvironment might promote melanoma growth, like previously observed with the murine B16 melanoma cell line [232].
Furthermore, to assess the role of NRF2 in individual type of immune cells, conditional NRF2 knockout models could be generated. For the generation of NRF2 conditional knockout mouse models, the *Nfe2l2* gene must be flanked by loxP sites and mice could be crossed with mice carrying the Cre recombinase under a specific immune cell lineage promoter. For T cell specific loss of NRF2 the *Foxp3*-Cre knock-in mice could be used [233] and for B cell conditional knockout of NRF2, the *Cd19*-Cre knock-in mice [234] could be utilized. To generate a NRF2 conditional knockout in both, the T and B cell lineage, mice with expression of Cre under the *CD2* promoter [235] should be used. To delete NRF2 in the myeloid cell lineage, such as in monocytes and macrophages, the Lyz2-Cre mouse [236] is a suitable model and for specific NRF2 deletion in NK cells, mice with a NKp46-Cre knock-in [237] could be evaluated.
In summary, tumor specific NRF2 reduces tumor immunogenicity by suppressing the antigenicity of melanoma and a pro-inflammatory signaling. This NRF2-dependent immune-suppression is partly mediated by PGE2, which suppresses the innate immune response.

6.4 Implications for cancer therapy

In lung adenocarcinoma (LUAD) NRF2 is activated by KEAP1 mutations, which makes it a good model for further studying NRF2-dependent immune-suppressive functions. In support of the results described in this thesis, the expression of the innate immune response genes *RSAD2*, *IFIH1* and *TMEM173* are elevated in KEAP1-mutant lung cancer cells (Figure 42A). Furthermore, KEAP1-mutant LUAD showed higher levels of infiltration of dendritic cells, CD4+ and CD8+ T cells, which was determined by TIMER analysis (Figure 42B). TIMER estimates tumor immune infiltrates from RNA expression data [164]. In line with this, it was previously reported that KEAP1-mutant LUAD is significantly associated with a T cell exclusion program, which causes immunotherapy resistances [207]. Thus, there are indications for an immune-suppressive role of NRF2 in various tumor entities.

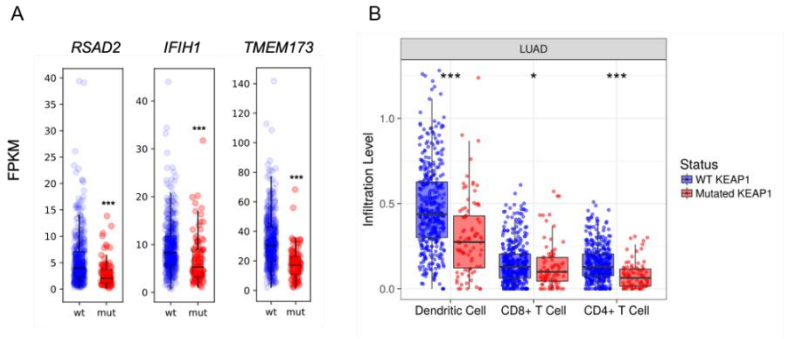

Figure 43 – Innate immune response in KEAP1-mutant lung adenocarcinoma
A: RNA expression of *RSAD2*, *IFIH1* and *TMEM173* in TCGA lung adenocarcinoma (TCGA, PanCancer Atlas), divided into KEAP1 wildtype and KEAP1 mutant tumors. Data were downloaded from the GDC portal (https://portal.gdc.cancer.gov). In case of IFIH1, one outlier was omitted from the plot, but was included into the boxplot calculation. **B**: Immune cell infiltration into KEAP1-mutant and KEAP1-wildtype lung adenocarcinomas (LUAD) as determined by the Tumor ImmuneEstimation Resource TIMER (https://cistrome.shinyapps.io/timer/). (The plots were generated by A. Marquardt, Comprehensive Cancer Center Mainfranken, Würzburg)

A recent study addressed the impact of NRF2 on melanoma immunotherapy. Zhu, et. al. demonstrated that NRF2 enhanced the expression of the immune checkpoint PD-L1 after UV-A radiation in melanocytes. Subsequently, they showed, that melanoma cells with shRNA mediated NRF2 knockdown had an enhanced response towards anti-PD-1 immunotherapy [112].
Therefore, it is likely that inhibitors targeting NRF2 would synergize with immune checkpoint inhibition in different tumor entities. Contrary to the availability of efficient NRF2 activators, currently no specific NRF2 inhibitors are accessible [86]. Thus, it might be more feasible to target the NRF2 downstream markers like those revealed in this thesis.
For example, pharmacological inhibition of COX2 showed promise in preclinical studies to synergize with immune checkpoint inhibition in melanoma and pancreatic cancer [136, 238]. Moreover, COX2 inhibitors are already approved as anti-inflammatory drugs, such as aspirin and ibuprofen. The effect of aspirin on immune checkpoint inhibition with PD-1 and CTLA-4 monoclonal antibodies in melanoma is currently evaluated in a

clinical phase II trial [239] and a similar clinical phase II trial is conducted in colorectal cancer [240].
Moreover, the results of this thesis supported the importance of the type I IFN response in tumor control and that activation of STING might synergize with immune checkpoint inhibition. The Achilles heel of immunotherapy seems to be a cold tumor microenvironment, which impairs T cell infiltration. Pharmacological activation of the host STING signaling pathway triggered T cell-mediated tumor regression by promoting T cell infiltration, thus turning immune-cold into immune-hot tumors. Activation of STING showed promising antitumor immunity and enhanced efficiency of immune checkpoint inhibition in melanoma, breast, and colon cancer *in vitro* and *in* vivo [241, 242]. Specific STING agonists have already been developed and are currently investigated in clinical trials in patients with advanced solid tumors and lymphomas. The effect of STING agonist on antitumor immunity is examined either alone or in combination with CTLA-4 or PD-1 immune checkpoint inhibitors [243-245].

A recent preclinical study in melanoma further confirmed that boosting the innate immune response helps to cope with intrinsic T cell resistance [246]. Such and colleagues showed that patient-derived melanoma cells with suppression of the tumor-intrinsic HLA class I (HLA I = human isoform of MHC I) antigen processing and presentation machinery (HLA-I APM) escaped CD8+ T cell recognition [246]. The activation of the RNA sensor RIG-I, part of the innate immune response, triggered re-expression of the HLA-I APM and facilitated T cell recognition and tumor regression. Furthermore, in an anti–PD-1 non-responder melanoma model, activation of RIG-1 restored HLA-1 APM and synergized with immune checkpoint blockage with the anti-PD1 inhibitor [246].
In summary, targeting the immune-suppressive effects of NRF2 has the potential to synergize with immune checkpoint inhibition and might overcome initial or acquired resistances towards immune checkpoint blockage.

7. Conclusion

In conclusion, the transcription factor NRF2 is activated in melanoma by oncogenic signaling, oxidative stress or cytokines, emerging cell-autonomously and from the tumor microenvironment. NRF2 depletion impaired cell cycle progression and resulted in reduced tumor growth. Besides the regulation of antioxidant effectors, NRF2 was responsible for maintaining and inducing the immune-modulator COX2. *PTGS2*, the gene encoding COX2, was not a direct transcriptional target of NRF2, but was induced in an ATF4-dependent manner downstream of NRF2. COX2 was robustly expressed only in presence of both transcription factors. COX2 mediates the generation of immune-relevant lipid mediators such as prostaglandin E2 (PGE2). High PGE2 levels were described to favor reduced T cell activation and tumor immune evasion. Furthermore, by suppression of MITF activity, NRF2 decreased melanoma immunogenicity by stabilizing the dedifferentiated melanoma phenotype, which is associated with reduction of melanoma-specific antigen presentation. In accordance with these potentially immune-suppressive features of NRF2, NRF2-deficient melanoma cells had a significantly longer tumor free survival compared to NRF2-proficient cells in an immunocompetent syngeneic melanoma mouse model. Next to the reduction of COX2, PGE2 and the induction of MITF, NRF2-ko melanomas had a strong activation of innate immune response genes, which correlated with immune cell infiltration in human melanoma datasets and NRF2 stabilization or PGE2 supplementation suppressed the innate immune response *in vitro*.

Therefore, NRF2 enables tumor immune evasion, by reducing the antigenicity and limiting the innate immune response of melanomas, leading to an immune-cold tumor microenvironment. Thus, NRF2 highly contributes to tumor maintenance, progression, and immune control in cutaneous melanoma. The results of this thesis are summarized in Figure 44.

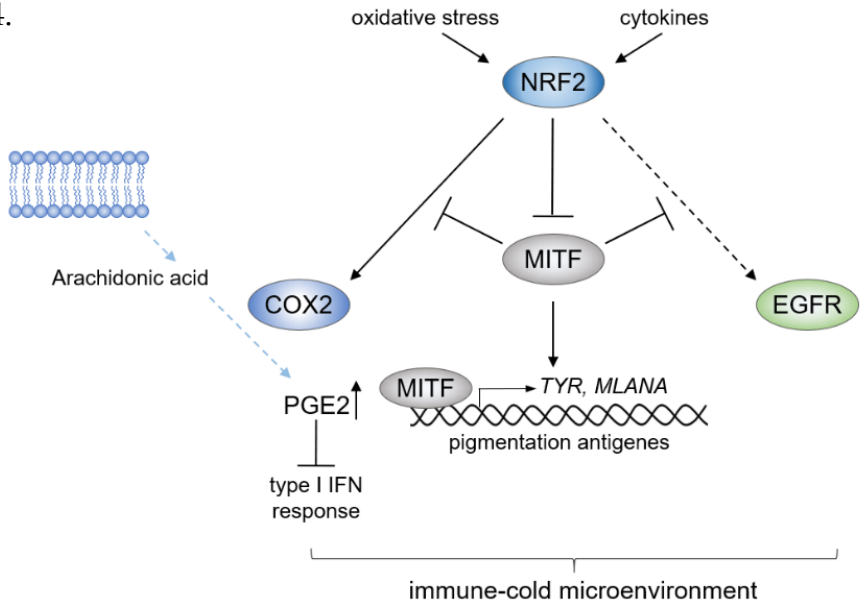

Figure 44 – NRF2 serves as stress-inducible hub for COX2 induction
Schematic overview of findings after NRF2 inhibition and activation in melanoma cell lines. In Brief, NRF2 is activated by intrinsic and extrinsic stress triggers. This activation enables melanoma dedifferentiation by suppression of MITF and EGFR stabilization.NRF2-dependent COX2 induction further favors an immune-cold tumor environment.

8. Bibliography

1. Apalla, Z, Lallas, A, Sotiriou, E, et al., (2017) Epidemiological trends in skin cancer. *Dermatology Practical & Conceptual*. **7**(2). DOI: 10.5826/dpc.0702a01.
2. Cui, R, Widlund, HR, Feige, E, et al., (2007) Central Role of p53 in the Suntan Response and Pathologic Hyperpigmentation. *Cell*. **128**(5): p. 853-864. DOI: 10.1016/j.cell.2006.12.045.
3. Neves, SR, Ram, PT, and Iyengar, R, (2002) G protein pathways. *Science*. **296**(5573): p. 1636-9. DOI: 10.1126/science.1071550.
4. Bertolotto, C, Abbe, P, Hemesath, TJ, et al., (1998) Microphthalmia gene product as a signal transducer in cAMP-induced differentiation of melanocytes. *J Cell Biol*. **142**(3): p. 827-35. DOI: 10.1083/jcb.142.3.827.
5. Valverde, P, Healy, E, Jackson, I, et al., (1995) Variants of the melanocyte-stimulating hormone receptor gene are associated with red hair and fair skin in humans. *Nat Genet*. **11**(3): p. 328-30. DOI: 10.1038/ng1195-328.
6. Abdel-Malek, ZA, Knittel, J, Kadekaro, AL, et al., (2008) The melanocortin 1 receptor and the UV response of human melanocytes--a shift in paradigm. *Photochem Photobiol*. **84**(2): p. 501-8. DOI: 10.1111/j.1751-1097.2008.00294.x.
7. Meierjohann, S, (2014) Oxidative stress in melanocyte senescence and melanoma transformation. *Eur J Cell Biol*. **93**(1-2): p. 36-41. DOI: 10.1016/j.ejcb.2013.11.005.
8. Yasumoto, K, Yokoyama, K, Shibata, K, et al., (1994) Microphthalmia-associated transcription factor as a regulator for melanocyte-specific transcription of the human tyrosinase gene. *Mol Cell Biol*. **14**(12): p. 8058-70. DOI: 10.1128/mcb.14.12.8058.
9. Yasumoto, K, Mahalingam, H, Suzuki, H, et al., (1995) Transcriptional activation of the melanocyte-specific genes by the human homolog of the mouse Microphthalmia protein. *J Biochem*. **118**(5): p. 874-81. DOI: 10.1093/jb/118.5.874.
10. Plettenberg, A, Ballaun, C, Pammer, J, et al., (1995) Human melanocytes and melanoma cells constitutively express the Bcl-2 proto-oncogene in situ and in cell culture. *Am J Pathol*. **146**(3): p. 651-9.
11. Quevedo, WC, Szabo, G, and Virks, J, (1969) Influence of Age and UV on the Populations of Dopa-positive Melanocytes in Human Skin. *Journal of Investigative Dermatology*. **52**(3): p. 287-290. DOI: 10.1038/jid.1969.45.
12. Clark, WH, Jr., Elder, DE, Guerry, Dt, et al., (1984) A study of tumor progression: the precursor lesions of superficial spreading and nodular melanoma. *Hum Pathol*. **15**(12): p. 1147-65.
13. Pollock, PM, Harper, UL, Hansen, KS, et al., (2003) High frequency of BRAF mutations in nevi. *Nat Genet*. **33**(1): p. 19-20. DOI: 10.1038/ng1054.
14. Shain, AH, Yeh, I, Kovalyshyn, I, et al., (2015) The Genetic Evolution of Melanoma from Precursor Lesions. *N Engl J Med*. **373**(20): p. 1926-36. DOI: 10.1056/NEJMoa1502583.
15. Miller, AJ and Mihm, MC, (2006) Mechanisms of disease - Melanoma. *New England Journal of Medicine*. **355**(1): p. 51-65. DOI: DOI 10.1056/NEJMra052166.
16. Shain, AH and Bastian, BC, (2016) From melanocytes to melanomas. *Nat Rev Cancer*. **16**(6): p. 345-58. DOI: 10.1038/nrc.2016.37.
17. Goldgar, DE, Cannon-Albright, LA, Meyer, LJ, et al., (1991) Inheritance of nevus number and size in melanoma and dysplastic nevus syndrome kindreds. *J Natl Cancer Inst*. **83**(23): p. 1726-33. DOI: 10.1093/jnci/83.23.1726.
18. Lawrence, MS, Stojanov, P, Polak, P, et al., (2013) Mutational heterogeneity in cancer and the search for new cancer-associated genes. *Nature*. **499**(7457): p. 214-218. DOI: 10.1038/nature12213.
19. Alexandrov, LB, Nik-Zainal, S, Wedge, DC, et al., (2013) Signatures of mutational processes in human cancer. *Nature*. **500**(7463): p. 415-21. DOI: 10.1038/nature12477.

20. Curtin, JA, Fridlyand, J, Kageshita, T, et al., (2005) Distinct sets of genetic alterations in melanoma. *N Engl J Med*. **353**(20): p. 2135-47. DOI: 10.1056/NEJMoa050092.
21. Lemmon, MA and Schlessinger, J, (2010) Cell signaling by receptor tyrosine kinases. *Cell*. **141**(7): p. 1117-34. DOI: 10.1016/j.cell.2010.06.011.
22. Cancer Genome Atlas, N, (2015) Genomic Classification of Cutaneous Melanoma. *Cell*. **161**(7): p. 1681-96. DOI: 10.1016/j.cell.2015.05.044.
23. Appenzeller, S, Gesierich, A, Thiem, A, et al., (2019) The identification of patient-specific mutations reveals dual pathway activation in most patients with melanoma and activated receptor tyrosine kinases in BRAF/NRAS wild-type melanomas. *Cancer*. **125**(4): p. 586-600. DOI: 10.1002/cncr.31843.
24. Krauthammer, M, Kong, Y, Bacchiocchi, A, et al., (2015) Exome sequencing identifies recurrent mutations in NF1 and RASopathy genes in sun-exposed melanomas. *Nat Genet*. **47**(9): p. 996-1002. DOI: 10.1038/ng.3361.
25. Elder, DE, Bastian, BC, Cree, IA, et al., (2020) The 2018 World Health Organization Classification of Cutaneous, Mucosal, and Uveal Melanoma: Detailed Analysis of 9 Distinct Subtypes Defined by Their Evolutionary Pathway. *Arch Pathol Lab Med*. **144**(4): p. 500-522. DOI: 10.5858/arpa.2019-0561-RA.
26. Suire, S, Condliffe, AM, Ferguson, GJ, et al., (2006) Gβγs and the Ras binding domain of p110γ are both important regulators of PI3Kγ signalling in neutrophils. *Nature Cell Biology*. **8**(11): p. 1303-1309. DOI: 10.1038/ncb1494.
27. Osaki, M, Oshimura, M, and Ito, H, (2004) PI3K-Akt pathway: its functions and alterations in human cancer. *Apoptosis*. **9**(6): p. 667-76. DOI: 10.1023/B:APPT.0000045801.15585.dd.
28. Prickett, TD, Agrawal, NS, Wei, X, et al., (2009) Analysis of the tyrosine kinome in melanoma reveals recurrent mutations in ERBB4. *Nat Genet*. **41**(10): p. 1127-32. DOI: 10.1038/ng.438.
29. Carvajal, RD, Antonescu, CR, Wolchok, JD, et al., (2011) KIT as a therapeutic target in metastatic melanoma. *JAMA*. **305**(22): p. 2327-34. DOI: 10.1001/jama.2011.746.
30. Schoenewolf, NL, Bull, C, Belloni, B, et al., (2012) Sinonasal, genital and acrolentiginous melanomas show distinct characteristics of KIT expression and mutations. *Eur J Cancer*. **48**(12): p. 1842-52. DOI: 10.1016/j.ejca.2012.02.049.
31. Hussussian, CJ, Struewing, JP, Goldstein, AM, et al., (1994) Germline p16 mutations in familial melanoma. *Nat Genet*. **8**(1): p. 15-21. DOI: 10.1038/ng0994-15.
32. Monzon, J, Liu, L, Brill, H, et al., (1998) CDKN2A mutations in multiple primary melanomas. *N Engl J Med*. **338**(13): p. 879-87. DOI: 10.1056/NEJM199803263381305.
33. Landi, MT, Bauer, J, Pfeiffer, RM, et al., (2006) MC1R germline variants confer risk for BRAF-mutant melanoma. *Science*. **313**(5786): p. 521-2. DOI: 10.1126/science.1127515.
34. Coit, DG, Andtbacka, R, Anker, CJ, et al., (2012) Melanoma. *J Natl Compr Canc Netw*. **10**(3): p. 366-400. DOI: 10.6004/jnccn.2012.0036.
35. Luke, JJ and Schwartz, GK, (2013) Chemotherapy in the management of advanced cutaneous malignant melanoma. *Clin Dermatol*. **31**(3): p. 290-7. DOI: 10.1016/j.clindermatol.2012.08.016.
36. Kim, G, McKee, AE, Ning, YM, et al., (2014) FDA approval summary: vemurafenib for treatment of unresectable or metastatic melanoma with the BRAFV600E mutation. *Clin Cancer Res*. **20**(19): p. 4994-5000. DOI: 10.1158/1078-0432.CCR-14-0776.
37. da Rocha Dias, S, Salmonson, T, van Zwieten-Boot, B, et al., (2013) The European Medicines Agency review of vemurafenib (Zelboraf(R)) for the treatment of adult patients with BRAF V600 mutation-positive unresectable or metastatic melanoma: summary of the scientific assessment of the Committee for Medicinal Products for Human Use. *Eur J Cancer*. **49**(7): p. 1654-61. DOI: 10.1016/j.ejca.2013.01.015.
38. Chapman, PB, Hauschild, A, Robert, C, et al., (2011) Improved survival with vemurafenib in melanoma with BRAF V600E mutation. *N Engl J Med*. **364**(26): p. 2507-16. DOI: 10.1056/NEJMoa1103782.

39. Flaherty, KT, Puzanov, I, Kim, KB, et al., (2010) Inhibition of mutated, activated BRAF in metastatic melanoma. *N Engl J Med*. **363**(9): p. 809-19. DOI: 10.1056/NEJMoa1002011.
40. Solit, DB and Rosen, N, (2011) Resistance to BRAF inhibition in melanomas. *N Engl J Med*. **364**(8): p. 772-4. DOI: 10.1056/NEJMcibr1013704.
41. Nazarian, R, Shi, H, Wang, Q, et al., (2010) Melanomas acquire resistance to B-RAF(V600E) inhibition by RTK or N-RAS upregulation. *Nature*. **468**(7326): p. 973-7. DOI: 10.1038/nature09626.
42. Kugel, CH, 3rd and Aplin, AE, (2014) Adaptive resistance to RAF inhibitors in melanoma. *Pigment Cell Melanoma Res*. **27**(6): p. 1032-8. DOI: 10.1111/pcmr.12264.
43. Meierjohann, S, (2017) Crosstalk signaling in targeted melanoma therapy. *Cancer Metastasis Rev*. **36**(1): p. 23-33. DOI: 10.1007/s10555-017-9659-z.
44. Abe, H, Kikuchi, S, Hayakawa, K, et al., (2011) Discovery of a Highly Potent and Selective MEK Inhibitor: GSK1120212 (JTP-74057 DMSO Solvate). *ACS Medicinal Chemistry Letters*. **2**(4): p. 320-324. DOI: 10.1021/ml200004g.
45. Flaherty, KT, Infante, JR, Daud, A, et al., (2012) Combined BRAF and MEK inhibition in melanoma with BRAF V600 mutations. *N Engl J Med*. **367**(18): p. 1694-703. DOI: 10.1056/NEJMoa1210093.
46. Menzies, AM and Long, GV, (2014) Dabrafenib and trametinib, alone and in combination for BRAF-mutant metastatic melanoma. *Clin Cancer Res*. **20**(8): p. 2035-43. DOI: 10.1158/1078-0432.CCR-13-2054.
47. Robert, C, Karaszewska, B, Schachter, J, et al., (2015) Improved overall survival in melanoma with combined dabrafenib and trametinib. *N Engl J Med*. **372**(1): p. 30-9. DOI: 10.1056/NEJMoa1412690.
48. Welsh, SJ, Rizos, H, Scolyer, RA, et al., (2016) Resistance to combination BRAF and MEK inhibition in metastatic melanoma: Where to next? *Eur J Cancer*. **62**: p. 76-85. DOI: 10.1016/j.ejca.2016.04.005.
49. Hodi, FS, O'Day, SJ, McDermott, DF, et al., (2010) Improved survival with ipilimumab in patients with metastatic melanoma. *N Engl J Med*. **363**(8): p. 711-23. DOI: 10.1056/NEJMoa1003466.
50. Pardoll, DM, (2012) The blockade of immune checkpoints in cancer immunotherapy. *Nat Rev Cancer*. **12**(4): p. 252-64. DOI: 10.1038/nrc3239.
51. Peggs, KS, Quezada, SA, Chambers, CA, et al., (2009) Blockade of CTLA-4 on both effector and regulatory T cell compartments contributes to the antitumor activity of anti-CTLA-4 antibodies. *J Exp Med*. **206**(8): p. 1717-25. DOI: 10.1084/jem.20082492.
52. Larkin, J, Chiarion-Sileni, V, Gonzalez, R, et al., (2015) Combined Nivolumab and Ipilimumab or Monotherapy in Untreated Melanoma. *N Engl J Med*. **373**(1): p. 23-34. DOI: 10.1056/NEJMoa1504030.
53. Topalian, SL, Sznol, M, McDermott, DF, et al., (2014) Survival, durable tumor remission, and long-term safety in patients with advanced melanoma receiving nivolumab. *J Clin Oncol*. **32**(10): p. 1020-30. DOI: 10.1200/JCO.2013.53.0105.
54. Wolchok, JD, Kluger, H, Callahan, MK, et al., (2013) Nivolumab plus ipilimumab in advanced melanoma. *N Engl J Med*. **369**(2): p. 122-33. DOI: 10.1056/NEJMoa1302369.
55. Ramos-Casals, M, Brahmer, JR, Callahan, MK, et al., (2020) Immune-related adverse events of checkpoint inhibitors. *Nat Rev Dis Primers*. **6**(1): p. 38. DOI: 10.1038/s41572-020-0160-6.
56. Gide, TN, Wilmott, JS, Scolyer, RA, et al., (2018) Primary and Acquired Resistance to Immune Checkpoint Inhibitors in Metastatic Melanoma. *Clin Cancer Res*. **24**(6): p. 1260-1270. DOI: 10.1158/1078-0432.CCR-17-2267.
57. Luke, JJ, Flaherty, KT, Ribas, A, et al., (2017) Targeted agents and immunotherapies: optimizing outcomes in melanoma. *Nat Rev Clin Oncol*. **14**(8): p. 463-482. DOI: 10.1038/nrclinonc.2017.43.

58. Harlin, H, Meng, Y, Peterson, AC, et al., (2009) Chemokine expression in melanoma metastases associated with CD8+ T-cell recruitment. *Cancer Res*. **69**(7): p. 3077-85. DOI: 10.1158/0008-5472.CAN-08-2281.
59. Ji, RR, Chasalow, SD, Wang, L, et al., (2012) An immune-active tumor microenvironment favors clinical response to ipilimumab. *Cancer Immunol Immunother*. **61**(7): p. 1019-31. DOI: 10.1007/s00262-011-1172-6.
60. Zaretsky, JM, Garcia-Diaz, A, Shin, DS, et al., (2016) Mutations Associated with Acquired Resistance to PD-1 Blockade in Melanoma. *N Engl J Med*. **375**(9): p. 819-29. DOI: 10.1056/NEJMoa1604958.
61. Shin, DS, Zaretsky, JM, Escuin-Ordinas, H, et al., (2017) Primary Resistance to PD-1 Blockade Mediated by JAK1/2 Mutations. *Cancer Discov*. **7**(2): p. 188-201. DOI: 10.1158/2159-8290.CD-16-1223.
62. Ford, K, Hanley, CJ, Mellone, M, et al., (2020) NOX4 Inhibition Potentiates Immunotherapy by Overcoming Cancer-Associated Fibroblast-Mediated CD8 T-cell Exclusion from Tumors. *Cancer Res*. **80**(9): p. 1846-1860. DOI: 10.1158/0008-5472.CAN-19-3158.
63. Weinberg, F, Ramnath, N, and Nagrath, D, (2019) Reactive Oxygen Species in the Tumor Microenvironment: An Overview. *Cancers (Basel)*. **11**(8). DOI: 10.3390/cancers11081191.
64. Cho, KJ, Seo, JM, and Kim, JH, (2011) Bioactive lipoxygenase metabolites stimulation of NADPH oxidases and reactive oxygen species. *Mol Cells*. **32**(1): p. 1-5. DOI: 10.1007/s10059-011-1021-7.
65. Kim, JH, Choi, TG, Park, S, et al., (2018) Mitochondrial ROS-derived PTEN oxidation activates PI3K pathway for mTOR-induced myogenic autophagy. *Cell Death Differ*. **25**(11): p. 1921-1937. DOI: 10.1038/s41418-018-0165-9.
66. Denat, L, Kadekaro, AL, Marrot, L, et al., (2014) Melanocytes as instigators and victims of oxidative stress. *J Invest Dermatol*. **134**(6): p. 1512-1518. DOI: 10.1038/jid.2014.65.
67. Jones, RG and Thompson, CB, (2009) Tumor suppressors and cell metabolism: a recipe for cancer growth. *Genes Dev*. **23**(5): p. 537-48. DOI: 10.1101/gad.1756509.
68. Edderkaoui, M, Nitsche, C, Zheng, L, et al., (2011) NADPH oxidase activation in pancreatic cancer cells is mediated through Akt-dependent up-regulation of p22phox. *J Biol Chem*. **286**(10): p. 7779-87. DOI: 10.1074/jbc.M110.200063.
69. Ueyama, T, Geiszt, M, and Leto, TL, (2006) Involvement of Rac1 in activation of multicomponent Nox1- and Nox3-based NADPH oxidases. *Mol Cell Biol*. **26**(6): p. 2160-74. DOI: 10.1128/MCB.26.6.2160-2174.2006.
70. Li, A, Ma, Y, Jin, M, et al., (2012) Activated mutant NRas(Q61K) drives aberrant melanocyte signaling, survival, and invasiveness via a Rac1-dependent mechanism. *J Invest Dermatol*. **132**(11): p. 2610-21. DOI: 10.1038/jid.2012.186.
71. Mehnert, JM and Kluger, HM, (2012) Driver mutations in melanoma: lessons learned from bench-to-bedside studies. *Curr Oncol Rep*. **14**(5): p. 449-57. DOI: 10.1007/s11912-012-0249-5.
72. Sies, H, (1997) Oxidative stress: oxidants and antioxidants. *Exp Physiol*. **82**(2): p. 291-5. DOI: 10.1113/expphysiol.1997.sp004024.
73. McGonigle, S, Dalton, JP, and James, ER, (1998) Peroxidoxins: A New Antioxidant Family. *Parasitology Today*. **14**(4): p. 139-145. DOI: 10.1016/s0169-4758(97)01211-8.
74. Lu, J and Holmgren, A, (2014) The thioredoxin antioxidant system. *Free Radic Biol Med*. **66**: p. 75-87. DOI: 10.1016/j.freeradbiomed.2013.07.036.
75. Corso, CR and Acco, A, (2018) Glutathione system in animal model of solid tumors: From regulation to therapeutic target. *Crit Rev Oncol Hematol*. **128**: p. 43-57. DOI: 10.1016/j.critrevonc.2018.05.014.
76. Anders, L, Ke, N, Hydbring, P, et al., (2011) A systematic screen for CDK4/6 substrates links FOXM1 phosphorylation to senescence suppression in cancer cells. *Cancer Cell*. **20**(5): p. 620-34. DOI: 10.1016/j.ccr.2011.10.001.

77. Park, HJ, Carr, JR, Wang, Z, et al., (2009) FoxM1, a critical regulator of oxidative stress during oncogenesis. *EMBO J*. **28**(19): p. 2908-18. DOI: 10.1038/emboj.2009.239.
78. Torrens-Mas, M, Gonzalez-Hedstrom, D, Abrisqueta, M, et al., (2017) PGC-1alpha in Melanoma: A Key Factor for Antioxidant Response and Mitochondrial Function. *J Cell Biochem*. **118**(12): p. 4404-4413. DOI: 10.1002/jcb.26094.
79. Vazquez, F, Lim, JH, Chim, H, et al., (2013) PGC1alpha expression defines a subset of human melanoma tumors with increased mitochondrial capacity and resistance to oxidative stress. *Cancer Cell*. **23**(3): p. 287-301. DOI: 10.1016/j.ccr.2012.11.020.
80. Leikam, C, Hufnagel, A, Walz, S, et al., (2014) Cystathionase mediates senescence evasion in melanocytes and melanoma cells. *Oncogene*. **33**(6): p. 771-82. DOI: 10.1038/onc.2012.641.
81. Sasaki, H, Sato, H, Kuriyama-Matsumura, K, et al., (2002) Electrophile response element-mediated induction of the cystine/glutamate exchange transporter gene expression. *J Biol Chem*. **277**(47): p. 44765-71. DOI: 10.1074/jbc.M208704200.
82. Koppula, P, Zhang, Y, Zhuang, L, et al., (2018) Amino acid transporter SLC7A11/xCT at the crossroads of regulating redox homeostasis and nutrient dependency of cancer. *Cancer Commun (Lond)*. **38**(1): p. 12. DOI: 10.1186/s40880-018-0288-x.
83. Blanco-Bose, WE, Murphy, MJ, Ehninger, A, et al., (2008) C-Myc and its target FoxM1 are critical downstream effectors of constitutive androstane receptor (CAR) mediated direct liver hyperplasia. *Hepatology*. **48**(4): p. 1302-11. DOI: 10.1002/hep.22475.
84. DeNicola, GM, Karreth, FA, Humpton, TJ, et al., (2011) Oncogene-induced Nrf2 transcription promotes ROS detoxification and tumorigenesis. *Nature*. **475**(7354): p. 106-9. DOI: 10.1038/nature10189.
85. Hayes, JD and Dinkova-Kostova, AT, (2014) The Nrf2 regulatory network provides an interface between redox and intermediary metabolism. *Trends Biochem Sci*. **39**(4): p. 199-218. DOI: 10.1016/j.tibs.2014.02.002.
86. Menegon, S, Columbano, A, and Giordano, S, (2016) The Dual Roles of NRF2 in Cancer. *Trends Mol Med*. **22**(7): p. 578-93. DOI: 10.1016/j.molmed.2016.05.002.
87. Gorrini, C, Harris, IS, and Mak, TW, (2013) Modulation of oxidative stress as an anticancer strategy. *Nat Rev Drug Discov*. **12**(12): p. 931-47. DOI: 10.1038/nrd4002.
88. Wu, KC, Cui, JY, and Klaassen, CD, (2011) Beneficial role of Nrf2 in regulating NADPH generation and consumption. *Toxicol Sci*. **123**(2): p. 590-600. DOI: 10.1093/toxsci/kfr183.
89. Agyeman, AS, Chaerkady, R, Shaw, PG, et al., (2012) Transcriptomic and proteomic profiling of KEAP1 disrupted and sulforaphane-treated human breast epithelial cells reveals common expression profiles. *Breast Cancer Res Treat*. **132**(1): p. 175-87. DOI: 10.1007/s10549-011-1536-9.
90. Dinkova-Kostova, AT and Talalay, P, (2010) NAD(P)H:quinone acceptor oxidoreductase 1 (NQO1), a multifunctional antioxidant enzyme and exceptionally versatile cytoprotector. *Arch Biochem Biophys*. **501**(1): p. 116-23. DOI: 10.1016/j.abb.2010.03.019.
91. Abraham, NG and Kappas, A, (2008) Pharmacological and clinical aspects of heme oxygenase. *Pharmacol Rev*. **60**(1): p. 79-127. DOI: 10.1124/pr.107.07104.
92. Mitsuishi, Y, Taguchi, K, Kawatani, Y, et al., (2012) Nrf2 redirects glucose and glutamine into anabolic pathways in metabolic reprogramming. *Cancer Cell*. **22**(1): p. 66-79. DOI: 10.1016/j.ccr.2012.05.016.
93. Zhang, DD, (2006) Mechanistic studies of the Nrf2-Keap1 signaling pathway. *Drug Metab Rev*. **38**(4): p. 769-89. DOI: 10.1080/03602530600971974.
94. Chen, W, Sun, Z, Wang, XJ, et al., (2009) Direct interaction between Nrf2 and p21(Cip1/WAF1) upregulates the Nrf2-mediated antioxidant response. *Mol Cell*. **34**(6): p. 663-73. DOI: 10.1016/j.molcel.2009.04.029.
95. Tebay, LE, Robertson, H, Durant, ST, et al., (2015) Mechanisms of activation of the transcription factor Nrf2 by redox stressors, nutrient cues, and energy status and the pathways through which it attenuates degenerative disease. *Free Radic Biol Med*. **88**(Pt B): p. 108-146. DOI: 10.1016/j.freeradbiomed.2015.06.021.

96. Rushworth, SA, MacEwan, DJ, and O'Connell, MA, (2008) Lipopolysaccharide-induced expression of NAD(P)H:quinone oxidoreductase 1 and heme oxygenase-1 protects against excessive inflammatory responses in human monocytes. *J Immunol*. **181**(10): p. 6730-7. DOI: 10.4049/jimmunol.181.10.6730.
97. Sanchez-Martin, P and Komatsu, M, (2018) p62/SQSTM1 - steering the cell through health and disease. *J Cell Sci*. **131**(21). DOI: 10.1242/jcs.222836.
98. Singh, A, Misra, V, Thimmulappa, RK, et al., (2006) Dysfunctional KEAP1-NRF2 interaction in non-small-cell lung cancer. *PLoS Med*. **3**(10): p. e420. DOI: 10.1371/journal.pmed.0030420.
99. Miura, S, Shibazaki, M, Kasai, S, et al., (2014) A somatic mutation of the KEAP1 gene in malignant melanoma is involved in aberrant NRF2 activation and an increase in intrinsic drug resistance. *J Invest Dermatol*. **134**(2): p. 553-556. DOI: 10.1038/jid.2013.343.
100. Satoh, H, Moriguchi, T, Saigusa, D, et al., (2016) NRF2 Intensifies Host Defense Systems to Prevent Lung Carcinogenesis, but After Tumor Initiation Accelerates Malignant Cell Growth. *Cancer Res*. **76**(10): p. 3088-96. DOI: 10.1158/0008-5472.CAN-15-1584.
101. Linker, RA and Haghikia, A, (2016) Dimethyl fumarate in multiple sclerosis: latest developments, evidence and place in therapy. *Ther Adv Chronic Dis*. **7**(4): p. 198-207. DOI: 10.1177/2040622316653307.
102. Belge, K, Bruck, J, and Ghoreschi, K, (2014) Advances in treating psoriasis. *F1000Prime Rep*. **6**: p. 4. DOI: 10.12703/P6-4.
103. Tao, S, Wang, S, Moghaddam, SJ, et al., (2014) Oncogenic KRAS confers chemoresistance by upregulating NRF2. *Cancer Res*. **74**(24): p. 7430-41. DOI: 10.1158/0008-5472.CAN-14-1439.
104. auf dem Keller, U, Huber, M, Beyer, TA, et al., (2006) Nrf transcription factors in keratinocytes are essential for skin tumor prevention but not for wound healing. *Mol Cell Biol*. **26**(10): p. 3773-84. DOI: 10.1128/MCB.26.10.3773-3784.2006.
105. Rocha, CR, Kajitani, GS, Quinet, A, et al., (2016) NRF2 and glutathione are key resistance mediators to temozolomide in glioma and melanoma cells. *Oncotarget*. **7**(30): p. 48081-48092. DOI: 10.18632/oncotarget.10129.
106. Shin, D, Kim, EH, Lee, J, et al., (2018) Nrf2 inhibition reverses resistance to GPX4 inhibitor-induced ferroptosis in head and neck cancer. *Free Radic Biol Med*. **129**: p. 454-462. DOI: 10.1016/j.freeradbiomed.2018.10.426.
107. Hintsala, HR, Jokinen, E, Haapasaari, KM, et al., (2016) Nrf2/Keap1 Pathway and Expression of Oxidative Stress Lesions 8-hydroxy-2'-deoxyguanosine and Nitrotyrosine in Melanoma. *Anticancer Res*. **36**(4): p. 1497-506.
108. Piskounova, E, Agathocleous, M, Murphy, MM, et al., (2015) Oxidative stress inhibits distant metastasis by human melanoma cells. *Nature*. **527**(7577): p. 186-91. DOI: 10.1038/nature15726.
109. Le Gal, K, Ibrahim, MX, Wiel, C, et al., (2015) Antioxidants can increase melanoma metastasis in mice. *Sci Transl Med*. **7**(308): p. 308re8. DOI: 10.1126/scitranslmed.aad3740.
110. Homma, S, Ishii, Y, Morishima, Y, et al., (2009) Nrf2 enhances cell proliferation and resistance to anticancer drugs in human lung cancer. *Clin Cancer Res*. **15**(10): p. 3423-32. DOI: 10.1158/1078-0432.CCR-08-2822.
111. Khamari, R, Trinh, A, Gabert, PE, et al., (2018) Glucose metabolism and NRF2 coordinate the antioxidant response in melanoma resistant to MAPK inhibitors. *Cell Death Dis*. **9**(3): p. 325. DOI: 10.1038/s41419-018-0340-4.
112. Zhu, B, Tang, L, Chen, S, et al., (2018) Targeting the upstream transcriptional activator of PD-L1 as an alternative strategy in melanoma therapy. *Oncogene*. DOI: 10.1038/s41388-018-0314-0.
113. Dankort, D, Curley, DP, Cartlidge, RA, et al., (2009) Braf(V600E) cooperates with Pten loss to induce metastatic melanoma. *Nat Genet*. **41**(5): p. 544-52. DOI: 10.1038/ng.356.

114. Chan, K, Lu, R, Chang, JC, et al., (1996) NRF2, a member of the NFE2 family of transcription factors, is not essential for murine erythropoiesis, growth, and development. *Proc Natl Acad Sci U S A*. **93**(24): p. 13943-8. DOI: 10.1073/pnas.93.24.13943.
115. Tietze, F, (1969) Enzymic method for quantitative determination of nanogram amounts of total and oxidized glutathione: applications to mammalian blood and other tissues. *Anal Biochem*. **27**(3): p. 502-22. DOI: 10.1016/0003-2697(69)90064-5.
116. Rahman, I, Kode, A, and Biswas, SK, (2006) Assay for quantitative determination of glutathione and glutathione disulfide levels using enzymatic recycling method. *Nat Protoc*. **1**(6): p. 3159-65. DOI: 10.1038/nprot.2006.378.
117. Dobin, A, Davis, CA, Schlesinger, F, et al., (2013) STAR: ultrafast universal RNA-seq aligner. *Bioinformatics*. **29**(1): p. 15-21. DOI: 10.1093/bioinformatics/bts635.
118. Li, B and Dewey, CN, (2011) RSEM: accurate transcript quantification from RNA-Seq data with or without a reference genome. *BMC Bioinformatics*. **12**: p. 323. DOI: 10.1186/1471-2105-12-323.
119. Love, MI, Huber, W, and Anders, S, (2014) Moderated estimation of fold change and dispersion for RNA-seq data with DESeq2. *Genome Biol*. **15**(12): p. 550. DOI: 10.1186/s13059-014-0550-8.
120. Langmead, B and Salzberg, SL, (2012) Fast gapped-read alignment with Bowtie 2. *Nat Methods*. **9**(4): p. 357-9. DOI: 10.1038/nmeth.1923.
121. Robinson, MD, McCarthy, DJ, and Smyth, GK, (2010) edgeR: a Bioconductor package for differential expression analysis of digital gene expression data. *Bioinformatics*. **26**(1): p. 139-40. DOI: 10.1093/bioinformatics/btp616.
122. Bankhead, P, Loughrey, MB, Fernández, JA, et al., (2017) QuPath: Open source software for digital pathology image analysis. *Sci Rep*. **7**(1): p. 16878. DOI: 10.1038/s41598-017-17204-5.
123. Davies, H, Bignell, GR, Cox, C, et al., (2002) Mutations of the BRAF gene in human cancer. *Nature*. **417**(6892): p. 949-54. DOI: 10.1038/nature00766.
124. Hodis, E, Watson, Ian R, Kryukov, Gregory V, et al., (2012) A Landscape of Driver Mutations in Melanoma. *Cell*. **150**(2): p. 251-263. DOI: 10.1016/j.cell.2012.06.024.
125. van 't Veer, LJ, Burgering, BM, Versteeg, R, et al., (1989) N-ras mutations in human cutaneous melanoma from sun-exposed body sites. *Mol Cell Biol*. **9**(7): p. 3114-6. DOI: 10.1128/mcb.9.7.3114.
126. Enomoto, A, Itoh, K, Nagayoshi, E, et al., (2001) High sensitivity of Nrf2 knockout mice to acetaminophen hepatotoxicity associated with decreased expression of ARE-regulated drug metabolizing enzymes and antioxidant genes. *Toxicol Sci*. **59**(1): p. 169-77. DOI: 10.1093/toxsci/59.1.169.
127. Strohecker, AM, Guo, JY, Karsli-Uzunbas, G, et al., (2013) Autophagy sustains mitochondrial glutamine metabolism and growth of BrafV600E-driven lung tumors. *Cancer Discov*. **3**(11): p. 1272-85. DOI: 10.1158/2159-8290.CD-13-0397.
128. Itoh, K, Chiba, T, Takahashi, S, et al., (1997) An Nrf2/small Maf heterodimer mediates the induction of phase II detoxifying enzyme genes through antioxidant response elements. *Biochem Biophys Res Commun*. **236**(2): p. 313-22. DOI: 10.1006/bbrc.1997.6943.
129. Joseph, EW, Pratilas, CA, Poulikakos, PI, et al., (2010) The RAF inhibitor PLX4032 inhibits ERK signaling and tumor cell proliferation in a V600E BRAF-selective manner. *Proc Natl Acad Sci U S A*. **107**(33): p. 14903-8. DOI: 10.1073/pnas.1008990107.
130. Hu, C, Eggler, AL, Mesecar, AD, et al., (2011) Modification of keap1 cysteine residues by sulforaphane. *Chem Res Toxicol*. **24**(4): p. 515-21. DOI: 10.1021/tx100389r.
131. Takaya, K, Suzuki, T, Motohashi, H, et al., (2012) Validation of the multiple sensor mechanism of the Keap1-Nrf2 system. *Free Radic Biol Med*. **53**(4): p. 817-27. DOI: 10.1016/j.freeradbiomed.2012.06.023.

132. Qu, X, Tang, Y, and Hua, S, (2018) Immunological Approaches Towards Cancer and Inflammation: A Cross Talk. *Front Immunol*. **9**: p. 563. DOI: 10.3389/fimmu.2018.00563.
133. Yan, MH, Wang, X, and Zhu, X, (2013) Mitochondrial defects and oxidative stress in Alzheimer disease and Parkinson disease. *Free Radic Biol Med*. **62**: p. 90-101. DOI: 10.1016/j.freeradbiomed.2012.11.014.
134. Fao, L, Mota, SI, and Rego, AC, (2019) Shaping the Nrf2-ARE-related pathways in Alzheimer's and Parkinson's diseases. *Ageing Res Rev*. **54**: p. 100942. DOI: 10.1016/j.arr.2019.100942.
135. Bottcher, JP, Bonavita, E, Chakravarty, P, et al., (2018) NK Cells Stimulate Recruitment of cDC1 into the Tumor Microenvironment Promoting Cancer Immune Control. *Cell*. **172**(5): p. 1022-1037 e14. DOI: 10.1016/j.cell.2018.01.004.
136. Zelenay, S, van der Veen, AG, Bottcher, JP, et al., (2015) Cyclooxygenase-Dependent Tumor Growth through Evasion of Immunity. *Cell*. **162**(6): p. 1257-70. DOI: 10.1016/j.cell.2015.08.015.
137. DeNicola, GM, Chen, PH, Mullarky, E, et al., (2015) NRF2 regulates serine biosynthesis in non-small cell lung cancer. *Nat Genet*. **47**(12): p. 1475-81. DOI: 10.1038/ng.3421.
138. Cheli, Y, Giuliano, S, Botton, T, et al., (2011) Mitf is the key molecular switch between mouse or human melanoma initiating cells and their differentiated progeny. *Oncogene*. **30**(20): p. 2307-18. DOI: 10.1038/onc.2010.598.
139. Du, J, Miller, AJ, Widlund, HR, et al., (2003) MLANA/MART1 and SILV/PMEL17/GP100 are transcriptionally regulated by MITF in melanocytes and melanoma. *Am J Pathol*. **163**(1): p. 333-43. DOI: 10.1016/S0002-9440(10)63657-7.
140. Hoek, KS, Eichhoff, OM, Schlegel, NC, et al., (2008) In vivo switching of human melanoma cells between proliferative and invasive states. *Cancer Res*. **68**(3): p. 650-6. DOI: 10.1158/0008-5472.CAN-07-2491.
141. Wellbrock, C and Arozarena, I, (2015) Microphthalmia-associated transcription factor in melanoma development and MAP-kinase pathway targeted therapy. *Pigment Cell Melanoma Res*. **28**(4): p. 390-406. DOI: 10.1111/pcmr.12370.
142. Riesenberg, S, Groetchen, A, Siddaway, R, et al., (2015) MITF and c-Jun antagonism interconnects melanoma dedifferentiation with pro-inflammatory cytokine responsiveness and myeloid cell recruitment. *Nat Commun*. **6**: p. 8755. DOI: 10.1038/ncomms9755.
143. Nakao, S, Ogtata, Y, Shimizu, E, et al., (2002) Tumor necrosis factor alpha (TNF-alpha)-induced prostaglandin E2 release is mediated by the activation of cyclooxygenase-2 (COX-2) transcription via NFkappaB in human gingival fibroblasts. *Mol Cell Biochem*. **238**(1-2): p. 11-8. DOI: 10.1023/a:1019927616000.
144. Subbarayan, V, Sabichi, AL, Llansa, N, et al., (2001) Differential expression of cyclooxygenase-2 and its regulation by tumor necrosis factor-alpha in normal and malignant prostate cells. *Cancer Res*. **61**(6): p. 2720-6.
145. Ji, Z, Erin Chen, Y, Kumar, R, et al., (2015) MITF Modulates Therapeutic Resistance through EGFR Signaling. *J Invest Dermatol*. **135**(7): p. 1863-1872. DOI: 10.1038/jid.2015.105.
146. Muller, J, Krijgsman, O, Tsoi, J, et al., (2014) Low MITF/AXL ratio predicts early resistance to multiple targeted drugs in melanoma. *Nat Commun*. **5**: p. 5712. DOI: 10.1038/ncomms6712.
147. Konieczkowski, DJ, Johannessen, CM, Abudayyeh, O, et al., (2014) A melanoma cell state distinction influences sensitivity to MAPK pathway inhibitors. *Cancer Discov*. **4**(7): p. 816-27. DOI: 10.1158/2159-8290.CD-13-0424.
148. Sensi, M, Catani, M, Castellano, G, et al., (2011) Human cutaneous melanomas lacking MITF and melanocyte differentiation antigens express a functional Axl receptor kinase. *J Invest Dermatol*. **131**(12): p. 2448-57. DOI: 10.1038/jid.2011.218.

149. Tsoi, J, Robert, L, Paraiso, K, et al., (2018) Multi-stage Differentiation Defines Melanoma Subtypes with Differential Vulnerability to Drug-Induced Iron-Dependent Oxidative Stress. *Cancer Cell*. DOI: 10.1016/j.ccell.2018.03.017.
150. Sanghvi, VR, Leibold, J, Mina, M, et al., (2019) The Oncogenic Action of NRF2 Depends on De-glycation by Fructosamine-3-Kinase. *Cell*. **178**(4): p. 807-819 e21. DOI: 10.1016/j.cell.2019.07.031.
151. Chorley, BN, Campbell, MR, Wang, X, et al., (2012) Identification of novel NRF2-regulated genes by ChIP-Seq: influence on retinoid X receptor alpha. *Nucleic Acids Res*. **40**(15): p. 7416-29. DOI: 10.1093/nar/gks409.
152. Zhao, C, Qiao, Y, Jonsson, P, et al., (2014) Genome-wide profiling of AP-1-regulated transcription provides insights into the invasiveness of triple-negative breast cancer. *Cancer Res*. **74**(14): p. 3983-94. DOI: 10.1158/0008-5472.CAN-13-3396.
153. Olagnier, D, Brandtoft, AM, Gunderstofte, C, et al., (2018) Nrf2 negatively regulates STING indicating a link between antiviral sensing and metabolic reprogramming. *Nat Commun*. **9**(1): p. 3506. DOI: 10.1038/s41467-018-05861-7.
154. Boehm, U, Klamp, T, Groot, M, et al., (1997) Cellular responses to interferon-gamma. *Annu Rev Immunol*. **15**: p. 749-95. DOI: 10.1146/annurev.immunol.15.1.749.
155. Ma, W, Lehner, PJ, Cresswell, P, et al., (1997) Interferon-gamma rapidly increases peptide transporter (TAP) subunit expression and peptide transport capacity in endothelial cells. *J Biol Chem*. **272**(26): p. 16585-90. DOI: 10.1074/jbc.272.26.16585.
156. Yang, Y, Waters, JB, Fruh, K, et al., (1992) Proteasomes are regulated by interferon gamma: implications for antigen processing. *Proc Natl Acad Sci U S A*. **89**(11): p. 4928-32. DOI: 10.1073/pnas.89.11.4928.
157. Darnell, JE, Jr., Kerr, IM, and Stark, GR, (1994) Jak-STAT pathways and transcriptional activation in response to IFNs and other extracellular signaling proteins. *Science*. **264**(5164): p. 1415-21. DOI: 10.1126/science.8197455.
158. Meraz, MA, White, JM, Sheehan, KC, et al., (1996) Targeted disruption of the Stat1 gene in mice reveals unexpected physiologic specificity in the JAK-STAT signaling pathway. *Cell*. **84**(3): p. 431-42. DOI: 10.1016/s0092-8674(00)81288-x.
159. Durbin, JE, Hackenmiller, R, Simon, MC, et al., (1996) Targeted disruption of the mouse Stat1 gene results in compromised innate immunity to viral disease. *Cell*. **84**(3): p. 443-50. DOI: 10.1016/s0092-8674(00)81289-1.
160. Gunderstofte, C, Iversen, MB, Peri, S, et al., (2019) Nrf2 Negatively Regulates Type I Interferon Responses and Increases Susceptibility to Herpes Genital Infection in Mice. *Front Immunol*. **10**: p. 2101. DOI: 10.3389/fimmu.2019.02101.
161. Kirkby, NS, Zaiss, AK, Wright, WR, et al., (2013) Differential COX-2 induction by viral and bacterial PAMPs: Consequences for cytokine and interferon responses and implications for anti-viral COX-2 directed therapies. *Biochem Biophys Res Commun*. **438**(2): p. 249-56. DOI: 10.1016/j.bbrc.2013.07.006.
162. Konno, H, Chinn, IK, Hong, D, et al., (2018) Pro-inflammation Associated with a Gain-of-Function Mutation (R284S) in the Innate Immune Sensor STING. *Cell Rep*. **23**(4): p. 1112-1123. DOI: 10.1016/j.celrep.2018.03.115.
163. Xia, T, Konno, H, and Barber, GN, (2016) Recurrent Loss of STING Signaling in Melanoma Correlates with Susceptibility to Viral Oncolysis. *Cancer Res*. **76**(22): p. 6747-6759. DOI: 10.1158/0008-5472.CAN-16-1404.
164. Li, T, Fan, J, Wang, B, et al., (2017) TIMER: A Web Server for Comprehensive Analysis of Tumor-Infiltrating Immune Cells. *Cancer Res*. **77**(21): p. e108-e110. DOI: 10.1158/0008-5472.CAN-17-0307.
165. Zou, Y, Hu, M, Lee, J, et al., (2015) Nrf2 is essential for timely M phase entry of replicating hepatocytes during liver regeneration. *Am J Physiol Gastrointest Liver Physiol*. **308**(4): p. G262-8. DOI: 10.1152/ajpgi.00332.2014.
166. Teh, MT, Wong, ST, Neill, GW, et al., (2002) FOXM1 Is a Downstream Target of Gli1 in Basal Cell Carcinomas. *Cancer Res*. **62**(16): p. 4773-4780. DOI: Published August 2002.

167. Zhang, Y, Qiao, WB, and Shan, L, (2018) Expression and functional characterization of FOXM1 in non-small cell lung cancer. *Onco Targets Ther*. **11**: p. 3385-3393. DOI: 10.2147/OTT.S162523.
168. Wierstra, I, (2013) The transcription factor FOXM1 (Forkhead box M1): proliferation-specific expression, transcription factor function, target genes, mouse models, and normal biological roles. *Adv Cancer Res*. **118**: p. 97-398. DOI: 10.1016/B978-0-12-407173-5.00004-2.
169. Monteiro, LJ, Khongkow, P, Kongsema, M, et al., (2013) The Forkhead Box M1 protein regulates BRIP1 expression and DNA damage repair in epirubicin treatment. *Oncogene*. **32**(39): p. 4634-45. DOI: 10.1038/onc.2012.491.
170. Zhang, N, Wu, X, Yang, L, et al., (2012) FoxM1 inhibition sensitizes resistant glioblastoma cells to temozolomide by downregulating the expression of DNA-repair gene Rad51. *Clin Cancer Res*. **18**(21): p. 5961-71. DOI: 10.1158/1078-0432.CCR-12-0039.
171. Tan, Y, Raychaudhuri, P, and Costa, RH, (2007) Chk2 mediates stabilization of the FoxM1 transcription factor to stimulate expression of DNA repair genes. *Mol Cell Biol*. **27**(3): p. 1007-16. DOI: 10.1128/MCB.01068-06.
172. Miyashita, A, Fukushima, S, Nakahara, S, et al., (2015) Investigation of FOXM1 as a Potential New Target for Melanoma. *PLoS One*. **10**(12): p. e0144241. DOI: 10.1371/journal.pone.0144241.
173. Smirnov, A, Panatta, E, Lena, A, et al., (2016) FOXM1 regulates proliferation, senescence and oxidative stress in keratinocytes and cancer cells. *Aging (Albany NY)*. **8**(7): p. 1384-97. DOI: 10.18632/aging.100988.
174. Schmit, F, Korenjak, M, Mannefeld, M, et al., (2007) LINC, a human complex that is related to pRB-containing complexes in invertebrates regulates the expression of G2/M genes. *Cell Cycle*. **6**(15): p. 1903-13. DOI: 10.4161/cc.6.15.4512.
175. Litovchick, L, Sadasivam, S, Florens, L, et al., (2007) Evolutionarily conserved multisubunit RBL2/p130 and E2F4 protein complex represses human cell cycle-dependent genes in quiescence. *Mol Cell*. **26**(4): p. 539-51. DOI: 10.1016/j.molcel.2007.04.015.
176. Sadasivam, S, Duan, S, and DeCaprio, JA, (2012) The MuvB complex sequentially recruits B-Myb and FoxM1 to promote mitotic gene expression. *Genes Dev*. **26**(5): p. 474-89. DOI: 10.1101/gad.181933.111.
177. Malhotra, D, Portales-Casamar, E, Singh, A, et al., (2010) Global mapping of binding sites for Nrf2 identifies novel targets in cell survival response through ChIP-Seq profiling and network analysis. *Nucleic Acids Res*. **38**(17): p. 5718-34. DOI: 10.1093/nar/gkq212.
178. Reddy, NM, Kleeberger, SR, Bream, JH, et al., (2008) Genetic disruption of the Nrf2 compromises cell-cycle progression by impairing GSH-induced redox signaling. *Oncogene*. **27**(44): p. 5821-32. DOI: 10.1038/onc.2008.188.
179. Sayin, VI, LeBoeuf, SE, Singh, SX, et al., (2017) Activation of the NRF2 antioxidant program generates an imbalance in central carbon metabolism in cancer. *Elife*. **6**. DOI: 10.7554/eLife.28083.
180. Hirotsu, Y, Katsuoka, F, Funayama, R, et al., (2012) Nrf2-MafG heterodimers contribute globally to antioxidant and metabolic networks. *Nucleic Acids Res*. **40**(20): p. 10228-39. DOI: 10.1093/nar/gks827.
181. Namani, A, Liu, K, Wang, S, et al., (2019) Genome-wide global identification of NRF2 binding sites in A549 non-small cell lung cancer cells by ChIP-Seq reveals NRF2 regulation of genes involved in focal adhesion pathways. *Aging (Albany NY)*. **11**(24): p. 12600-12623. DOI: 10.18632/aging.102590.
182. Calo, E and Wysocka, J, (2013) Modification of enhancer chromatin: what, how, and why? *Mol Cell*. **49**(5): p. 825-37. DOI: 10.1016/j.molcel.2013.01.038.
183. Biddie, SC, John, S, Sabo, PJ, et al., (2011) Transcription factor AP1 potentiates chromatin accessibility and glucocorticoid receptor binding. *Mol Cell*. **43**(1): p. 145-55. DOI: 10.1016/j.molcel.2011.06.016.

184. Angel, P and Karin, M, (1991) The role of Jun, Fos and the AP-1 complex in cell-proliferation and transformation. *Biochimica et Biophysica Acta (BBA) - Reviews on Cancer*. **1072**(2-3): p. 129-157. DOI: 10.1016/0304-419x(91)90011-9.
185. Chinenov, Y and Kerppola, TK, (2001) Close encounters of many kinds: Fos-Jun interactions that mediate transcription regulatory specificity. *Oncogene*. **20**(19): p. 2438-52. DOI: 10.1038/sj.onc.1204385.
186. Zanconato, F, Forcato, M, Battilana, G, et al., (2015) Genome-wide association between YAP/TAZ/TEAD and AP-1 at enhancers drives oncogenic growth. *Nat Cell Biol*. **17**(9): p. 1218-27. DOI: 10.1038/ncb3216.
187. Friling, RS, Bergelson, S, and Daniel, V, (1992) Two adjacent AP-1-like binding sites form the electrophile-responsive element of the murine glutathione S-transferase Ya subunit gene. *Proc Natl Acad Sci U S A*. **89**(2): p. 668-72. DOI: 10.1073/pnas.89.2.668.
188. Venugopal, R and Jaiswal, AK, (1998) Nrf2 and Nrf1 in association with Jun proteins regulate antioxidant response element-mediated expression and coordinated induction of genes encoding detoxifying enzymes. *Oncogene*. **17**(24): p. 3145-56. DOI: 10.1038/sj.onc.1202237.
189. Zgheib, E, Limonciel, A, Jiang, X, et al., (2018) Investigation of Nrf2, AhR and ATF4 Activation in Toxicogenomic Databases. *Front Genet*. **9**: p. 429. DOI: 10.3389/fgene.2018.00429.
190. Bentley, NJ, Eisen, T, and Goding, CR, (1994) Melanocyte-specific expression of the human tyrosinase promoter: activation by the microphthalmia gene product and role of the initiator. *Mol Cell Biol*. **14**(12): p. 7996-8006. DOI: 10.1128/mcb.14.12.7996.
191. Luo, C, Lim, JH, Lee, Y, et al., (2016) A PGC1alpha-mediated transcriptional axis suppresses melanoma metastasis. *Nature*. **537**(7620): p. 422-426. DOI: 10.1038/nature19347.
192. Shin, JM, Kim, MY, Sohn, KC, et al., (2014) Nrf2 negatively regulates melanogenesis by modulating PI3K/Akt signaling. *PLoS One*. **9**(4): p. e96035. DOI: 10.1371/journal.pone.0096035.
193. Lekmine, F, Chang, CK, Sethakorn, N, et al., (2007) Role of microphthalmia transcription factor (Mitf) in melanoma differentiation. *Biochem Biophys Res Commun*. **354**(3): p. 830-5. DOI: 10.1016/j.bbrc.2007.01.075.
194. Rambow, F, Marine, JC, and Goding, CR, (2019) Melanoma plasticity and phenotypic diversity: therapeutic barriers and opportunities. *Genes Dev*. **33**(19-20): p. 1295-1318. DOI: 10.1101/gad.329771.119.
195. Carreira, S, Goodall, J, Denat, L, et al., (2006) Mitf regulation of Dia1 controls melanoma proliferation and invasiveness. *Genes Dev*. **20**(24): p. 3426-39. DOI: 10.1101/gad.406406.
196. Landsberg, J, Kohlmeyer, J, Renn, M, et al., (2012) Melanomas resist T-cell therapy through inflammation-induced reversible dedifferentiation. *Nature*. **490**(7420): p. 412-6. DOI: 10.1038/nature11538.
197. Coulie, PG, Brichard, V, Van Pel, A, et al., (1994) A new gene coding for a differentiation antigen recognized by autologous cytolytic T lymphocytes on HLA-A2 melanomas. *J Exp Med*. **180**(1): p. 35-42. DOI: 10.1084/jem.180.1.35.
198. Fassler, M, Diem, S, Mangana, J, et al., (2019) Antibodies as biomarker candidates for response and survival to checkpoint inhibitors in melanoma patients. *J Immunother Cancer*. **7**(1): p. 50. DOI: 10.1186/s40425-019-0523-2.
199. Falletta, P, Sanchez-Del-Campo, L, Chauhan, J, et al., (2017) Translation reprogramming is an evolutionarily conserved driver of phenotypic plasticity and therapeutic resistance in melanoma. *Genes Dev*. **31**(1): p. 18-33. DOI: 10.1101/gad.290940.116.
200. Ferguson, J, Smith, M, Zudaire, I, et al., (2017) Glucose availability controls ATF4-mediated MITF suppression to drive melanoma cell growth. *Oncotarget*. **8**(20): p. 32946-32959. DOI: 10.18632/oncotarget.16514.
201. Pakos-Zebrucka, K, Koryga, I, Mnich, K, et al., (2016) The integrated stress response. *EMBO Rep*. **17**(10): p. 1374-1395. DOI: 10.15252/embr.201642195.

202. Chen, D, Fan, Z, Rauh, M, et al., (2017) ATF4 promotes angiogenesis and neuronal cell death and confers ferroptosis in a xCT-dependent manner. *Oncogene*. **36**(40): p. 5593-5608. DOI: 10.1038/onc.2017.146.
203. Shi, Z, Yu, X, Yuan, M, et al., (2019) Activation of the PERK-ATF4 pathway promotes chemo-resistance in colon cancer cells. *Sci Rep*. **9**(1): p. 3210. DOI: 10.1038/s41598-019-39547-x.
204. Smith, MP, Rowling, EJ, Miskolczi, Z, et al., (2017) Targeting endothelin receptor signalling overcomes heterogeneity driven therapy failure. *EMBO Mol Med*. **9**(8): p. 1011-1029. DOI: 10.15252/emmm.201607156.
205. Park, SH, Kim, JH, Ko, E, et al., (2018) Resistance to gefitinib and cross-resistance to irreversible EGFR-TKIs mediated by disruption of the Keap1-Nrf2 pathway in human lung cancer cells. *FASEB J*: p. fj201800011R. DOI: 10.1096/fj.201800011R.
206. Krall, EB, Wang, B, Munoz, DM, et al., (2017) KEAP1 loss modulates sensitivity to kinase targeted therapy in lung cancer. *Elife*. **6**. DOI: 10.7554/eLife.18970.
207. Cristescu, R, Mogg, R, Ayers, M, et al., (2018) Pan-tumor genomic biomarkers for PD-1 checkpoint blockade-based immunotherapy. *Science*. **362**(6411). DOI: 10.1126/science.aar3593.
208. Hastings, K, Yu, HA, Wei, W, et al., (2019) EGFR mutation subtypes and response to immune checkpoint blockade treatment in non-small-cell lung cancer. *Ann Oncol*. **30**(8): p. 1311-1320. DOI: 10.1093/annonc/mdz141.
209. Dong, ZY, Zhang, JT, Liu, SY, et al., (2017) EGFR mutation correlates with uninflamed phenotype and weak immunogenicity, causing impaired response to PD-1 blockade in non-small cell lung cancer. *Oncoimmunology*. **6**(11): p. e1356145. DOI: 10.1080/2162402X.2017.1356145.
210. Ayeni, D, Miller, B, Kuhlmann, A, et al., (2019) Tumor regression mediated by oncogene withdrawal or erlotinib stimulates infiltration of inflammatory immune cells in EGFR mutant lung tumors. *J Immunother Cancer*. **7**(1): p. 172. DOI: 10.1186/s40425-019-0643-8.
211. Eberhart, CE, Coffey, RJ, Radhika, A, et al., (1994) Up-regulation of cyclooxygenase 2 gene expression in human colorectal adenomas and adenocarcinomas. *Gastroenterology*. **107**(4): p. 1183-1188. DOI: 10.1016/0016-5085(94)90246-1.
212. DuBois, RN, Abramson, SB, Crofford, L, et al., (1998) Cyclooxygenase in biology and disease. *The FASEB Journal*. **12**(12): p. 1063-1073. DOI: 10.1096/fasebj.12.12.1063.
213. Wang, D and Dubois, RN, (2010) Eicosanoids and cancer. *Nat Rev Cancer*. **10**(3): p. 181-93. DOI: 10.1038/nrc2809.
214. Schütze, S, Wiegmann, K, Machleidt, T, et al., (1995) TNF-Induced Activation of NF-κB. *Immunobiology*. **193**(2-4): p. 193-203. DOI: 10.1016/s0171-2985(11)80543-7.
215. Ulivi, V, Giannoni, P, Gentili, C, et al., (2008) p38/NF-kB-dependent expression of COX-2 during differentiation and inflammatory response of chondrocytes. *J Cell Biochem*. **104**(4): p. 1393-406. DOI: 10.1002/jcb.21717.
216. Jin, J, Zhao, L, Zou, W, et al., (2018) Activation of Cyclooxygenase-2 by ATF4 During Endoplasmic Reticulum Stress Regulates Kidney Podocyte Autophagy Induced by Lupus Nephritis. *Cell Physiol Biochem*. **48**(2): p. 753-764. DOI: 10.1159/000491904.
217. Luo, B, Lin, Y, Jiang, S, et al., (2016) Endoplasmic reticulum stress eIF2alpha-ATF4 pathway-mediated cyclooxygenase-2 induction regulates cadmium-induced autophagy in kidney. *Cell Death Dis*. **7**(6): p. e2251. DOI: 10.1038/cddis.2016.78.
218. Vivas-Garcia, Y, Falletta, P, Liebing, J, et al., (2020) Lineage-Restricted Regulation of SCD and Fatty Acid Saturation by MITF Controls Melanoma Phenotypic Plasticity. *Mol Cell*. **77**(1): p. 120-137 e9. DOI: 10.1016/j.molcel.2019.10.014.
219. Schmitt, A, Schmitz, W, Hufnagel, A, et al., (2015) Peroxiredoxin 6 triggers melanoma cell growth by increasing arachidonic acid-dependent lipid signalling. *Biochem J*. **471**(2): p. 267-79. DOI: 10.1042/BJ20141204.

220. Wiemer, AJ, Hegde, S, Gumperz, JE, et al., (2011) A live imaging cell motility screen identifies prostaglandin E2 as a T cell stop signal antagonist. *J Immunol*. **187**(7): p. 3663-70. DOI: 10.4049/jimmunol.1100103.
221. Burdette, DL, Monroe, KM, Sotelo-Troha, K, et al., (2011) STING is a direct innate immune sensor of cyclic di-GMP. *Nature*. **478**(7370): p. 515-8. DOI: 10.1038/nature10429.
222. Fuertes, MB, Woo, SR, Burnett, B, et al., (2013) Type I interferon response and innate immune sensing of cancer. *Trends Immunol*. **34**(2): p. 67-73. DOI: 10.1016/j.it.2012.10.004.
223. Falahat, R, Perez-Villarroel, P, Mailloux, AW, et al., (2019) STING Signaling in Melanoma Cells Shapes Antigenicity and Can Promote Antitumor T-cell Activity. *Cancer Immunol Res*. **7**(11): p. 1837-1848. DOI: 10.1158/2326-6066.CIR-19-0229.
224. DuPage, M, Mazumdar, C, Schmidt, LM, et al., (2012) Expression of tumour-specific antigens underlies cancer immunoediting. *Nature*. **482**(7385): p. 405-9. DOI: 10.1038/nature10803.
225. Jerby-Arnon, L, Shah, P, Cuoco, MS, et al., (2018) A Cancer Cell Program Promotes T Cell Exclusion and Resistance to Checkpoint Blockade. *Cell*. **175**(4): p. 984-997 e24. DOI: 10.1016/j.cell.2018.09.006.
226. Leibowitz, MS, Srivastava, RM, Andrade Filho, PA, et al., (2013) SHP2 is overexpressed and inhibits pSTAT1-mediated APM component expression, T-cell attracting chemokine secretion, and CTL recognition in head and neck cancer cells. *Clin Cancer Res*. **19**(4): p. 798-808. DOI: 10.1158/1078-0432.CCR-12-1517.
227. Kelland, LR, (2004) Of mice and men: values and liabilities of the athymic nude mouse model in anticancer drug development. *Eur J Cancer*. **40**(6): p. 827-36. DOI: 10.1016/j.ejca.2003.11.028.
228. Christianson, SW, Greiner, DL, Schweitzer, IB, et al., (1996) Role of natural killer cells on engraftment of human lymphoid cells and on metastasis of human T-lymphoblastoid leukemia cells in C57BL/6J-scid mice and in C57BL/6J-scid bg mice. *Cell Immunol*. **171**(2): p. 186-99. DOI: 10.1006/cimm.1996.0193.
229. Mombaerts, P, Iacomini, J, Johnson, RS, et al., (1992) RAG-1-deficient mice have no mature B and T lymphocytes. *Cell*. **68**(5): p. 869-877. DOI: 10.1016/0092-8674(92)90030-g.
230. Leiter, EH, (1993) The NOD Mouse: A Model for Analyzing the Interplay Between Heredity and Environment in Development of Autoimmune Disease. *ILAR Journal*. **35**(1): p. 4-14. DOI: 10.1093/ilar.35.1.4.
231. Kobayashi, EH, Suzuki, T, Funayama, R, et al., (2016) Nrf2 suppresses macrophage inflammatory response by blocking proinflammatory cytokine transcription. *Nat Commun*. **7**: p. 11624. DOI: 10.1038/ncomms11624.
232. Zhu, H, Jia, Z, Trush, MA, et al., (2016) Nrf2 Deficiency Promotes Melanoma Growth and Lung Metastasis. *Reactive Oxygen Species*. DOI: 10.20455/ros.2016.853.
233. Zhou, X, Jeker, LT, Fife, BT, et al., (2008) Selective miRNA disruption in T reg cells leads to uncontrolled autoimmunity. *J Exp Med*. **205**(9): p. 1983-91. DOI: 10.1084/jem.20080707.
234. Rickert, RC, Rajewsky, K, and Roes, J, (1995) Impairment of T-cell-dependent B-cell responses and B-1 cell development in CD19-deficient mice. *Nature*. **376**(6538): p. 352-5. DOI: 10.1038/376352a0.
235. de Boer, J, Williams, A, Skavdis, G, et al., (2003) Transgenic mice with hematopoietic and lymphoid specific expression of Cre. *Eur J Immunol*. **33**(2): p. 314-25. DOI: 10.1002/immu.200310005.
236. Clausen, BE, Burkhardt, C, Reith, W, et al., (1999) Conditional gene targeting in macrophages and granulocytes using LysMcre mice. *Transgenic Res*. **8**(4): p. 265-77. DOI: 10.1023/a:1008942828960.

237. Narni-Mancinelli, E, Chaix, J, Fenis, A, et al., (2011) Fate mapping analysis of lymphoid cells expressing the NKp46 cell surface receptor. *Proc Natl Acad Sci U S A*. **108**(45): p. 18324-9. DOI: 10.1073/pnas.1112064108.
238. Markosyan, N, Li, J, Sun, YH, et al., (2019) Tumor cell-intrinsic EPHA2 suppresses anti-tumor immunity by regulating PTGS2 (COX-2). *J Clin Invest*. **129**(9): p. 3594-3609. DOI: 10.1172/JCI127755.
239. Clinicaltrials.gov - Bethesda (MD): National Library of Medicine (US) - Prostaglandin Inhibition and Immune Checkpoint Blockade in Melanoma Identifier: NCT03396952 [cited 29 September 2020] - available from https://clinicaltrials.gov/ct2/show/NCT03396952?term=aspirin&cond=Melanoma&draw=2&rank=3.
240. Clinicaltrials.gov - Bethesda (MD): National Library of Medicine (US) - PD-1 Antibody Combined With COX Inhibitor in MSI-H/dMMR or High TMB Colorectal Cancer (PCOX) Identifier:NCT03638297 [cited 29 September 2020] - available from: https://clinicaltrials.gov/ct2/show/NCT03638297?term=cox2%2C+pd1&cond=Cancer&draw=2&rank=1.
241. Marloye, M, Lawler, SE, and Berger, G, (2019) Current patent and clinical status of stimulator of interferon genes (STING) agonists for cancer immunotherapy. *Pharm Pat Anal*. **8**(4): p. 87-90. DOI: 10.4155/ppa-2019-0013.
242. Corrales, L, Glickman, LH, McWhirter, SM, et al., (2015) Direct Activation of STING in the Tumor Microenvironment Leads to Potent and Systemic Tumor Regression and Immunity. *Cell Rep*. **11**(7): p. 1018-30. DOI: 10.1016/j.celrep.2015.04.031.
243. Clinicaltrials.gov - Bethesda (MD): National Library of Medicine (US) - Study of MK-1454 Alone or in Combination With Pembrolizumab (MK-3475) in Participants With Advanced/Metastatic Solid Tumors or Lymphomas (MK-1454-001) Identifier:NCT03010176 [cited 29 September 2020] - available from: https://clinicaltrials.gov/ct2/show/NCT03010176?term=NCT03010176&draw=2&rank=1.
244. Clinicaltrials.gov - Bethesda (MD): National Library of Medicine (US) -Study of the Safety and Efficacy of MIW815 With PDR001 to Patients With Advanced/Metastatic Solid Tumors or Lymphomas Identifier:NCT03172936 [cited 29 September 2020] - available from: https://clinicaltrials.gov/ct2/show/NCT03172936?term=NCT03172936&draw=2&rank=1.
245. Clinicaltrials.gov - Bethesda (MD): National Library of Medicine (US) -Safety and Efficacy of MIW815 (ADU-S100) +/- Ipilimumab in Patients With Advanced/Metastatic Solid Tumors or Lymphomas Identifier: NCT02675439 [cited 29 September 2020] - available from: https://clinicaltrials.gov/ct2/show/NCT02675439?term=NCT02675439&draw=2&rank=1.
246. Such, L, Zhao, F, Liu, D, et al., (2020) Targeting the innate immunoreceptor RIG-I overcomes melanoma-intrinsic resistance to T cell immunotherapy. *J Clin Invest*. **130**(8): p. 4266-4281. DOI: 10.1172/JCI131572.

9. Appendix

9.1 List of predicted direct NRF2 target genes and motif analysis

NRF2 direct target genes were predicted by comparison of the ChIP-Seq data and the expression data after NRF2 knockdown in UACC-62 melanoma cell lines. All genes with a peak around 5 kb around the TSS were set as direct target genes predicted by the Binding and Expression Target Analysis (BETA-basic). The complete list of predicted direct target genes is shown in Table 22.

Table 22 – Predicted direct target genes with peaks ±5 kb of the TSS of the nearest gene

NRF2 induced		NRF2 repressed	
DMSO	**SFN**	**DMSO**	**SFN**
G6PD	*G6PD*	*COA6*	*MVP*
ANXA2P2	*EBF1*	*GCNT2*	*VPS11*
GPD2	*ARHGAP35*	*LRP8*	*PROC*
HMOX1	*ZNF184*	*SQSTM1*	*TNPO1*
TBC1D13	*IL1R1*	*PRDX1*	*GPX4*
KEAP1	*ANXA2P2*	*CNTNAP4*	*PSCA*
ME1	*TRIM58*	*NLN*	*ETFB*
LBR	*COL19A1*	*SGTB*	*NEAT1*
NQO1	*GPD2*	*SLC48A1*	*COA6*
TMCC2	*LAMB3*		*CA8*
FTH1	*HMOX1*		*SIGLEC17P*
KRT3	*TM4SF1*		*PSMG3-AS1*
	TM4SF1-AS1		*GCNT2*
	LINC00297		*ST3GAL4*
	ZNF680		*NEFH*
	SETD1B		*LRP8*
	TBC1D13		*EPB41*
	ARHGEF12		*NUDT6*
	MED20		*SFTPC*
	NUP153		*JKAMP*
	SSH1		*MIR22HG*
	CHAF1B		*HIST1H4B*
	NDRG1		*NAPB*
	MAP3K19		*LINC00589*
	ZNF746		*BLVRB*
	DCC		*SQSTM1*
	GRPR		*ABCB6*
	COL19A1		*GABARAPL1*
	FLRT2		*CAMKK1*
	MPZ		*ZFAND5*
	C9orf3		*DGAT2L6*
	MATR3		*HM13-AS1*
	PDE6H		*SGK2*

	ANXA2		*SQSTM1*
	PCOLCE2		*MIR4458HG*
	ADCY7		*CDKN1A*
	ANGPT1		*LINC01269*
	MEPE		*ANKRD28*
	DIXDC1		*ALDOA*
	POPDC3		*AIFM2*
	PFN2		*NINJ2*
	NEIL3		*MIR6073*
	PDCL		*PSMB6*
	SFXN5		*FAM219A*
	LAMC1		*TNPO1*
	LINC00563		*PRDX1*
	SLC1A5		*BCL2L13*
	AGBL5		*MAFG*
	BRD2		*ZBTB20*
	DBF4B		*LINC-PINT*
	STYK1		*DGCR6L*
	SH3TC2		*LINC00570*
	CDK14		*SCARNA20*
	CREB5		*MIR22HG*
	E2F6		*ASPSCR1*
	OR4F3		*EGLN3*
	CLTC		*GABARAPL1*
	ROBO2		*ABHD4*
	SMARCD2		*MIR22HG*
	BLMH		*PLS3*
	PTGES3		*OPN3*
	HTATIP2		*ABCC2*
	CLPB		*MIR619*
	KEAP1		*CNTNAP4*
	LBR		*HSPB8*
	ME1		*PITHD1*
	F2RL2		*UBL3*
	SH3KBP1		*NLN*
	GCLM		*SGTB*
	SLC3A2		*SLC48A1*
	EGF		*LINC00884*
	TBXAS1		*LGI3*
	SRXN1		*TNK2*
	C1orf198		*SPTSSA*
	SLC7A11		*PRDX1*
	AHCYL1		*CES1*
	ZNF3		*MAFG*
	SRSF2		*SCARB1*
	CLIC2		*SLC48A1*
	NFE2L2		*CDK5R1*

	GSTP1		*ACTR3*
	UBC		*SLC22A23*
	CLTC		*HIST1H4A*
	MORF4L1		*ADAM23*
	TXN		*TLCD2*
	CBX6		*ATP6V1E1*
	NQO1		*LINC01087*
	ZMYND8		*MTFR1L*
	COTL1		
	MTMR2		
	EIF6		
	MSN		
	SH3BP5		
	MGST1		
	UBC		
	PMF1		
	IL13RA2		
	RAB35		
	CDKN3		
	BAG2		
	MUC5B		
	UBC		
	PES1		
	ADAM9		
	STARD13		
	TMCC2		
	TPM4		
	FAM83D		
	HJURP		
	CEP85		
	IPO8		
	CDCA4		
	MIR29C		
	PREX1		
	SYTL2		
	FTH1		
	AKIRIN2		
	FZD7		
	IPO8		
	KRT3		
	ASPH		

With the derived ChIP-Seq data, sequence motif analysis for overrepresented transcription factor binding sites (TFBS) were conducted. The motif analysis was performed with the SeqMotif package of the galaxy platform. The table 23 displays the IDs of the 15 most overrepresented TFBS with similarity to the *NFE2L2* binding motif.

Table 23 – Overrepresented TFBS determined by the SeqMotif package

Rank	DMSO			SFN		
	TF	ID	similarity to top	TF	ID	similarity to top
1	NFE2L2	MC00339		NFE2L2	MC00339	
2	MAFG	MCS00327	0.936	FOSL1	MC00351	0.877
3	MAFB	UP00045	0.945	Tbx21	MC00356	0.877
4	MAF	M00983	0.974	JUNB	MC00371	0.864
5	JUN	MC00321	0.922	MAF	M00983	0.942
6	JUNB	MC00371	0.888	JUN	MC00321	0.887
7	FOSL1	MC00351	0.900	FOS	MC00330	0.879
8	Tbx21	MC00356	0.900	MAFF	MS00326	0.936
9	BACH1	M00495	0.991	BACH1	M00495	0.943
10	NFE2	MS00336	0.899	BACH2	M00490	0.857
11	MAFF	MS00326	0.974	NFE2	MS00336	0.865
12	BACH2	M00490	0.891	MAFK	MS00331	0.921
13	MAFK	MS00331	0.971	FOXB1	MS00343	0.893
14	FOXB1	MS00343	0.936	ATF4	M00514	0.869
15	ATF4	M00514	0.933	JUND	MC00456	0.906

9.2 List of Figures

9.3 List of Tables

9.4 Abbreviations

#	
4-OHT	4-hydroxytamoxifen
A	
aa	Amino acid
AA	Arachidonic acid
AMP	adenosine monophosphate
APS	Ammonium peroxodisulfate
ATP	Adenosine triphosphate
B	
bp	Base pair
BCC	Basal cell carcinoma
BSA	Bovine serum albumine
C	
CDK	Cyclin dependent kinase
cDNA	complementary deoxyribonucleic acid
ChIP	Chromatin immunoprecipitation
ChIP-Seq	Chromatin immunoprecipitation sequencing
Ct	Cycle threshold
Ctrl	Control
Cys	Cysteine
D	
d	days
DABCO	1,4-Diazabicyclo[2.2.2]octane
ddH_2O	Double-distilled water
DEPC	Diethyl pyrocarbonate
DMEM	Dulbecco's modified eagle medium
DNA	Deoxyribonucleic acid
dNTP	Deoxyribonucleotide triphosphate
Dox	Doxycycline
DTNB	5, 5'-Dithiobis(2-nitrobenzoic acid)
E	
ECL	Enhanced chemiluminescence solution
EDTA	Ethylenediaminetetraacetic acid
EGF	Epidermal growth factor
F	
FBS	Fetal bovine serum
FCS	Fetal calf serum
G	
G2	Gap2 phase
gDNA	Genomic deoxyribonucleic acid
GFP	green fluorescent protein
GMP	Guanosine monophosphate
GOI	Gene of interest
GSH	glutathione
GSSG	Glutathione disulfide
H	
h	hours
HG	Housekeeping gene
HRP	Horseradish peroxidase
I	
IB	Immunoblot
IBMX	3-isobutyl-1-methylxanthine
IF	Immunofluorescence
IFN-α/-γ	Interferon alpha/gamma
IHC	Immunohistochemistry
IL-2	Interleukine-2
IRES	internal ribosome entry site
ITS	Insulin, transferrin, selenium supplement
K	
K	Lysine
kb	Kilobase
kDA	Kilodalton
KO	knockout
L	
LB	Luria Bertani
M	
M phase	Mitosis and cytokinesis
MCC	Merkel cell carcinoma
α-MSH	alpha-melanocyte-stimulating hormone
MTT	3-(4,5-Dimethylthiazol-2-yl)-2,5-diphenyltetrazoliumbromid
N	
NMSC	Non-melanoma skin cancer
NRF2	Nuclear Factor, Erythroid 2 Like 2 protein
NSCLC	Non-small cell lung cancer

O	
OptiMEM	Opti-Minimum essential medium
P	
PAGE	Polyacrylamide gel electrophoresis
PBS	Phosphate buffered saline
PCR	Polymerase chain reaction
PFA	Paraformaldehyde
PGE2	Prostaglandin E2
PMSF	Phenylmethylsulphonyl fluoride
P/S	Penicillin-Streptomycin
Q	
qPCR	Quantitative real-time polymerase chain reaction
R	
RNA	Ribonucleic acid
RNA-Seq	Ribonucleic acid sequencing
ROS	Reactive oxygen species
rpm	Rounds per minute
RT	Room temperature
RTK	Receptor tyrosine kinases
S	
SB	Sleeping beauty
SCC	Squamous cell carcinoma
SD	Standard deviation
SDS	Sodium dodecyl sulfate
SFN	R,S-Sulforaphane
siRNA	Small interfering ribonucleic acid
SKCM	Skin cutaneous melanoma
SSA	5-Sulfosalicylic acid hydrate
T	
TAE	Tris-acetic acid-EDTA buffer
TBS	Tris-buffered saline
TBS-T	Tris-buffered saline-Tween
TE	Tris-EDTA buffer
TEMED	N'N'N'N'-tetramethyl ethylene-diamine
tBHQ	tert-butylhydroquinone
TME	Tumor microenvironment
TNFα	Tumor necrosis factor alpha
TPA	12-O-tetradecanoylphorbol 13-acetate
trame	trametinib
Tris	Tris(hydroxymethyl)aminomethane
Trx	Thioredoxin
U	
UV	Ultraviolet
UVR	Ultraviolet radiation
V	
Vem	vemurafenib
VGP	Vertical-growth-phase
W	
WB	Western blot
wt	wildtype

9.5 Curriculum vitae

9.6 Publication list and conference contributions

9.6.1 Publications

Jessen C, Kreß JKC, Baluapuri A, Hufnagel A, Schmitz W, Kneitz S, Roth S, Marquardt A, Appenzeller S, Ade CP, Glutsch V, Wobser M, Friedmann-Angeli JP, Mosteo L, Goding CR, Schilling B, Geissinger E, Wolf E, Meierjohann S. "The transcription factor NRF2 enhances melanoma malignancy by blocking differentiation and inducing COX2 expression" *Oncogene*. **in press**, https://doi.org/10.1038/s41388-020-01477-8

Appenzeller S, Gesierich A, Thiem A, Hufnagel A, **Jessen C**, Kneitz H, Regensburger M, Schmidt C, Zirkenbach V, Bischler T, Schilling B, Siedel C, Goebeler ME, Houben R, Schrama D, Gehrig A, Rost S, Maurus K, Bargou R, Rosenwald A, Schartl M, Goebeler M, Meierjohann S. "The identification of patient-specific mutations reveals dual pathway activation in most patients with melanoma and activated receptor tyrosine kinases in BRAF/NRAS wild-type melanomas." *Cancer*. 2019;125(4):586-600. https://doi.org/10.1002/cncr.31843

Huggins IJ, Bos T, Gaylord O, **Jessen C**, Lonquich B, Puranen A, Richter J, Rossdam C, Brafman D, Gaasterland T, Willert K. "The WNT target SP5 negatively regulates WNT transcriptional programs in human pluripotent stem cells." *Nat Commun*. 2017;8(1):1034. https://doi.org/10.1038/s41467-017-01203-1

9.6.2 Conference contributions

09/2019 **Talk at the 22nd ESPCR meeting** in Brussels, Belgium
Talk title: "NRF2 maintains melanoma growth by regulating stress-induced resistance factors."

10/2018 **Poster at the 13th Eureka International GSLS student Symposium** in Würzburg, Germany
Poster title: „The involvement of the redox regulator NRF2 in melanoma tumor evasion"

10/2017 **Poster at the 12th Eureka International GSLS student Symposium** in Würzburg, Germany
Poster title: „The role of the transcription factor NRF2 and its target genes in melanoma"

03/2017 **Poster at the 19th International AEK Cancer Congress** in Heidelberg, Germany
Poster title: „The role of the transcription factor NRF2 and its target genes in melanoma"

10/2016 **Poster at the 11th Eureka International GSLS student Symposium** in Würzburg, Germany
Poster title: „NRF2 and its target genes in melanoma"

9.7 Acknowledgements

Zuallererst möchte ich mich bei Prof. Dr. Svenja Meierjohann bedanken, welche mir das Vertrauen schenkte auch nach meiner Masterarbeit an einem spannenden Projekt in ihrer Arbeitsgruppe weiterzuarbeiten. In den letzten fünf Jahre hat sie mich immer wieder mit Ihrer positiven und enthusiastischen Art motiviert und unterstützt. Darüber hinaus haben ihre konstruktiven Anregungen in besonderem Maße zum Gelingen dieser Arbeit beigetragen.

Des Weiteren danke ich den Mitgliedern meines Thesis-Komitees, Prof. Dr. Thomas Rudel und Prof. Dr. Stefan Gaubatz für ihren wissenschaftlichen Input und ihre Ratschläge während meiner Promotionszeit.

Für die gute Zusammenarbeit und experimentelle, sowie bioinformatische Unterstützung bedanke ich mich bei Dr. Carsten Ade, Dr. Susanne Kneitz, Dr. Werner Schmitz, Dr. Grit Weinstock, Apoorva Baluapuri, Dr. Silke Appenzeller, Andre Marquardt, Prof. Dr. Eva Geissinger, Sabine Roth und Prof. Dr. Andreas Rosenwald.

Ein besonderer Dank geht an alle ehemaligen und derzeitigen Mitglieder der Meierjohann Arbeitsgruppe. Allen voran Anita Hufnagel, welche stets ein offenes Ohr für jegliche Probleme hatte, egal ob wissenschaftlicher oder privater Natur. Außerdem danke ich Madlen Staus, Rupesh Paudel, Tamsanqa Hove, Julia Kreß und Vanessa Zirkenbach für unseren wissenschaftlichen Austausch und die großartigen Kaffee-, Eis- und Eiskaffeepausen.

Für die angenehme Arbeitsatmosphäre und Hilfsbereitschaft bedanke ich mich bei allen Freunden und Kollegen der Lehrstühle „Physiologischen Chemie I bzw. Biochemie und Zellbiologie“ und der Entwicklungsbiochemie.

Ein wichtiger Halt außerhalb des Labors waren meine Familie und Freunde, vielen Dank an alle, die mich während meiner Promotion unterstützt haben. Ihr habt immer an mich geglaubt, auch wenn ihr nicht genau verstanden habt, womit ich mich überhaupt beschäftige.

Zuletzt danke ich meinem Freund Marco, der mich in dieser herausfordernden Phase ertragen, unterstützt und ermutigt hat. Vielen Dank für dein offenes Ohr und unsere wissenschaftlichen Diskussionen am Esstisch.

9.8 Affidavit

9.8.1 Affidavit

I hereby confirm that my thesis entitled “NRF2 links antioxidant and immune-relevant features in melanoma” is the result of my own work. I did not receive any help or support from commercial consultants. All sources and / or materials applied are listed and specified in the thesis.

Furthermore, I confirm that this thesis has not yet been submitted as part of another examination process neither in identical nor in similar form.

Würzburg, 08.10.2020 _____
Place, Date Signature

9.8.2 Eidesstattliche Erklärung

Hiermit erkläre ich an Eides statt, die Dissertation „NRF2 verknüpft antioxidative und immunrelevante Eigenschaften im Melanom“ eigenständig, d.h. insbesondere selbstständig und ohne Hilfe eines kommerziellen Promotionsberaters, angefertigt und keine anderen als die von mir angegebenen Quellen und Hilfsmittel verwendet zu haben.

Ich erkläre außerdem, dass die Dissertation weder in gleicher noch in ähnlicher Form bereits in einem anderen Prüfungsverfahren vorgelegen hat.

Würzburg, 08.10.2020 _____
Ort, Datum Unterschrift